Universidad de Oviedo

Programa de Doctorado en Energía y Control de Procesos

COMPARACIÓN DE SISTEMAS DE CONTROL Y ESTRATEGIAS DE OPTIMIZACIÓN EN PLANTAS DE ENERGÍA SOLAR DE CICLO COMBINADO INTEGRADO (ISCC)

Doctorando:

Adham Mohamed Abdelhalim Abdelfattah

Gijón, 2024

Universidad de Oviedo

PhD Program in Energy and Process Control

COMPARISON OF CONTROL SYSTEMS AND OPTIMIZATION STRATEGIES IN INTEGRATED SOLAR COMBINED CYCLE (ISCC) POWER PLANTS

PhD Candidate:

Adham Mohamed Abdelhalim Abdelfattah

Gijón, 2024

Universidad de Oviedo

Departamento de Energía

Programa de Doctorado en Energía y Control de Procesos

COMPARACIÓN DE SISTEMAS DE CONTROL Y ESTRATEGIAS DE OPTIMIZACIÓN EN PLANTAS DE ENERGÍA SOLAR DE CICLO COMBINADO INTEGRADO (ISCC)

Doctorando:

Adham Mohamed Abdelhalim Abdelfattah

Directores:

Dr. Inés María Suárez Ramón

Dr. Andrés Meana Fernández

Gijón, 2024

Universidad de Oviedo

Department of Energy

PhD Program in Energy and Process Control

COMPARISON OF CONTROL SYSTEMS AND OPTIMIZATION STRATEGIES IN INTEGRATED SOLAR COMBINED CYCLE (ISCC) POWER PLANTS

PhD Candidate:

Adham Mohamed Abdelhalim Abdelfattah

Supervisors:

Dr. Inés María Suárez Ramón

Dr. Andrés Meana Fernández

Gijón, 2024

Universidad de Oviedo

RESUMEN DEL CONTENIDO DE TESIS DOCTORAL

1.- Título de la Tesis	
Español/Otro Idioma: Comparación de sistemas de control y estrategias de optimización en plantas de energía solar de ciclo combinado integrado (ISCC)	Inglés: Comparison of control systems and optimization strategies in integrated solar combined cycle (ISCC) power plants

2.- Autor	
Nombre: Adham Mohamed Abdelhalim	
Programa de Doctorado: Energía y Control de Procesos	
Órgano responsable: Centro Internacional de Posgrado	

RESUMEN (en español)

La incorporación de energía termosolar a las centrales de ciclo combinado representa un importante avance para aumentar su potencia y eficiencia energética. Con el objetivo de mejorar el rendimiento y la sostenibilidad de la generación de energía, esta tesis examina los beneficios y desafíos de esta hibridación. Al utilizar energía solar térmica para aumentar la generación eléctrica a partir de combustibles, las centrales híbridas termosolares de ciclo combinado integran dicha energía en ciclos convencionales de turbinas de gas y de vapor, mejorando la eficiencia energética y reduciendo las emisiones de carbono.

El objetivo de esta tesis es estudiar los aspectos técnicos y medioambientales de la integración de la energía termosolar en centrales de ciclo combinado. El fin de la investigación es maximizar la utilización de la energía solar y la integración adecuada mediante la optimización del funcionamiento del sistema híbrido. Se examinaron diferentes configuraciones y esquemas de operación, en los que la energía solar térmica se integró tanto en el ciclo superior de gas como en el ciclo inferior de vapor. Se aplicaron dos estrategias de operación: ahorro de combustible, para reducir la cantidad de combustible consumido en la planta, y el aumento de potencia, para maximizar la potencia de salida global de la planta híbrida. También se evalúa la capacidad de la hibridación para reducir las emisiones de gases de efecto invernadero y la dependencia de los combustibles fósiles, destacando sus beneficios medioambientales.

Se ha implementado un modelo termodinámico de una central eléctrica real de ciclo combinado utilizando el software MATLAB. Posteriormente, se ha modificado el modelo para estudiar el rendimiento del sistema híbrido para diferentes posiciones de integración de la energía solar térmica y distintos esquemas de operación. El estudio muestra que la integración de la energía solar térmica en las centrales de ciclo combinado puede mejorar en gran medida su eficiencia térmica, aumentando la producción de energía y disminuyendo el consumo de combustible. Los resultados indican que las plantas híbridas pueden aumentar su eficiencia hasta en un 5% de media y su potencia de salida en un 8,5%.

Esta investigación pone de manifiesto la importancia de utilizar la energía solar térmica como alternativa renovable y sostenible al gas natural, con el objetivo de construir una infraestructura energética más resiliente y respetuosa con el medio ambiente. También muestra los beneficios de integrar la energía solar térmica en una central eléctrica de ciclo combinado para mejorar su producción de energía y su eficiencia energética. En este sentido, los resultados clave, las ideas y las directrices proporcionadas en este trabajo pretenden contribuir a generar futuros avances en la generación de energía sostenible.

Universidad de Oviedo

RESUMEN (en Inglés)

A significant step forward in the goal of increasing power output and energy efficiency is the incorporation of solar thermal power into combined cycle power plants. Aiming to improve the performance and sustainability of power generation, this work examines the benefits and challenges of this hybrid technology. By utilizing solar heat to increase fuel-based electricity generation, hybridized solar thermal combined cycle power plants integrate solar thermal energy into conventional gas turbine and steam cycles, improving energy efficiency and reducing carbon emissions.

The objective of this thesis is to study technical and environmental aspects of integrating solar thermal power into combined cycle power plants. The goal of the research is to maximize solar energy utilization and adequate integration by optimizing the operation of the hybrid system. Different setups and operating schemes were examined, where solar thermal power was integrated into the top gas cycle and into the bottom steam cycle. Two operating strategies were applied: fuel saving, to reduce the amount of fuel consumption in the power plant, and power boosting, to maximize the overall output power of the hybrid plant. The ability of hybridization to reduce greenhouse gas emissions and the dependence on fossil fuels is also discussed, highlighting their environmental benefits.

A thermodynamic model of a real combined cycle power plant has been implemented using MATLAB software. Afterwards, the model has been modified to study the performance of the hybrid system for different solar thermal power integration positions and operating schemes. The study shows that integrating solar thermal power into combined cycle power plants can greatly improve their thermal efficiency, increasing power output and decreasing fuel consumption. The results indicate that hybrid plants can increase their efficiency by up to an average of 5% and their output power by 8.5%.

This research highlights the importance of using solar thermal energy as a renewable and sustainable alternative to natural gas, aiming to build a more resilient and ecologically friendly energy infrastructure. It also emphasizes the value of integrating solar thermal power in a combined cycle power plants to enhance power output and energy efficiency. The key results, insights and guidelines provided in this work aim to contribute to future advancements in sustainable power generation.

SR. PRESIDENTE DE LA COMISIÓN ACADÉMICA DEL PROGRAMA DE DOCTORADO EN ENERGÍA Y CONTROL DE PROCESOS

ACKNKOWLEDGEMENTS

It has taken a lot of time, many obstacles, and gratifying experiences to finish this Ph.D. thesis. Without the help, direction, and inspiration of numerous people-for whom I am incredibly thankful-it would not have been feasible.

First and foremost, I want to sincerely thank Dr. Inés María Suárez Ramón, my supervisor, for all of her help and support during my study. Your knowledge and commitment have been priceless, and your mentoring has influenced both my professional and academic development.

Additionally, I want to express my gratitude to Dr. Andrés Meana Fernández. Your unwavering encouragement, support, and perceptive disputes have been invaluable in helping me to refine my research and finish this thesis. Your deep attention to detail has been a great help, and your advice has been really helpful as I have navigated the challenges of my study.

On a personal note, I want to extend my sincere appreciation to my family for their never-ending support and affection. Thank you to my parents, Mohamed and Nehad, and my sister, Rovaida, for inspiring me to follow my aspirations and believing in me.

To my wife, Hagar, your endurance, comprehension, and constant backing have been my rock. Your assistance and sacrifices have enabled this accomplishment.

ABSTRACT

A significant step forward in the goal of increasing power output and energy efficiency is the incorporation of solar thermal power into combined cycle power plants. Aiming to improve the performance and sustainability of power generation, this work examines the benefits and challenges of this hybrid technology. By utilizing solar heat to increase fuel-based electricity generation, hybridized solar thermal combined cycle power plants integrate solar thermal energy into conventional gas turbine and steam cycles, improving energy efficiency and reducing carbon emissions.

The objective of this thesis is to study technical and environmental aspects of integrating solar thermal power into combined cycle power plants. The goal of the research is to maximize solar energy utilization and adequate integration by optimizing the operation of the hybrid system. Different setups and operating schemes were examined, where solar thermal power was integrated into the top gas cycle and into the bottom steam cycle. Two operating strategies were applied: fuel saving, to reduce the amount of fuel consumption in the power plant, and power boosting, to maximize the overall output power of the hybrid plant. The ability of hybridization to reduce greenhouse gas emissions and the dependence on fossil fuels is also discussed, highlighting their environmental benefits.

A thermodynamic model of a real combined cycle power plant has been implemented using MATLAB software. Afterwards, the model has been modified to study the performance of the hybrid system for different solar thermal power integration positions and operating schemes. The study shows that integrating solar thermal power into combined cycle power plants can greatly improve their thermal efficiency, increasing power output and decreasing fuel consumption. The results indicate that hybrid plants can increase their efficiency by up to an average of 5% and their output power by 8.5%.

This research highlights the importance of using solar thermal energy as a renewable and sustainable alternative to natural gas, aiming to build a more resilient and ecologically friendly energy infrastructure. It also emphasizes the value of integrating solar thermal power in a combined cycle power plants to enhance power output and energy efficiency. The key results, insights and guidelines provided in this work aim to contribute to future advancements in sustainable power generation.

RESUMEN

La incorporación de energía termosolar a las centrales de ciclo combinado representa un importante avance para aumentar su potencia y eficiencia energética. Con el objetivo de mejorar el rendimiento y la sostenibilidad de la generación de energía, esta tesis examina los beneficios y desafíos de esta hibridación. Al utilizar energía solar térmica para aumentar la generación eléctrica a partir de combustibles, las centrales híbridas termosolares de ciclo combinado integran dicha energía en ciclos convencionales de turbinas de gas y de vapor, mejorando la eficiencia energética y reduciendo las emisiones de carbono.

El objetivo de esta tesis es estudiar los aspectos técnicos y medioambientales de la integración de la energía termosolar en centrales de ciclo combinado. El fin de la investigación es maximizar la utilización de la energía solar y la integración adecuada mediante la optimización del funcionamiento del sistema híbrido. Se examinaron diferentes configuraciones y esquemas de operación, en los que la energía solar térmica se integró tanto en el ciclo superior de gas como en el ciclo inferior de vapor. Se aplicaron dos estrategias de operación: ahorro de combustible, para reducir la cantidad de combustible consumido en la planta, y el aumento de potencia, para maximizar la potencia de salida global de la planta híbrida. También se evalúa la capacidad de la hibridación para reducir las emisiones de gases de efecto invernadero y la dependencia de los combustibles fósiles, destacando sus beneficios medioambientales.

Se ha implementado un modelo termodinámico de una central eléctrica real de ciclo combinado utilizando el software MATLAB. Posteriormente, se ha modificado el modelo para estudiar el rendimiento del sistema híbrido para diferentes posiciones de integración de la energía solar térmica y distintos esquemas de operación. El estudio muestra que la integración de la energía solar térmica en las centrales de ciclo combinado puede mejorar en gran medida su eficiencia térmica, aumentando la producción de energía y disminuyendo el consumo de combustible. Los resultados indican que las plantas híbridas pueden aumentar su eficiencia hasta en un 5% de media y su potencia de salida en un 8,5%.

Esta investigación pone de manifiesto la importancia de utilizar la energía solar térmica como alternativa renovable y sostenible al gas natural, con el objetivo de construir una infraestructura energética más resiliente y respetuosa con el medio ambiente. También muestra los beneficios de integrar la energía solar térmica en una central eléctrica de ciclo combinado para mejorar su producción de energía y su eficiencia energética. En este sentido, los resultados clave, las ideas y las directrices proporcionadas en este trabajo pretenden contribuir a generar futuros avances en la generación de energía sostenible.

TABLE OF CONTENTS

LIST OF TABLES

LIST OF FIGURES

NOMENCLATURE

Abbreviations

ABB	Asea Brown Boveri
AS-1	Andasol-1
AU	Astronomical unit
BBC	Brown, Boveri & Cie
CapEx	Capital expenditure
CATT2	Computer-Aided Thermodynamics software
CC	Combined cycle
CF	Capacity factor
CLFR	Compact linear Fresnel reflector
CO_2	Carbon dioxide
CR	Central receiver
CSP	Concentrated solar power
DEWA	Dubai Electricity and Water Authority
DNI	Direct normal irradiance
DSG	Direct steam generation
EF	Emission factor
EPC	Egyptian Petrochemicals Company
ETC	Evacuated tube collector
FPC	Flat plate collector
GHG	Greenhouse gases
GT	Gas turbine
HCE	Heat collector element
HX	Heat exchanger
HP	High pressure
HRSG	Heat recovery steam generator
HTF	Heat transfer fluid
HYCS-FF	Hybrid concentrated solar fossil fuel
IdealAir	MATLAB toolbox for the air properties
IPCC	Intergovernmental Panel on Climate Change
IR	Infrared
IRENA	International renewable energy agency
ISCC	Integrated solar combined cycle
IST	Industrial solar technology
LCOE	Levelized cost of electricity
LFR	Linear Fresnel reflector
LP	Low pressure
NASA	National Aeronautics and Space Administration
NGCC	Natural gas combined cycle
NIP	Pyrheliometer
PCM	Phase change material
PDR	Parabolic dish reflector
PSA	Plataforma Solar de Almeria
PTC	Parabolic trough collector

PV	Photovoltaic
RES	Renewable energy resources
R&D	Research and Development
RH	Reheat
SBS	Spectral beam splitting
SEGS	Solar electric generating systems
SH	Superheater
SolarPACES	Solar Power And Chemical Energy Systems
SPT	Solar power tower
SSG	Solar steam generator
ST	Steam turbine
TES	Thermal energy storage
T-Q	Temperature-Heat
US	United States of America
UV	Ultraviolet
XSteam	MATLAB toolbox for the steam properties

Mathematical symbols

A_{col}	Area of solar collectors (m^2)
c	Specific heat (kJ/kg.K)
C	Heat capacity rate (kW/K)
C_r	Heat capacity ratio
d_n	Day number
e_{gas}	Chemical exergy of the natural gas (kJ/kg)
$EF_{NG \rightarrow CO_2}$	Emission factor between natural gas and CO_2
E_i	Equation of time
F_{solar}	Solar fraction
G_{bn}	Direct normal radiation (W/m^2)
HR	Heat rate
h_i	Specific enthalpy at state i (kJ/kg)
k	Heat capacity ratio
LHV	Lower heating value (kJ/kg)
$LMTD$	Logarithmic mean temperature difference
L_{loc}	Local longitude (degree)
L_{st}	Standard longitude (degree)
$\dot{m}_i$	Mass flowrate of fluid I (kg/s)
n	Yearly frequency (production days/year)
NTU	Number of transfer unit
P_i	Pressure at stage “i” (bar)
$\dot{Q}_{cc}$	Heat supplied in combustion chamber (kW)
$\dot{Q}_f$	Thermal heat supplied by fuel (W)
$\dot{Q}_i$	Heat transfer rate exchanged by component “I” (kW)
$\dot{Q}_{solar}$	Solar thermal heat, W
r_p	Pressure ratio
t	Time interval (s)
T_i	Temperature at stage “i” (K)

U	Overall heat transfer coefficient (W/m^2.K)
w_i	Specific work (kJ/kg)
w_{i_s}	Specific work of isentropic process (kJ/kg)
W	Collector mirror width (m)
$\dot{W}_i$	Power of component "i" (kW)
$\dot{W}_{solar}$	Solar power (W)
$\dot{W}_{Total}$	ISCC total power (W)
x	Shading factor

Greek letters

Δ	Increment
α	Absorptance
∂	Day angle (radian)
δ	Declination, degree
ε	Effectiveness, emissivity
η	Efficiency (%)
η_{solar}	Solar conversion efficiency (%)
$\eta_{solar\ field}$	Solar field efficiency (%)
θ	Angle of incidence (degree)
θ_z	Zenith angle (degree)
ρ	Specular reflectance
Φ	Latitude (degree)
τ	Transmittance
ω	Hour angle (degree)

Subscripts

a	Air
c	Compression
cc	Combustion chamber
col	Solar collectors
$comp$	Air compressor
eff	Effective
f	Fuel
GC	Gas cycle
GT	Gas turbine
loc	Local
opt	Optical
p	Pressure
s	Steam
SC	Steam cycle
st	Standard
ST	Steam turbine
$Total$	Combined cycle output power
v	Volume

CHAPTER ONE

INTRODUCTION

In this first chapter, the global energy context and clean energy crisis are discussed, where the importance of renewable energy resources in power generation for the essential needs is highlighted. Additionally, this chapter presents the difficulties and disadvantages of gas power plants that contributed to the shift in the use of renewable energy resources for generating power. Finally, the research methodology based on the main objectives is discussed and an outline of the thesis document is presented.

1.1 Global climate change crisis

The global climate change crisis that the world is currently experiencing is unprecedented in scope and complexity. This crisis is having a significant impact on markets, politics, and economies across the globe. The past decade has been the warmest on record due to the catastrophic acceleration of the global climate change problem. NASA reports that since the late 19th century, the average surface temperature of the Earth has increased by around 1.1°C [1], mostly as a result of rising carbon dioxide emissions and human activity. If immediate action is not taken, the Intergovernmental Panel on Climate Change (IPCC) cautions that the rate of warming by 2030 is likely to be higher than 1.5°C [2]. The effects are dire: since 1880, sea levels have risen by roughly 20 cm [3], and the rate is increasing. Furthermore, there has been an increase in the frequency and severity of extreme weather events including hurricanes, wildfires, and droughts. Over $100 billion in damages were caused globally by climate-related disasters in 2023 alone, underscoring the critical need for action to avert this escalating problem [4].

There is a scarcity of affordable, safe, and low-carbon large-scale energy solutions worldwide. The world will continue to face two energy issues as long as fossil fuels dominate our energy system: hundreds of millions of people lack access to clean energy, and the climate change and other negative health effects like air pollution. To guarantee that everyone has access to clean and safe energy, the current state of the world energy use, its effects, and how they have evolved over time must be understood. International energy commerce is undergoing a significant reorientation that will address long-standing vulnerabilities while also posing new market concerns.

Primary energy world consumption increased by +297% over the past 58 years, it is annotated as 43,361 TWh in 1965 and 172,119 TWh in 2023 [5]. Primary energy comprises the energy required by the end user for things like heating, transportation, and power, as well as inefficiencies and energy lost during the conversion of raw materials into a form that can be used. The same trend happens in all continents around the universe, Asia witnessed the highest increasing rate of 1,602% to reach a consumption of 91,422 TWh in 2023 [5]. In contrast, Europe showed one of the lowest rates, +49%, as the consumption of primary energy increased from 19,275 to 28,667 TWh during the period 1965-2023 [5]. Currently, China, United States and India take the lead of countries with the highest primary energy consumption with consumption of 47,428 , 26,189 and 10,838 TWh respectively [5]. The past statistics reflect the significant effect of the energy production sources to provide this enormous energy quantity.

Fossil fuel consumption has been increasing rapidly during the past decades. The world noticed an absolute increase of +99,736 TWh in consumption between the period 1965

to 2023, which represents an increasing percentage of +246% [5]. Figure 1.1 shows the fossil fuel consumption growth for continents between 1965-2023, Asia has the largest rate of consumption growth, with 77,848 TWh in 2023 compared to 4948 TWh in 1965 (+1473%) [5]. With respective consumption of 1560 and 4661 TWh, Oceania and South America exhibited the lowest consumption among the continents in 2023 [5]. China, with the world largest population, surpassed all other countries in terms of fossil fuel use, consuming 38,677 TWh in 2023 [5].

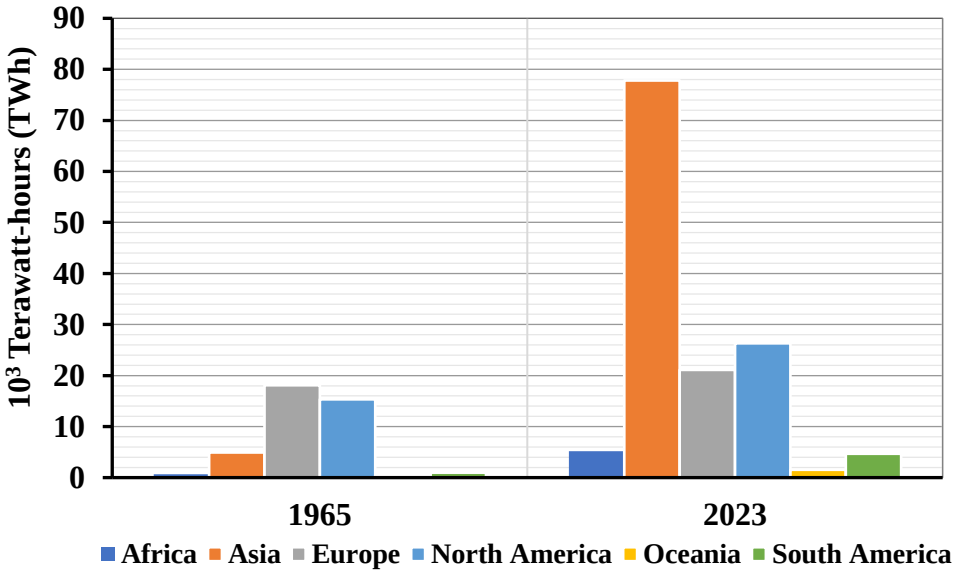

Figure 1.1 Primary energy consumption from fossil fuel [5]

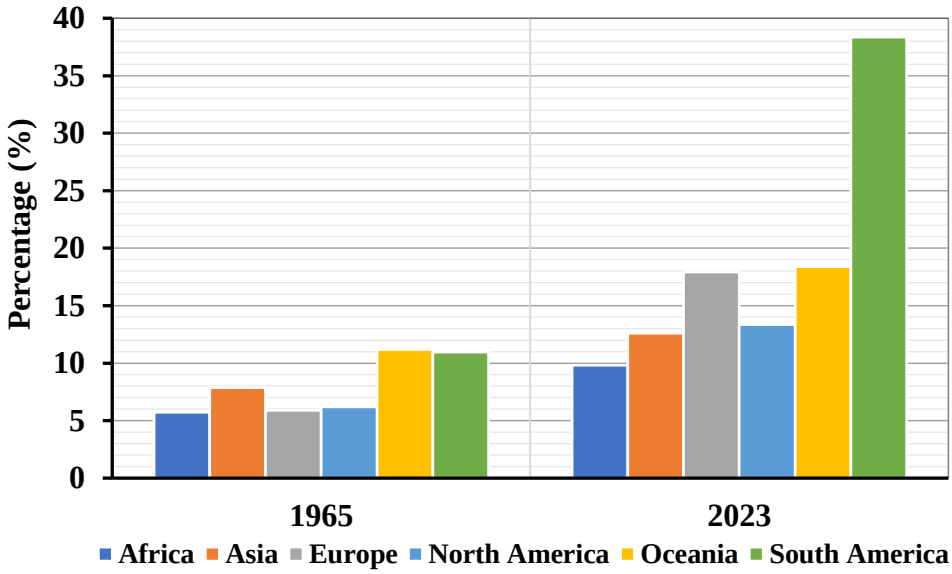

Figure 1.2 Share of primary energy consumption from renewable sources [5]

Presently, about one-seventh of the primary energy in the globe comes from renewable technology [5]. Figure 1.2 shows the share of primary energy consumption from renewable resources for all the continents over the past 58 years. In 1965, the renewable energy technologies were not well known for the energy production sector around the world, where only 6.45% of the world primary energy come from renewable resources [5]. The technological revolution and the need for clean energy has led to a great interest

in using the renewable energy sources over the past decades where lots of efforts have been carried out by most of the countries in the renewable energy field. Comparing the renewable energy consumption for 1965 to 2023 shows the significant expansion of renewable consumption, When it comes to the percentage of primary energy consumed from renewable sources, Norway and Sweden lead the way with 72.09 and 53.89% respectively [5]. Among every continent, South America has the largest percentage of energy originating from renewable sources in 2023, 38.3% [5]. Particularly in nations like Brazil, its significant reliance on hydropower is probably the cause of this sharp increase. Europe is another region that is growing quickly; by 2023, renewable energy will account for almost 18% of all energy consumed there as shown in Figure 1.2. Through initiatives like the European Green Deal, which encourages investments in solar, wind, and biofuels, the region has demonstrated its commitment to renewable energy [5].

1.2 The energy transition

Urbanization, improved lifestyles, and demand for electricity on a global scale are steadily rising along with world population growth and the per capita energy consumption rate of modern life, thus global energy demand is driving up [6]. Energy efficiency and the diversification of electrical energy resources are essential for sustainable development given the sharp rise in the world energy needs. In order to enable the necessary global grid diversification, numerous renewable energy sources (RES) are currently undergoing research and development (R&D). The penetration of RESs is steadily rising in many different energy sectors, including thermal energy (heating or cooling), fuel (transportation), and electric power, as shown in Figure 1.3. Only 30% of the total worldwide power consumption is from renewable energy [7]. As a result, decision-makers in the power production industry are becoming more and more focused on the positive aspects of using renewable energy over other sources.

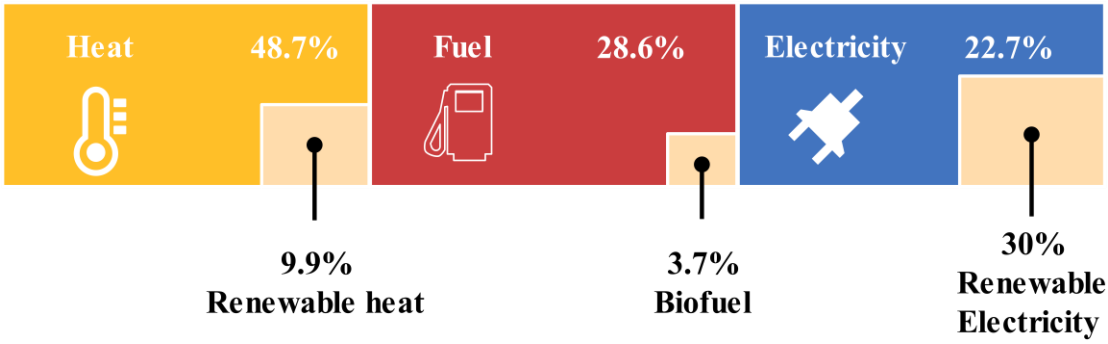

Figure 1.3 Renewable energy in total final energy consumption, by final energy use, 2020 [7]

Over 80% of the primary energy produced today comes from fossil fuels, of which coal accounts for 27% [8], [9]. The international renewable energy agency (IRENA) predicts that the share of renewable energy will climb to 66% by 2050 from its present prediction of 28% by 2030, which means that current supply must expand by at least ten times [10]. Furthermore, from its current supply of 30%, renewable energy is expected to increase to 57% by 2030 and 86% by 2050 in the power sector [11]. Figure 1.4 shows the renewable energy evolution in electricity generation for the past 10 years, solar and wind share increased 9.3% , from 2.8% in 2012 to 12.1% in 2022 [7].

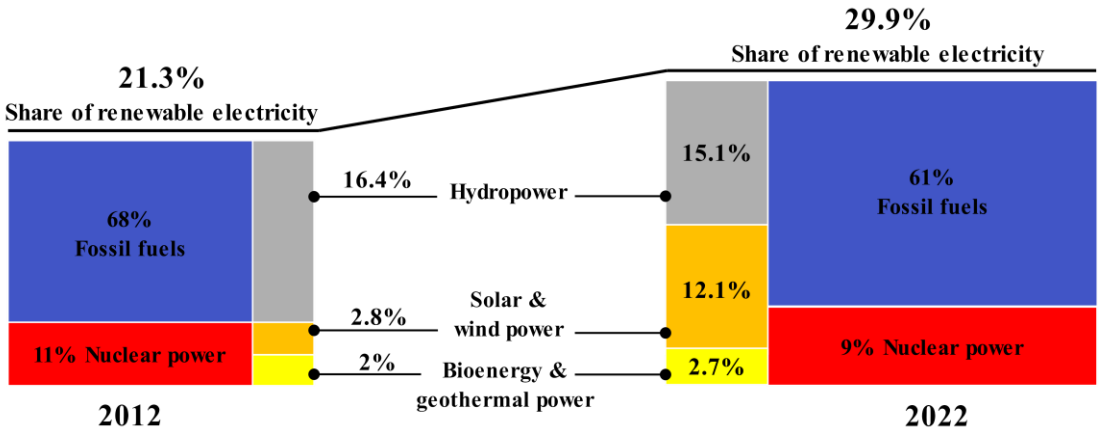

Figure 1.4 Share of renewable electricity generation, by energy, 2012-2022 [7]

Figure 1.5 shows the present state of RESs around the world as of 2010-2023. In 2023, there were 3.8 TW of installed capabilities. More than 1.4 TW of this capacity came from solar energy resources, 1.2 TW from hydropower, and 1 TW from wind energy sources [12].

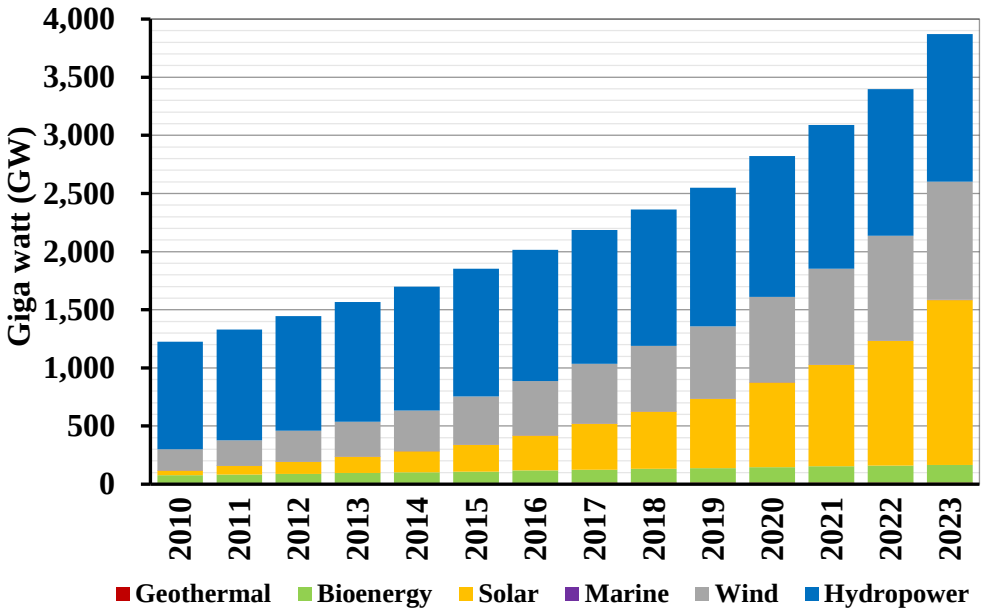

Figure 1.5 Total installed capacity per renewable energy source worldwide [12]

In agreement with earlier statistics, there is a lot of interest in using renewable sources, like solar energy, to generate electricity and fuels because of the rising energy demand and the corresponding rise in greenhouse gas emissions. Figure 1.6 reflects the global orientation towards the expansion of utilization of solar energy and how much the investment in such technology has swelled up during the previous past years. The total solar investment has increased by 36% from 2018 to 2022 to reach a total of 310 billion dollars in 2022 [7].

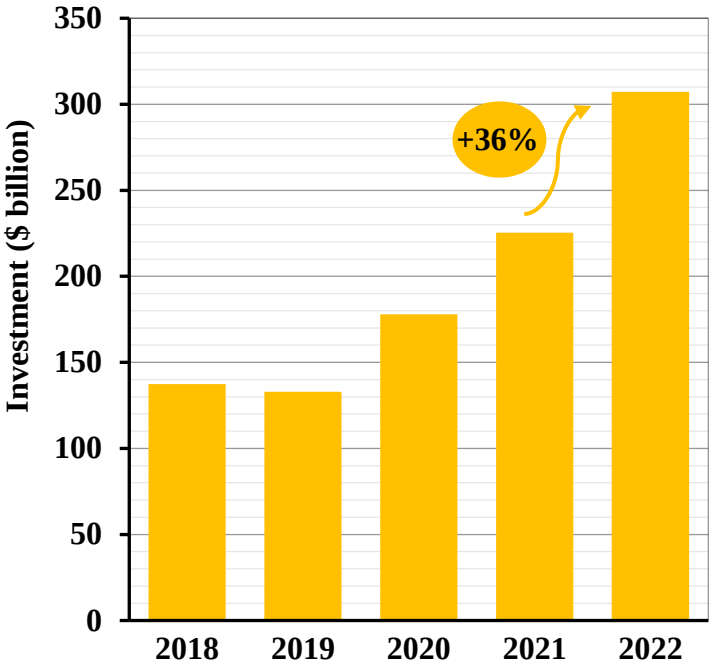

Figure 1.6 Global investment in Solar technology, 2018-2022 [7]

1.3 Challenges and drawbacks of gas power plants

One of the primary sources that contributes significantly to the global share of electricity production are gas power plants. Simple-cycle gas turbines, which use heated gas to drive a turbine, and combined-cycles, which use the waste thermal energy of the gas turbine exhaust gases to generate steam to power a steam turbine, are the two most popular types of power plants. With a 22% global share in gas power generation, natural gas ranks second in terms of power generation sources, after coal [13]. In addition to being utilized extensively to generate electricity, natural gas is a fuel that may be used for cooking, heating, and in the chemical industry. As a result, over the past 20 years, there has been a net increase in the world consumption of natural gas, partially due to the rising energy demand.

Global gas power generation increased from around 6,017 terawatt-hours in 2020 to a peak of nearly 6,100 terawatt-hours in 2021. With 528 GW, the United States has the largest gas power capacity of any nation and nearly one-third of the global operating capacity with 987 natural gas power stations installed, as shown in Figure 1.7. The US ranks fourth in the world among the nations with the most gas power capacity under development, with plans to add about 33 GW of new gas capacity in the upcoming years. Asia is predicted to see the most expansions of power plants [13].

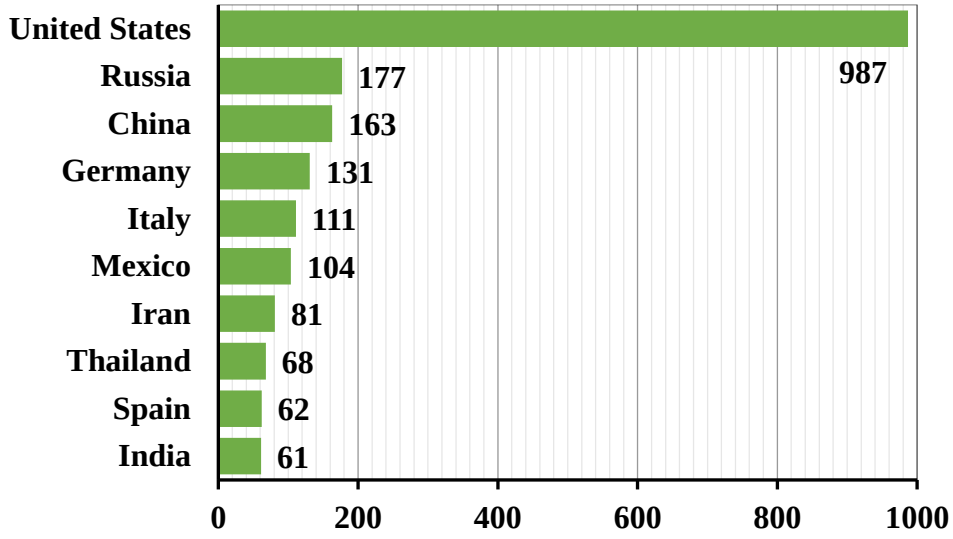

Figure 1.7 Number of natural gas power stations worldwide as of 2022 [13]

1.4 Integrating solar energy with gas power stations: A hybrid approach to sustainable energy

Combining renewable energy sources with conventional ones offers a promising pathway in the search for sustainable energy solutions. Solar energy is one of the most widely available and environmentally renewable energy sources. The overall sustainability and efficiency of energy production can be greatly increased when solar energy is combined with gas power plants.

Gas power plants offer a consistent and manageable energy output because of their well-established infrastructure. They do, however, contribute to the depletion of scarce natural resources and cause greenhouse gas emissions. These plants can lower their operating cost and carbon footprint by incorporating solar energy to offset a portion of their fuel usage. By utilizing a hybrid technique that combines solar thermal energy with gas power during the strongest solar hours, non-renewable resource consumption is minimized, and a more reliable energy supply is guaranteed.

Furthermore, increased grid stability and energy security may result from the use of solar and gas energy together. The steady output from gas power plants may efficiently mitigate the solar power, guaranteeing a steady supply even in the absence of Sunlight. This synergy facilitates the shift to a more sustainable energy system while simultaneously encouraging a cleaner environment. As we move towards a future where energy requirements are satisfied without endangering the health of our planet, we must embrace such hybrid solutions.

1.5 Research gaps

Although integrating solar energy into gas power plants has the potential to improve efficiency and sustainability, there are still several research gaps unaddressed. The field of power production through the combination of renewable energy resources with gas power plants is still developing over the past decade. Surveying the literature, contribution could be made to the optimization of hybrid power plants systems to

maximize their energy output. Research on integrated solar combined cycle (ISCC) power plants is crucial to achieve a more sustainable energy future. Some of the consulted previous works addressed the possibility of solar thermal power integration in a combined cycle (CC) power plant, whether in the top gas cycle, or within the bottom steam cycle, with most of them seeking to increase plant output power generation.

The research gap could be summarized as the lack of a comprehensive study that discusses different possibilities for solar energy integration within a combined cycle power plant throughout integrating solar thermal power at several positions (in the top gas cycle and in the bottom steam cycle) to optimize its energy efficiency and reduce fuel consumption and carbon emissions as much as possible; all of them considering two different operating strategies: fuel saving and power boosting. A detailed comparison between the different integrating positions and operating strategies would provide valuable guidance in this field.

1.6 Thesis objectives

The summary of the literature review presented before and that will be discussed in the next chapter shows the significance of the objectives of this work. The worldwide trend during this era is to provide clean and carbon free energy solutions that will protect the planet from the expected environmental disasters in the near future. The fundamental objective of this work is to generate knowledge about ISCCs and analyze their performance under some selected configurations to achieve either: fuel saving or power boosting. The specific objectives can be summarized as follows:

1. Implement a complete model for an operating combined cycle power plant.
2. Modify the combined cycle power plant model by integrating a solar field to build a complete ISCC model.
3. Study the optimum operating conditions for fuel saving and power boosting for different ISCC configurations.

1.7 Research Methodology

To fulfill the proposed thesis objectives, the research methodology was developed as follows:

- Firstly, a literature review on the thesis topic was conducted to understand the topic and find the research gaps in the past relevant research.
- Next, a complete thermodynamic model for an operating combined cycle power plant was implemented based on the available operating data in MATLAB.
- After that, the integrated solar combined cycle model was developed where different ISCC models were studied for various solar integration positions (some at the top gas cycle and others at the bottom steam cycle) under different operating strategies: fuel saving and power boosting.
- Finally, results of each ISCC model were analyzed and different operating constraints were revealed. The optimum configurations for each operating strategy were highlighted and compared.

1.8 Thesis outline

In this section, the structure of this document and the main topics discussed in each chapter are provided. The introduction "Chapter 1" where the motivation for the work is presented and overview of the root of the problem are depicted. "Chapter 2" presents the literature review; previous related works are discussed to find the research gaps in the study of the integrated solar combined cycle power plants. "Chapter 3", the methodology of implementing the thermodynamic model for the combined cycle and the integrated solar combined cycle power plant is presented. In "Chapter 4" the results are presented and compared to find the optimum cases that should be considered. Finally, "Chapter 5" concludes the work by highlighting the key conclusions and the accomplishment of the thesis objectives. An overview of possible future research lines is also presented.

CHAPTER TWO

LITERATURE REVIEW

In this chapter, a literature review of research on integrated solar combined cycles (ISCC) is presented. The ISCC mainly consists of a combined cycle and a solar field. The first section will define the components of the combined cycle separately, then the solar field technology will be explained. Other renewable resources will also be presented and compared with the solar field technology. Moreover, different operating schemes for the ISCC will be discussed.

2.1 Natural gas combined cycles

A combined cycle (CC) power plant is a type of power plant that uses both gas turbine and steam turbine technologies to generate electricity. It is designed to increase overall efficiency by capturing waste heat from the gas turbine in a Heat Recovery Steam Generator (HRSG) to power a steam turbine, as shown in Figure 2.1. CC have been found to achieve efficiencies up to 60% and are now widely used throughout the world as the primary source of electricity [14].

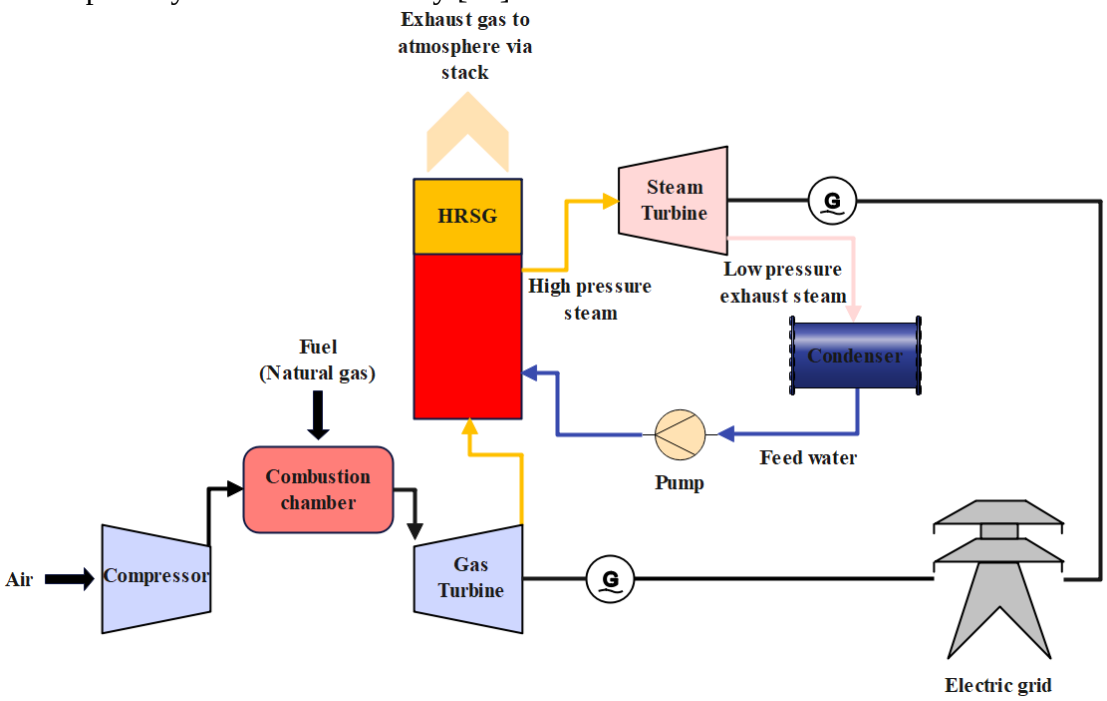

Figure 2.1 Combined cycle power plant [15]

2.1.1 Top gas cycle

George Brayton first proposed the Brayton cycle for application in the reciprocating oil-burning engine he created around 1870 [16]. Only gas turbines, where both the compression and expansion processes occur in rotating machinery, are employed nowadays. Gas turbines usually operate on an open cycle. The gas turbine cycle consists of three main components: compressor, combustion chamber and turbine. Fresh air (1) is brought into the compressor at ambient temperatures, as a result temperature and pressure increase. In the combustion chamber (2), the fuel is added and burnt under constant pressure with the high-pressure air introduced. Within the turbine (3), the resulting high-temperature gases expand to atmospheric pressure and generate power as shown in Figure 2.2 [16]. Finally, exhaust gases are sent to the HRSG.

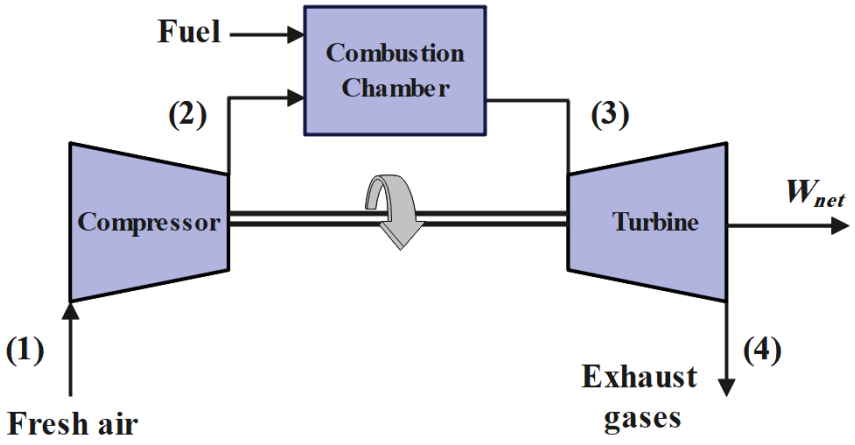

Figure 2.2 Gas turbine cycle diagram

2.1.2 Heat recovery steam generator (HRSG)

A heat recovery steam generator is a heat exchanger that recovers thermal energy from the exhaust gases of a gas turbine then heats water for generating steam for the bottom steam cycle, boosting efficiency from a range of 35% to 40% for a simple gas turbine cycle to a range of 55% to 60% in a combined cycle. The HRSG is composed of three main modules: the economizer, the evaporator, and the superheater as shown in Figure 2.3. The first stage of water heating is through the economizer. It employs low grade heat to warm the feedwater that is returning from the steam turbine to the boiler. Then water is fed into the evaporator which heats up the water to its boiling point.

Water and steam are separated in a steam drum at the evaporator. From the upper part of the drum, the separated steam is extracted and transported to the third module, also known as the superheater. The saturated water at the bottom of the drum is recirculated through the evaporator. In the superheater, the temperature of the steam is increased over saturation conditions before entering the steam turbine. The three modules are placed so that the superheater is exposed to the hottest gas. The evaporator comes next, and before the exhaust gas is expelled via the plant stack, the economizer absorbs heat from the coolest exhaust gas. Many contemporary combined cycle plants use HRSGs with two or three economizer-evaporator and drum-superheater configurations to supply steam at two or three pressure levels, with the components organized by decreasing order of steam and water temperature.

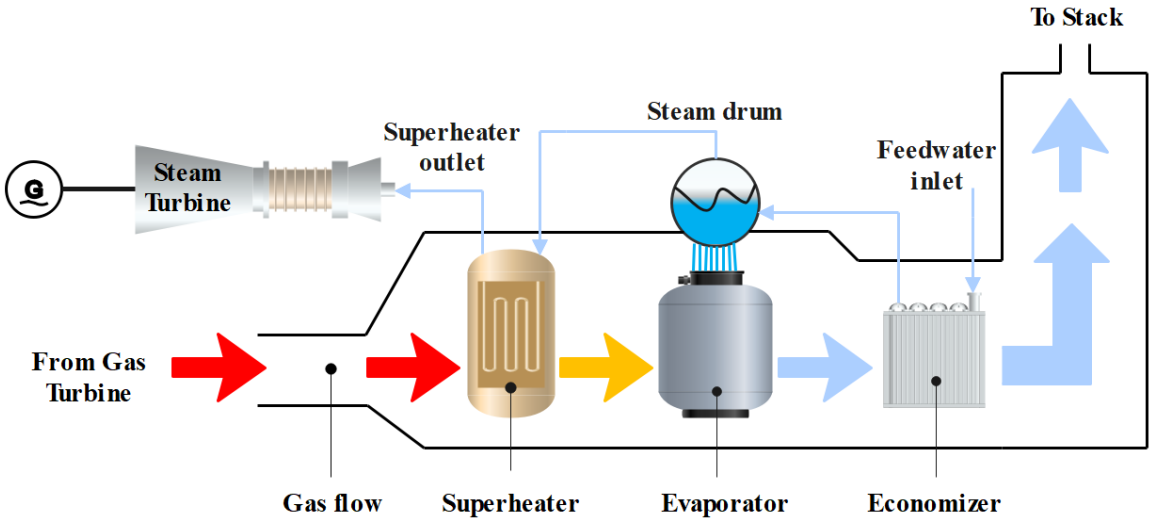

Figure 2.3 Heat recovery steam generator diagram [17]

2.1.3 Bottom steam turbine cycle

When exhaust gases are passed through the HRSG, steam is generated. Superheated steam, generated at the superheater, enters the steam turbine, where it expands and generates power by rotating a shaft connected to an electric generator. Steam from the turbine outlet is directed to the condenser. In the condenser steam is condensed at constant pressure by rejecting heat to a cooling medium such as a lake or a river. The cycle is completed when saturated liquid water enters the condensate pump flowing back to the HRSG as shown in Figure 2.1.

The following section will study one of the most mature renewable energy resources, solar energy, and its beneficial impact on the environment by reducing CO_2 emissions from non-renewable energy sources. It will also describe how solar energy could be integrated with traditional electricity generation systems to help reducing climate change effects.

2.2 Solar radiation

The Sun is a gigantic sphere, $1.39 \cdot 10^9$ m diameter, of hot and luminous gases which is mostly made of hydrogen and helium [18]. It produces energy by nuclear fusion in its core, which releases a massive amount of heat and light as hydrogen atoms unite to form helium. Through the Sun layers, this energy moves outward and eventually reaches the surface, where it is released as radiation in the form of Sunlight. Only 8 minutes and 20 seconds after leaving the Sun, which is $1.5 \cdot 10^{11}$ m away from Earth, solar energy reaches the Earth. The effective blackbody temperature of the Sun is 5762 K [18]. The central zone has much greater temperature, which ranges from $8 \cdot 10^6$ to $40 \cdot 10^6$ K. Generating about $3.8 \cdot 10^{20}$ MW, or 63 MW per square meter. The Earth only blocks $1.7 \cdot 10^{14}$ kW, a very small percentage of the total radiation emitted [18]. Even with this tiny portion, the amount of solar radiation that falls on Earth for 30 minutes would be sufficient to cover global energy needs for an entire year.

Solar radiation is a general word for the electromagnetic radiation that the Sun emits. It is also sometimes referred to the solar resources or just solar rays. A multitude of devices can be used to collect solar radiation and transform it into useful forms of energy, such as heat and electricity. However, the technological viability and cost-effectiveness of these systems in a particular area depends on the available solar

resource available. Any given point on the Earth surface receives a different amount of solar radiation depending on the geographic location, time of day, season, local landscape, and local weather. The Sun shines on the surface of the Earth at various angles, from 0° (just above the horizon) to 90° (straight overhead). The more slanted Sun rays are, the longer they travel through the atmosphere, the more dispersed and hazier they become. The cold polar regions never receive a high solar radiation level since the Earth is spherical, and because of the tilted axis of rotation, these regions get no Sun rays at all for a portion of the year.

Some of the Sunlight is absorbed, dispersed, and reflected as it travels through the atmosphere by air molecules, water vapor, clouds, dust, pollutants, forest fires, and volcanoes. This is called diffuse solar radiation. Direct beam solar radiation is the type of solar radiation that directly reaches the surface of the Earth. Global solar radiation is the total of both diffuse and direct Sun radiation. Direct beam radiation can be reduced by atmospheric conditions by 10% on clear, dry days and by 100% on days with heavy clouds. Total radiation on a horizontal surface or total radiation on a surface that tracks the Sun are the two common ways that solar energy is measured. The density of solar energy in the atmosphere is roughly 1360 W/m^2, but on the surface of the planet, it drops to 1000 W/m^2 [19].

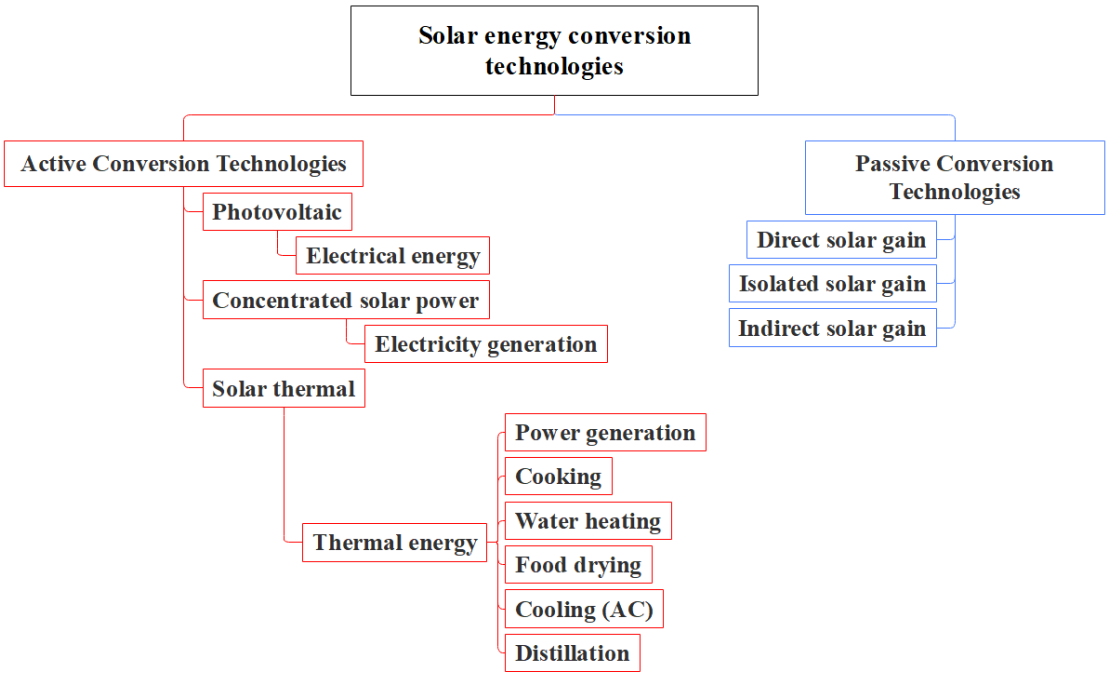

Figure 2.4 Classification of solar energy conversion technologies [20]

As depicted in Figure 2.4, solar energy conversion technologies may be divided into active and passive technologies. While an active solar system absorbs solar radiation, passive technologies involve capturing solar energy without converting solar thermal or electromagnetic energy [20]. Passive systems are built in a way that maximizes the utilization of solar heat or light through placement, design, or material selection where passive solar heating systems are considered to be a simple and cost-effective way to take advantage of the free solar renewable energy and displace the need for electricity, natural gas, or other active energy systems. Orienting buildings to receive as much sunshine as possible, using thermal mass materials like brick or concrete that absorb

heat during the day and release it at night, and installing windows or shading systems to regulate the amount of Sunlight entering a space are a few examples. Passive systems emphasize the utilization of solar energy through architectural elements and materials that support natural heating, cooling, and lighting. They are less complicated and require no external energy to operate.

Active systems have components that transform solar energy into more useful forms, such electricity or hot water. In order to transform solar energy into heat and power, the active solar system needs mechanical and electrical apparatus (such as pumps or fans). Photovoltaic (PV) and concentrated solar power (CSP) technologies are two categories of active solar energy technology. In an active solar space heating system, a solar collector which holds a heat-transfer medium such as air or liquid captures the Sun thermal energy that will further be distributed through the system, is an essential part of the heating system. In the realm of producing electricity, the solar collector functions as the connecting element between solar energy and power plants, solar collector is integrated with a combined cycle power plant to captures solar energy and transfer it to useful form. The following section will discuss the differences between solar collector types and how the solar energy is collected and transferred to useful heat in the power generation systems.

2.3 Solar collectors

Solar energy collectors are designed to capture and concentrate solar thermal energy to be converted to useful heat. By absorbing sunlight and converting it into thermal energy, they play a critical part in solar heating systems. This energy can be used for room heating, water heating, or even power generation. They work in tandem with heat exchangers to transform solar thermal energy into the internal energy of the transport medium. The solar collector is one of the important parts of any solar system. Solar collectors are commonly utilized to provide clean and renewable energy in residential, commercial, and industrial applications. There are basically two types of solar collectors: non-concentrating or stationery and Sun tracking or concentrating.

Figure 2.5 Flat plate solar collector

2.3.1 Non-concentrating collectors

Non-concentrating collectors are the type of solar collector in which the collector area (the area that intercepts solar radiation) is the same as the absorber area (the area absorbing solar energy). Flat plate (FPC) and evacuated tube (ETC) collectors are shown in Figures 2.5 and 2.7.

2.3.1.1 Flat plate collectors (FPC)

The flat plate collector is shown in Figure 2.5. Its components include an absorber plate, header tubes, liquid tubes, copper risers and glazing as shown in Figure 2.6. The operating temperature range for FPC is 30-80°C [21]. The clear cover minimizes radiation heat losses as well as convection losses with the aid of the air layers between the absorber plate and the glass. The absorber surface absorbs heat from the Sun rays. The fluid tubes transport medium carries the heat that the absorber plate has gathered to be stored or used.

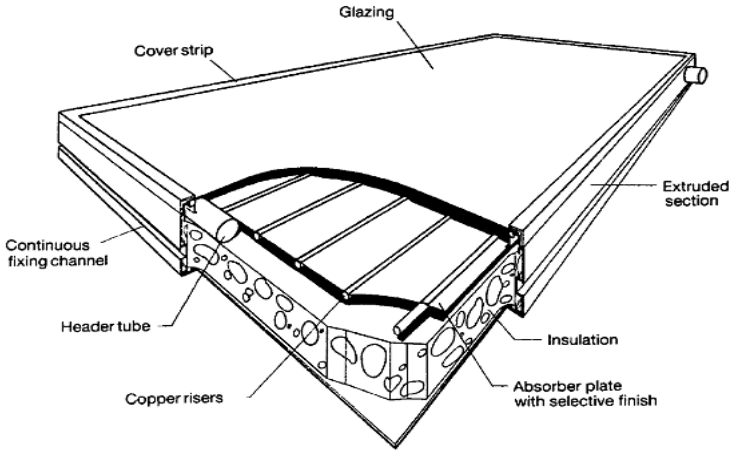

Figure 2.6 Flat plate collector components [21] (with permission from copyright owner)

The FPC are often stationary and do not track the Sun, so they should be pointed directly towards the equator, facing south in the northern hemisphere and north in the south. The tilt angle varies from 10-15° more or less depending on the application and location latitude [22].

Figure 2.7 Evacuated tube solar collector

2.3.1.2 Evacuated tube collectors (ETC)

ETCs transfer heat with high efficiency by using liquid-vapor phase change material as a working fluid. An example of an installed ETC is shown in Figure 2.7. The operating temperature range of ETC is 50-200°C [21]. The main component of ETC is a heat pipe (a very effective thermal conductor commonly made of copper) that is enclosed inside a vacuum-sealed tube as shown in Figure 2.8. A sealed copper pipe is connected to a black copper fin that fills the tube (absorber plate). Each tube has a metal tip that protrudes from the top and is connected to the sealed pipe (condenser). A tiny amount of fluid, which is typically methanol, that goes through an evaporating-condensing cycle is contained in the heat pipe. This cycle begins with the liquid being evaporated by solar heat. The vapor then moves to the heat sink zone, where it condenses and releases latent heat. The procedure is then repeated with the condensed fluid returning to the solar collector [21]. As illustrated in Figure 2.8, these tubes are installed with the metal tip up into a heat exchanger (manifold). Heat from the tubes is transferred from the manifold to water, or glycol. After passing by another heat exchanger, the heated liquid transfers its heat to water kept in a solar storage tank or to a storage system by means of another heat exchanger [21].

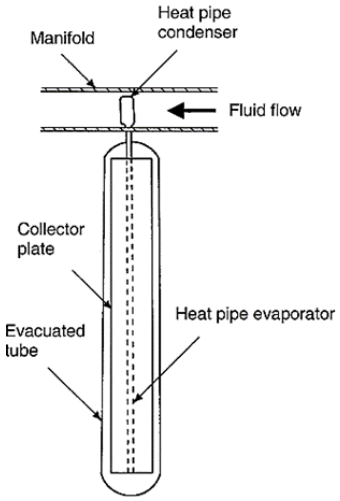

Figure 2.8 Schematic diagram of an evacuated tube collector [21] (with permission from copyright owner)

2.3.2 Concentrating collectors

Concentrating solar collectors are collectors where the area intercepting solar radiation is greater, sometimes hundreds of times greater, than the absorber area. Solar energy is concentrated onto an absorber via a highly reflective collector. The collector typically moves throughout the day to follow the Sun so the radiation is always concentrated on the absorber. There are different types of concentrating collectors: Linear Fresnel reflectors (LFR), Heliostat field collectors, parabolic dish reflectors (PDR), and parabolic trough collector (PTC). The four technologies will be discussed in detail in the following sections. Their main advantages are [23]:

1. With the same solar energy-collecting surface, the working fluid in a concentrator system can attain a substantially greater temperature than in a flat plate system. As a result, thermodynamic efficiency increases. Therefore, they are typically used in solar thermal power plants.

2. Cost per unit area is lower than for a flat plate collector because its reflecting surfaces are simpler and requires less material.
3. Surface treatment and vacuum insulation (to reduce heat loss and increase the efficiency of the collector) are commercially viable due to the receiver comparatively small area.

Their shortcomings are:

1. Concentrating systems need some kind of Sun tracking mechanism.
2. Reflective surfaces require routine cleaning and maintenance.
3. Concentrator systems do not capture diffuse solar light; they rely on the concentration ratio.

2.3.2.1 Linear Fresnel reflectors (LFR)

With a network of linear mirror strips, LFR technology directs light onto a fixed receiver positioned on a linear tower as shown in Figure 2.9. The LFR may be pictured as a fragmented reflector similar to a parabolic trough, without the shape restriction, enormous absorbers can be built, and the absorber is not required to move. Figure 2.10 displays the arrangement of a component of LFR collector field. The primary benefit of this kind of system is that it uses less expensive flat or less curved reflectors rather than parabolic glass reflectors. They are mounted close to the ground, reducing the need for structural support.

This kind of reflector can also resemble the disassembled reflector of a parabolic-trough system. Although the capital cost of the reflectors is reduced for Fresnel reflectors design, the efficiency is lower than for parabolic-trough reflectors [24],[25]. The annual solar-to-electric efficiency is typically between 8 and 10% for the LFR CSP plants, which have capacities ranging from 10 to 200 MW [26].

Giorgio Francia [27], a major solar revolutionary who created both linear and two-axis tracking Fresnel reflector systems in Genoa, Italy in the 1960s, was the first to put this theory into practice. The systems demonstrated that high temperatures could be obtained using both methods, but he switched to two-axis tracking, presumably due to the lack of secondary optics and improved selective coatings [28].

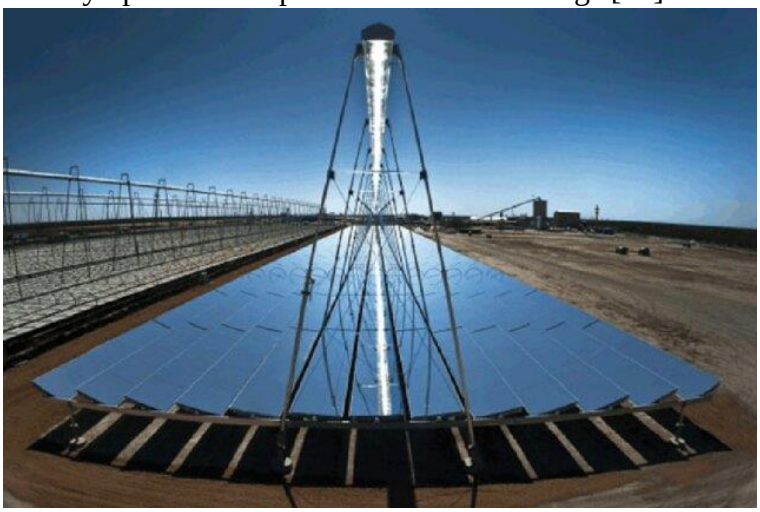

Figure 2.9 Linear Fresnel reflector (LFR) [29] (with permission from copyright owner)

A thorough project design study for 10 and 100 MWe LFR power plants was performed by the FMC Corporation in 1979 for the US Department of Energy (DOE). A 1.68 km linear cavity absorber supported by 61 m towers would have been employed in the larger facility. But due to a lack of financing from DOE, the project was never implemented [28].

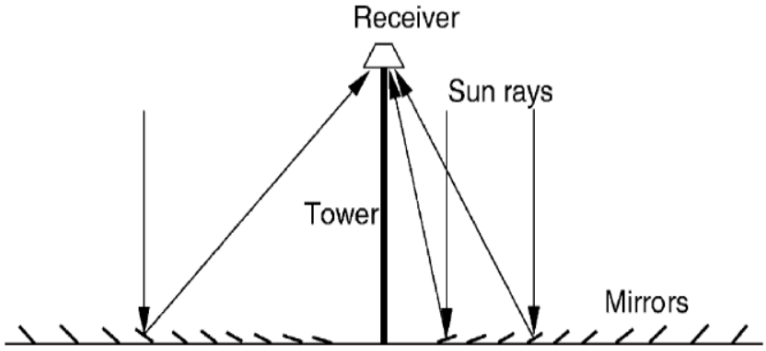

Figure 2.10 An illuminated downward-facing receiver schematic from an LFR field [21] (with permission from copyright owner)

The LFR technology has the drawback of requiring more space between reflectors to avoid blocking and shading between neighboring reflectors. The height of the absorber towers can be increased to prevent blocking, however, doing so raises costs. At Sydney University in Australia [21] a compact linear Fresnel reflector (CLFR) technology has been designed as shown in Figure 2.11. In essence, this is an alternate approach to prevent shading. Individual reflectors have the ability to direct reflected Sun radiation to at least two towers if they are situated close enough. The ability to put closely spaced reflectors without shading or blocking is made possible by the addition of this variable in the reflector orientation, which allows for significantly denser arrays [28].

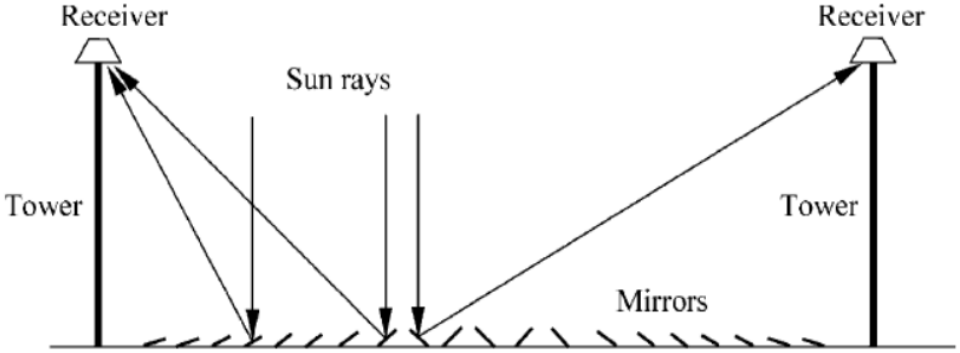

Figure 2.11 Schematic diagram of the CLFR [21] (with permission from copyright owner)

When the costs of ground preparation, array substructure, tower construction, steam line thermal losses, and steam line are taken into account, the avoidance of high reflector spacing, and tower heights is a significant financial concern. High array ground coverage might result in the maximum system output for a given ground area if the technology is to be deployed in a location with restricted land availability, like in metropolitan areas or close to existing power plants [28].

The largest LFR CSP plant, with a collector width of 24 m and a reflector area of 2500 m, was constructed as a prototype in 1999 by the Belgian company Solarmundo [30].

The largest operational linear Fresnel-reflector CSP plant, Reliance Areva solar power plant, was set up in India in 2014. It has a 125 MW capacity and was expected to generate 280,000 MWh of power annually. This plant encountered a number of difficulties as the project was halted and eventually abandoned after the earliest stages of construction and certain test operations. The main causes of this were financial issues, insufficient policy support, and technical difficulties related to the technology at that scale. In addition, two linear Fresnel-reflector based CSP plants were constructed for demonstration: the 5 MW Kimberlina Solar Thermal Power Plant in the United States in 2008 and the 1 MW Rende-CSP Plant in Italy in 2010. In contrast, two LFR power plants were constructed in 2012 for commercial production: the 30 MW Puerto Errado 2 Thermosolar Power Plant in Spain and the 9 MW Liddell Power Station in Australia [31].

2.3.2.2 Heliostat field collectors

Heliostat field collectors are a collection of mirrors, also known as heliostats, that follow and reflect Sunlight onto a central receiver that is usually fixed atop a tall tower as shown in Figure 2.12. Every heliostat is designed to track the Sun path throughout the day in order to focus the most solar energy possible onto the receiver. A heat transfer fluid (HTF), such as molten salt, steam or water, or synthetic oil is present in the receiver. The HTF heats up to extremely high temperatures as the receiver is exposed to concentrated Sunlight. A heat exchanger is used to transfer the heat from the molten salt or oil to water when it is utilized as the HTF. The water boils and produces high-pressure steam as a result of this heat transfer. After that, the steam is directed into a steam turbine, which turns an electric generator to produce electricity. The entire process is a closed-loop cycle in which the steam is frequently condensed back into water for use in the steam generation cycle and the cooled HTF is recycled back to the receiver. Steam generator, turbine generator, and supporting hardware make up the power-conversion system, which turns thermal energy into electricity and feeds it into the utility grid. Heliostat field collectors are well-known for their high efficiency and capacity to integrate thermal energy storage for power generation even after sunset. They are frequently utilized in solar power tower systems.

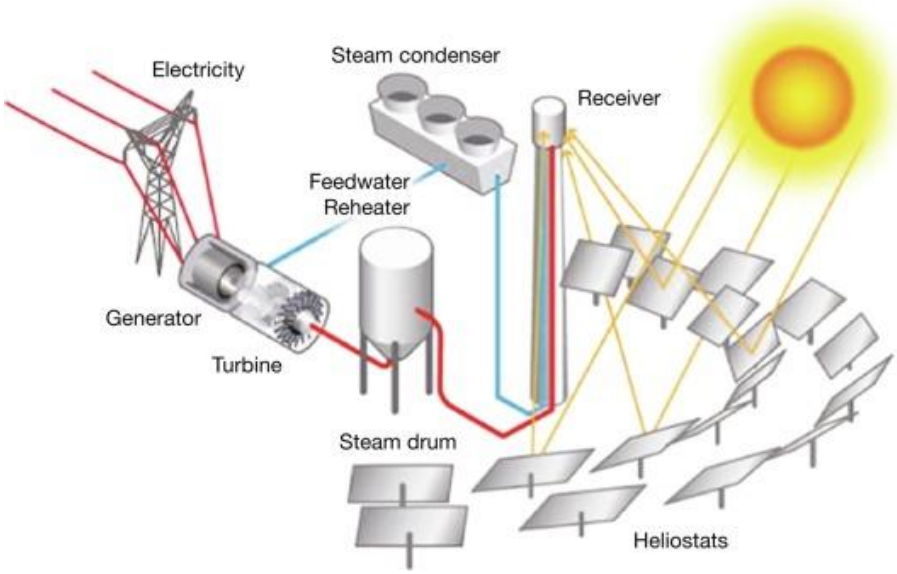

Figure 2.12 Heliostat field collector [32] (with permission from copyright owner)

Central receivers offer the following advantages [21]:

1. They minimize the need for thermal energy transport by collecting solar energy and transmitting it to a single receiver.
2. They are very effective in gathering energy and converting it to electricity, generally achieving concentration ratios from 300 to 1500.
3. They benefit from economies of scale due to their typically large size.

The heliostats each have a reflecting surface area of 50 to 150 m^2. On the receiver, the solar flux hits at values from 200 to 1000 kW/m^2. This high flux allows operating at high temperatures of more than 1500°C. Central receiver systems have the capacity to operate for more than half of the yearly hours at nominal power thanks to thermal energy storage and can be easily integrated in fossil-fueled plants for hybrid operation in a wide variety of options.

Since they allow many options between the integration in a conventional Rankine cycle up to gas turbine cycles at temperatures above 1000°C, central receiver systems have a significant potential for mid-term cost reduction of electricity compared to parabolic trough technology [33], [34].

Large plants with capacities between 100 and 200 MW can use air, molten salt, water/steam, or liquid sodium as the working fluid in the heliostat field collectors [26], [30]. United States Department of Energy Projects in California during the 1980s and 1990s proved that a solar power tower (SPT) could collect and store heat in order to produce utility-scale energy continuously, twenty-four hours a day. The first commercial power tower facility "Solar One" started operation in 1982 in California [31]. Rather than being a fully functional commercial facility, it was essentially regarded as a demonstration project. It was the first large-scale solar tower to demonstrate the viability of the technology, and it functioned from 1982 to 1986. Later, in the 1990s, the plant underwent an upgrade to "Solar Two" in order to include advances, namely the use of molten salt for thermal energy storage. However, the "Planta Solar 10" power facility in Seville, Spain, which began operations in 2007, was the first completely functional commercial solar tower facility and a major turning point in the CSP industry [35]. "Planta Solar 10" was the first plant of its kind to commercially supply electricity to a grid, with an 11.02 MW capacity. The facility has a total land area of 0.55 km^2, and its estimated annual planned power generation is 23,400 MWh. In 2009, more than 5000 households were powered by the modular two-tower Sierra Sun Tower in the Mojave Desert. In California, USA, construction of the 392 MW three-tower Ivanpah Solar Electric Generating System began in 2010. There are roughly 175,000 mirrors in this the plant. Thanks to this plant, more than 350,000 residences were powered, and more than 1000 jobs opportunities were provided [36]. In a power-tower CSP facility, the heliostats represent the largest capital expenditure (CapEx) [37].

The global total operational gross installed capacity of SPT-CSP plants is currently 618.42 MW [38], and it is growing quickly. "Nour III", was operated in 2018, is the largest plant utilizing this technology in the world with capacity 150 MW [31]. Around the world, there are numerous of small pilot-scale facilities such as: "Plataforma Solar de Almería PSA", that started operations in the 1980s, in Spain with 50 kW capacity

that is used for research and experimentation purposes rather than for the large-scale commercial production of electricity [39], and "SOLGATE" project, was operational in 2022-2004, in Spain with 50-100 kW capacity that focuses on the integration of gas turbines with solar power towers for the purpose of demonstrating novel solar tower technology on a small scale as part of the European research program [40]. Among CSP technologies, SPT is expanding the fastest. The majority of the power-tower-based facilities that are now under development will be located in China and have a capacity of approximately 995 MW in the near future [31].

2.3.2.3 Parabolic dish reflectors (PDR)

A parabolic dish reflector is a point-focus collector that follows the Sun in two axes as schematically seen in Figure 2.13, concentrates solar energy onto a receiver that is situated at the focal point of the dish. The key components of a PDR system are: reflector/dish, receiver, tracking system and power conversion unit. In order to efficiently reflect the beam into the thermal receiver, the dish must track the Sun. The dish reflects solar energy where it is absorbed by the receiver and transferred as thermal energy to a circulating fluid (HTF). The thermal energy can then be either piped to a central power-conversion system or transformed into electricity using an engine-generator directly connected to the receiver. Stirling engines and similar systems use the heat collected by the receiver to power an engine that converts thermal energy into mechanical energy and ultimately into electrical energy. In alternative systems, power cycles such as steam turbines or Rankine cycles can be powered by the heated HTF to generate electricity.

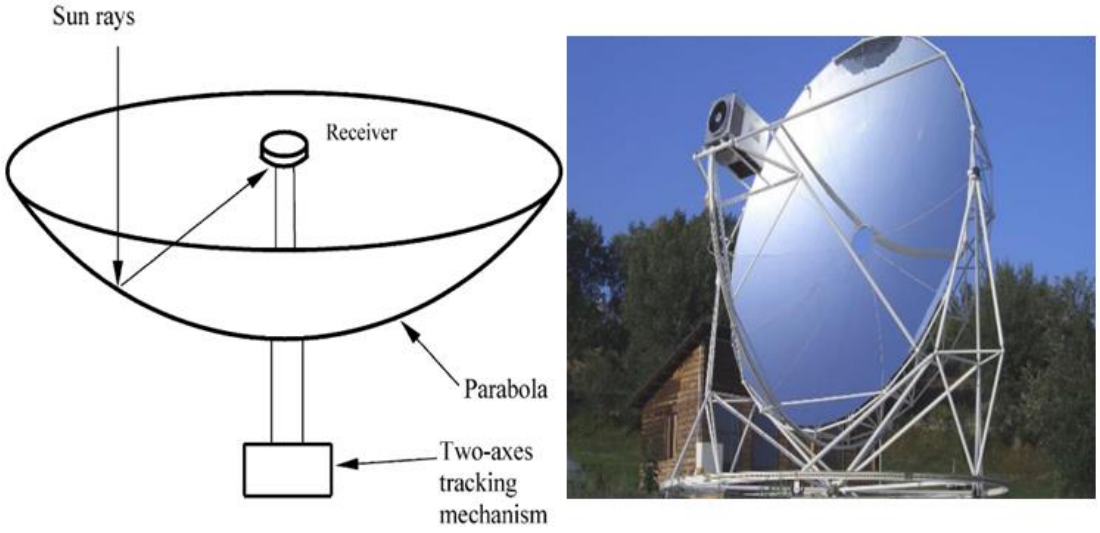

Figure 2.13 Parabolic dish reflectors (PDR) [21], [41] (with permission from copyright owner)

Among all solar technologies, PDR has one of the greatest solar to electric conversion efficiencies [42]. The system curved mirrors, thanks to the tracking system, are the reason for its efficiency; in contrast, other technologies, like the PTC and heliostat field collectors, suffer from cosine losses, which cause the projected area to decrease [21], [43], [44]. Cosine losses area are reductions in the system efficiency caused by the Sun beams angle in relation to the dish orientation. The reason for these losses is that the reflector alignment to gather sunlight perpendicular to its surface is not always precise.

When sunlight strikes the dish at a 90-degree angle, efficiency is maximized; however, when the angle varies from this ideal alignment (particularly at different times of the day or year), less Sunlight is effectively captured, which limits the amount of energy that can be focused onto the receiver. Depending on the angle of the incoming solar rays, the effective area of the dish that collects Sunlight varies. The part of the dish surface area that the Sun "sees" while it is at a specific angle is basically the projected area. . On an equivalent basis of the systems, PDR has higher solar-to-electric efficiencies than SPTs and PTCs, respectively [45]. One of the special benefits of the SPD over other CSP technologies is that it may be easily installed in small, isolated grids and does not require a perfectly flat ground [46].

Temperatures higher than 1500°C can be reached with parabolic dish systems. Power generation capacity of a single parabolic-dish CSP system can range from 0.01 to 0.5 MW [47], [48]. It is common to refer to parabolic dishes as distributed-receiver systems since the receivers are dispersed across a collector field, similarly to parabolic troughs. Parabolic dishes have several noteworthy benefits:

1. They have high efficiency as they are continually oriented towards the Sun.
2. They often have concentration ratios between 100 and 1000, making them extremely effective for power conversion and thermal energy absorption.
3. They have interchangeable collector and receiver components that can run on their own or as a component of a larger dish system.

Solar Power And Chemical Energy Systems (SolarPACES) organization [31] states that two parabolic dish CSP facilities have been built to date (both are currently non-operational); the Tooele Army Depot in Tooele, Utah, is home to the only active and commercial SPD facility in the United States that was operated in 2012. The 1.5 MW facility comprises of 429 solar dishes powered by Stirling engines. The plant uses helium as its working fluid and has a closed-loop cooling system. The plant main goal is to provide 30% of the US Army base in Tooele electrical needs. On the other hand, the 1.5 MW parabolic dish facility was operated in 2010, the Maricopa Solar Project (Maricopa), is located in Peoria, Arizona, in the United States, it consists of 60 solar dishes and uses Hydrogen as HTF.

2.3.2.4 Parabolic trough collectors (PTC)

Due to extensive system experience and industrial growth to manufacture and sell these systems, parabolic trough technology is the most sophisticated of solar thermal technologies. PTC represents the most mature concentrated solar power technology, with high thermal efficiency values and light structure and a relatively low cost generating temperatures up to 400 °C, generally high enough for most of industrial heating processes and applications. PTCs are constructed in modules; each one is usually installed atop support structures that are securely fastened to the ground in order to provide stability and ideal Sun alignment as shown in Figure 2.14. The support structure, which is often composed of steel or aluminum, offers the parabolic trough mirrors and receivers a sturdy and rigid framework. This structure is made to endure external factors like wind and thermal expansion in addition to supporting the weight of the trough.

Figure 2.14 Parabolic trough collectors

A reflective sheet is bent into a parabolic form to create PTCs. Along the receiver focal line there is a dark colored metal tube covered by a glass tube, which prevents heat losses, is placed to form an external surface receiver as shown in Figure 2.15. The receiver surface is often covered with a selective coating that absorbs thermal radiation and has low emittance. The glass disadvantage is that radiation must travel across the glass to reach the absorber, adding a transmittance loss of only 10% when the glass is clean [49]. To increase transmissivity, the glass envelope typically incorporates an antireflective coating. Evacuating the space between the glass cover tube and the receiver can further limit convective heat loss and improve the collector performance, especially for high temperature applications [49].

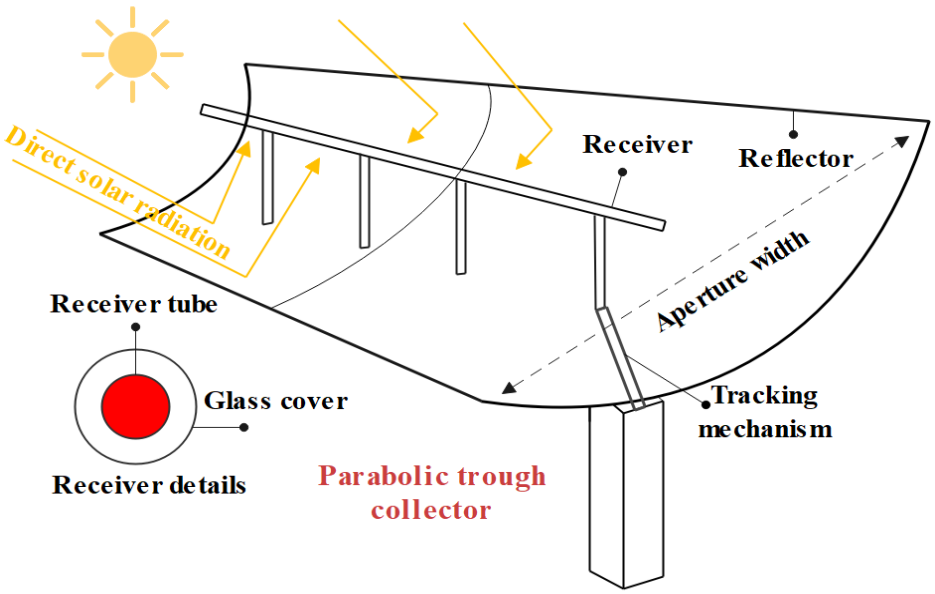

Figure 2.15 Parabolic trough collector schematic diagram [50]

The heat transfer fluid (HTF) which transfers the solar thermal energy to power cycles to generate electricity, is usually molten salts, water, or synthetic oils, where, despite being more expensive, oil is preferable due to its higher boiling point and low volatility. Heat pipes have been suggested by Dongdong et al.[51] as linear PTC receivers. The key benefit of the heat pipe is that it can keep a constant temperature even with uneven

radiation at the trough collector. As heat is not transferred from the HTF to the pipe, heat losses are low. PTC systems employing a heat pipe as a receiver have a lifetime of 15-20 years when operating below 380°C and a thermal efficiency of 65% at that temperature [51].

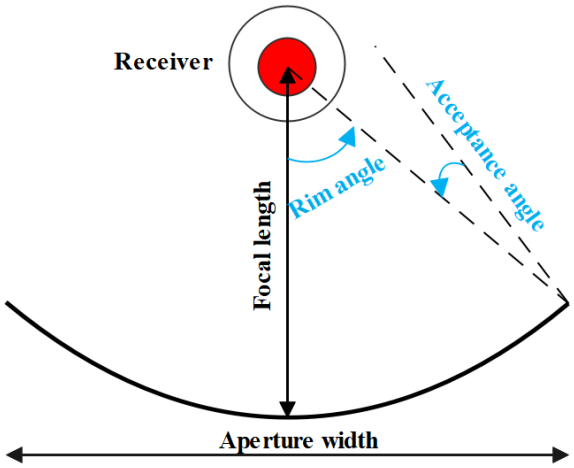

Figure 2.16 Acceptance and rim angles

A solar tracking system must be dependable and accurate, returning the collector to its original location at the end of the day or throughout the night, also during periods of intermittent cloud coverage. Furthermore, tracking mechanisms must safeguard collectors, protecting them from harmful environmental and operating conditions such as wind gusts, overheating, and failure of the thermal fluid flow system. The tracking mechanism required precision is determined by the collector acceptance angle as shown in Figure 16, maximum angular deviation from optimal alignment where solar radiation can be effectively concentrated onto the receiver tube without significant loss of efficiency.

The collector can be oriented in either a north-south direction and follow the Sun from east to west, or in an east-west orientation and track the Sun from north to south. The first tracking mode has the benefit of requiring very little collector adaptation during the day and ensuring that the full aperture always faces the Sun at noon, but the collector productivity during the early and late hours of the day is significantly diminished due to large incidence angles (cosine loss). A horizontal north-south trough field often gathers a little bit more energy over the course of a year than a horizontal east-west one [21]. The north-south field gathers more energy in the summer and less in the winter. An east-west field produces a more consistent annual production because it gathers more energy in the winter than a north-south field.

Among all revised technologies, parabolic troughs have the highest installation ratio, 82%, with parabolic dish being present in less than 1% of installations, as shown in Figure 2.17. A comparison between different types of concentrating solar collectors is shown in Table 2.1. The following is a summary of the factors that led to widespread use of parabolic trough technology today over other competitive technologies [52]:

a. **Mature and proven technology**
   Having been successfully utilized for decades in commercial applications, PTCs are the most advanced and commonly used CSP technology. They are

dependable for producing solar power on a big scale because of their lengthy history, especially in areas like Spain and the United States.

b. Scalability

PTCs can be used in medium- and large-scale installations. Adding more trough arrays to their modular design enables gradual expansion.

c. Cost-Effectiveness

PTC systems are less expensive than less developed technologies like solar power towers or parabolic dish systems because of economies of scale brought about by their widespread use. Components like tracking systems, receivers, and mirrors have comparatively low manufacturing costs.

d. Efficient Solar Tracking

PTCs use single-axis tracking systems, which are less complicated and costly than the dual-axis tracking needed by parabolic dishes or solar power towers. As a result, they are simpler to use and maintain and continue to gather energy effectively throughout the day.

e. Hybridization Potential

PTC systems can be easily combined with traditional power plants to make hybrid systems that use solar energy in addition to electricity derived from fossil fuels. This is typically observed in integrated solar combined cycle (ISCC) power plants.

f. Lower operating temperatures

PTCs are easier to maintain over time since they work at moderate temperatures (300-400°C), which lessens operational, and material issues such thermal stress. This sets them apart from solar power towers.

g. Reliability and Simplicity

PTC systems require less sophisticated tracking and receiver systems than solar power towers and parabolic dishes, which have more complicated designs. This simplicity results in lower maintenance costs and increases operating reliability. In contrast to solar power towers, which necessitate precise construction and alignment of a large heliostat field around a central tower, PTC systems are comparatively simpler to install.

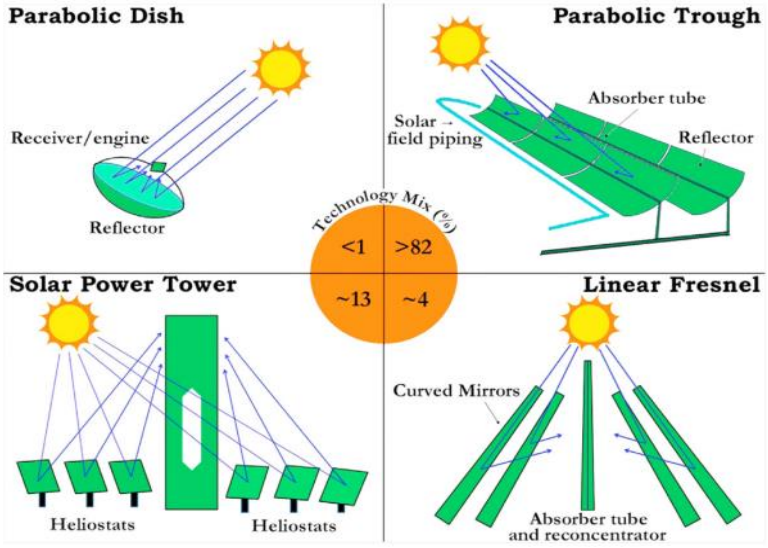

Figure 2.17 Different CSP technologies and their installed ratios [53] (with permission from copyright owner)

PTC systems provide a balanced mix of mature technology, cost-effectiveness, scalability, dependability, and simpler integration with thermal storage and conventional power plants when compared to other concentrating solar technologies. solar power towers and parabolic dish systems.

Several structural ideas have been put forth, including collector shape (double V-trusses and steel framework structures with central torque tubes) and collector material (fiber glass) [54]. The design and construction of Euro Trough, which uses an advanced lightweight structure to enable cost-effective solar power generation, represents significant development [55], [56].

Table 2.1 Concentrating solar collectors [24], [57], [58], [59]

Collector type	Description	Operating temp. range (°C)	Relative cost	Concentration ratio (Sun)	Tracking	Efficiency (%)
Parabolic trough collectors (PTC)	-Parabolic sheet of reflective material -Linear receiver (metal pipe with heat transfer fluid)	50-400	Low	15-45	One-Axis	~18
Linear Fresnel reflectors (LFR)	-Linear Fresnel mirror array -Low or high mounted pipe as receiver	50-300	Very low	10-40	One-Axis	~12
Heliostat field collectors (solar power tower)	-Large heliostat field with tall tower in its center -Receiver: water/HTF boiler at top	300-2000	High	150-1500	Two-Axis	25-28
Parabolic dish reflectors (PDR)	-Large reflective parabolic dish with engine receiver at focal point.	150-1500	Very high	100-1000	Two-Axis	~30

The collector aperture and the rim angle optimization were described by Kalogirou et. al. [23]. The rim angle is the angle, as measured from the focal point, between the outer edge of the parabolic mirror and the focal line, which is where the receiver tube is positioned as shown in Figure 16. PTCs underwent extensive research and commercial development in the 1980s, and several businesses joined the market to manufacture one-axis tracked solar collectors for the temperature range from 50 to 300°C. The solar collector made by the Industrial Solar Technology (IST) Corporation is one such instance. In the United States, IST built a number of process heat facilities with up to 2700 m2 of collector aperture area [62]. For effectiveness and durability, the IST

parabolic trough has undergone extensive testing and evaluation by Sandia [63] and the German Aerospace Centre (DLR) [62].

In Cairo, Egypt, the first parabolic-trough system was built in 1912 [43]. There are currently 77 parabolic-trough power plants in operation worldwide [31], the majority of which are found in Spain and the US. There are two plants in Morocco, two in Italy, two in South Africa, one in Canada, three plants in India, one each in Algeria, Egypt, the United Arab Emirates, and Thailand. There are 47 parabolic trough power stations in Spain with total capacity of 2.3 GW, net turbine capacities ranging from 22.5 MW to 50 MW [60]. 2008 saw the installation of the first parabolic trough system, known as Andasol-1 (AS-1), which had a 49.9 MW capacity, close to Granada. The plant annual solar resource was calculated to be 2136 kWh/m^2. A total of 158,000 MWh of electricity is expected to be generated annually. The two biggest parabolic trough plants in Spain are Helios I and Helios II, which together occupy 2,600,000 m^2 of land. Up till 2016, the operational parabolic trough plants in Spain had an installed capacity of 1871.9 MW. The Southern California power plants, with a total installed capacity of 354 MWe [61], are the largest deployment of this kind of system. The earliest of these facilities is a 14 MW electric (MWe) plant, followed by six 30 MWe facilities and the two most recent 80 MWe facilities [61]. This type of collector is also used in Plataforma Solar de Almeria (PSA), a facility in southern Spain, primarily for experimental reasons with a total installed capacity of 1.2 MW [62].

2.4 Concentrating Solar Power (CSP) hybrid technologies

Researchers and developers across the globe are taking an interest in CSP because of its benefits (low operating costs, strong potential for scaling up, and great efficiency) [63], [64]. Concentrated solar energy is converted into electricity in CSP plants. A concentrator, a high temperature solar receiver, a fluid transport system, and a power generation block (such as a Rankine cycle, Brayton cycle, or combined cycle) are the four main parts of a conventional plant [65]. The International Energy Agency (IEA) projects that by 2050, CSP plants will produce 11% of the world electricity [66]. With their current production capacity, CSP technologies assist in cutting CO_2 emissions by 12 Mt/year [67]. On the other hand, CSP systems presents hurdles in terms of cost reduction and technological advancement, particularly in terms of reducing radiation loss. Costs have decreased by more than 55% since 2010 [68]. The total capacity of CSP-based power plants worldwide is now 6,475 MW, 1592 MW are in the development stage and 1547 MW are under construction, according to IRENA [69]. Spain and the USA are the largest producers of CSP, with Spain leading at 2304 MW of capacity, followed by the USA with 1740 MW [31].

Several important advantages of CSP systems could be concluded as following [70]:

a) **Sustainability:** they do not generate emissions and are a renewable energy source.
b) **Integration:** In order to reduce emissions from fuel combustion, CSP systems can be combined with fossil fuel-based power or energy production systems.
c) **Efficiency:** In regions with strong direct solar radiation, CSP systems can offer higher efficiency compared to other CSP systems, but they are more restricted to specific geographic areas.

d) **Scalability:** The CSP system can be readily scaled to either pilot or industrial levels.

Some CSP hybrid technologies, including photovoltaic, biomass, geothermal, wind and combined cycle power plants will be studied in the following section.

2.4.1 Photovoltaic/concentrated solar power (PV-CSP)

There are two main technologies utilized in the solar energy industry to generate power. These are Solar Photovoltaics (PV), which generates electricity using light energy, and Concentrated Solar Power (CSP), which generates electricity using solar thermal radiation. PV systems are significantly simpler than CSP systems because they employ solar cells instead of moving parts to directly convert Sunlight into electricity. Due to its many advantages over both PV-alone and CSP-alone technologies, the photovoltaic/concentrated solar power (PV-CSP) hybrid technology is regarded as one of the current areas of focus in the solar energy sector. As noted by Ju et. al [71], the power from PV has a significant influence on the connected grid because large-scale electric energy storage technologies are still unable to meet market demand. Furthermore, the majority of solar energy is converted to heat, which raises the temperature of the cells and reduces the efficiency and lifespan of PV systems. They also stated that the PV-CSP hybrid system has higher power quality when producing electricity than the PV-alone system. The cost of producing power can be lowered as compared to the CSP-alone system. There will also be a significant increase in total generating efficiency. With the increasing maturity of PV and CSP technologies in recent years, the development of PV-CSP hybrid systems has accelerated. The International Energy Agency (IEA) projects that by 2030, the global installed capacity of PV will reach 1721 GW, while for CSP will reach 261 GW [72].

Comparing CSP power facilities to PV plants, the former have greater initial investment costs. CSP plants do, however, yield higher economic returns than PV power plants [73]. According to the IRENA roadmap, worldwide solar PV power output is expected to increase from its current supply of approximately 3% to 13% by 2030 and 25% by 2050 [74], [75]. As a result, improving solar energy conversion efficiency is a common problem, mostly because of technological limitations. The efficiency of existing CSP and PV technologies ranges from 12 to 30 percent on average [76], [77], [78]. The integration costs rise to such an extent that PV supply shares become much less competitive, allowing CSP systems to develop at a faster rate and finally overtake PV [79].

The characteristics of PV and CSP technologies complement one another. There are now several methods for the hybridization. For instance, a PV system can be used to supply station-service power (the power needed to run the plant, including the pumps, tracking, and control systems) for a CSP plant; it can be combined with a CSP system to provide stable power output for an entire day, and it can operate at a relatively high efficiency by utilizing spectral beam splitting (SBS) technology with a PV system [71]. Spectral Beam Splitting (SBS) is a technology that divides the solar spectrum and directs different portions of it to different energy conversion methods. It is used in hybrid PV-CSP systems to improve the efficiency of solar energy conversion. In this system, the lower-energy solar radiation, such as infrared radiation, is directed towards the CSP system for thermal energy collection, while the higher-energy solar radiation, such as ultraviolet and visible light, is directed towards PV cells to generate electricity. The hybrid PV-CSP technology has recently drawn more attention from around the

globe and been added to the development agenda. The main benefits of PV-CSP hybrid system are as follows [71]:

a) Because of the hybrid system stability brought about by the power output characteristics of the CSP system, power quality will increase and the impact of PV systems on the grid will decrease.

b) The goal of PV-CSP hybrid systems is to maximize solar energy utilization, including waste heat recovery from PV cells and solar radiation SBS. This can lead to a decrease in the LCOE and an increase in overall generating efficiency.

There are several PV-CSP plants around the world, the biggest is the "NOOR" solar project that was established by the Dubai Electricity and Water Authority (DEWA), the largest electric utility in the UAE [31]. It is the largest CSP complex, which is located at the Mohamed Bin Rashed Al Maktoum solar park. The plant combines both central tower and parabolic trough CSP technologies. A total of 700 MW is anticipated in early 2024 when the three 200 MW molten salts trough segments are anticipated to come online, after the 100 MW tower CSP segment that went online in 2023. The fourth phase of the solar park includes 150 MW of PV with the 700 MW of the CSP. It is planned to reach a total capacity of 5 GW by 2030.

The development of large-scale solar power facilities would benefit from the advancements of the PV-CSP mentioned earlier. One of the ten actions and milestones of the CSP technology development is the PV-CSP hybrid technology, according to the Solar Thermal Electricity Technology Roadmap of the IEA (2014) [80]. While this field of study is still in development, it has been anticipated that hybrid PV-CSP technology will undergo extensive research and that additional commercial PV-CSP hybrid power plants will soon be built in certain areas with enough solar radiation and meteorological conditions.

2.4.2 Biomass-CSP hybrid systems

Apart from PV systems, CSP coupled to biomass can also improve the performance of standalone plants. Biomass offers CSP plants the possibility of operating continuously with only renewable sources, with many biomass resources appropriate for hybridization in various places in the world. Considering more than one biomass source increases the number of possible places for CSP-biomass hybridization, but at the expense of a larger initial investment. Several feasibility and technology evaluation studies have been carried out, such as in India [81], Brazil [82], [83], Indonesia [83], Australia [84], [85], [86], and Europe [87], even though CSP-biomass hybridization is still in its early phases of development. Such hybridizations have a global warming potential (GWP) up to ten times lower than CSP plants without biomass [83]. Furthermore, in comparison to standalone CSP and biomass facilities, it can offer higher market penetration.

Different hybrid configurations of CSP and biomass technologies provide unique financial and efficiency benefits. The study conducted by Peterseim et al. [88] covered several hybrid systems (Table 2.2). Gasification and solar towers get the highest energy efficiency of 33.2%, while fluidized bed and Fresnel technologies have the lowest specific investment (€/MW). There is a 33% variation in the specific investments between the 17 scenarios, with the efficiency increasing by 13% from scenario 1 to 16.

Table 2.2 Comparison of various CSP-Biomass hybridization schemes [88]

CSP technology	CSP working fluid	Biomass technology	Peak net efficiency (%)	Specific investment (M€/MW)
Parabolic trough	Thermal oil	Grate	29.3	4.11
Parabolic trough	Thermal oil	Fluidized bed	29.5	4.05
Parabolic trough	DSG	Fluidized bed	30.3	3.93
Fresnel	DSG	Fluidized bed	30.4	2.95
Parabolic trough	DSG	Fluidized bed	31.5	3.81
Fresnel	DSG	Fluidized bed	31.5	2.83
Solar tower	DSG	Fluidized bed	31.5	3.19
Parabolic trough	Molten salt	Fluidized bed	32.2	3.81
Fresnel	DSG	Fluidized bed	32.5	2.76
Solar tower	DSG	Fluidized bed	32.5	3.13
Solar tower	Molten salt	Fluidized bed	32.3	3.19
Parabolic trough	Molten salt	Fluidized bed	32.7	3.81
Solar tower	DSG	Fluidized bed	33.0	3.07
Solar tower	Molten salt	Fluidized bed	32.8	3.19
Parabolic trough	Molten salt	Gasification	32.8	3.81
Solar tower	DSG	Gasification	33.2	3.07
Solar tower	Molten salt	Gasification	32.9	3.19

Exchange rate 1 AU$ = 0.61€ [89]

For CSP-biomass hybridizations, choosing the right capacity is essential because the trends for cost scaling with plant size for standalone CSP and biomass plants are the opposite [83]. CSP plants should have a capacity of at least 50 MWe to the initial investment. In contrast, because of the higher logistical cost associated with transporting biomass, the capacity of biomass plants is limited to below 50 MWe. However, at the penalty of the decreased efficiency, a small plant is consistently supplied with biomass. For biomass facilities to benefit from economies of scale, a minimum capacity of 5 MWe is advised [84].

When the plant capacity increases, the specific investment drops. CSP-biomass hybridization can result in significant cost savings of up to 50% [84]. In comparison to a standalone CSP system, multiple researchers have found investment reductions of 43% and 69% [86], [88]. Hybridization lowers biomass consumption and land utilization by 14-29% as compared to a biomass-only plant [81]. However, the cost of CSP is so high that the decrease in land utilization may not offset the higher initial investment. Technological developments and local fabrication of CSP components can drastically lower the investment.

Despite these difficulties, Spain has been home to the first commercial hybrid CSP-biomass facility since 2012 (Termosolar Borges) [90], [91]. It is powered by two 22

MW thermal biomass units that run on forest waste biomass and energy crops and a parabolic trough CSP. Figure 2.18 shows the plant schematic diagram.

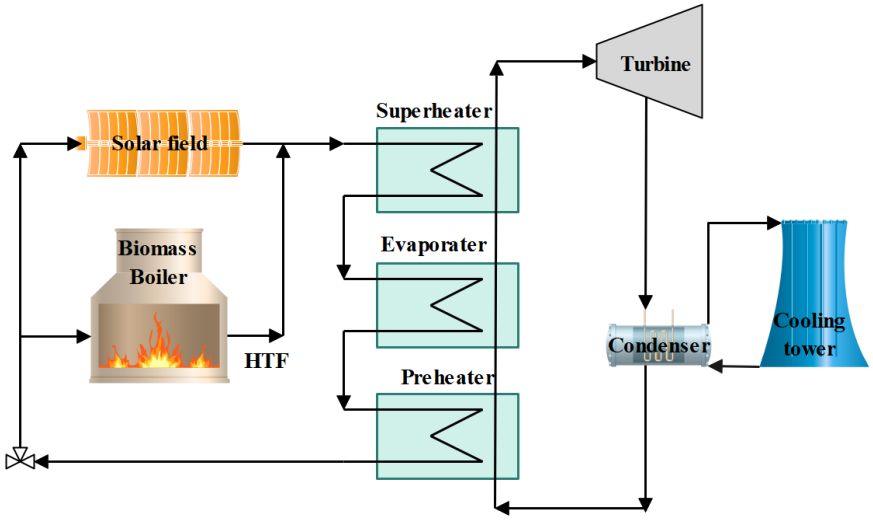

Figure 2.18 Termosolar Borges power plant in Spain [90], [91]

2.4.3 Geothermal-CSP hybrid systems

Another renewable resource that has the potential to be hybridized with CSP is geothermal energy. Geothermal power plants produce electricity by harnessing the thermal energy found beneath the surface of the Earth. There are various ways to use geothermal resources, depending on their nature and temperature:

a) Dry steam from geothermal wells can be put straight into a turbine to produce electricity.
b) In flash systems, steam is produced in a flash chamber at high pressure from hot water, which powers a turbine. The most prevalent kind of geothermal power plants are flash systems.
c) The third class of plants generate low-boiling-point organic fluid vapors by harnessing low-temperature geothermal resources.

Part of those systems operate on organic Rankine cycles, known as binary geothermal plants. There have been several databases of globally planned and operating geothermal projects [92], [93].

Geothermal plants have high capacity factors and run at baseload because of their steady source of energy. However, the low resource temperature (~150-200°C) decreases power plant efficiency to around 12% [92], increasing specific installation cost. Over time, geothermal well depletion decreases the plant power output. Some of the difficulties that standalone geothermal and CSP plants currently encounter can be solved by hybridization with CSP (≥380°C).

For hybridization of CSP with geothermal energy, two integration strategies are presented in Figure 2.19 [94]:

a) Using solar energy to preheat the geothermal brine (left).
b) Using solar energy to superheat the steam before it enters the turbine (right).

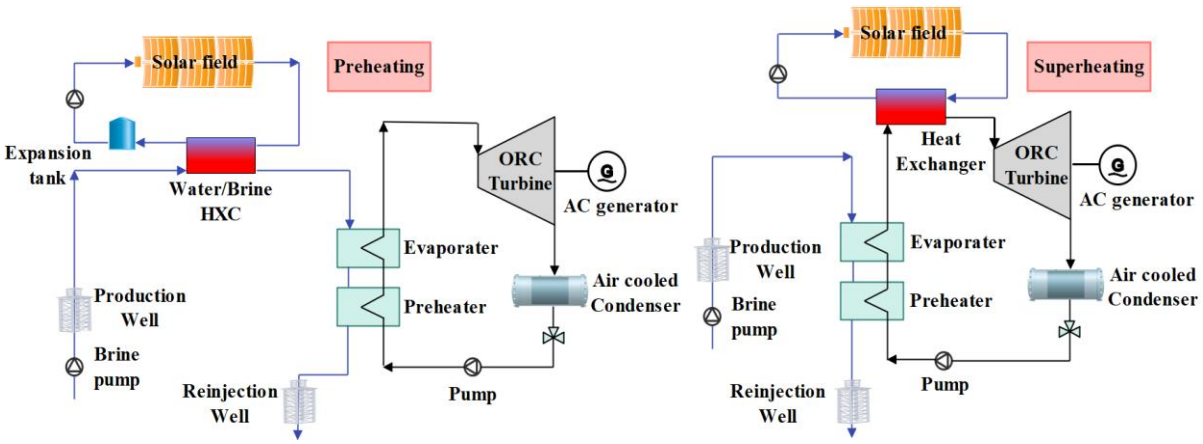

Figure 2.19 Integration schemes for CSP-geothermal hybridization [94]

When it comes to adapting an existing geothermal power plant, the preheating configuration is the most straightforward as shown in Figure 2.19, left [94]. Since the CSP increases brine temperature almost to the design point, no major changes to plant operation or control are required. This also extends the useful life of the plant because well depletion will take longer. Nevertheless, the use of solar energy at a lower temperature means higher exergy destruction and a decrease of plant solar-to-electricity efficiency. On the other hand, in the superheating configuration (right), the working fluid receives high-temperature solar energy input before entering the turbine, leading to a higher solar-to-electricity efficiency. Additionally, plant overall energy and exergy efficiency are increased. Due to modifications to control and operating conditions of the power plant, the retrofit cost in this arrangement is much greater.

The first hybrid solar-geothermal plant is the 33.1 MWe Stillwater triple hybrid binary power plant in Nevada, USA [95], from 2009. A 26.4 MWe PV unit was built later in 2012 to increase production during warmer summer months. Additional 2 MWe were added to the system capacity by installing PT collectors, which preheat the incoming geothermal brine by introducing 17 MW of solar thermal energy. The plant serves as a case study example of the hybridization of different renewable energy sources. It is anticipated that the combined plant will generate about 200 GWh of energy per year. The initial cost of the facility was projected as $15 million for the parabolic trough system in 2013.

The performance of hybrid plants is greatly dependent on the choice of the solar field size. In Australia and New Zealand, Zhou et al. [96], [97], [98] have reported on the impact of solar field size on the hybrid plant performance. The working fluid was superheated in these studies before entering the turbine by parabolic trough technology. The findings showed that, while the solar contribution to the system falls as the geothermal temperature rises, it increases with the solar collector area. Power output is also significantly influenced by the type of operation method used. The authors reported a net overall exergy efficiency of 12.4%. The hybrid plant yearly production exceeded the standalone geothermal plant by 73.6%.

Peterseim et al. have published a brief study on the viability of CSP-geothermal hybrid plants in Australia [84]. According to the analysis, plant electricity output rose from 6.3 MWe to 8.4 MWe for parabolic trough hybrid plants and 9.9 MWe for solar tower hybrid ones. Additionally, the plant thermal efficiency for a solar tower and parabolic

trough hybrid plants increased from 10.2% to 14.1% and 12.5%, respectively. At night, thermal storage devices or additional fuel were necessary for superheating.

Lentz et al. [99], [100] examined three hybrid setups for the Mexican geothermal facility Cierro Prieto with parabolic troughs. The results showed that the hybrid system could increase power output by increasing the steam flowrate. The integration of parabolic trough collectors with a supercritical binary plant for four distinct locations has been also examined by Astolfi et al. [101]. At San Diego, Imperial, and Pisa, the highest yearly average solar-to-electricity efficiency, solar share, and capacity factor were 9.4%, 27.9%, and 71.1%, respectively. According to the economic results, hybridization could result in 50% lower costs than standalone solar power facilities.

For a hybrid CSP-geothermal power plant, Zhou [102] examined the performance of the organic Rankine cycle at the subcritical and supercritical stages. The supercritical plant generated 4-17% more power than the subcritical plant while lowering the cost of solar energy by 4-19% and the solar capital by 6-24%. On the other hand, Boghossian [103] did not discover any synergy between a parabolic trough CSP system and a Kalina hybrid cycle running on a geothermal brine. According to the author, electricity output was 29% lower than in standalone plants. Enhancements to the system thermodynamic performance could include regeneration, reheating, switching working fluids, and using solar energy at other points in the cycle.

2.4.4 Wind-CSP hybrid systems

Right now, wind energy is the one of the most affordable renewable energy sources and is globally accessible, but the field of CSP hybridization with wind energy has not received much attention. This is primarily because, in contrast to other thermal energy sources like biomass and geothermal, wind and CSP do not have a broad synergy in terms of infrastructure sharing, as shown in the schematic in Figure 2.20. As a result, CSP-wind integration is known as a light hybrid [84]. But since wind speed is lower during the day and summer than it is at night and in the winter, solar energy can balance wind generation to produce power more evenly.

Currently, there is no large scale commercial operational hybrid wind-CSP. Researchers in this field have shared their explanations, ideas and suggestions regarding its feasibility. According to a study by Kost et al. [105], a CSP-wind portfolio of energy generation is more financially feasible in North Africa than standalone CSP. Sioshansi et al. [106] have examined several arrangements for the implementation of wind and solar power facilities in Texas, USA. According to their analysis, hybrid plant deployments with up to 67% CSP may result in a profitable return on investments. The outcomes are, nevertheless, susceptible to CSP and power transmission costs. Due to the implementation of many wind farms and CSP plants in Australia, Peterseim et al. [84] have indicated the potential of CSP-wind hybrid plants. South Australia has several areas that show a great potential with wind speeds above 7 m/s and direct normal irradiance (DNI) exceeding 19.1 MJ/m^2/day. The authors also propose that the thermal energy storage system of the CSP plant could be charged by the excess power generated by the wind farm during the night. However, for this integration to be financially sustainable, there must be a 260% difference in electricity price during day and night.

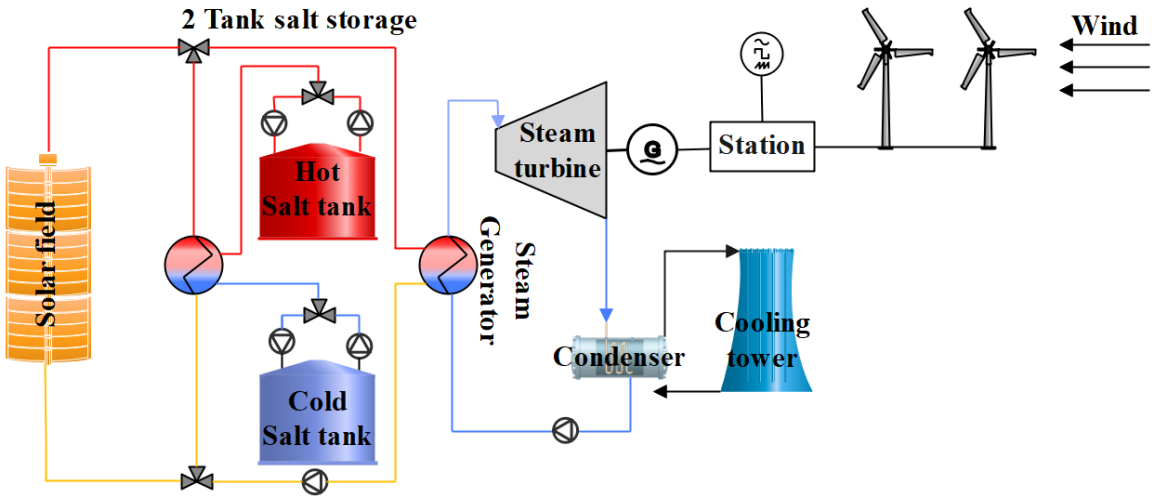

Figure 2.20 Schematic of a wind-CSP hybrid plant [104]

To provide steady renewable power in the Andalusian region of Spain, Santos-Alamillos et al. [107] have also examined the hybridization of CSP with wind farms. According to their study, the best locations for wind and CSP plants can generate reliable baseload power while overcoming the unpredictability of standalone CSP and wind plants. Their performance was also improved when thermal storage was added.

Vick et al. [108] have examined the operation of a CSP-wind hybrid plant in the Texas Panhandle to evaluate whether CSP-wind hybrids could match the utility electricity load better than a standalone wind farm. At night, when electricity usage is at its lowest, standalone wind farms generate the most electricity, and vice versa. It was determined that the optimal combination for the utility energy load was a 33 MWe CSP plant with 6 hours of thermal storage and a 67 MWe wind farm. But compared to the wind farm ($64/MWh), the hybrid plant had a higher levelized cost of electricity (LCOE), $108-129/MWh.

In Southern Minnesota, an 800 MWe wind farm hybridized with a 705 MWe parabolic trough solar field was studied by Reichling et al. [109]. A power output curve closer to the load demand curve was achieved by hybridization. Additionally, CO_2 emissions (10.8 g/kWh) were lower than for the electricity generated from a parabolic trough solar field (13.4 g/kWh) but slightly higher than those of standalone wind power (10.2 g/kWh). The hybrid plant LCOE is higher than the solo wind plant (67.8 $/MWh) at 123 $/MWh. If solar technology investment costs are reduced by 75%, the hybrid plant LCOE would be just 7% of the wind plant LCOE.

On the Greek island of Skyros, hybridization of CSP with wind for energy autonomy has been examined by Petrakopoulou et al. [110] with 3.3 Mwe wind turbines and a10 MWe solar facility. Total capacity was increased to 16.6 MWe using two wind turbines, and the plant mean annual efficiency is 19.2%, in the range of typical CSP and wind power plant efficiencies. Electricity cost was 400 €/MWh. According to reports, the hybrid plant has a better exergy efficiency and a lower land use, making it a viable choice for energy autonomy in isolated areas like islands.

2.4.5 Combined cycle power plant-CSP hybrid systems

When compared to Brayton and Rankine cycle power plants, combined cycles offer higher efficiency values, which makes integrating solar energy into them appealing (although their sustainability is the main reason for solar integration). The integration between a combined cycle (CC) power plant and a CSP is usually called an integrated solar combined cycle (ISCC). Solar integration can be performed into the top or the bottom cycle, or into both cycles. In solar thermal power plants, steam is usually generated by solar collectors to power thermodynamic cycles. One approach is to generate steam directly into the absorber tube – direct team generation (DSG). The second approach is to transfer solar thermal energy from the collectors to heat transfer fluid (HTF) and use a heat exchanger to generate steam. ISCC technology is the focus of this work, so the next section is fully dedicated to its description.

2.5 Integrated solar combined cycle (ISCC)

There is wide agreement on the synergies between fossil and solar technologies in the literature [111], [112], as higher ambient temperatures during days of high solar irradiation led to the decrease in the production of conventional combined cycle power plants. ISCC operation results in high solar-to-electric efficiency rates, offering a higher thermal performance than original combined cycle power plants. Hence, ISCCs are considered an alternative to fossil fuel power plants. Recent growth in natural gas consumption for electricity generation has established a considerable base for integrating concentrated solar energy as a complement. Solar energy is a plentiful resource in many nations; therefore, including this resource will help preserve some non-renewable energy resources. All current gas-powered plants might be upgraded with a solar field for a relatively small cost, increasing their base power. Traditional concentrated solar thermal plants require more thermal energy storage capability than ISCC thermal power plants. In addition, ISCCs produce power on demand for less money than standalone concentrated thermal power and a lot less than photovoltaic plants, as gas can be used when solar energy cannot meet the demand.

Around the world, mainly in countries with high solar irradiation, several ISCC plants are either under construction or in service. Table 2.3 shows some examples, entirely coupled to PTC solar fields. It is expected that the number of ISCCs around the world will grow in the upcoming years, as they are catching more attention due to their promising future for clean electricity generation.

Table 2.3 ISCC power plants worldwide [113], [114], [115]

Power plant	Country	Technology	Total Installed capacity (MW)	Solar installed capacity (MW)	Status
Agua Prieta II	Mexico	PT	465	12	Operating since 2017
Ain Beni Mathar	Morocco	PT	472	20	Operating since 2011
Archmide	Italy	PT	750	4.7	Operating since 2010
City of Medicine Hat	Canada	PT	-	1.1	Operating since 2014
Duba 1	Saudi Arabia	PT	550	43	Operating since 2023
Hassi R'Mel	Algeria	PT	150	25	Operating since 2011
Kuraymat	Egypt	PT	120	20	Operating since 2011
Martin Next Generation Solar Energy Center	USA	PT	3780	75	Operating since 2010
Waad Al-Shamal	Saudi Arabia	PT	1390	50	Operating since 2018

Victorville 2	USA	PT	563	50	Under construction
Yazd	Iran	PT	461	17	Operating since 2010

In the following subsection, the two hybridization techniques used to transfer solar thermal energy to the CC power plant will be studied. Then, different hybridization configurations based on the solar field integration position will be investigated.

2.5.1 Hybridization techniques

Collectors in solar thermal power plants are typically used to generate steam to power a thermodynamic cycle. The two techniques are direct steam generation (DSG) into the absorber tube, and solar thermal energy transfer from the collectors to a heat transfer fluid (HTF) and to steam through a heat exchanger, as shown in Figure 2.21.

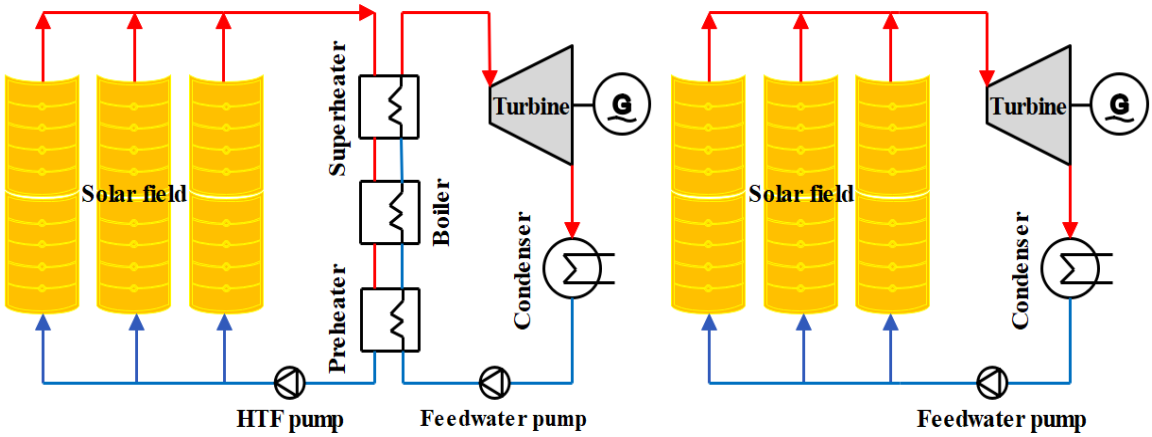

Figure 2.21 PTC solar power plant: oil as HTF (left) and DSG (right) [116]

2.5.1.1 Direct steam generation (DSG)

In DSG, water is heated directly in the solar receiver, generating steam that powers a turbine and generates electricity. With this approach, the system becomes simpler as it does not require an intermediary heat transfer fluid. DSG is frequently utilized in solar towers or parabolic trough CSP technologies. To achieve steam preheating, evaporation, and steam superheating, the solar field is coupled to the steam circuits. All feedwater is delivered to the collector inlet during the first (once-through) phase, and as it passes through the collector rows, it is heated up to superheated vapor. In the third step, referred to as the recirculation phase, a water-steam separator is positioned at the end of the collector row evaporating portion.

In order to compare the performance of a 220 MW DSG-ISCC to a traditional CC power plant, the system performance was examined in two different climates by Montes et al. [117], Las Vegas (US), which has a hot and dry climate, and Almería (Spain), which has a sub-desertic Mediterranean climate. The proposed plant is shown in Figure 2.22. Although the CC power plant performs worse in Las Vegas because of the higher temperatures, the simulation using the program TRANSYS showed that the DSG-ISCC performs better in Las Vegas than in Almeria due to solar hybridization, where global efficiencies were 52.18% and 51.90% for Las Vegas and Almería respectively. Furthermore, an economic study showed that the ISCC power plant levelized cost of electricity (LCOE) is lower in Las Vegas (80.52 vs. 81.29 €/MWh for the original CC), but it is higher in Almeria (80.55 vs. 80.35 €/MWh for the original CC).

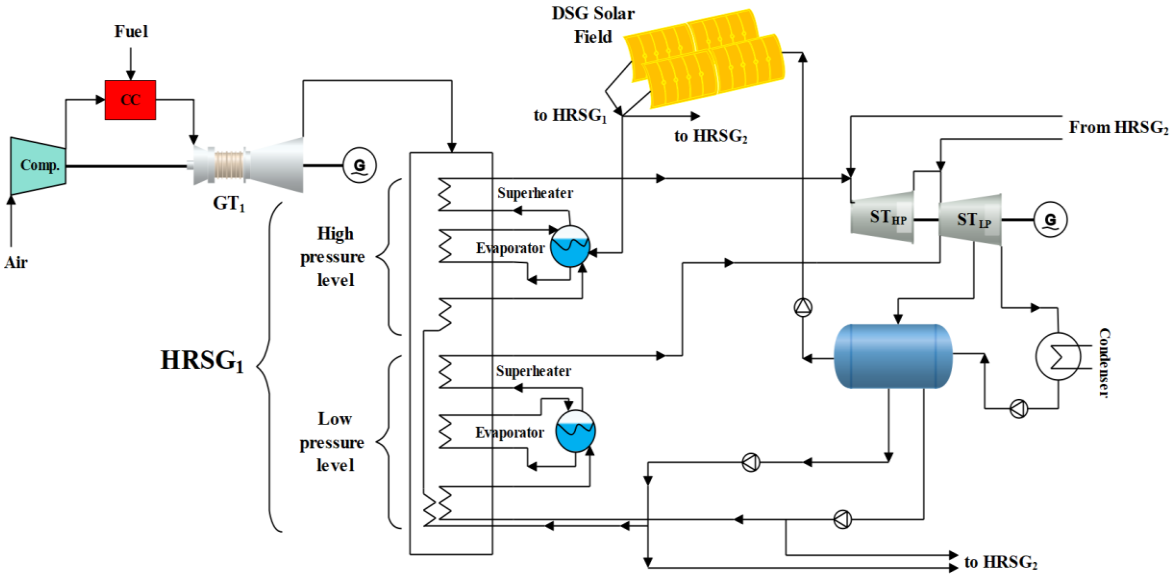

Figure 2.22 DSG-ISCCS with double pressure level proposed by Montes et al. [117]

Integrating DSG technology into the Brayton cycle is also possible, as studied by Craig et al. [118], who integrated a parabolic trough solar field into the top Brayton cycle of a CC. They have demonstrated the viability of the suggested concept, claiming great dependability and little financial risk. It has been noted that adding a 100 MW solar thermal energy source to a 40 MW gas turbine improved the performance and resulted in a solar fraction between 57 and 59%.

A novel idea was introduced by Livshits and Kribus [119], using solar radiation collected by a medium temperature parabolic trough solar field to improve the thermodynamic efficiency of a steam-injection gas turbine. The installation of a condenser to recover and recycle the injected water was part of the suggested concept, as illustrated in Figure 2.23. They were able to achieve a nominal performance similar to the value of four commercial gas turbines, using the Honeywell Unisim software. According to the results, it is possible to achieve a total conversion efficiency of 40-55% and a solar fraction up to 50%. Another benefit of the suggested approach is that it has an incremental efficiency of 22-37% and solar-to-electricity efficiency of roughly 15-24%, exceeding that of contemporary solar power plants.

For the purpose of studying the performance of DSG-ISCCs under the climate conditions of Libya, Elsaket [120] generated a mathematical code. The main goal of the study was to transform the existing 4 x 51 MW ISCC shown in Figure 2.24 into an ISCC with DSG. According to the results, the solar field has an efficiency around 78% in the Libyan environment. Plant capacity was increased to 286.12 MW, resulting in yearly fossil fuel savings around 151,260 tons and a reduction of 468,910 tons of CO_2.

In Yulin, China, Li and Yang [121] examined a two-stage solar input DSG-ISCC consisting of a single gas turbine, a dual pressure-single reheat HRSG, and a steam turbine, as shown in Figure 2.25. Hourly, monthly, and annual performance values were optimized and evaluated using ASPEN PLUS process simulation software. The optimization showed that the ideal design pressure and temperature for the reheat and low pressure steam, respectively, are 16 bar and 560 °C, and 5 bar and 320 °C, at the

design point. The proposed approach offered an increase of roughly 1.2% and 2.5%, respectively, in net solar-to-electricity efficiency (up to 30%) and overall energy efficiency (up to 61%) as compared to one-stage solar input DSG-ISCCS.

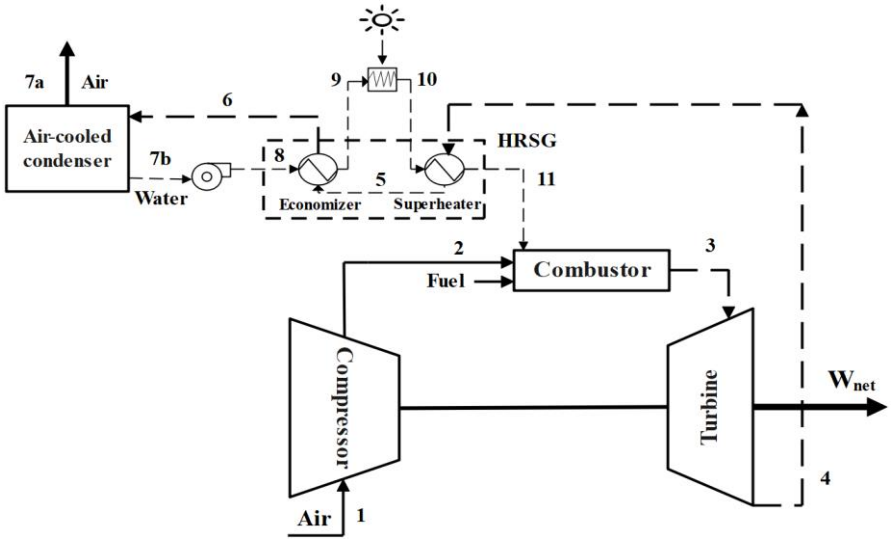

Figure 2.23 Solar steam injected Brayton cycle concept [119]

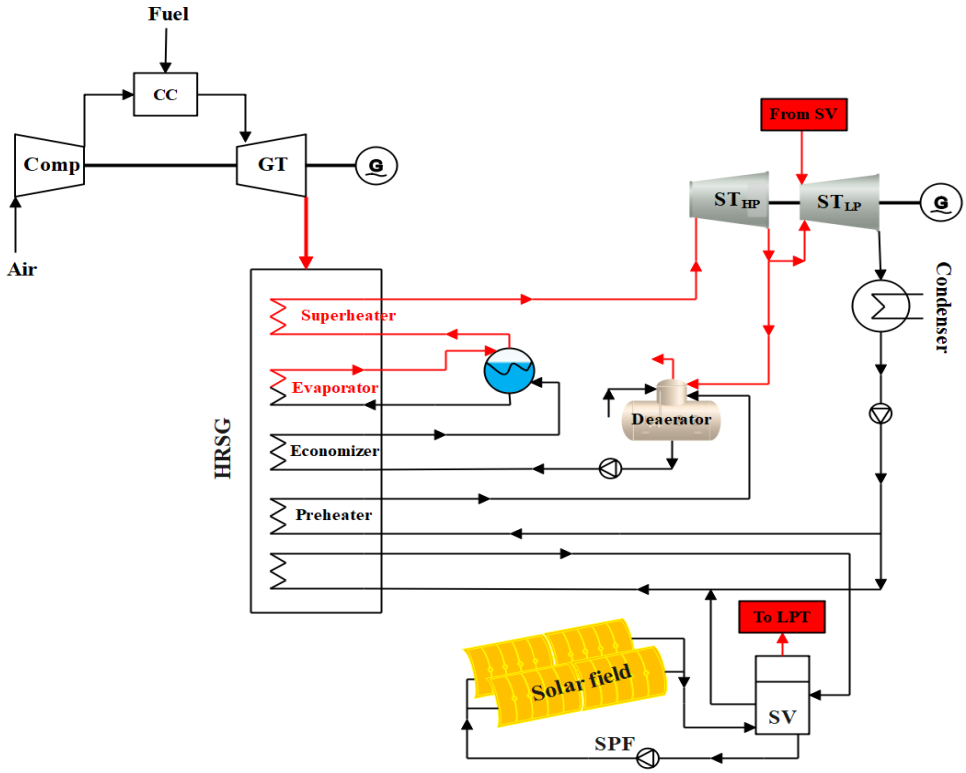

Figure 2.24 DSG proposed plant in Libya [120]

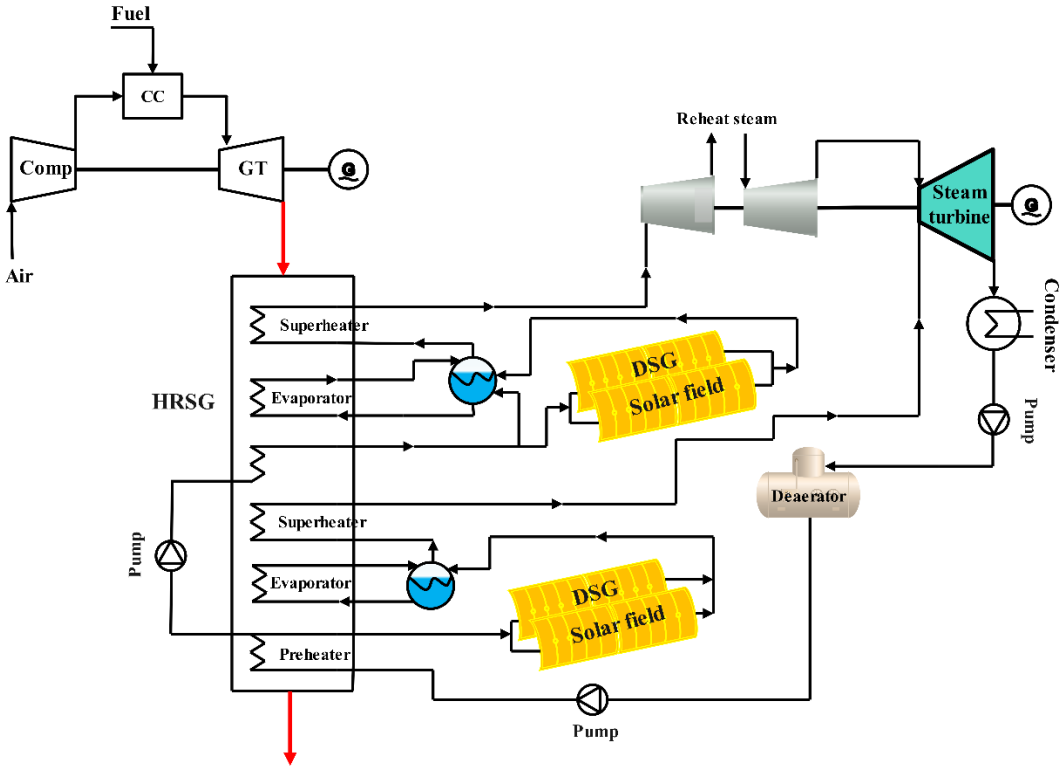

Figure 2.25 Advanced DSG-ISCC with two stage solar input for improving overall performance [121]

2.5.1.2 Heat transfer fluid (HTF)

Commercial use of HTF technology began in 1984 [122]. According to this idea, the solar field reflective region collects the DNI and transfers it to the absorber tubes, raising the temperature of a HTF circulated throughout the solar field. Through the so-called Solar Steam Generator (SSG), the HTF transmits solar thermal energy to the power cycle, generating steam. HTFs can be synthetic oils, molten salts, or non-freezing hydrocarbons. The benefits of using HTF outweigh the drawbacks of DSG, particularly the high vapor pressure and possibility of freezing if the plant is operated in cold regions. However, HTFs like oil can cause fires when they leak. Also, they become exceedingly viscous at low temperatures, requiring extra pumping power. Nowadays, lots of existing HTF-ISCCs are operating in the world. Figure 2.26 shows a well-known configuration of this technology, the 140 MW Kuraymat HTF-ISCC in Egypt, operating since 2011 [123]. Investigations have revealed that the solar area can, on average, offer almost extra 8% energy than projected. A model of this plant was created by Abdel Dayem et al. [124], who discovered that increasing DNI might result in a 10% increase in turbine power and a 25% increase in solar share.

In Iran [125], six thermal power plants were compared in terms of technical and economic aspects, considering several configurations and capacities, including ISCCs with a 67 MW solar field, ISCCs with a 67 MW solar field and fuel backup, ISCCs with a 33 MW solar field, ISCCs with a 33 MW solar field and fuel backup, SEGS (Solar Electric Generating System), and a simple gas turbine (GT). It was determined that ISCCs with a 67 MWe solar field (the highest capacity) was the best configuration. During 30 years of operation, a power plant like this could save 59 M$ in fuel

consumption and prevent 2.4 million tons of CO_2 emissions. Its LCOE is 10% and 33% cheaper than those of a CC and a GT, respectively. Another ISCC configuration suggested by Hosseini [125] et al. is shown in Figure 2.27. The annual performance of Hassi R'Mel HTF-ISCC was modelled using TRNSYS software by Derbal-Mokrane et al. [126]. According to the findings, the power plant can produce 150 MW with 52% efficiency. The solar share was about 30 MW of the total output power of the plant.

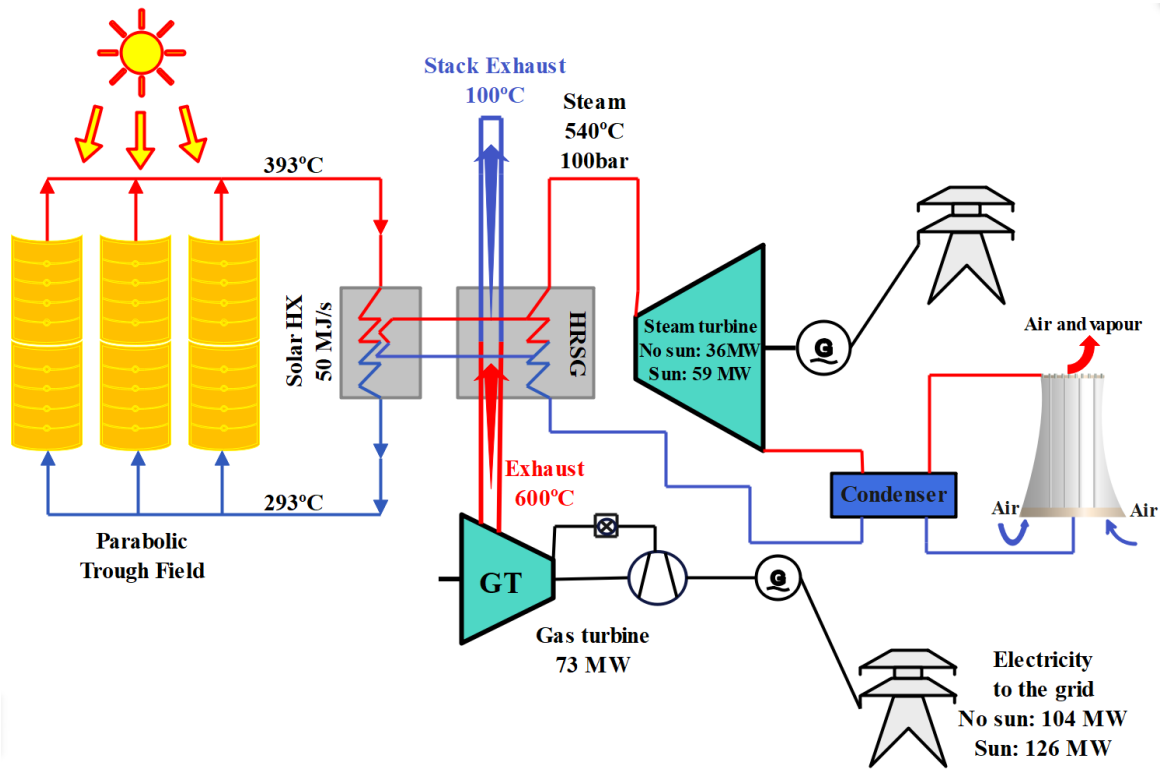

Figure 2.26 Kuraymat HTF-ISCC in Egypt [123]

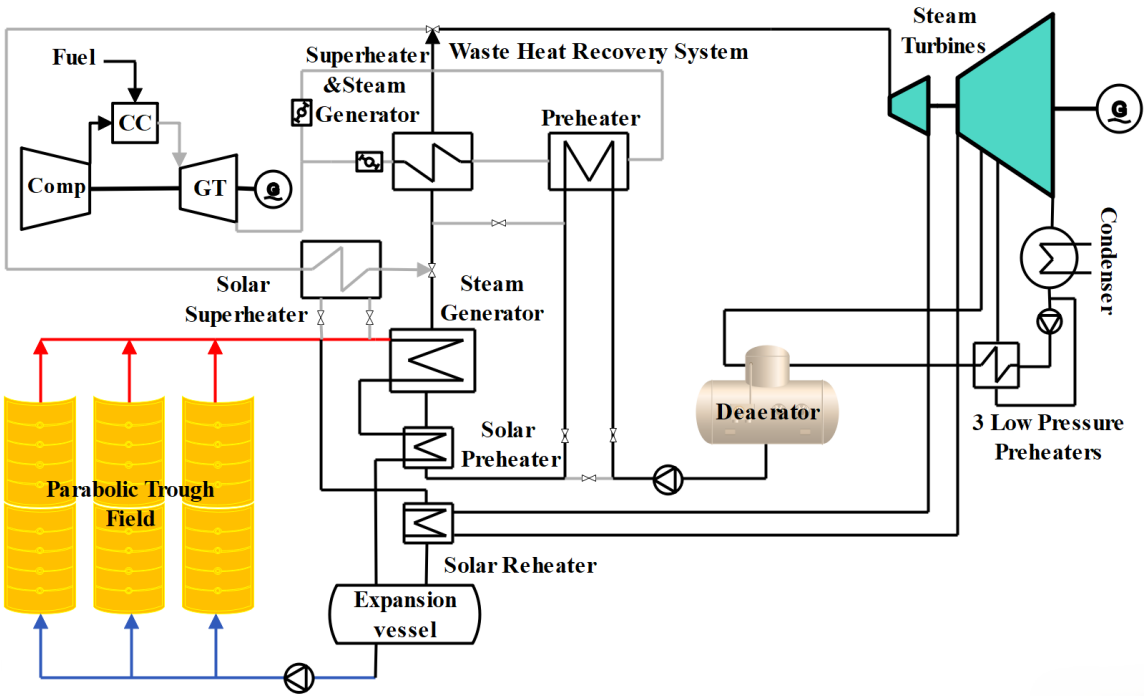

Figure 2.27 HTF-ISSC suggested by Hosseini et al. [125]

In Libya, Elhaj et al. [127] developed a mathematical model in Visual Basic 6.0 to predict the effects of converting an existing gas turbine in Misurata city into a HTF-ISCC. The Desalsolar 1.0 software database was used to collect meteorological data, and Computer-Aided Thermodynamics software (CATT2) was used to determine the parameters of the steam. They examined how the integrated solar combined cycle system performed depending on solar concentration ratio and the efficacy of the SSG. According to the reports, both electricity production and thermal efficiency increased.

Using FORTRAN, Behar et al. [128], [129] generated a mathematical program to analyze the performance of the Hassi R'Mel ISCC. They proposed a HTF-ISCC with a basic pressure level consisting of two 47 MW gas turbines, an 80 MW oversized steam turbine, and a solar field with a reflective area of 183,120 m^2. At the design point, it was discovered that the HTF-ISCC electricity production and efficiency were higher than those of the combined cycle power plant (134 MW, 57.5%), 157 MW and 67%.

Kane and Favrat [130] investigated the effect of the pressure level and flow interaction between the HRSG and SSG on the energy efficiency of the HTF-ISCC to improve the network of heat exchangers. They considered three different pressure levels: a single pressure level for both HRSG and SSG, a double pressure level for HRSG and a single pressure level for SSG, and a double pressure level for both heat exchangers. Different arrangements of steam between the HRSG and the SSG were studied for each situation. The results showed that the ISCC with double pressure can improve thermal efficiency, becoming the ideal configuration for the power plant.

Allani et al. [131] investigated the technical and financial viability of implementing HTF-ISCCs in Tunisia under the context of the PAESI project (Project d'Aménagement Energétique Solaire Intégré). The suggested design aims to generate 58 MW at night when operating in combined cycle mode and to deliver roughly 88 MW of electricity during sunny periods. Two gas turbines and a steam turbine form the combined cycle. The solar field proposed is composed of PTCs and a SSG connected to the HRSG and a buffer tank. The authors investigated two operating strategies to study thermal efficiency, greenhouse gas emissions, and financial aspects. They discovered that maximizing power generation has a greater potential to reduce CO_2 emissions than maximizing cycle efficiency, and the smaller the solar field, the more economically viable the plant is. Additionally, they claim that the ISCC has greater merit than SEGS.

2.5.2 Hybridization configurations

CSP plants are normally integrated within a power plant to produce additional steam for use in the NGCC steam turbine [132], [133] if it is integrated in the steam cycle, or to preheat the compressed air in the gas turbine before entering the combustion chamber [134], when integrated when the top Brayton cycle. Figure 2.28 presents different options for solar field integration positions, where different positions of solar energy integration can lead to different impacts on the ISCC system performance. The next section illustrates different types of hybridization configurations.

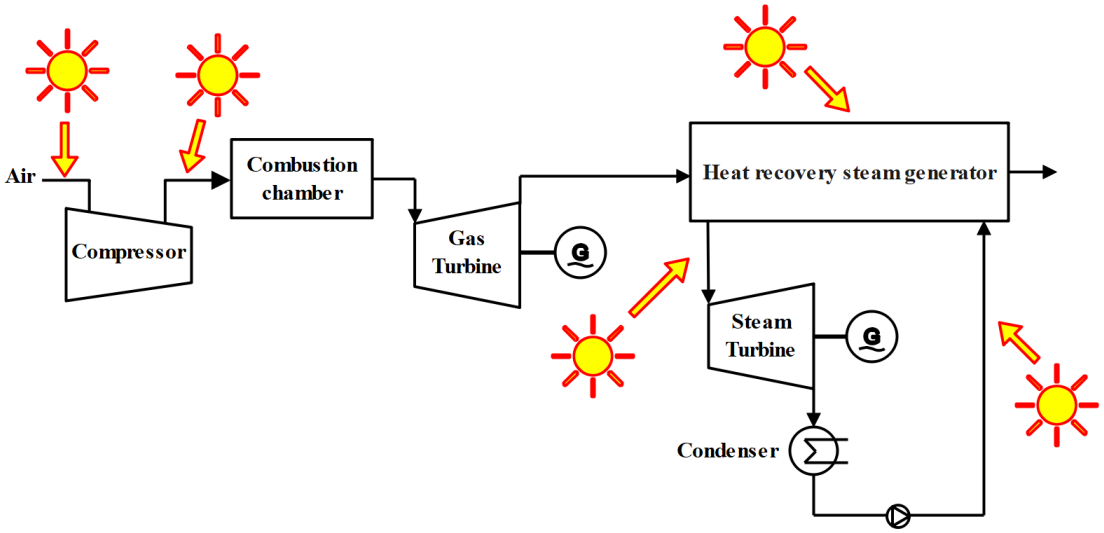

Figure 2.28 Different solar energy integration positions [135]

2.5.2.1 Gas cycle hybridization configurations

In comparison to Rankine-based cycles, the integration of solar energy into Brayton cycles is less developed and more recent. While using medium temperature heat sources, such as PTC solar technology and synthetic oil, the Brayton cycle has a less effective performance. The maximum temperature should increase from 400 °C to 1000 °C to achieve competitive performances. Since the concentrated solar receiver is typically integrated before the combustion chamber, high concentration systems are typically suggested [136], [137]. Fossil-solar hybrid plants have been also suggested, requiring systems with lower solar concentration ratios since the solar contribution might be used to preheat combustion air. Optimizing energy recovery and reducing energy losses is key to increasing regenerative contribution, which will increase system sustainability and efficiency.

In these configurations, the steam cycle is not modified [138]. One of the main advantages of gas cycle hybridization over steam cycle hybridization is the higher thermomechanical conversion efficiency. Solar thermal energy is proposed to be injected into the Brayton cycle at its maximum temperature, so conversion efficiency of the gas cycle hybridization will be greater than when it is injected in the steam Rankine cycle [139]. Without using HTFs, Amelio et al. [139] suggested heating the combustion air by directing it through PTCs, as shown in Figure 2.29. As a result, the compressed air is sent to the solar field to be preheated to 580°C before entering the combustion chamber. The results showed that the ISCC average annual global efficiency was 60.9%, while it was only 51.4% for the reference CC plant without solar integration. Natural gas consumption was 152,236 tons for the ISCC instead of the original 180,397 tons for the CC plant. The authors predicted a 22% reduction in fossil fuel consumption at design conditions and a 15.5% reduction when considering annual performance. Therefore, the extra cost of solar field components could be recovered in less than 5 years.

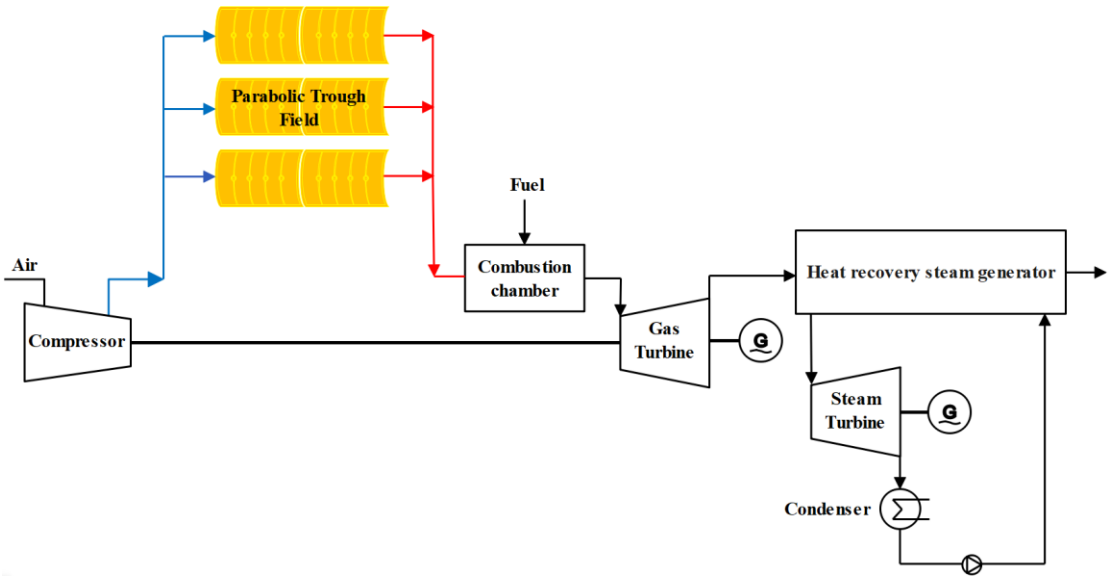

Figure 2.29 Gas turbine integration configuration [139]

In the work of Duan et al. [140], a setup for preheating the combustion air was presented, where preheated water was added to the HRSG with air leaving the compressor as shown in Figure 2.30. Even though the air is first chilled, a higher temperature is ultimately reached thanks to the solar contribution.

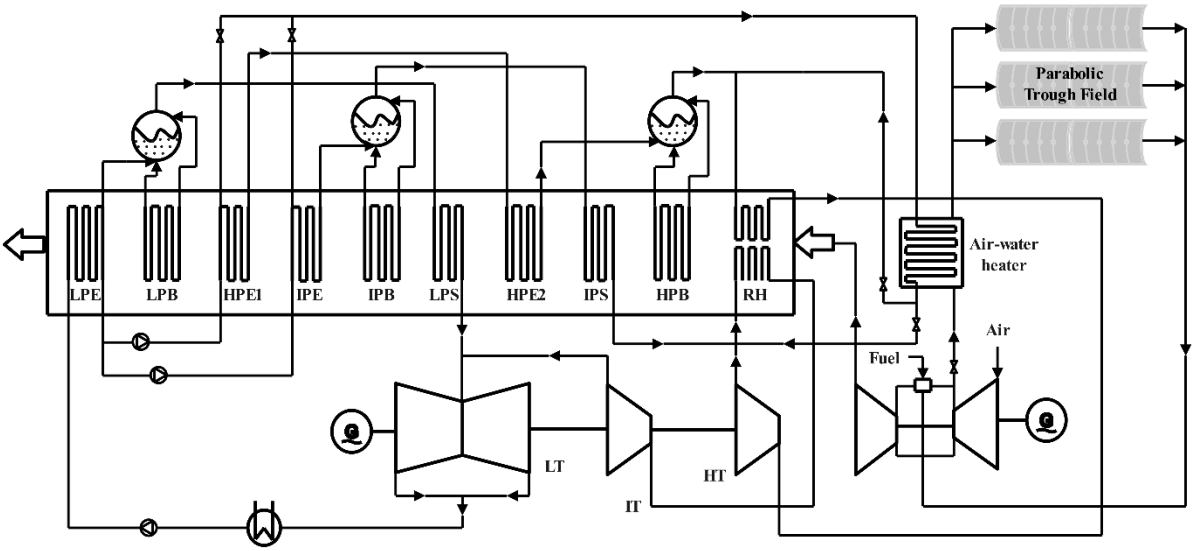

Figure 2.30 ISCC system diagram with novel integration configuration proposed by Duan et al. [140]

Although PTC is the most spread technology for the ISCC in the worldwide, Solar Tower technology (ST) has been also studied and presented in several integrations (within Brayton and Rankine cycles) within the ISCC [141]. First, it can be used to heat the compressed air, as shown in Figure 2.31, before it enters the combustion chamber. Second, the thermal power can be combined with the heat from the GT exhaust gas to generate steam for the steam turbine. Thirdly, it can be used to generate steam for the steam turbine while recovering heat from the GT exhaust to heat the compressed air. Fourth, the Brayton cycle could be used as a backup system at night (in CCGT mode) and the ST-Rankine could generate baseload during the day at the same utility power station.

Investigations were performed on the thermodynamic and financial behavior of ST-ISCCs. The ST technology has received a lot of research interest, and there are some commercial ST power plants operating in various regions of the world. From a thermodynamic and financial standpoint, the combination of this technology with the ISCC has a lot of potential. However, compared to the PTC, the ST technology is less mature. There are some obstacles which can be divided into three categories: A-technology maturity, B-financial and policy considerations, and C-technical considerations. The following are some of the topics that require research:

a) The effect of tower height on the ST-ISCC levelized cost of electricity (LCOE).
b) The impact of the ST-ISCC plant on local air quality.
c) Techno-economic analysis of the operational ST-ISCC.

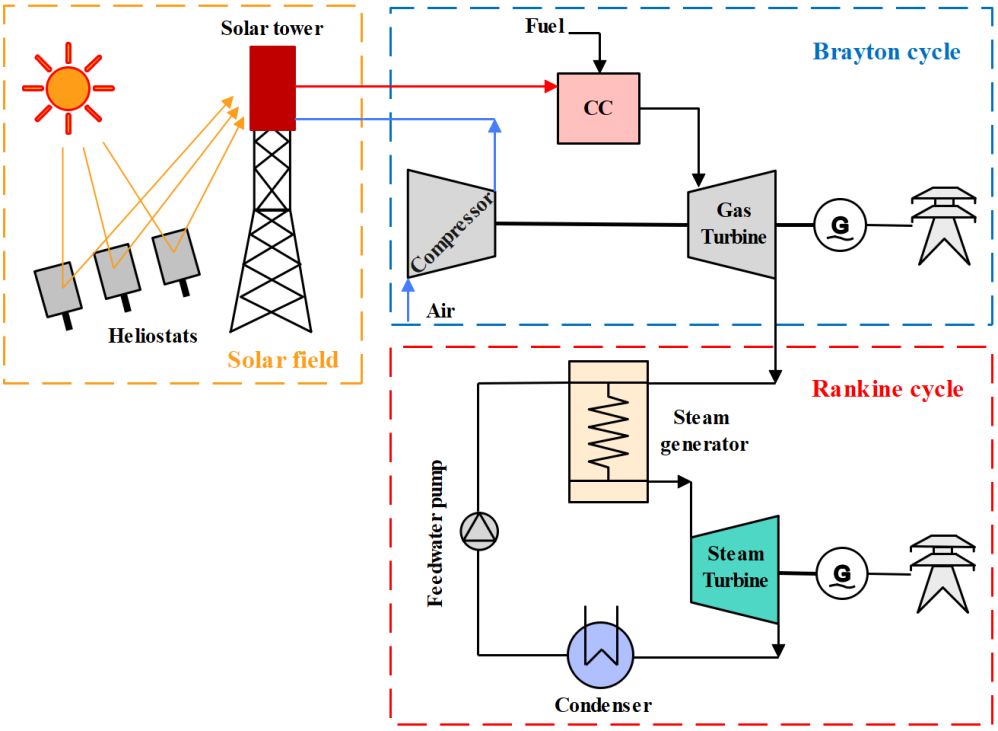

Figure 2.31 Schematic representation of a solar tower ISCCS power plant [141]

Rovira et al. [138] compared the annual performance of a reference CC with the performance of two ISCC layouts that differ in the options for integrating solar heat: a conventional ISCC scheme in which solar heat is used to directly evaporate water at the high pressure level of the steam cycle and a second scheme in which the solar heat is used to preheat combustion air. Three different solar concentration technologies (LFR, PTC, and ST) were examined. The results showed that, because of the pressure drop in the heat exchanger, the ISCC with combustion air preheating suffered a reduction in annual energy output compared to the reference CC, but DSG, on the other hand, boosted generation. However, the former option had a significantly better solar-to-electricity efficiency, with PTC and ST achieving rates above 40%. Therefore, Rovira et al. proved in this work that, in comparison to steam cycle integration, solar integration in the GT has higher overall and solar-to-electricity efficiency. Currently, there are no ISCC facilities in operation that incorporate solar energy into the top cycle

due to insufficient advances in the technology of solar receivers that can withstand high temperatures and pressures.

2.5.2.2 Steam cycle hybridization configurations

Solar field integration into the bottom Rankine cycle in a CC power plant is a common ISCC configuration. Compared to top cycle integration, this option is technologically more advanced and delivers greater reliability with less financial risks [118]. This arrangement, the most popular solar combined cycle configuration, was first presented by the company Luz Solar International and drew on the prior knowledge from commercial operation of SEGS plants between 1984-1990 [142].

Figure 2.32 shows different steam cycle hybridization configurations based on HTF technology that include a SSG, in which the HTF generates steam [142]. In contrast, configurations based on DSG technology do not require any steam generator, because steam is generated directly in the troughs of the solar field [142]. Solar integration depends on the SSG function: preheating, evaporating or superheating, as shown in Figure 2.32 [142]. Most ISCC plants that have been constructed, or that are currently being planned, have solar field designs that supply thermal energy in parallel to HRSGs. Following Aghdam et al. [143], integrating the solar field before the bottom steam cycle superheater increased plant capacity from 714 to 728 MW and efficiency by 2%.

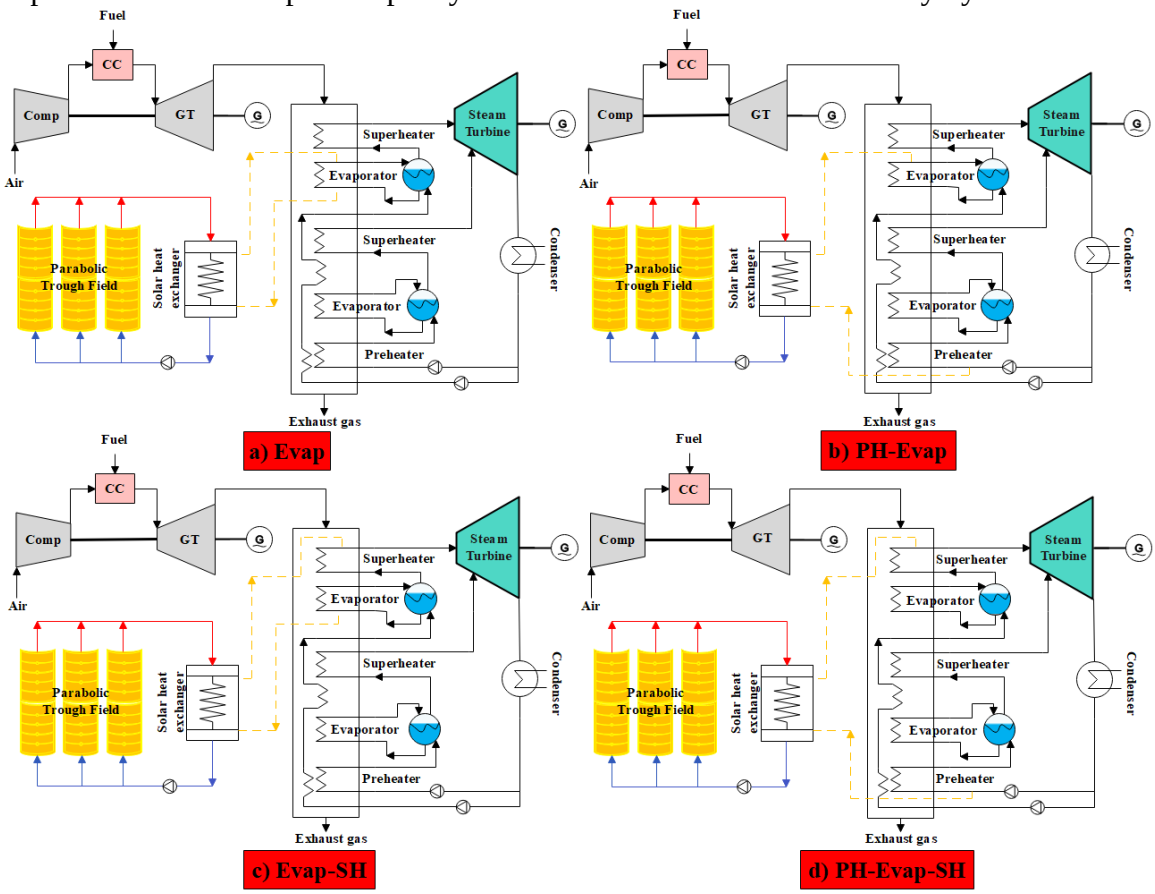

Figure 2.32 Steam Cycle hybridization configurations [142]

An ISCC plant with two gas turbines and a steam cycle was presented in earlier research, where heat exchangers that evaporated the preheated water before it returns to the steam drum allowed solar energy to be incorporated in parallel to the boiler, as

shown in Figure 2.33 [131]. The system benefits and the specifications for the boilers, heat exchangers for the solar generator and the HRSG were studied, and one of the earliest economic analyses was provided. Also, the need for financial incentives was highlighted, due to economic unfeasibility given the cost scenario [130], [144].

The implementation of facilities in developing nations at the turn of the century, such as Algeria, Egypt, or Morocco, funded by the Global Environment Facility Agency, encouraged research on ISCCs. The economic viability and production costs of various layouts were the main matters of these investigations. Today, several ISCC plants have been implemented, some of them thanks to this funding. There are also plants in Yazd (Iran), the Martin Next Generation Solar Energy Centre (USA), the Archimede (Italy), Hassi R'mel (Algeria), Kuraymat (Egypt), Ain Beni Mathar (Morocco), and Agua Prieta II (Mexico). Most built or planned plants have solar field arrangements that provide heat in parallel to the HRSG. Except for Archimede, where the HTF is molten salts, solar energy is transferred to steam with a second steam generator fed by synthetic oil from the solar field [145]. As a result, solar energy helps to evaporate water, as in the Hassi R'Mel and Yazd plants [128]. In other plants, such as Archimede and Beni Mathar, solar heat also contributes to some degree of preheating and superheating.

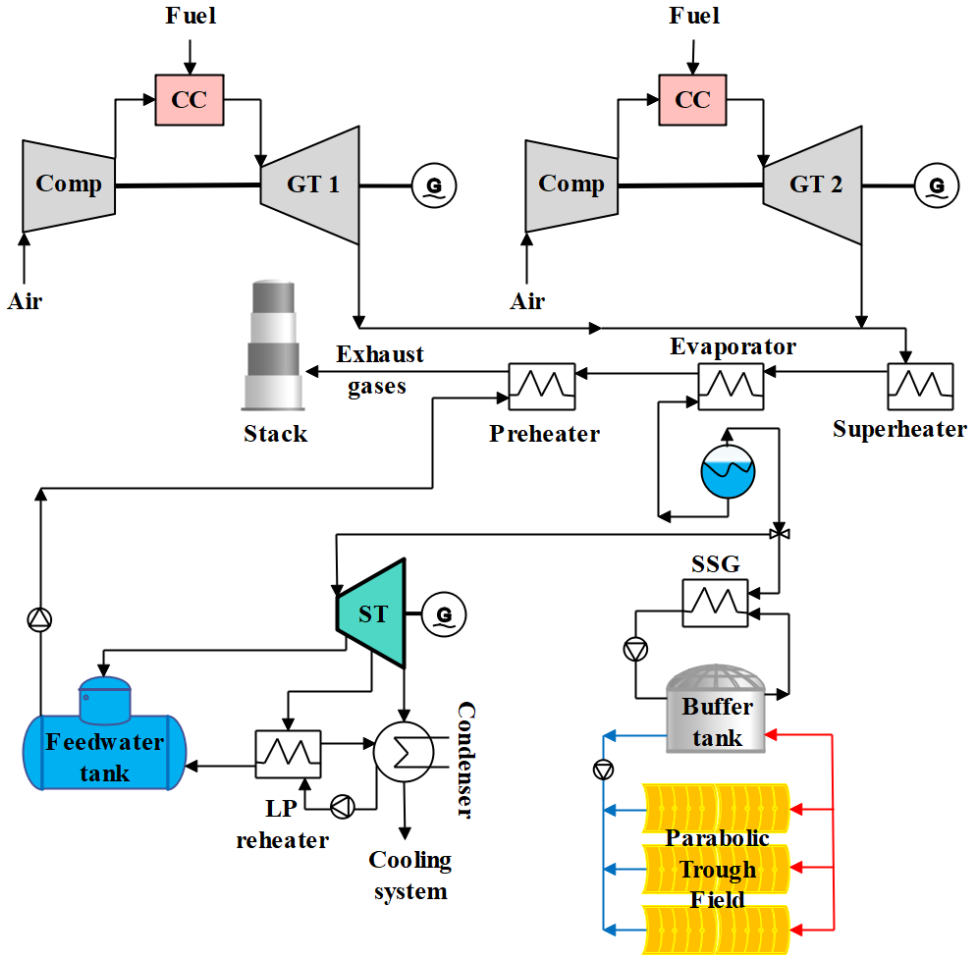

Figure 2.33 Proposed ISCC with two gas turbines [131]

Other studies have also considered other solar concentration devices. For instance, Manente et al. [146] compared ISCC plants using PTC, LFR, and CR and concluded

that a solar concentration as high as in CR was not required to reach a 30% solar-to-electric efficiency. Due to the challenge of controlling the two-phase fluid in the solar field, the use of a HTF is more practical than that of a DSG, but the latter has also been investigated, given the advantage of not having a separate steam generator. Using DSG in parallel to the high pressure evaporator of the HRSG, Rovira et al. [138] compared the annual performance of ISCC cycles with three solar concentration technologies: PTC, LFR, and CR. The results showed a higher performance for PTC for both locations studied, with solar-to-electric efficiency reaching 37%. In line with the previous results, Behar [147] suggested that the most effective way to integrate solar power at the bottom steam cycle is to use PTCs with synthetic oil as HTF.

The choice of the most appropriate integration position in the cycle for solar energy is a crucial issue when the plant incorporates a HRSG with 2 or 3 pressure levels. This analysis has been the subject of numerous publications. For instance, Calise et al. [148] conducted a dynamic study of an ISCC with solar integration in the HRSG low pressure level. The behavior of the ISCC layout with integration into the intermediate pressure level was studied by Brodrick et al. [149]. The case of integration at the three pressure levels was examined by Bonforte et al. [150], along with a control system to divide the solar heat supply among the three evaporators. They concluded that the tiny additional fuel savings outweigh the increase in installation costs. In a dual pressure HRSG, Rovira et al. [142] analyzed four potential integration schemes as shown in Figure 2.32, considering evaporation with HTF and DSG, as well as preheating and superheating. In comparison to preheating the water, they figured that when solar heat was applied for evaporation at the high pressure level, the HRSG irreversibility was reduced. They also mentioned that the lowest solar field efficiency was obtained when integration is at the superheating level at the bottom steam cycle due to the lower convective heat transfer coefficient, which makes the temperature difference between tube and steam increase. In order to determine whether heat exchangers at all pressure levels benefited from solar integration, Mabrouk et al. [151] designed a solar boiler coupled to a HRSG. They deduced that the optimal option was the high pressure evaporator, and that integration at high temperature exchangers was preferable. Elmohlawy [152] discovered that injecting steam at the high pressure level increased thermal efficiency by 1.2%. Ameri and Mohammadzadeh [153] found that when the solar field was integrated before the bottom steam cycle superheater, the total power output of a 300 MW plant increased by 6 MW and carbon emissions decreased by 10 g/kWh.

ISCC performance is influenced by the type of solar collector. However, several variables, including regional climate, plant operating circumstances, etc., affect the choice of collector. Franchini et al. study [154] compared the effectiveness of parabolic troughs and solar tower central receiver systems in Seville, Spain. They conducted an hourly transient analysis, finding that, during summer, parabolic troughs outperformed solar tower, reaching up to 60% thermal efficiency. On the other hand, compared to parabolic troughs, solar towers offer more energy at a higher efficiency, according to the annual performance report. The parabolic trough HTF-ISCC and air tower ISCC were compared by Horn et al. [155] who concluded that the LCOE was greater than that of the reference combined cycle plant (24 $/MWh) for both the parabolic trough and solar tower systems, 31 $/MWh. Dersch et al. [156] performed a comparison of

ISCC, SEGS, and CCGT. According to the study, an ISCC had the maximum efficiency at 68.6% compared to a SEGS 34.7%. SEGS, however, provided reduced greenhouse gas (GHG) emissions.

In the literature, several unique ISCC methods with solar integration into the bottom cycle have also been investigated. An advanced zero emission power cycle with carbon capture and storage, with a competitive solar-to-electricity efficiency, was proposed by Gunasekaran et al. [157]. They found an inverse relationship between solar share and solar-to-electricity efficiency. The performance of a 390 MWe CCGT plant was predicted by Manente [158] with a model used to study hybridization with solar energy. According to the analysis, the original plant equipment and capacity had to be significantly altered to add 50 MWe of solar electricity. The optimization of the HRSG and SSG to raise an ISCC plant exergy efficiency has been researched by Kane et al. [144]. The findings indicate that electricity cost with a 15-20% solar share is 20-30% more than that of combined cycle plants with comparable capacity. However, if the price of solar collectors drops and carbon credits are introduced, costs might decrease. Dersch et al. [156], Price et al. [159] and Kelly et al. [160], stated that the extracted inlet water flow in the SSG should be about 10% of the total water flow injected into the steam cycle of the CC plant [161].

To compare both hybridization types, Oda et al. [162] analyzed the performance of three different solar integration positions in a CC power plant, as shown in Figure 2.34. In the first case (I), solar thermal energy was integrated for preheating compressed air and providing supplemental heat to the bottom Rankine cycle. In the second case (II), solar heat was added to the bottom cycle without preheating the compressed air. In the third case (III), it was used for preheating compressed air at the top Brayton cycle. The results showed that solar integration at the bottom cycle increased overall efficiency, as collected in Table 2.4. However, solar integration at the top cycle made the solar component more efficient [163]. The explanation of the highest efficiency of case II may be attributed to the fact that the reduction of heat losses balances the increase in combustion losses.

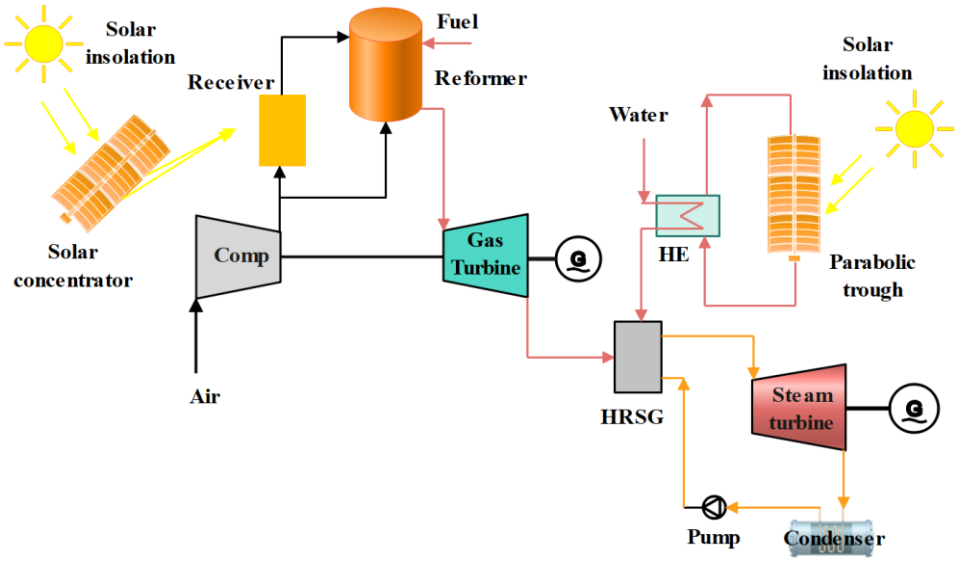

Figure 2.34 Possible configurations for solar integration into a combined cycle [163]

Similar findings have been reported by Barigozzi et al. [164], who examined the performance of solar integration into the top and bottom cycles. The analysis indicated that solar integration into the top cycle leads to higher solar-to-electricity efficiency. Integration into the bottom cycle, however, increases power production.

Table 2.4 Solar integration in top and bottom cycle of a combined cycle power plant [162], [163]

Plant	Solar integration position	η_i (%)	η_{ii} (%)
Case I	Top & bottom	26.2	27.1
Case II	Bottom	29.8	30.9
Case III	Top	27.5	28.3

2.5.2.3 Decision making criteria for the hybridization point selection

Specifications of the power plant must be determined after considering several aspects. For standalone CSP to be commercially viable, the DNI must be at least 1,800 kWh/m^2/year [165]. However, 1,700 kWh/m^2/year can appropriate for ST ISCC in areas with abundant natural gas supply [141]. The solar integration position is a critical parameter that must be intensively studied when designing the plant. Overall efficiency is the most important factor that designers focus on, where using solar energy for evaporation of high pressure steam can lead to higher solar conversion efficiency values than just preheating [111]. Power plant performance can be improved by HRSG optimization, but it is not so crucial for determining the best configuration [142]. Solar conversion efficiency can be introduced as:

$$\eta_{solar} = \frac{\dot{W}_{solar}}{\dot{Q}_{solar}} = \frac{\dot{W}_{fossil+solar} - \dot{W}_{fossil}}{\dot{Q}_{solar}} \tag{2.9}$$

Here, $\dot{W}_{solar}$ is the electricity power output generated from the solar heat, $\dot{W}_{fossil}$ is the plant electricity power output when the ISCC plant is not using solar power and $\dot{W}_{fossil+solar}$ is the plant electricity power output when the ISCC plant uses solar power from the solar field. $\dot{Q}_{solar}$ is the total heat absorbed from the solar field.

Secondly, it may be better to maximize solar fraction because solar integration into NGCC plants frequently requires system modifications. Solar fraction is the ratio of solar heat boosted electricity generation to total electricity generation:

$$F_{solar} = \frac{\dot{W}_{solar}}{\dot{W}_{fossil+solar}} \tag{2.10}$$

Typically, solar heat is used to supplement or partially replace the heat supply of one or more heat exchangers in the HRSG. To reach a high solar fraction, the size of the pertinent heat exchanger(s) must be relatively large, as mentioned by Zhu et al. [111]. In the same work, it was mentioned that feedwater (not steam) should be extracted from the HRSG for solar collectors, increasing solar input due to the use of latent heat and the potential use of direct steam generation.

On the other hand, gas cycle parameters should be considered when integrating the solar field into the top gas cycle. The GT performance is affected by variables that influence the mass flowrate or density of the air entering the compressor. Ambient conditions (temperature, humidity, and pressure) are thought to be significant factors on the operation of such power plants [166], [167]. The effect of temperature is substantially greater than that of other ambient factors [132].

The relationship between ambient conditions and output power for GT was investigated, finding that GT efficiency decreases by 0.1% for every 1°C increase in ambient temperature above ISO conditions [168]. At the same time, power decreases by 1.47 MW [134], [169]. Zhu et al. [111] verified this strong relation between the GT cycle efficiency and the change in ambient temperature, finding that the GT cycle efficiency dropped from 36.5% to 34.6% when ambient temperature changed from 0°C to 35°C. The mass flowrate entering the compressor and the gas turbine decreases as the ambient temperature rises, reducing power production. The gas turbine cycle efficiency is often insensitive to ambient pressure, because it is mostly governed by ambient temperature and the pressure ratio [170]. In a case study, power production decreased from 171 MWe to 140 MWe (18% reduction) as ambient temperature increased from 0°C to 35°C at 0.96 bar. Similar results were found for the decrease of ambient pressure [111].

2.5.3 ISCC operation modes

Depending on the effects on the original combined cycle power plant, there are two main operation modes for solar power integration: power boosting and fuel saving, as depicted in Figure 2.35. Both modes will be deeply discussed in this subsection based on the work presented by Zhang et al. [135]. A single-pressure reheating Rankine cycle was selected as the bottom cycle for generating the T-s diagram of a CC system with an ideal Brayton cycle and Rankine cycle, as shown in the diagram in Figure 3.36.

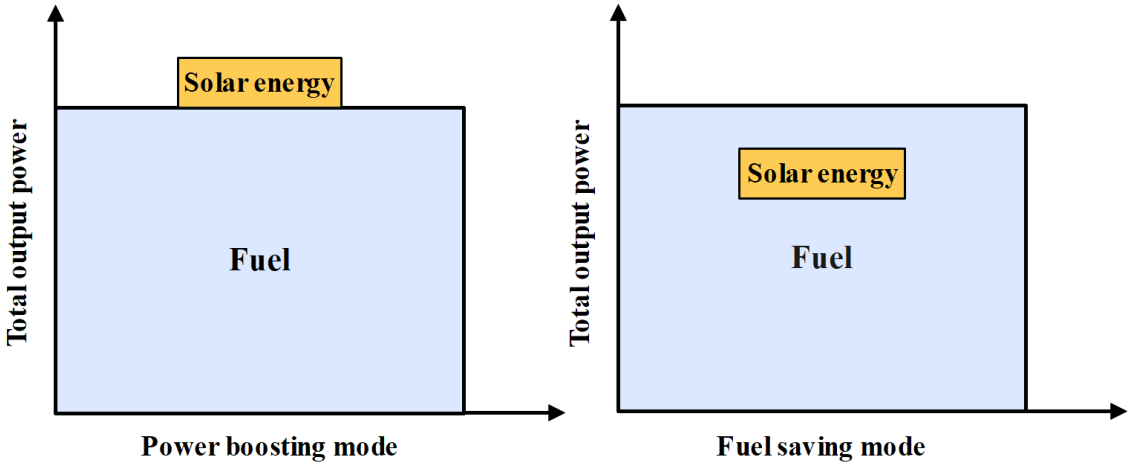

Figure 2.35 ISCC operation modes

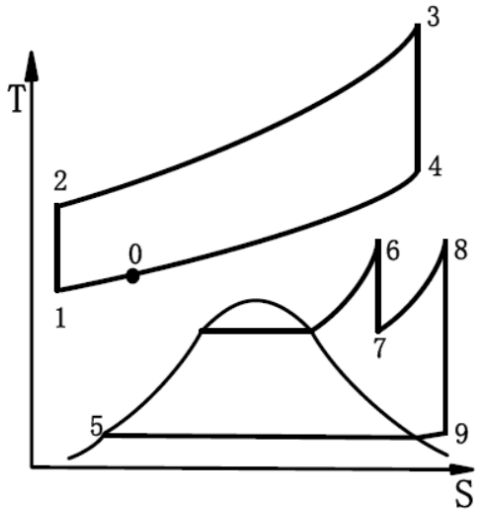

Figure 2.36 T-S diagram of the CC plan (with permission from copyright owner) [135]

2.5.3.1 Fuel saving mode

To operate an ISCC in fuel saving mode, solar energy is typically included into the top Brayton cycle, where the compressed air is heated after the compressor outlet. Due to the integration of solar energy, the fuel flowrate is reduced because the air enters the combustion chamber at higher temperature (2' instead of 2, as shown in Figure 2.37). In addition, the bottom cycle is not significantly impacted by solar integration, as the gas turbine conditions do not change. Another option for fuel saving is integrating solar power into the bottom steam cycle. As a result, less energy is required at the HRSG and less fuel may be burnt in the combustion chamber, with the solar contribution covering part of the required thermal energy.

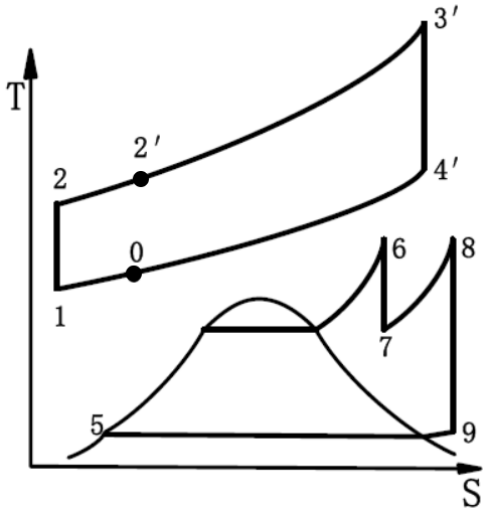

Figure 2.37 T-S diagram of fuel saving type ISCC system (with permission from copyright owner) [135]

2.5.3.2 Power boosting mode

In power boosting mode, fuel consumption remains constant, and solar energy is typically incorporated into the steam bottom cycle system to heat the feedwater, main steam, reheated steam, and the exhaust gases from the top cycle turbine. The integrated

solar thermal heat results in an increase in steam parameters or steam flowrate, leading to an increase in the output power. Solar thermal heat could be also integrated in the top Brayton cycle to increase the output power of the gas cycle and resulting in an increase in the output power. There are two subtypes of power-boosting type: mass flowrate and parameter-boosting.

Mass flow rate boosting mode

In the mass flow rate boosting type, the working fluid mass flowrate ($\dot{m}_{water}$) is increased while the thermodynamic properties of the relevant states remain unchanged. The top Brayton cycle parameters are kept constant.

Parameter boosting mode

The parameters of the working medium increase, as shown in Figure 2.38, while the mass flowrate of the working medium ($\dot{m}_{water}$) is kept constant. Based on the position of integration, parameter boosting mode is divided into two subtypes: SH (superheater) parameter-boosting and RH (reheat) parameter-boosting. The top Brayton cycle parameters are kept constant in all power boosting modes.

Some researchers have performed a comparative study between fuel saving and power boosting operational schemes to find an optimum one. El-Sayed [171] found that the power boosting mode is more cost-effective than the fuel-saving mode after researching the operation of a DSG-ISCC in Kuraymat, Egypt.

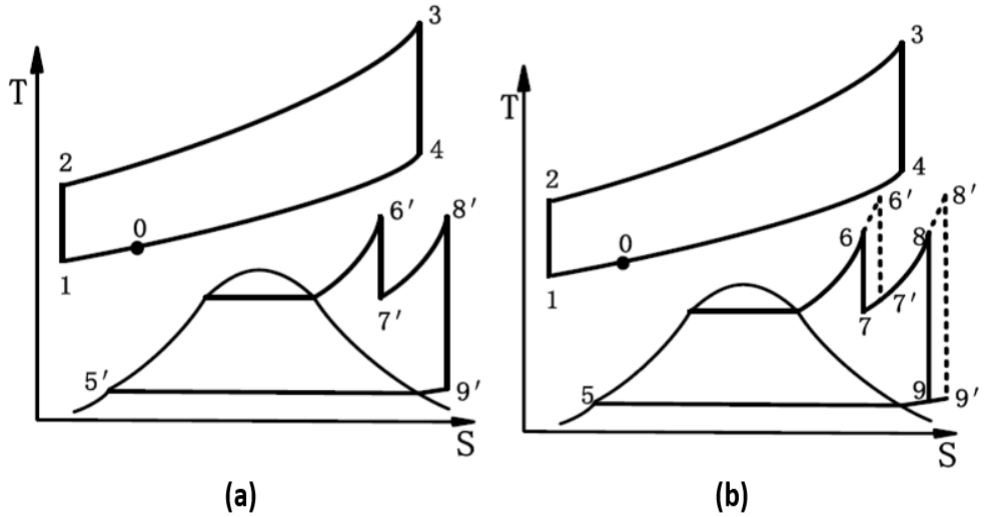

Figure 2.38 T-S diagram of ISCC boosting types (a) mass flowrate (b) parameter (with permission from copyright owner) [135]

2.5.4 Solar dispatching mode

Electricity must be always available on demand. To meet this need, it is necessary to continuously monitor the electric grid demand and match it with electric generation. Some electricity resources are more reliable because they are available when needed, while others are more environmentally friendly. Nuclear, coal, and natural gas are all dispatchable fuel sources. They are referred to as baseload resources. Wind, solar, and hydroelectricity production are a few examples of non-dispatchable fuel resources, although part of hydroelectric power can also be categorized as baseload fuel. Despite these resources are environmentally friendly, they are not always readily available.

Most energy providers use a wide mix of resources, using both dispatchable and non-dispatchable power sources, providing a continuous electricity flow [172].

To overcome the non-dispatchability of the CSP, ISCC plants have successfully integrated solar power into the grid [173]. When comparing ISCC plants to a single NGCC, lower operating and capital costs, with a potential gain in operational flexibility, are attained [174]. Alqahtani et al [175] proved that a ISCC working on a solar dispatching mode will have a favorable effect on the economy and the environment. This ISCC power plant is designed to run in a dispatching mode, where the CSP solar steam is integrated into the NGCC steam turbine to increase power generation. Another work by Dersch et al. [156] discussed the dispatchability of the ISCC, where two strategies were investigated: solar dispatching and scheduled load operation for an annual performance study in California and Spain. The operation of the plant followed a demand curve set in the scheduled load mode, while no uniform load profile was present in the solar dispatching mode. The CC and ISCC gas turbines run continuously at full capacity, with the only factors affecting the gas turbine output being the site elevation and ambient temperature. If solar energy was available, the power of the steam turbine would increase, increasing plant power production. In the scheduled load operation mode, the annual electricity yield was constant across all configurations, but in the mode of solar dispatching operation, power output depended on the plant layout and local climate. The output and solar share of the ISCC was higher in California, with higher solar irradiation. Additionally, solar share was higher in the solar dispatching mode than in the scheduled load. It was concluded that, independently of the operating mode (solar dispatching or scheduled load), the plant power level was guaranteed.

Solar dispatching operation mode was also studied by Li et al. [176]. Their system functioned as a DSG-ISCC power plant during sunny hours, working as a traditional CC power plant under off-design conditions when solar energy was not available. The gas turbine ran continuously at full capacity disregarding the effect of ambient temperature changes, and the steam turbine was scaled up to handle the solar thermal energy input. For DSG-ISCC systems without thermal storage, a higher solar capacity resulted in a higher capacity factor. The ideal solar multiple as 1.3, resulting in the best LCOE of 0.063 $/kWh and a peak annual thermal efficiency of 54.09%. When the solar multiple was 1.2, a maximum yearly thermal efficiency of 54.66% and a minimal LCOE of 0.064 $/kWh could be attained. Large solar field sizes, or solar multiples, especially those incorporating thermal storage, increase the number of hours the system can operate at full capacity. Another work discussed the dispatchability of the ISCC [177], where an ISCC with up to 10% to 15% of total capacity from solar energy could be economically viable. In comparison to a standalone CSP plant, integrating the CSP into an ISCC lowered the LCOE of solar-generated power by 35-40% and offered the benefit of dispatchability.

2.5.5 ISCC performance parameters

There are generally two different assessment indices for fuel-saving and power-boosting ISCCs. The amount of fuel saved (FS) for the fuel-saving type ISCC system is typically used to compare the performance of the ISCC system to the original CC system. In the contrary, when comparing the performance of the power-boosting type

ISCC system to the original CC system, the increased output power ($\Delta \dot{W}_{Total}$) is typically assessed. It is, however, very difficult to assess and compare the performances of CC units with varied capacities.

The amount of fuel saved because of the solar contribution can be calculated using the heat rate (HR) ratio in Eq. (2.13), which takes the efficiency inverse value for CC configurations and should be reduced in ISCCs [142]:

$$HR = \frac{\dot{m}_f \,.\, LHV}{\dot{W}_{GC} + \dot{W}_{SC}} \tag{2.11}$$

where $\dot{m}_f$ is the fuel flowrate in kg/s, LHV is the lower heating value in kJ/kg and $\dot{W}_{GC}$ and $\dot{W}_{SC}$ are the total power output of the gas and steam cycles in kW. It is common practice to establish an incremental solar efficiency (η_{solar}) [178] that compares the additional output brought on by solar integration with solar pure thermal power plants. The equation below provides this common definition [138]:

$$\eta_{solar} = \frac{\left(\dot{W}_{GT} + \dot{W}_{SC}\right)_{ISCC} - \left(\dot{W}_{GT} + \dot{W}_{SC}\right)_{CCGT}}{\dot{Q}_{net,solar}} \tag{2.12}$$

The traditional definition has been altered to incorporate the solar fuel-saving mode. The change entails determining what proportion of the whole production is attributable to solar contribution; this production should equal the product of solar energy and solar-to-electricity efficiency ($\eta_{sol-to-elec}$) [138]:

$$\dot{W}_{solar} = \dot{Q}_{net,solar} \cdot \eta_{sol-to-elec} \tag{2.13}$$

The thermal efficiency of the field can be used to study solar field performance [142]:

$$\eta_{solar\ field} = \frac{\dot{Q}_{net,solar}}{DNI \,.\, A_{col}} \tag{2.14}$$

Where A_{col} is the total solar field collector area in m^2.

CHAPTER THREE

METHODOLOGY

In this chapter, the developed model will be presented, and each part of the system will be described in a separate section. A real existing combined cycle power plant has been taken as a reference case, where the integration of a solar field has been studied. The main objective was to develop an ISCC model through the integration of a solar field into the CC model to improve the performance of the standalone CC. First, the combined cycle model will be discussed, considering the top gas cycle, the bottom steam cycle and the heat recovery steam generator. Then, the ISCC model will be described and compared with the combined cycle model. ISCC configurations have been grouped into two categories: gas cycle integration and steam cycle integration. The two integration categories have been analyzed for two operation strategies: fuel saving (FS) and power boosting (PB).

The thermodynamic model of the combined cycle (CC) power plant has been implemented in MATLAB software [179]. To obtain air and water properties for the top gas and bottom steam cycles, Ideal Air [180] and X-Steam [181] toolboxes were used. In order to evaluate the performance of the CC, a set of thermodynamic equations based on the mass and energy balances of the cycle components were solved. The properties of each thermodynamic state, the air and fuel mass flowrates, efficiency and net power of the cycle were calculated. The sequence of the methodology was to develop the thermodynamic model of the existing CC in MATLAB, and then to incorporate the solar field by modifying the original model to consider the entire ISCC configuration. Finally, the energy performance and environmental impact of the ISCC was assessed for different solar integration positions and operation strategies.

3.1 Combined cycle power plant

The combined cycle power plant model is based on a real existing 90.5 MW CC power plant, property of Egyptian Petrochemicals Company (EPC) in Alexandria, Egypt (latitude 31° 12’ N, longitude 29° 55’ E, elevation 18 m) [182]. The combined cycle consists of a top gas cycle, a bottom steam cycle and HRSG, as shown in Figure 3.1. The gas turbine is a ‘GT8C’ turbine built by Asea Brown Boveri (ABB) with a rating of 64.2 MW, while the steam turbine is a ‘DK-M 045’ turbine constructed by Brown, Boveri & Cie (BBC) with a rating of 26.3 MW. The overall cycle thermal efficiency is 56.13%. The main technical data of the CC are shown in Table 3.1. The schematic T-s diagram of the original combined cycle, shown in Figure 3.2 [183], helps to evaluate the power plant efficiency, performance, and possible optimization actions.

3.1.1 Top gas cycle

The top gas cycle consists of three main components: a compressor, a combustion chamber and a gas turbine, as shown in Figure 3.3. The compressor takes fresh ambient air (1g) and compresses it to a higher temperature and pressure (2g), according to the compressor pressure ratio. Fuel and compressed air are sent to a combustion chamber, where the fuel is burnt at constant pressure, and the resulting high temperature gases (3g) are sent to the turbine. The gases expand to ambient pressure (4g) in the turbine generating power. Finally, the exhaust gases from the turbine are sent to the HRSG.

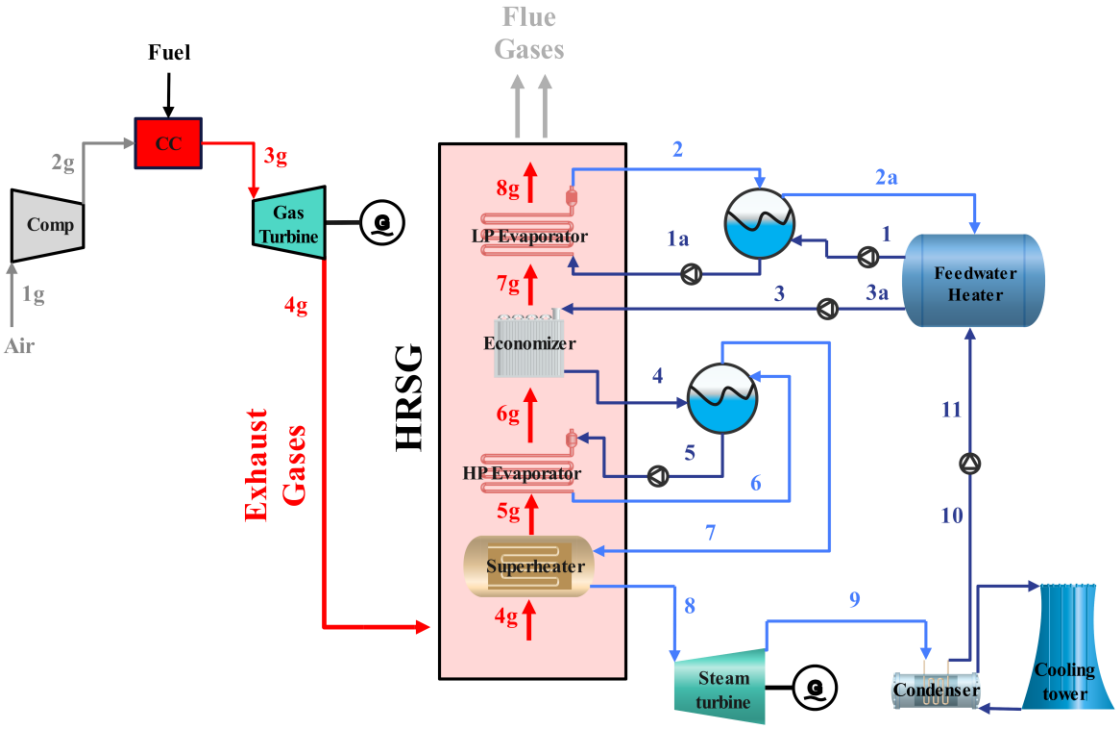

Figure 3.1 Original combined cycle power plant diagram

Table 3.1 Technical data of the combined cycle power plant

Gas cycle	**Compressor**	
	Inlet Ambient temperature (°C)	24
	Inlet pressure (bar)	1
	Combustion chamber	
	Inlet pressure (bar)	15.7
	Inlet temperature (°C)	378
	Turbine	
	Inlet temperature (°C)	1174
	Exhaust temperature (°C)	549
	Exhaust mass flowrate (kg/s)	174.7
Steam cycle	Inlet steam pressure (bar)	43
	LP evaporator pressure (bar)	2.4
	Condenser pressure (bar)	0.08
	Inlet steam temperature (°C)	457
	Economizer outlet temperature (°C)	228
	LP evaporator mass flowrate (kg/s)	5
	HP evaporator mass flowrate (kg/s)	25
Combined cycle	Total power output (MW)	90.5
	Cycle efficiency (%)	56.13

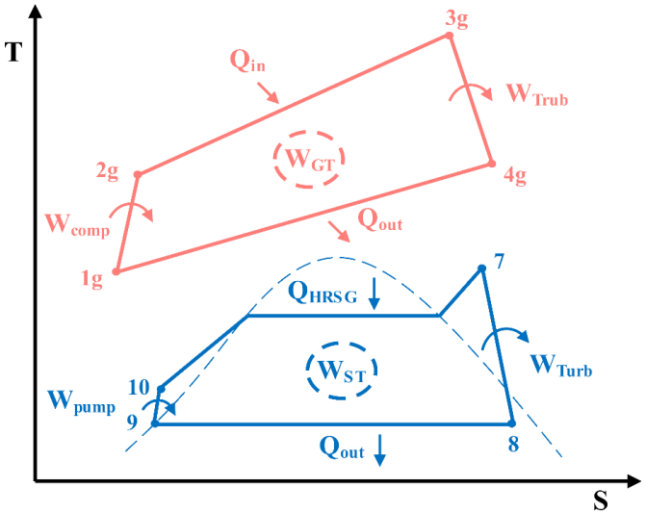

Figure 3.2 Schematic T-s diagram for the original combined cycle [183]

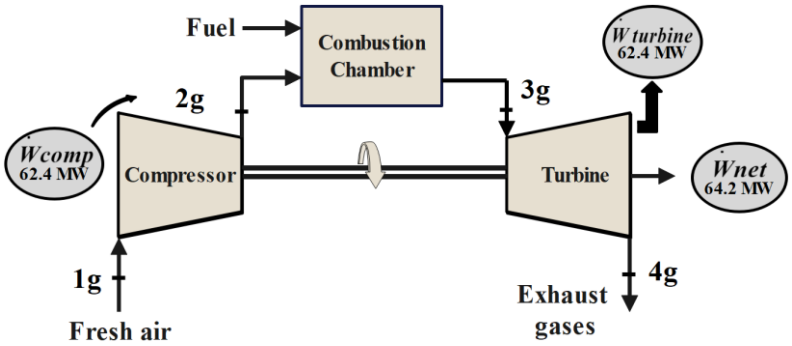

Figure 3.3 Gas cycle schematic diagram

The pressure ratio r_p is the ratio between operating pressures P_{ig} in bar. Temperatures T_{ig} in K may be calculated as well:

$$r_p = \frac{P_{2g}}{P_{1g}} = \frac{P_{3g}}{P_{4g}} \tag{3.1}$$

$$r_c^{\frac{k-1}{k}} = \frac{T_{2g}}{T_{1g}} \tag{3.2}$$

The heat capacity ratio k is:

$$k = \frac{c_p}{c_v} \tag{3.3}$$

where the specific heat at constant pressure and constant volume c_p and c_v are in kJ/(kg·K). The gas turbine and compressor power $\dot{W}_{GT}$ and $\dot{W}_{comp}$, the heat supplied in the combustion chamber $\dot{Q}_{cc}$, and the net power of the gas cycle $\dot{W}_{GC}$ in kW are:

$$\dot{W}_{GT} = \dot{m}_g \cdot (h_{3g} - h_{4g}) \tag{3.4}$$

$$\dot{W}_{comp} = \dot{m}_a (h_{2g} - h_{1g}) \tag{3.5}$$

$$\dot{Q}_{cc} = \dot{m}_f \cdot LHV = \dot{m}_g h_{3_g} - \dot{m}_a h_{2g} \tag{3.6}$$

$$\dot{W}_{GC} = \dot{W}_{GT} - \dot{W}_{comp} \tag{3.7}$$

where h_{ig} is the specific enthalpy in kJ/kg and the mass flowrates of the gases $\dot{m}_g$, air $\dot{m}_a$, and fuel $\dot{m}_f$ are expressed in kg/s. The lower heating value LHV of natural gas is 47,000 kJ/kg [184]. Finally, the thermal efficiency of the top gas cycle is obtained as:

$$\eta_T = \frac{\dot{W}_{G_{net}}}{\dot{Q}_{cc}} \tag{3.8}$$

3.1.2 Bottom steam cycle

The steam cycle of the CC consists of a steam turbine, a condenser, and a preheater. Hot exhaust gases leaving the gas turbine are directed to the HRSG to heat up water circulated in the bottom steam cycle to generate steam. Superheated steam is then directed to the steam turbine to produce work. The steam turbine power $\dot{W}_{ST}$ is calculated as:

$$\dot{W}_{ST} = \dot{m}_s \cdot (h_8 - h_9) \tag{3.9}$$

where the steam mass flowrate $\dot{m}_s$ in kg/s and the enthalpy of steam h_i in kJ/kg. The power of the high-pressure pump $\dot{W}_{hp_{pump}}$ and the feedwater pump $\dot{W}_{fw_{pump}}$ are:

$$\dot{W}_{hp_{pump}} = \dot{m}_s \cdot (h_3 - h_{3a}) \tag{3.10a}$$

$$\dot{W}_{fw_{pump}} = \dot{m}_s \cdot (h_{11} - h_{10}) \tag{3.10b}$$

The net power of the steam cycle $\dot{W}_{SC}$, in kW, can be calculated as:

$$\dot{W}_{SC} = \dot{W}_{ST} - \dot{W}_{hp_{pump}} - \dot{W}_{fw_{pump}} \tag{3.11}$$

Hence, the power plant total net power $\dot{W}_{Total}$ and efficiency η_{CC} could be obtained as:

$$\dot{W}_{Total} = \dot{W}_{GC} + \dot{W}_{SC} \tag{3.12}$$

$$\eta_{CC} = \frac{\dot{W}_{GC} + \dot{W}_{ST}}{\dot{Q}_{cc}} \tag{3.13}$$

3.1.3 Heat recovery steam generator (HRSG)

In the HRSG, heat is exchanged between the exhaust hot gases coming out of the gas turbine and the water/steam from the steam cycle. In the CC model, there are four heat exchangers: superheater, High Pressure (HP) evaporator, economizer, and Low pressure (LP) evaporator, in addition to the feedwater heater.

Since values of the product of the heat transfer coefficient 'U' and the total heat exchanger surface 'A', as well as the specific configuration of the heat exchangers of the real power plant were unavailable, the Effectiveness-Number of Transfer Units (ε-NTU) method [185] along with a simplified analysis of an equivalent counterflow heat exchanger that operates with the same terminal temperatures and heat transfer rates as the original power plant were used to calculate equivalent 'UA' values. The available power plant data was used to obtain the pinch and approach temperatures, enabling validation of the model.

The ε-NTU method is a practical technique to predict the output fluid temperatures when the heat transfer coefficient and the input temperatures of the operating fluids are known. Based on the available data from the CC power plant, the ε-NTU method was

applied iteratively for all the heat exchangers until the values for the outlet temperatures of the fluids converged.

The real heat transfer rate in any heat exchanger can be computed by calculating the heat absorbed by the cold fluid or the heat released by the hot fluid. Figure 3.4 shows a schematic diagram of the heat exchanging process between the hot gases and the steam.

Figure 3.4 Heat transfer flow diagram of heat exchangers

The heat lost by the exhaust gases $\dot{Q}_{Heat\ lost}$ and the heat gained by the steam $\dot{Q}_{Heat\ gained}$ was calculated as follows:

$$\dot{Q}_{Heat\ lost} = \dot{m}_{hot}\left(h_{hot,in} - h_{hot,out}\right) \quad (3.14)$$

$$\dot{Q}_{Heat\ gained} = \dot{m}_{cold}\left(h_{cold,out} - h_{cold,in}\right) \quad (3.15)$$

where $\dot{Q}$ is the heat transfer rate in (kW), $\dot{m}$ is the flowrate of the hot gases in (kg/s), and h_i is the enthalpy for inlet and the outlet of the hot and cold fluids (kJ/kg). The log mean temperature difference (*LMTD*) is an indicator for the heat transfer process, where the larger the *LMTD*, the more heat is transferred. It is an average temperature difference between the hot and cold fluids at the two ends as shown in Figure 3.5. Initially, outlet temperatures of the fluids are assumed to calculate a first value of the *LMTD*. Then, new values of the outlet temperatures were determined through calculations. The *LMTD* is calculated using the following expression [185]:

$$LMTD = \frac{\Delta T_1 - \Delta T_2}{\ln\left(\Delta T_1 / \Delta T_2\right)} \quad (3.16)$$

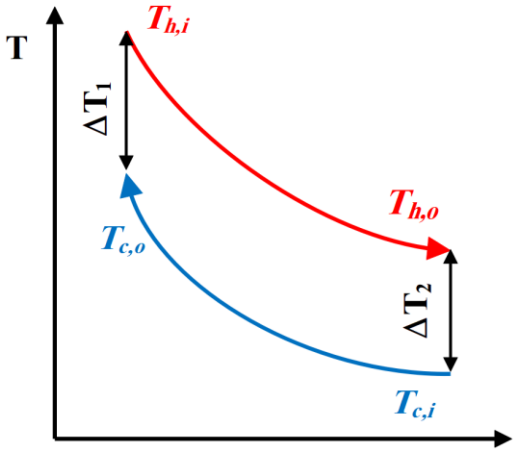

Figure 3.5 Temperature profiles in a counter flow heat exchanger [186]

where ΔT_1 and ΔT_2 represent the temperature differences between the hot and cold fluids at the inlet and outlet respectively in K. Therefore, Equation (3.16) could be reformulated as:

$$LMTD = \frac{\left(T_{hot,in} - T_{cold,out}\right) - \left(T_{hot,out} - T_{cold,in}\right)}{\ln\left(\frac{T_{hot,in} - T_{cold,out}}{T_{hot,out} - T_{cold,in}}\right)} \tag{3.17}$$

The heat transfer coefficient (U) in the heat exchanger could be calculated as a function of the heat transfer area (A) as follows:

$$UA = \frac{\dot{Q}}{LMTD} \tag{3.18}$$

where U is the heat transfer coefficient (W/m^2 K), and A is the total contact area of exchanging heat (m^2). Once UA is calculated with the previous equation, the Number of Transfer Units (NTU) could be obtained as [185]:

$$NTU = \frac{UA}{C_{\min}} \tag{3.19}$$

Here, C_{min} is the smaller of the two heat capacity rates (C_{cold}&C_{hot}) of cold and hot fluids in (kW/K). The fluid with a lower heat capacity rate will undergo greater change in temperature as compared to fluid with higher heat capacity rate. To calculate the heat capacitance rate of any of the fluids two parameters are needed, the mass flowrate $\dot{m}_i$ in (kg/s) and the specific heat C_{P_i} in (kJ/kg·K) of the fluid. Specific heat is based on the average temperatures of inlet and outlet for each fluid.

$$C_{hot} = \dot{m}_{hot}.C_{P_{hot}} \tag{3.20}$$

$$C_{cold} = \dot{m}_{cold}.C_{w_{cold}} \tag{3.21}$$

If $C_{hot} > C_{cold}$, $C_{min} = C_{cold}$ if $C_{hot} < C_{cold}$, $C_{min} = C_{hot}$.

Effectiveness (ε) and NTU relationships have been developed for a wide range of heat exchanger layouts. Most of these correlations involve the ratio C_r of the smaller and larger of the heat capacity rates (C_{min}) and (C_{max}) as:

$$C_r = \frac{C_{min}}{C_{\max}} \tag{3.22}$$

The best way to figure out the performance of a heat exchanger is to calculate its thermal effectiveness (ε) which is the ratio of the actual rate of heat transfer that will occur from hot to cold fluid to the maximum possible rate of heat transfer rate for given inlet temperatures of the fluids. The (ε) depends on the heat exchanger geometry, flow pattern (parallel flow, counter flow, cross flow, etc.) and the number of transfer units. As the heat exchangers have a single pass in counterflow regime, the relationship between Ɛ and NTU could be explained as follows:

$$\varepsilon = \frac{1 - exp[-NTU.(1 - C_r)]}{1 - C_r.exp[-NTU.(1 - C_r)]} \tag{3.23}$$

In case of phase change heat transfer process, such as boiling or condensation, $C_r \cong 0$ because of the saturation of temperature during the phase change process. Therefore, Equation 3.23 will be represented as:

$$\varepsilon = 1 - exp[-NTU] \tag{3.24}$$

Once ε is calculated, it can be expressed in another formula, to relate actual and maximum possible thermal energy transfer rates $\dot{Q}_{actual}$ and $\dot{Q}_{maximum}$ in kW, as:

$$\varepsilon = \frac{\dot{Q}_{actual}}{\dot{Q}_{maximum}} \tag{3.25}$$

The maximum possible heat that could be exchanged $\dot{Q}_{maximum}$ is expressed as:

$$\dot{Q}_{maximum} = C_{min}.\left(T_{hot,in} - T_{cold,in}\right) \tag{3.26}$$

Now, the effectiveness ε in Equation (3.25) could be reformed as:

$$If\ C_c < C_h : C_{min} = C_c \qquad \varepsilon = \frac{\left(T_{cold,out} - T_{cold,in}\right)}{\left(T_{hot,in} - T_{cold,in}\right)} \tag{3.27a}$$

$$If\ C_h < C_c : C_{min} = C_h \qquad \varepsilon = \frac{\left(T_{hot,in} - T_{hot,out}\right)}{\left(T_{hot,in} - T_{cold,in}\right)} \tag{3.27b}$$

The fluid inlet $T_{i,in}$ and outlet $T_{i,out}$ temperatures are in K. A new value for the first fluid (with C_{min}) outlet temperature $T_{1,out}$ could be obtained. The actual heat transfer rate $\dot{Q}_{actual}$, neglecting losses, is calculated from one of the following formulas:

$$\dot{Q}_{actual} = \dot{m}_{hot}.C_{p_{hot}}.\left(T_{hot,in} - T_{hot,out}\right) \tag{3.28a}$$

$$\dot{Q}_{actual} = \dot{m}_{cold}.C_{p_{cold}}.\left(T_{cold,out} - T_{cold,in}\right) \tag{3.28b}$$

Finally, as the first fluid (with C_{min}) outlet temperature is known, the actual heat transfer rate $\dot{Q}_{actual}$ could be computed using one part of Equation (3.28) then a new value for the second fluid (with C_{max}) outlet temperature $T_{2,out}$ could be determined using the other part of the equation. The final fluids outlet temperatures are calculated iteratively until the values of Equations (3.27 & 3.28) converge.

The original combined cycle temperature-heat transfer rate diagram, which displays the progression of temperatures across the HRSG, is shown in Figure 3.6. The nomenclature of thermodynamic statuses follows the CC power plant diagram in Figure 3.1. The following UA values could fit the power plant data: 449 kW/K for the feedwater heater, 164.5 kW/K for the low pressure evaporator, 175.5 kW/K for the economizer, 475 kW/K for the high pressure evaporator, and 84.5 kW/K for the superheater. The pinch and approach temperatures are 17.5 K and 28 K.

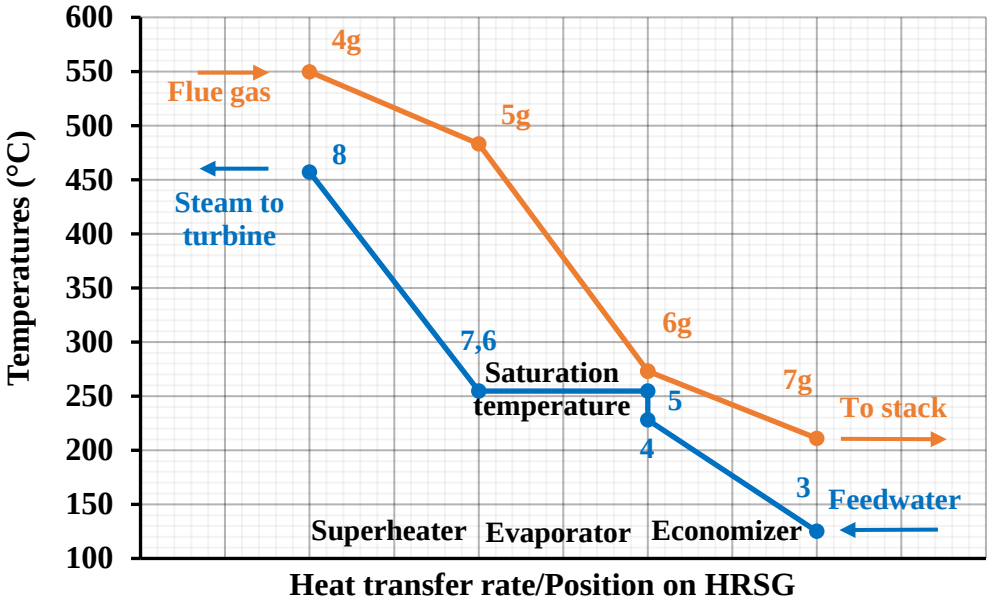

Figure 3.6 T-Q diagram for the original combined cycle

3.1.3.1 Validation of the model

As described in the preceding subsection, some data of the reference EPC power plant was used as input data in the model, while the rest (intermediate temperatures, pinch and approach points) were used to validate the model. Table 2 presents a comparison between the model values and the actual EPC power plant values. Table 3.2 presents a comparison between the model values and the actual EPC power plant values. Because of the strong agreement between the results, the developed model can be used to analyze solar power integration into the original combined cycle.

Table 3.2 Thermodynamic model vs actual values from the EPC power plant

Operating & design conditions	Model	EPC power plant
Gas turbine cycle		
Air mass flow rate, kg/s	171.2	171.2
Air to fuel ratio	50	50
Pressure ratio, r_p	15.7	15.7
Turbine inlet temperature, °C	1174	1100
Exhaust temperature, °C	549	540
Power output, MW	90,569	90,569
Top gas cycle efficiency, %	39.84%	39.84%
Steam Turbine cycle		
LP steam mass flow rate, kg/s	5	5
HP steam mass flow rate, kg/s	25	25
Turbine inlet pressure, bar	43	43
Power output, MW	26,292	26,292
Bottom steam cycle efficiency, %	27.1	NA

Operating & design conditions	Model	EPC power plant
Heat recovery steam generator (HRSG)		
Pinch point temperature, K	17.5	17.5
Approach temperature, K	28	28
Stack temperature, °C	160	172
(UA) Feedwater heater, kW/K	449	NA
(UA) Low pressure evaporator, kW/K	164.5	NA
(UA) Economizer, kW/K	175.5	NA
(UA) High pressure evaporator, kW/K	475	NA
(UA) Superheater, kW/K	84.5	NA
Combined cycle		
Total output power, MW	90,569	90,569
Efficiency, %	56.13	56.13

3.2 Integrated solar combined cycle

In this section, the validated thermodynamic model presented in the previous section is modified to analyze the performance of different ISCCs configurations for two operating strategies, fuel saving (FS) and power boosting (PB). Five different integrating positions are studied, as shown in Figure 3.7. First, the fuel saving technique will be presented for all the configurations (gas and steam), then the power boosting technique for all the configurations will follow.

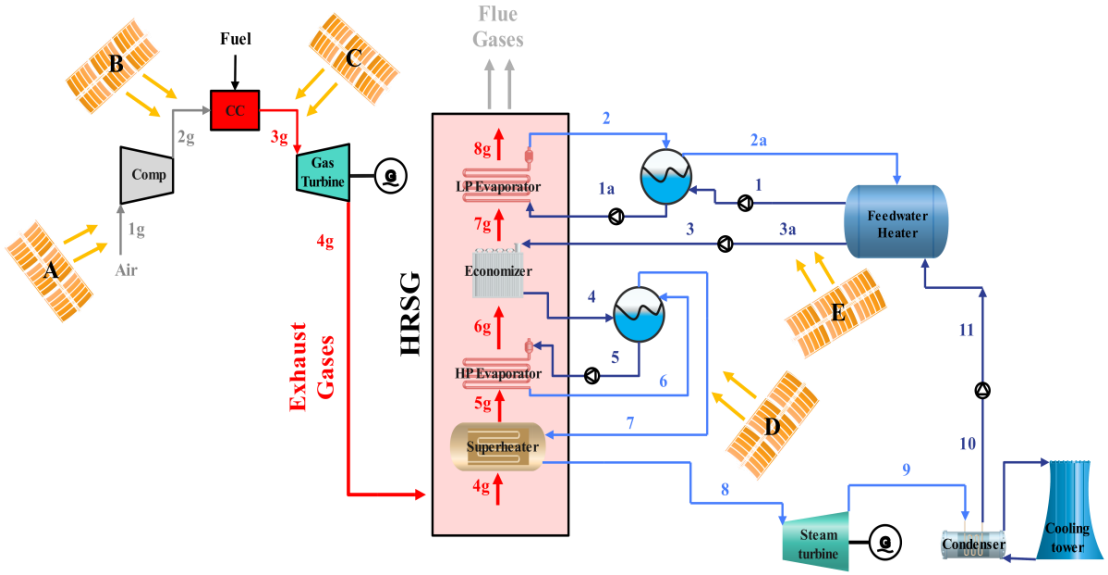

Figure 3.7 Solar field integration options

3.2.1 Fuel saving mode

The solar field is integrated into the gas/steam cycle to add more heat to the combined cycle, this additional heat will help to save the maximum possible amount of fuel without fluctuating the overall output power of the combined cycle. The gas cycle solar integration model is different than the steam cycle solar integration model, despite having the same idea of saving fuel and keeping the output power constant.

3.2.1.1 Gas cycle integration

To integrate solar field into the gas turbine cycle of a combined cycle power plant, there are three different possible positions of integration as shown in Figure 3.8:

- **Case A** "Before compressor": Ambient air is heated by solar field before being compressed in the next compression stage.
- **Case B** "After compressor / Before combustion chamber": Compressed air is heated before introducing the fuel in the combustion chamber.
- **Case C** "After combustion chamber / Before gas turbine": hot gases are heated up before being introduced to the gas turbine.

Each case will be studied based on some conditions according to the position of integration. Operating conditions for each case are represented clearly in the following section. The most common option is "case B" as revealed in the literature. "Case A" and "case C" will be studied and compared with "case B". To calculate the percentage of fuel saved "FS", the following formula could be used:

$$FS = \frac{\dot{m}_f - \dot{m}_{f_{new}}}{\dot{m}_f} \cdot 100\% \tag{3.29}$$

Where $\dot{m}_f$ and $\dot{m}_{f_{new}}$ are fuel flowrates for the CC and the ISCC respectively expressed in (kg/s). After determining the amount of fuel saved, the natural gas lower heating value LHV (47,000 kJ/kg) [184] and the natural gas/CO_2 emission ratio $EF_{NG \to CO_2}$ (0.252 kg/kWh) [187] was used to determine the reduction in CO_2 emissions:

$$\text{Savings}_{CO_2} = \dot{m}_{f_{saved}} \cdot LHV \cdot EF_{NG \to CO_2} \cdot \Delta t \tag{3.30}$$

Where $\dot{m}_{f_{saved}}$ is the reduction in fuel usage, in kg/h, as a result of integrating solar thermal power and Δt is the monthly average operating solar hours of Alexandria, Egypt (275 solar hours/month) [188].

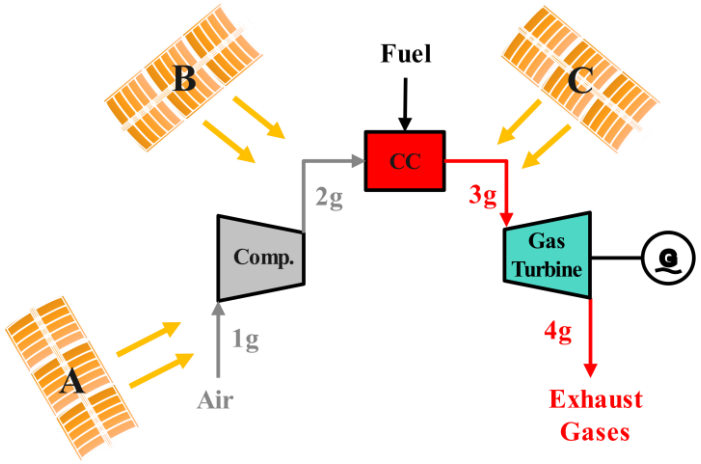

Figure 3.8 Gas cycle integration configurations

Case A: Before air compressor

In this scheme solar field is integrated before the compressor stage as shown in Figure 3.9 to preheat the ambient air at constant pressure before compression stage. The assumptions maintained for this case are the following:

- Inlet and outlet temperatures of the compressor stage increased.
- Air and fuel mass flowrates are modified depending on the amount of integrated solar heat.
- The work of compressor increased as the inlet temperature increased.
- Inlet and outlet turbine conditions are constant.
- The work of the turbine is constant.
- Overall output power of the gas turbine cycle decreased.
- Fuel mass flowrate decreased.
- Steam turbine cycle is virtually not affected.
- Overall output power of the ISCC decreased.

The MATLAB model is described as a group of simultaneous Equations (3.31-3.34) that are solved to obtain the modified parameters as a result of the additional amount of solar heat integrated into the ISCC power plant. Results proved that the integration of solar field before the compression stage to heat up the ambient air will lead to an increase of the work done by the compressor, as more work is needed to compress higher temperature air.

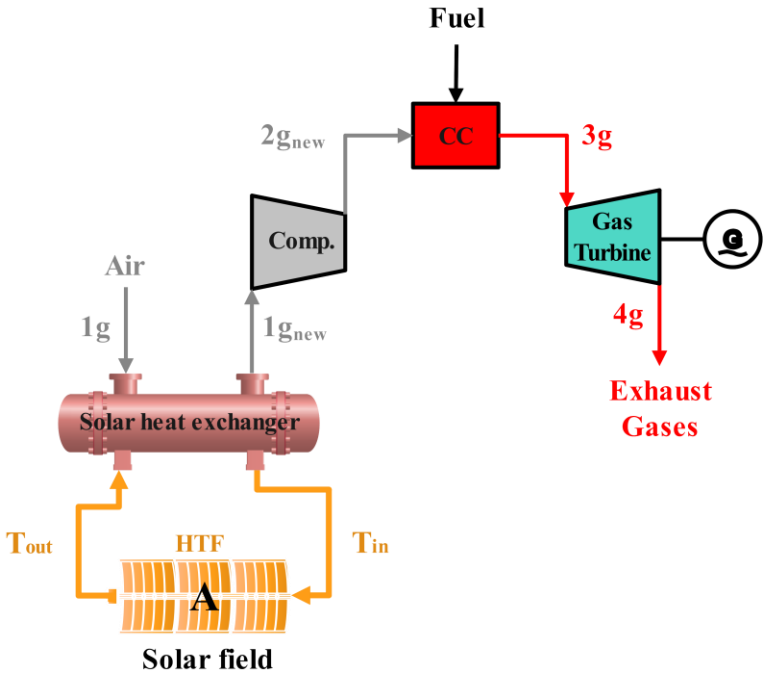

Figure 3.9 Gas cycle integration (Case A: before compressor)

The mass balance of the flowrates is shown in Equation 3.30.

$$\dot{m}_g = \dot{m}_{a_{new}} + \dot{m}_{f_{new}} \tag{3.31}$$

The amount of heat added in the combustion chamber can be expressed as following:

$$\dot{Q}_{cc} = \dot{m}_g \cdot h_{3_g} \tag{3.32}$$

Since, stage 3 (turbine inlet) conditions are kept constant, the amount of heat added to the combustion chamber could be represented in another form as follows:

$$\dot{Q}_{cc} = \left(\dot{m}_{a_{new}} \cdot h_{2g_{new}}\right) + \left(\dot{m}_{f_{new}} \cdot LHV\right) \tag{3.33a}$$

$$\dot{Q}_{cc} = \left(\dot{m}_a \cdot h_{2g}\right) + \left(\dot{m}_f \cdot LHV\right) \tag{3.33b}$$

The solar heat integrated in the gas turbine cycle could be calculated by Equation 3.34 assuming no heat losses.

$$\dot{Q}_{Solar} = \dot{m}_{a_{new}} \cdot \left(h_{1g_{new}} - h_{1g}\right) \quad (3.34)$$

Case B: After air compressor

The second integration option in the gas turbine cycle is the integration of the solar field after the air compressor (before the combustion chamber) as shown in Figure 3.10, where the compressed air is heated up by the additional solar heat integrated with the combined cycle. Fuel is then added to the heated compressed air and burnt together in the combustion chamber to produce hot combustion gases that passes by the turbine to generate power. The operating conditions for this scheme would be:

- Air and fuel mass flowrates are modified depending on the amount of integrated solar heat.
- The work of compressor is constant.
- Inlet and outlet gas turbine conditions are constant.
- The specific work of the turbine is constant.
- The overall output power of the top gas cycle is constant.
- Fuel mass flowrate decreased.
- The bottom steam cycle is virtually not affected.
- The overall output power of the ISCC is constant.

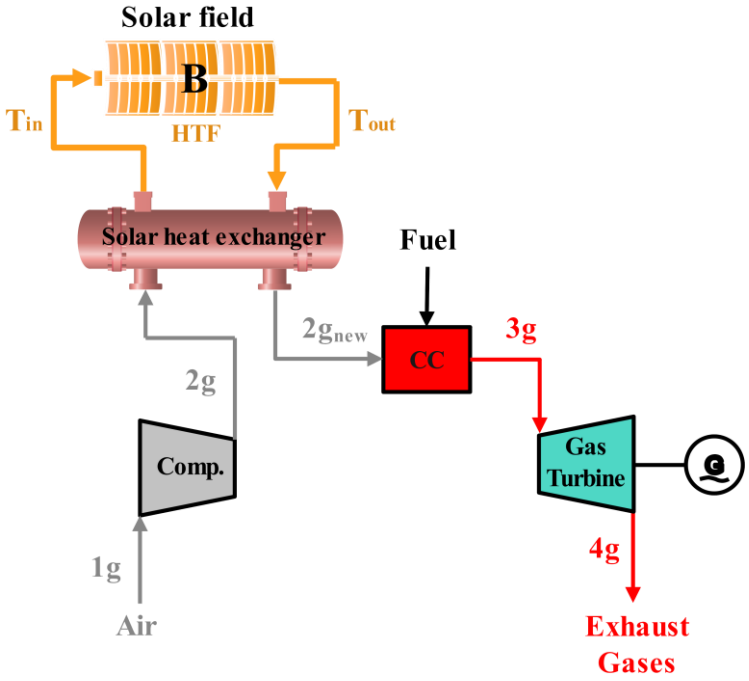

Figure 3.10 Gas cycle integration (Case B: After compressor)

The same model as "case A" is used, as shown in the previous Equations (3.31-3.34). The main difference between the first two options (A & B) is the work of compressor, where, in "case A" the compressor does more work to compress the heated ambient air, but in "case B", as solar field is integrated after the compressor, the work of the compressor is the same as the original CC this is because the input temperature to the

compressor did not increase as in "case A". The power of the compressor could be calculated from the following equation:

$$\dot{W}_{comp} = \dot{m}_{a_{new}}(h_{2g} - h_{1g}) \tag{3.35}$$

The energy balance in the combustion chamber is reformulated as:

$$\dot{m}_{a_{new}} \cdot h_{2g_{new}} + \dot{Q}_{add} = \dot{m}_{a_{new}} \cdot h_{2g_{new}} + \dot{m}_{f_{new}} \cdot LHV = \dot{m}_g h_{3g} \tag{3.36}$$

The solar heat integrated in the gas turbine cycle could be calculated by the following equation assuming no heat losses.

$$\dot{Q}_{Solar} = \dot{m}_{a_{new}} \cdot (h_{2g_{new}} - h_{2g}) \tag{3.37}$$

Unlike "case A", the overall output power of the ISCC could be maintained as the same as for the original CC.

Case C: After combustion chamber

The third position for integrating the solar field within the CC is after the combustion chamber stage (before the gas turbine) as shown in Figure 3.11. Heating up hot gases by the solar field is a critical challenge as the temperature of the gases leaving the combustion chamber is very high.

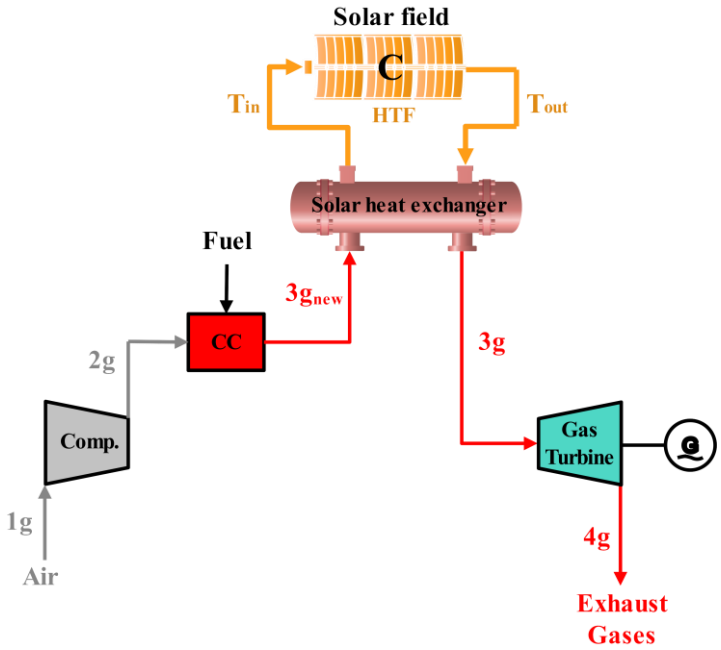

Figure 3.11 Gas cycle integration (Case C: After combustion chamber)

Stage (3g) is a very important stage in the gas turbine cycle in this configuration, where the solar field is integrated after the combustion chamber. It is the highest temperature that the cycle can reach and has a significant impact on the gas turbine performance, which in turn directly affects the gas turbine cycle overall output power. The model for this integration configuration works with the same concept as the previous configuration "case B", where all the conditions of "case B" are applied. Inlet and outlet conditions of the turbine are always kept constant so the integrated solar heat at this stage will help in decreasing the amount of fuel burnt in the combustion chamber and subsequently will decrease the temperature of stage (3g) as shown in Figure 3.11.

The energy balance in the combustion chamber can be represented as:

$$\dot{m}_{a_{new}} \cdot h_{2g} + \dot{Q}_{add} = \dot{m}_{a_{new}} \cdot h_{2g} + \dot{m}_{f_{new}} \cdot LHV = \dot{m}_g h_{3g_{new}} \quad (3.38)$$

The solar heat integrated in the gas turbine cycle can be calculated by the following equation assuming no heat losses:

$$\dot{Q}_{Solar} = \dot{m}_{a_{new}} \cdot (h_{3g} - h_{3g_{new}}) \quad (3.39)$$

3.2.1.2 Steam cycle integration

Solar heat can be integrated into the steam turbine cycle to reduce fuel consumption, where it could be coupled with one or more of the heat exchangers in the HRSG to add extra heat to the bottom steam cycle. The bottom cycle additional energy coupling will result in an increase in the water/steam characteristics, working medium (water/steam) mass flowrate and output power. Solar thermal power integrated will balance the reduction in the output power from the gas turbine as less fuel is burnt in the combustion chamber. In this section two steam cycle integration configurations will be studied:

a) **Integration at superheater:** High pressure and temperature outlet vapor from the HP drum is heated by the integrated solar thermal power before passing by the superheater stage.
b) **Integration at Economizer:** Feedwater is heated to increase its temperature before being heated in the economizer stage.

Case D: Integration at superheater

In this configuration, high pressure vapor from the outlet of the HP drum is heated by the integrated solar heat, as shown in Figure 3.12. Then, steam will be superheated in the superheater stage before passing by the steam turbine to generate power. Integrated solar heat in the lower steam cycle will add more heat to the lower cycle affecting the distribution of temperature in the HRSG as temperatures of water/steam will increase, thus, the steam turbine will produce more power.

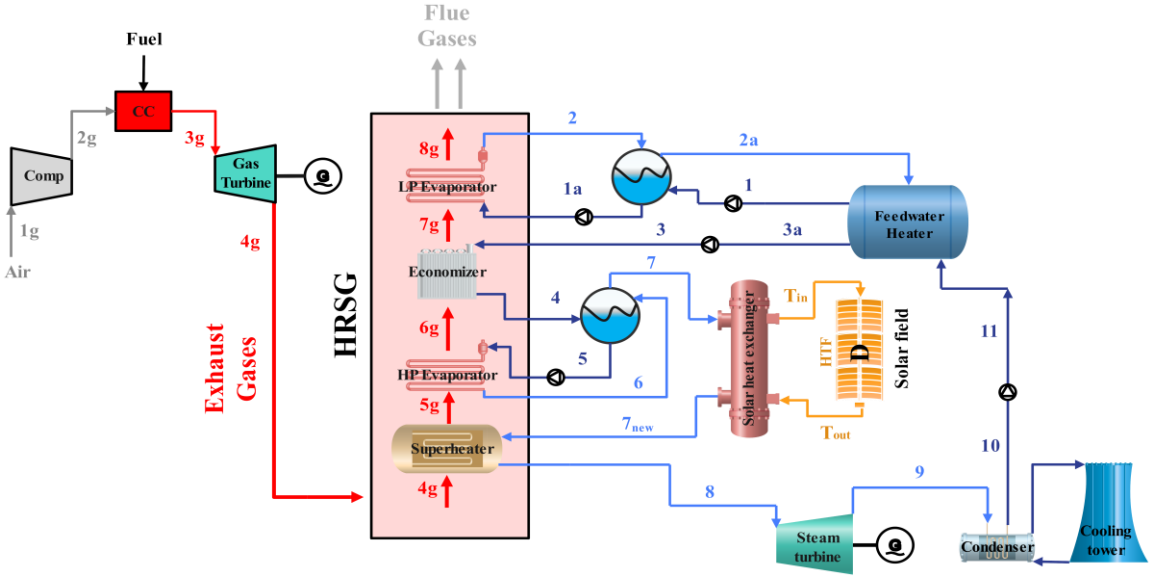

Figure 3.12 Steam cycle integration (Case D: at superheater)

In the fuel saving operating technique, the overall output power of the ISCC should be kept constant and the extra power added by the integration of solar heat should reduce fuel consumption. In this case, the additional power produced by the steam turbine will compensate for the reduction in the gas turbine power to keep the overall ISCC output power constant. If gas turbine in the ISCC produces less power than that in the CC, therefore, there will be a reduction in the fuel mass flowrate in the combustion chamber, compared to the original fuel consumption rate, and a certain amount of fuel will be saved depending on the amount of solar heat integrated in the ISCC.

Implementing the model of the ISCC (superheater) requires continuous monitoring of the temperatures inside the HRSG to prevent reversibility of heat exchange process between the water/steam and the hot gases. By integrating the solar heat inside the HRSG temperature of water/steam increases and after a certain amount of additional heat any extra heat will be wasted, as the system will reverse the heat exchange process between water/steam and gases. The solar heat integrated into the steam turbine cycle could be calculated by the following equation assuming no heat losses:

$$\dot{Q}_{Solar} = \dot{m}_s \cdot \left(h_{7_{new}} - h_7\right) \tag{3.40}$$

Case E: Integration at economizer

The last configuration studied at the bottom steam cycle increases the temperature of feedwater at the economizer stage, as shown in Figure 3.13. Integrated solar thermal power will provide the steam cycle with additional heat that will raise the temperature distribution along the HRSG. If the fuel saving strategy is applied to the configuration, the additional heat will allow to reduce fuel flowrate consumption because the steam cycle will generate more power to keep overall output power constant. One of the challenges affecting the results is controlling the heat transfer process to prevent the reversal of heat exchange between the hot gases and the steam. The solar heat integrated into the steam turbine cycle, assuming no heat losses, can be calculated as:

$$\dot{Q}_{Solar} = \dot{m}_s \cdot \left(h_{3_{new}} - h_3\right) \tag{3.41}$$

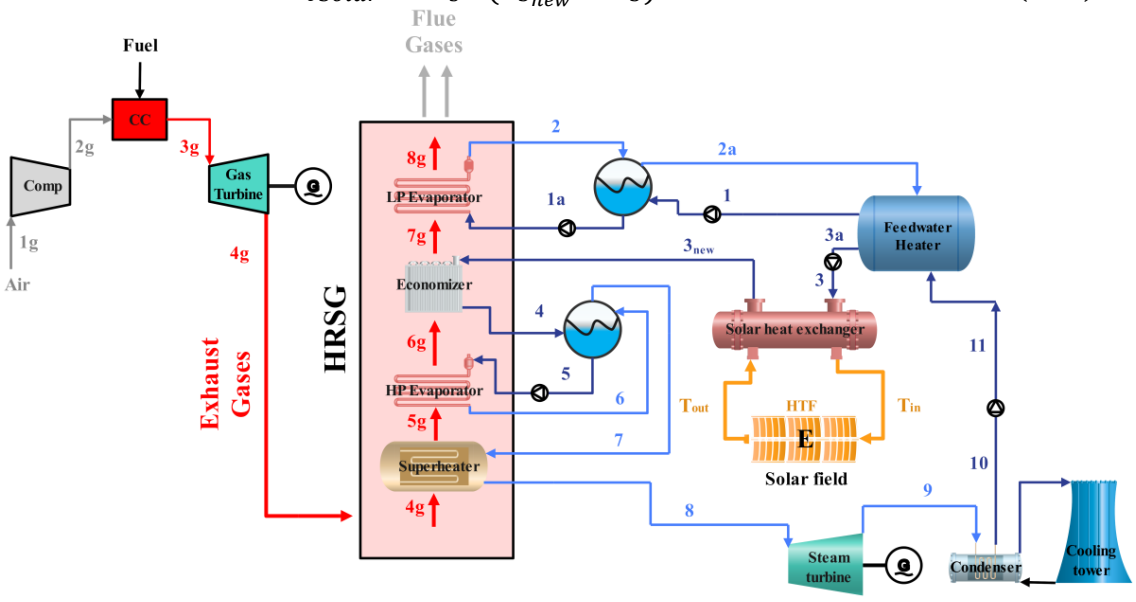

Figure 3.13 Steam cycle integration (Case E: at economizer)

3.2.2 Power boosting mode

The power boosting mode integrates the solar field into the CC to increase the cycle output power. Solar field integration may be performed at the top gas cycle or the bottom steam cycle. In this work, the same five integration positions studied for the fuel saving mode will be studied for the power boosting mode, as shown in Figure 3.14.

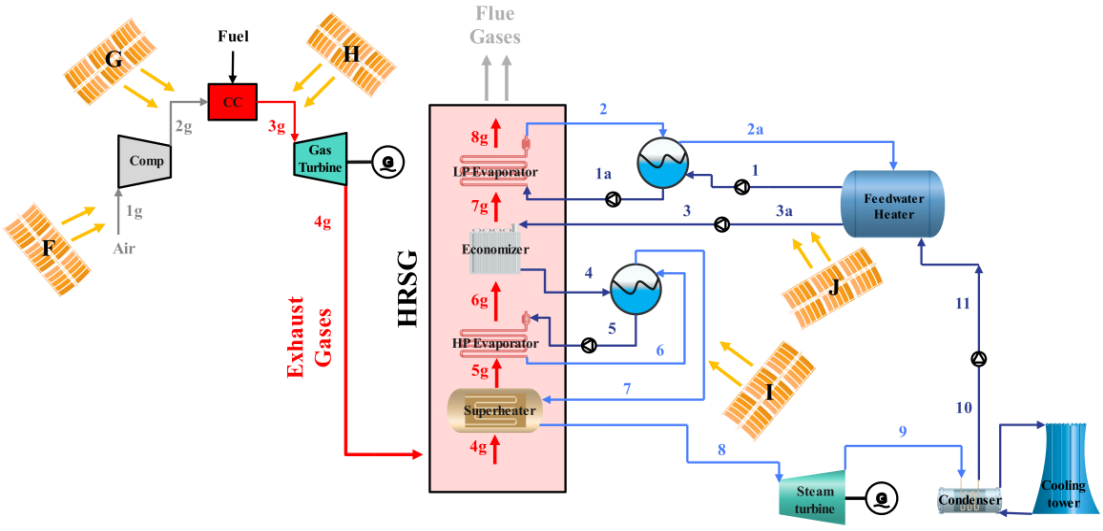

Figure 3.14 Solar field integration options (power boosting mode)

To calculate the boosted power, the following formula is used, where $\dot{W}_{Total}$ and $\dot{W}_{Total_{new}}$ are the net output power of the original CC and ISCC in kW:

$$PB = \frac{\dot{W}_{Total_{new}} - \dot{W}_{Total}}{\dot{W}_{Total}} \cdot 100\% \qquad (3.42)$$

3.2.2.1 Gas cycle integration

Three different possible positions for integration (F, G & H) into the gas turbine cycle were studied, as shown in Figure 3.14.

Case F: Before air compressor

The solar field is integrated before the compressor to preheat ambient air before compression, as shown in Figure 3.9. The assumptions performed are:

- Inlet air temperature of the compressor stage increases.
- Air and gases mass flowrates change depending on the integrated solar power.
- Fuel mass flowrate is constant.
- The work of the compressor increases.
- Inlet and outlet turbine conditions are constant.
- The gas turbine cycle output power decreases.
- The steam turbine cycle is virtually unaffected.

The MATLAB model for this configuration is similar to the model implemented in "case A" but with different operating conditions following the commented assumptions. Equations (3.31-3.34) were also used to solve the model for "case F".

Nevertheless, "Case F" failed to achieve power boosting due to the huge increase in the compressor power, leading to a decrease of the total power instead of power boosting.

Case G: After air compressor

The solar field is integrated after the air compressor, before the combustion stage, as shown in Figure 3.10, to preheat compressed air. The fuel is then burnt with this compressed air in the combustion chamber to generate hot gases and power the gas turbine. The modelling assumptions for this configuration scheme are as follows:

- Air and gases mass flowrates change with integrated solar power.
- Fuel mass flowrate is constant.
- Compression work increases.
- Inlet and outlet gas turbine conditions are constant.
- The gas turbine output increases.
- The steam turbine cycle is virtually unaffected.
- Power output of the ISCC increases.

The same MATLAB model as in "case F" was used, based on Equations (3.31-3.34), but with different operating conditions to adapt to the power boosting strategy. "Case G" showed good possibilities, allowing to boost the gas turbine cycle power thanks to the integrated solar thermal power. Since the fuel flowrate and input and output conditions of the gas turbine are kept constant, the integrated solar thermal power allows to introduce more air to the combustion chamber; thus, a higher gas flowrate will power the gas turbine. Even though the steam cycle output power is not directly affected by solar integration, the increase in the gas turbine cycle power leads to an increase in overall ISCC output power.

Case H: After combustion chamber

The third position for integrating the solar field within the gas turbine cycle is after the combustion chamber stage, before the gas turbine inlet, as shown in Figure 3.11. Stage (3g) is always the highest temperature in any gas cycle configuration, and it has a strong impact on the performance of the gas turbine. A similar model to the one of "case G" is used, adapted to integrate solar power after the combustion chamber.

3.2.2.2 Steam cycle integration

The solar heat can be also integrated into the steam cycle, where it can be coupled with one or more of the HRSG heat exchangers. The additional integrated power can increase the working fluid (steam) mass flowrate or the operating conditions, leading to an increase in the steam cycle output power. Keeping the same operating conditions for the gas turbine cycle, the overall ISCC output power will increase. Two integration positions at the steam cycle solar heat integration were studied:

a) **Integration before the superheater:** outlet steam from the HP drum at high pressure and temperature is heated by the integrated solar thermal power before entering the superheater stage.
b) **Integration before the economizer:** Feedwater is heated to increase its temperature before entering the economizer stage.

There are two operating techniques for power boosting: “flowrate boosting”, in which the working fluid mass flowrate increases while fluid thermodynamic states (temperature, pressure...etc.) remain constant; and “parameter boosting”, in which all the thermodynamic states are boosted but the mass flowrate is kept constant. Both techniques were studied at the two integration positions.

Flowrate boosting mode

The working fluid mass flowrate increases, while the thermodynamic states it follows are kept constant. The top Brayton cycle parameters are not affected.

a) Case I: Integration before the superheater

In this configuration, the high pressure and temperature steam in the HP drum is heated by the solar field, as shown in the configuration in Figure 3.12. Thanks to the integrated solar power, the steam mass flowrate that enters the HRSG superheater may be increased, changing the temperature distribution inside the HRSG. The additional steam mass flowrate through the steam turbine generates more power, boosting output power.

b) Case J: Integration before the economizer

Finally, the solar thermal power may be integrated before the economizer to preheat feedwater, changing the temperature distribution inside the HRSG. With the flowrate power boosting mode, the working fluid flowrate (steam) increases, increasing the steam cycle output power. The gas cycle operation is kept constant, so overall ISCC output power increases.

Parameter boosting mode

In this configuration, the working fluid mass flowrate is kept constant while its thermodynamic states (temperature, pressure, etc.) are increased thanks to the integration of solar thermal power. The top Brayton cycle operating parameters are kept constant. The same integration positions I and J introduced for the flowrate boosting strategy will be analyzed.

3.3 Solar field technology selection

Based on the integration position, the solar field must be adapted to different temperature conditions. Different concentrating solar collector technologies, presented in Table 3.3, were examined for each configuration. The literature claims that Therminol VP-1 as HTF and PTC as solar field technology are commonly used in ISCCs, thanks to the low dynamic viscosity and excellent heat capacity of Therminol VP-1 over a wide operating temperature range [189]. However, 390°C is the maximum operating temperature of Therminol VP-1, so solar molten salts, that can reach temperatures as high as 550ºC, could be an alternative HTF [190]. PDR or heliostats will be the only choice at much higher temperatures.

Table 3.3 Concentrating solar collectors [21], [191]

Collector type	Parabolic trough collectors (PTC)	Parabolic dish reflectors (PDR)	Heliostat field collectors (solar power tower)
Description	-Parabolic sheet of reflective material -Linear receiver (metal pipe with heat transfer fluid)	-Large reflective parabolic dish with stirring high engine receiver at focal point	-Large heliostat field with tall tower in its center -Receiver: water/HTF boiler at top
Operating temp. range (°C)	50-400	150-1500	300-2000
Relative cost	Low	Very high	High
Concentration ratio (Sun)[a]	15-45	100-1000	150-1500
Tracking	One-Axis	Two-Axis	Two-Axis
Efficiency (%)	~18	~30	~25-28

[a] Ratio of the effective area of the aperture to the receiver/absorber area of the collector

3.4 Absorbed solar energy

In this section, the model of the solar field, based on PTCs, is discussed based on the work of Duffle & Beckman [192] and Iqbal [193]. The amount of thermal energy absorbed by the solar collector $Q_{absorbed}$, later transferred to the ISCC, will be introduced, with all the factors affecting the quality and amount of absorbed solar heat.

The Sun is made entirely of gas, held by gravitational forces. Its physical structure is intricate and may be divided into several sections. The core is the innermost, hottest and densest region. The interior, located above the core, contains nearly all the mass of the Sun. Nearly all solar energy comes from the core and interior, working as a fusion reactor, with the outer zones propagating this energy. Most of the solar radiation that reaches the Earth atmosphere travels through the photosphere, which is the Sun surface.

The amount of solar radiation that reaches the Earth is inversely proportional to the square of the distance between the Earth of the Sun. For a mean distance of 1 astronomical unit (1 AU = $1.496 \cdot 10^{11}$ m), maximum solar radiation outside the Earth atmosphere is around almost 1.37 kW/m^2. Over a year, it fluctuates by around 3% depending on the relative distance between the Earth and Sun. Around January 3rd, the Earth is at its closest position to the Sun (perihelion ~ 0.983 AU), while around July 4th, it is at its farthest position (aphelion ~ 1.017 AU). Around April 4th and October 5th, the mean distance is reached.

Part of the energy from solar radiation that enters the atmosphere is lost by diffraction due to interactions with air molecules, water (vapor and droplets), and dust. Another portion in the ultraviolet spectrum is absorbed by the ozone layer and in the infrared by water vapor and carbon dioxide. Scattered or diffuse radiation travels in two directions:

some of it returns to space, and some of it hits the ground. The rest of radiation, which reaches the Earth surface directly in line from the solar disc, is called beam radiation.

Direct normal radiation (G_{bn}) is the beam radiation that strikes the Earth surface perpendicularly. The total solar radiation or global radiation, i.e. the sum of the diffuse and beam solar radiation on a surface, is crucial for the construction of flat-plate collectors and for the estimation of heating and cooling loads in buildings. In concentrating devices, only the direct normal radiation is used. A Normal Incidence Pyrheliometer (NIP) can be used to measure its value. The NIP is a device for measuring solar radiation at normal incidence from the Sun. Figure 3.15 shows the direct normal radiation for a summer day (September 2nd, 2023) in Alexandria, Egypt [194].

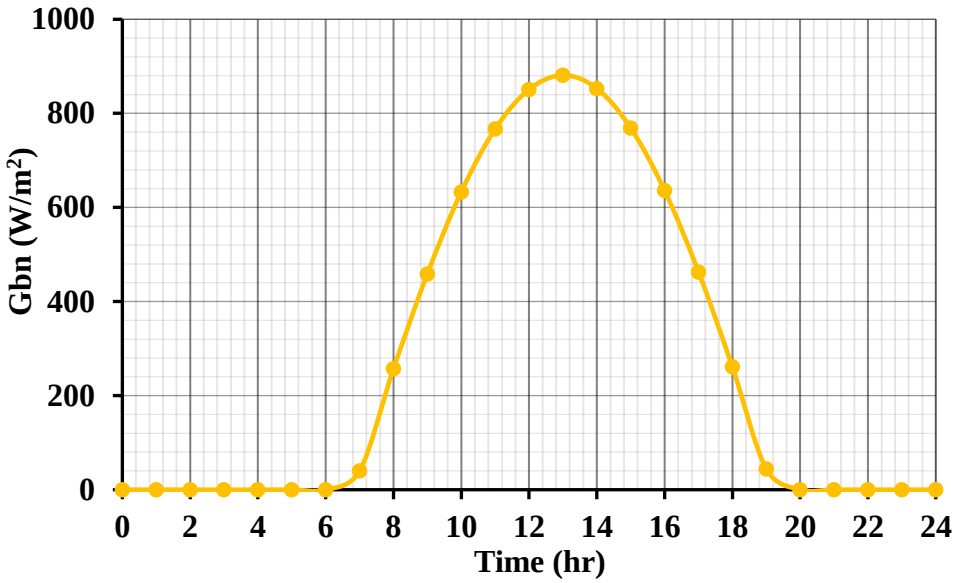

Figure 3.15 Direct normal radiation in Alexandria, Egypt on 2nd September 2023 [194]

As the position of the Sun in the sky and atmospheric effects on scattering and absorbing radiation change over time, direct normal radiation changes between dawn and dusk. The normal to the surface of the collector must be collinear to the incoming solar beam direction to maximize energy collection. The angle formed by the normal to the surface and the beam radiation direction is known as the angle of incidence θ, as shown in Figure 3.16. As a result, throughout the day, the incoming solar beam radiation also changes.

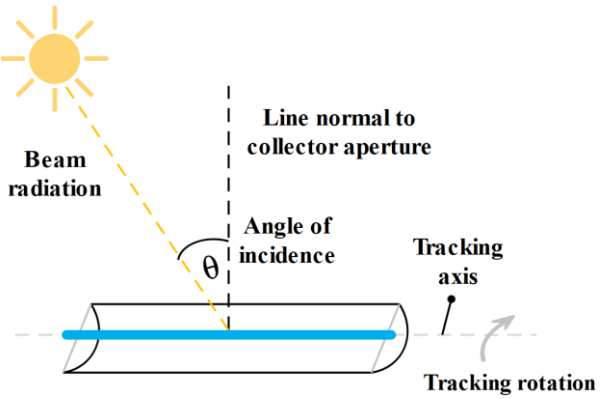

Figure 3.16 Angle of incidence [195]

Solar collectors must move to track the Sun to reduce the angle of incidence, with the best results being obtained when the collector surface is rotated around two axes. Many concentrating collectors track the Sun by rotating around a horizontal north-south axis, as shown in Figure 3.17, left. Due to this constraint, only the portion of the solar beam radiation perpendicular to the single-axis-tracking collector surface will be captured.

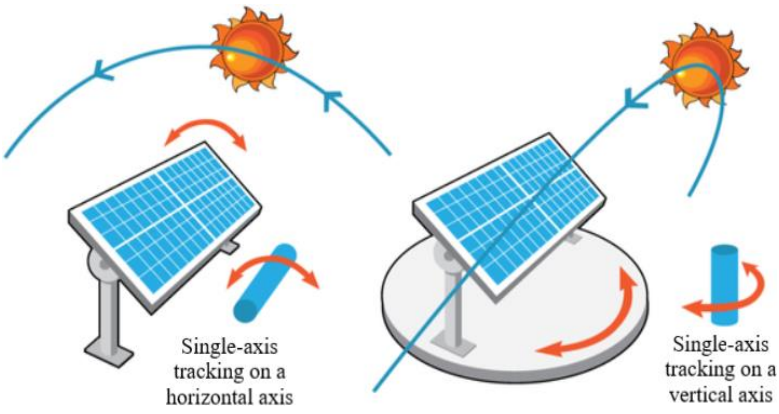

Figure 3.17 Single axis solar tracking [196]

The value of the useful solar beam radiation can be obtained by multiplying its value by the cosine of the angle of incidence. For a plane rotated about a horizontal north-south axis with continuous adjustment to minimize the angle of incidence, Duffle & Beckman [192] provide a formula for calculating it:

$$\cos\theta = (\cos^2\theta_z + \cos^2\delta \sin^2\omega)^{1/2} \quad (3.43)$$

The angles θ_z, δ and ω define the position of the Sun during its daily path relative to the horizontal coordinates, as shown in Figure 3.18 by Iqbal [193], which depicts the celestial sphere viewed by a collector at location C on the Earth surface.

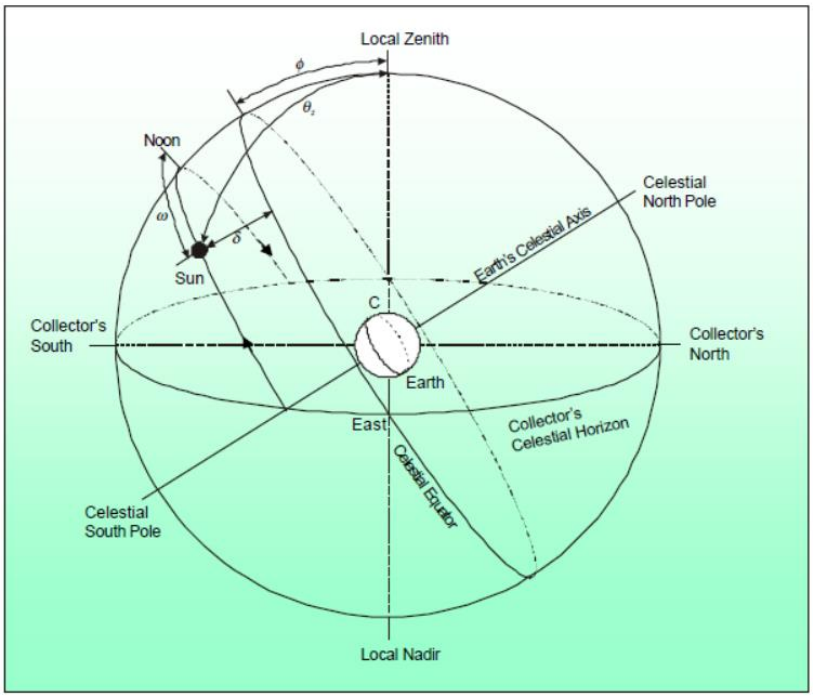

Figure 3.18 Celestial sphere and Sun coordinates relative to collector on Earth at point C (with permission from copyright owner) [197]

The celestial poles are the intersections of the celestial sphere with the polar axis of the Earth, and the celestial Equator is its intersection with the equatorial plane of the Earth. The local zenith is the intersection point between the celestial sphere and the normal to the Earth surface at the position C of the collector. The celestial horizon of the collector becomes a large circle in the celestial sphere defined by a plane parallel to the surface of the collector.

The zenith angle, θ_z, is defined as the angle between the vertical (the local zenith) and the solar beam direction, falling between $0° \leq \theta_z \leq 90°$. The zenith angle and the incidence angle, θ, become equal only at solar noon.

The declination angle, $,\delta,$ is the angular location of the Sun at solar noon (on the local meridian). Its range is between -23.45° and 23.45°. During winter solstice (December 21st or 22nd), it becomes minimum, while during summer solstice (June 21 or 22), it becomes maximum. At the vernal equinox (March 20th or 21st) and the autumnal equinox (September 22nd or 23rd), it becomes zero. The maximum daily declination change, which happens during equinoxes, is less than 0.5°. Figure 3.19 represents the solar declination with the Earth at the center of a celestial sphere that the Sun revolves around.

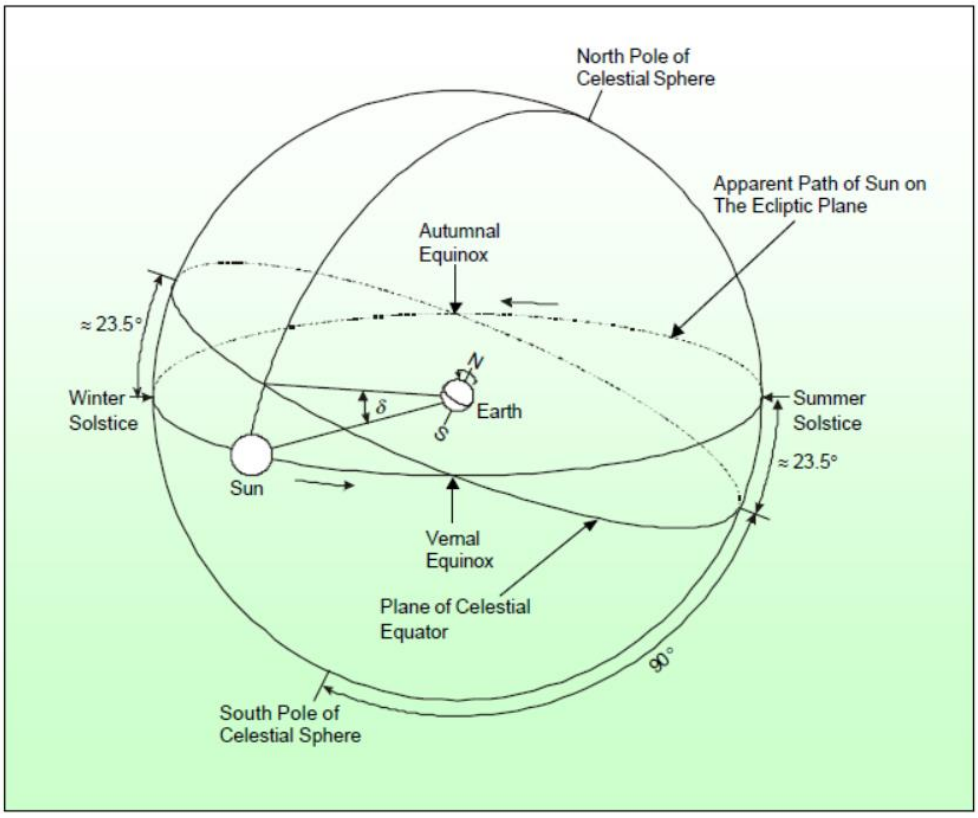

Figure 3.19 Celestial Sphere showing Sun declination angle (with permission from copyright owner) [197]

There have been several expressions for approximating the value of solar declination. According to Spencer, as cited by Iqbal [193], the following expression for δ, in degrees, is:

$$\begin{aligned}\delta = \ & (0.006918 - 0.399912\cos\partial + 0.070257\sin\partial \\ & - 0.006758\cos(2\partial) + 0.000907\sin(2\partial) \\ & - 0.002697\cos(3\partial) + 0.00148\sin(3\partial))\ (180/\pi)\end{aligned} \tag{3.44}$$

In the previous equation, ∂, in radians, is the day angle:

$$\partial = 2\pi(d_n - 1)/365 \tag{3.45}$$

where d_n is the year day count from 1 on January 1st to 365 on December 31st, considering that February has 28 days. The use of Equation (3.43) is advised in digital machines since it provides an estimate of d_n with a maximum inaccuracy of 0.0006 rad (<3').

Perrin de Brichambaut also expressed δ, in degrees, through the following equation, as cited in Iqbal [193]:

$$\delta = \ \sin^{-1}\left\{0.4\sin\left[\frac{360}{365}(d_n - 82)\right]\right\} \tag{3.46}$$

Cooper supplied an additional straightforward equation for δ, in degrees, as cited by Iqbal [193]:

$$\delta = 23.45\sin\left[\frac{360}{365}(d_n + 284)\right] \tag{3.47}$$

The hour angle ω is the angle at which the Sun moves east or west of the local meridian by the rotation of the Earth, at 15°/h. This angle is negative in the morning and positive in the afternoon. At solar noon, ω is 0°. Local clock noon is generally not equal to solar noon, which happens when the Sun is on the local meridian [192]. Therefore, standard time must be changed to solar time for calculations. The time deviation is due to two reasons. Firstly, the longitude at the local meridian, L_{loc}, and the longitude at the meridian on which the Local Standard Time is based, L_{st}, are different. For example, in the case of Alexandria (Egypt), the local longitude is 29.95527º E, and the standard longitude for the Egypt Standard Time is 30º E. And secondly, Earth rotational disturbances, which have an impact on when the Sun crosses the collector meridian, are considered in a second correction term, E_i. Hence, in minutes:

$$Solar\ Time - Standard\ Time = 4\ (L_{st} - L_{loc}) + \ E_i \tag{3.48}$$

where E_i is the equation of time, described by Spencer, as cited by Iqbal [193]:

$$\begin{aligned}E_i = 229.18(& 0.000075 + 0.001868\cos\partial - 0.032077\sin\partial \\ & - 0.014615\cos(2\partial) - 0.04089\sin(2\partial))\end{aligned} \tag{3.49}$$

Local time in summer can be daylight saving time, 60 minutes later than standard time:

$$Daylight\ Saving\ Time - Standard\ Time = 60 \tag{3.50}$$

Finally, another angle in Figure 3.18 is the latitude Φ or position of the collector north or south from the Earth Equator. For example: the latitude, Φ, for Alexandria (Egypt)

is 31.21564º N. The four angles depicted in Figure 3.18 are related through the equation provided by Duffie & Beckman [192]:

$$\cos\theta_z = \cos\Phi\cos\delta\cos\omega + \sin\Phi\sin\delta \tag{3.51}$$

This equation allows to calculate the hour angle at sunset, ω_{sunset}, knowing that the zenith angle, θ_z, is 90° at this time:

$$\cos\omega_{sunset} = -\tan\Phi\ \tan\Phi \tag{3.52}$$

By symmetry, the sunrise hour angle $\omega_{sunrise}$ is:

$$\omega_{sunrise} = -\omega_{sunset} \tag{3.53}$$

As the Sun spins at 15°/h, the time at dawn, in hours, can be obtained as:

$$Sunrise\ Hour = Solar\ Noon + \omega_{sunrise}/15 \tag{3.54}$$

And finally, the hour angle ω is expressed as:

$$\omega = \omega_{sunrise} + (Solar\ Time - Sunrise\ Hour)\cdot 15 \tag{3.55}$$

In summary, Equation (3.43) is used to obtain the angle of incidence, , by including the zenith angle, θ_z, rom Equation (3.51), the declination, δ, from Equation (3.44), and the hour angle, ω, from Equation (3.55). Then, the reduced beam radiation incident on an unshaded single axis tracking collector can be calculated by multiplying the cosine of the angle of incidence by the intensity of the solar beam radiation.

However, there are extra losses due to end losses and shadowing caused by the heat collector element (HCE) structures (Figure 3.20). Sun rays are focused on the HCE by reflection when they hit the ends of a trough collector. Figure 3.21 shows a HCE layout, while heat transfer at the HCE is depicted in Figure 3.22. Part of the HCE end will never receive solar radiation, so the cosine of the angle of incidence is changed using a function known as 'incidence angle modifier' to consider these optical losses.

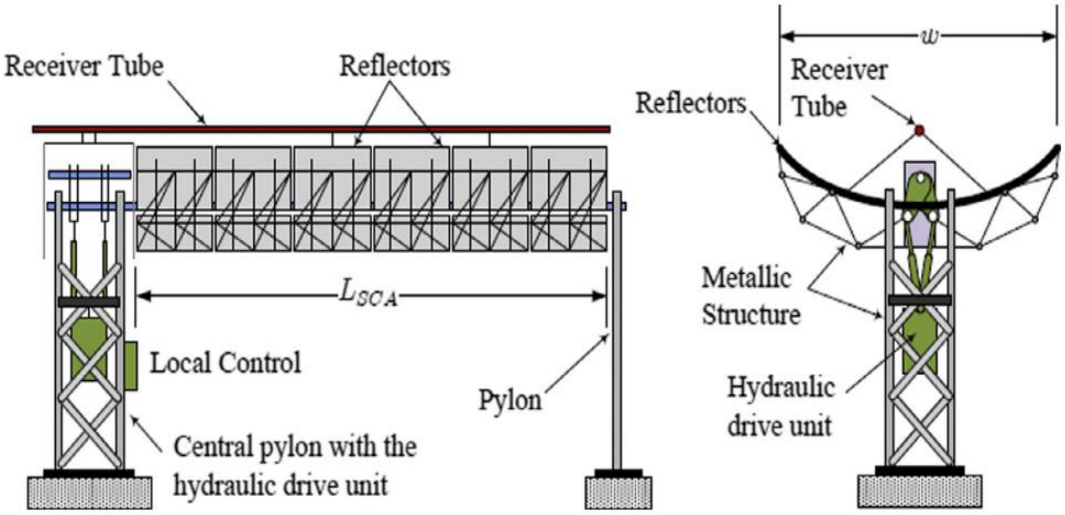

Figure 3.20 Solar collector assembly (with permission from copyright owner) [198]

The incidence angle modifier function is obtained, for $\cos\theta > 0.9$:

$$\begin{aligned} F(\cos\theta) = {} & -938564.84377331(\cos\theta)^6 + 5222972.5393731(\cos\theta)^5 \\ & - 12093484.903502\,(\cos\theta)^4 \\ & + 14912235.279499(\cos\theta)^3 \\ & - 10327122.89884\,(\cos\theta)^2 + 3808006.9842855\,\cos\theta \\ & - 584041.2051114 \end{aligned} \tag{3.56}$$

whereas for $\cos\theta \leq 0.9$:

$$\begin{aligned} F(\cos\theta) = {} & 7995.6488341455\,(\cos\theta)^8 - 45016.702352137\,(\cos\theta)^7 \\ & + 110302.75784952\,(\cos\theta)^6 \\ & - 153602.39131907\,(\cos\theta)^5 \\ & + 132938.65779691\,(\cos\theta)^4 \\ & - 73211.270566734\,(\cos\theta)^3 \\ & + 25050.730094871\,(\cos\theta)^2 - 4867.542978969\cos\theta \\ & + 411.23466109821 \end{aligned} \tag{3.57}$$

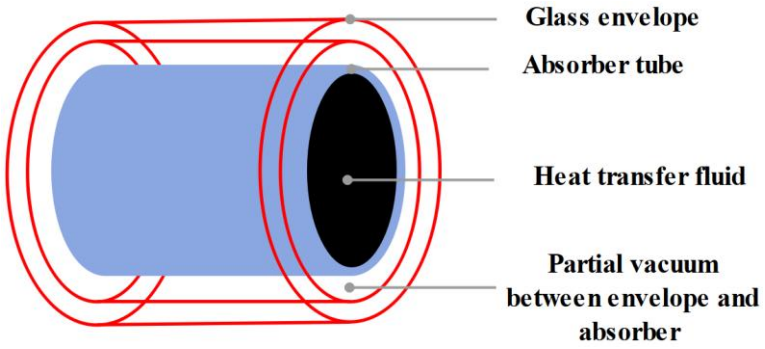

Figure 3.21 Heat collector element (HCE) [197]

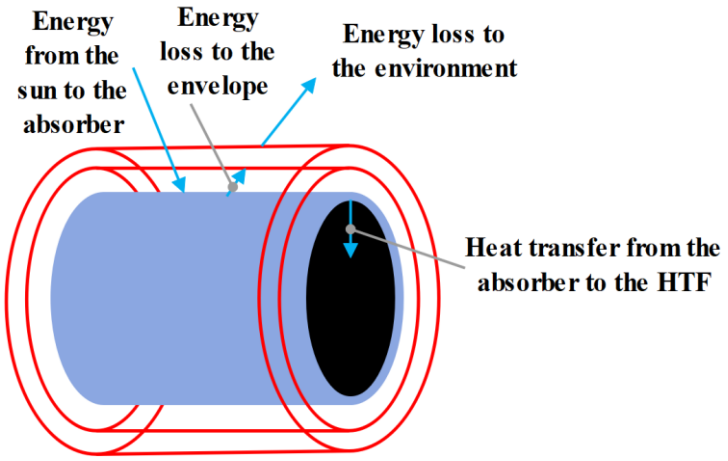

Figure 3.22 Heat transfer at the HCE [197]

The amount of solar energy absorbed per unit length equals the intensity of the incoming solar beam radiation multiplied by the incidence angle modifier, multiplied by the collector width. This is only true, though, if the collectors do not shade one another. Usually, collectors are organized in rows separated by a distance $L_{Spacing}$, as

in the trough collector field depicted in Figure 3.23. The front rows may shade the rows behind, as shown in Figure 3.24. Figure 3.25 shows the shading effect for different Sun positions. As observed in Figure 3.25-B, during the morning, the collectors will be partially shaded until a specific zenith angle is reached. The effective collector aperture reached by the solar beam radiation decreases, reducing the effective collector width and the solar energy absorption. Figures 3.25-C and 3.25-D show that shading disappears once a particular zenith angle is attained. The same behavior will appear when dusk arrives, only in reverse order (D-C-B-A).

Figure 3.23 Aerial view of CSP trough plants at Kramer Junction, California [199]

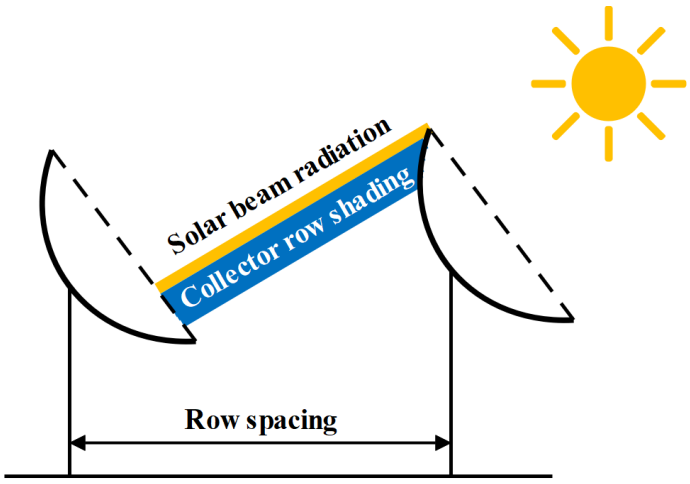

Figure 3.24 Shading in multiple row parabolic trough collector [200]

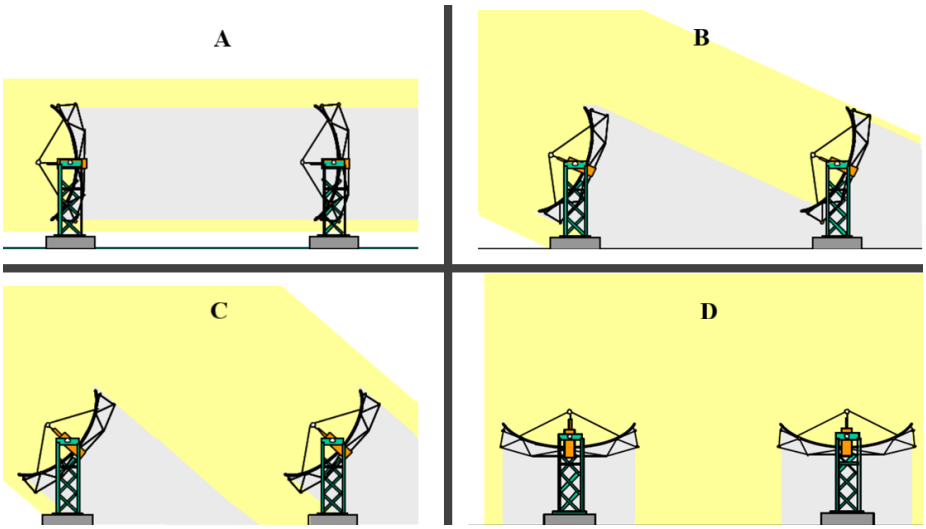

Figure 3.25 Shading effect for various Sun positions (with permission from copyright owner) [197]

Finding an equation for the effective collector width is key for assessing optical losses from shading. If W is the collector width, the effective collector width will be:

$$W_{eff} = x \,.\, W \tag{3.58}$$

where x: $[0,1]$ is the level of shading, from 0 – full shading to 1 – no shading.

Further optical energy losses can result from radiative properties of the mirror, the envelope, and the absorber of the solar collector. First, the trough mirror reflects solar beam radiation, which is then focused onto the HCE. However, there will be specular reflection and diffuse reflection [192], and diffuse reflection on the trough mirrors will not contribute significantly to the radiation acting on the absorber since it is dispersed in all directions. The ratio of the specular reflected radiation to the solar beam radiation incident on the trough mirror is known as the specular reflectance ρ.

In addition, before being absorbed, the specular radiation passes through the glass enclosure of the HCE, as shown in Figure 3.22. At the interface between the two media, there will be some reflection due to the difference in the refractive index [192], so part of the energy will not pass across the interface. If absorption of the glass envelope is neglected, the amount of radiation that reaches the absorber may be determined by adding up the portions of the solar beam radiation that passed across the interface. The transmittance τ is the share of radiation transmitted through the glass envelope after considering radiation losses caused by reflection and absorption

Finally, the surface of the absorber tube in the HCE absorbs the share of incoming solar beam radiation called absorptance α. In concentrating solar field models, reflectance ρ, transmittance τ and absorptance α are usually between 0.9 and 1.

The radiation reflected to the glass envelope by the absorber is partially reflected there back to the absorber, giving it another chance to be absorbed. This effect happens in the annulus between the absorber tube and the glass envelope and leads to a slight increase in the amount of solar radiation absorbed that could be explained by the

product of the transmittance and absorptance $\tau\alpha$ [192]. An appropriate approximation for most practical solar collectors is:

$$(\tau\alpha) \cong 1.01\tau\alpha \tag{3.59}$$

Consequently, optical efficiency from radiation properties is:

$$\varepsilon_{opt} = \rho\tau\alpha \tag{3.60}$$

And the absorbed solar energy is finally:

$$Q_{absorbed} = G_{bn} \,.\, F(\cos\theta) \,.\, W_{eff} \,.\, \varepsilon_{opt} \,.\, \gamma \tag{3.61}$$

where γ is a factor varying with the amount of dirt on the mirrors and the number of broken collectors in the field.

CHAPTER FOUR

RESULTS AND DISCUSSION

In this chapter, the results of the solar thermal power integration with the combined cycle power plant at different positions based on two operating schemes, fuel saving and power boosting, will be discussed. Based on the operational limitations of each approach, five solar integration positions were examined. For every configuration, the maximum solar thermal power that could be integrated to guarantee the proper functioning of the HRSG was assessed.

4.1 Fuel saving

Three different integration options into the gas cycle and two options into the steam cycle were studied, as shown in Figure 4.1. The gas cycle integration options results will be presented first, followed by the steam cycle integration results.

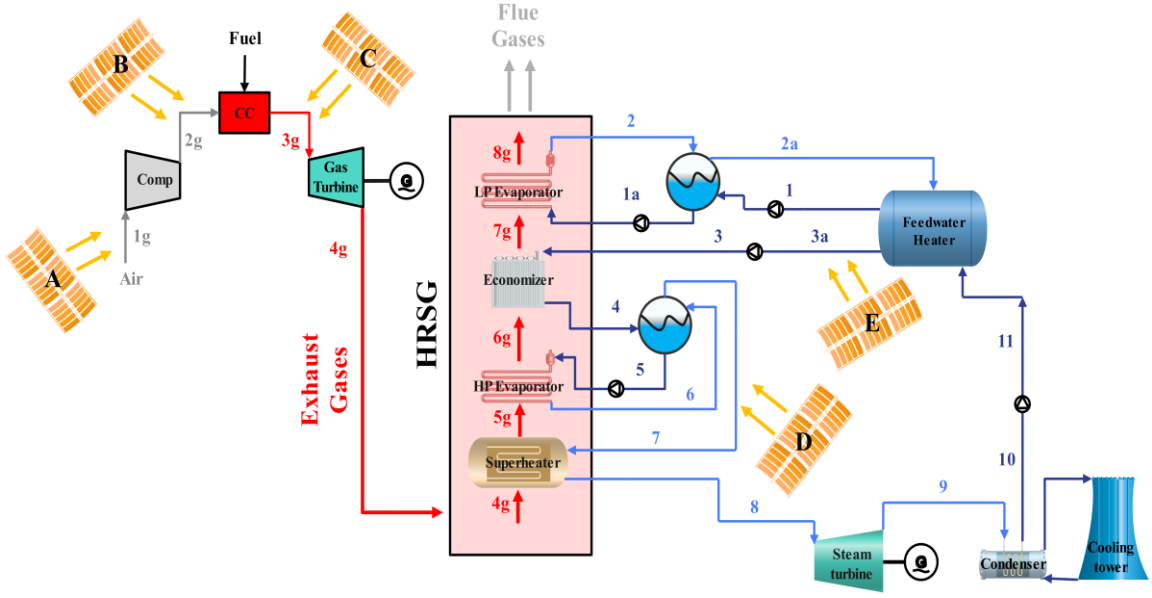

Figure 4.1 Solar field integration options for fuel saving

4.1.1 Solar field integration at the top gas cycle

- **Case A "Before air compressor":** Ambient air is heated by solar field before the compression stage.
- **Case B "After compressor / Before combustion chamber":** Compressed air is heated before entering the combustion chamber.
- **Case C "After combustion chamber / Before gas turbine":** hot gases are heated up before entering the gas turbine.

4.1.1.1 Case A "Before air compressor"

In "case A", the solar field heats up ambient air before compression, as shown in Figure 4.2. Since the integration is in the gas cycle and the input and output conditions of the gas turbine are kept constant, the steam cycle is virtually not affected by the integration of the solar field. For this solar integration option, the results were analyzed at solar power values from 1 to 5 MW in 1 MW increments, as shown in Table 4.1. The results, collected in Table 4.1, show that the integration of the solar field before the compression stage will increase compression work, as the air to be compressed is now hotter.

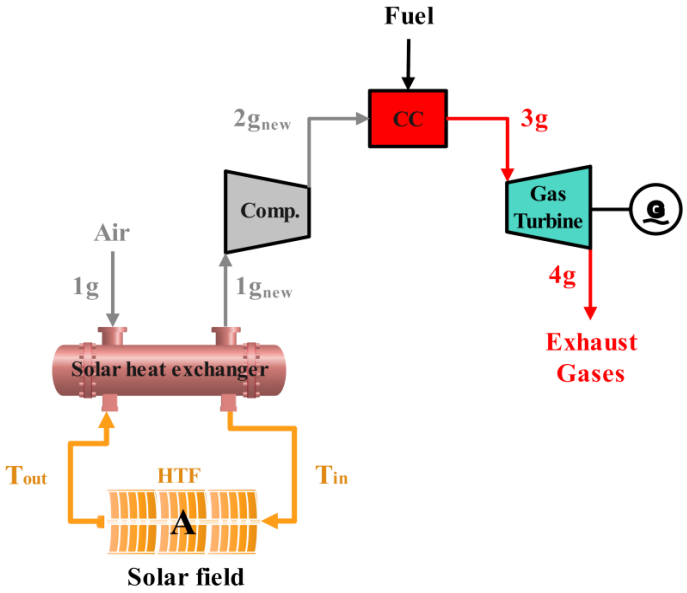

Figure 4.2 Case A: solar field integrated before air compressor for fuel saving

Table 4.1 Original CC vs ISCC (case A) "Fuel saving"

Solar heat integration	**Original CC**	**ISCC Case A**	**ISCC Case A**	**ISCC Case A**	**ISCC Case A**	**ISCC Case A**
Integrated solar heat (MW)	--	1	2	3	4	5
Mass flowrates	**Original CC**	**ISCC Case A**	**ISCC Case A**	**ISCC Case A**	**ISCC Case A**	**ISCC Case A**
Air to fuel ratio	50	50.72	51.47	52.23	53.02	53.83
Turbine gas flowrate (kg/s)	174.7					
Air flowrate (kg/s)	171.27	171.32	171.37	171.42	171.46	171.51
Fuel flowrate (kg/s)	3.42	3.37	3.33	3.28	3.23	3.18
Fuel saving (%)	--	1.39	2.79	4.19	5.59	6.99
LP evaporator mass flowrate (kg/s)	5					
LP evaporator mass flowrate (kg/s)	25					
Operating temperatures	**Original CC**	**ISCC Case A**	**ISCC Case A**	**ISCC Case A**	**ISCC Case A**	**ISCC Case A**
Compressor inlet (°C)	24	30	35.5	41.5	47	53
Combustion chamber inlet (°C)	378	390	402	414	426	438
Gas turbine inlet (°C)	1174					
Gas turbine outlet (°C)	549					
Cycle efficiency	**Original CC**	**ISCC Case A**	**ISCC Case A**	**ISCC Case A**	**ISCC Case A**	**ISCC Case A**
Gas turbine cycle (%)	39.84	39.37	38.9	38.42	37.94	37.44
Combined cycle (%)	56.13	55.79	55.45	55.11	54.76	54.4
Cycle power breakdown	**Original CC**	**ISCC Case A**	**ISCC Case A**	**ISCC Case A**	**ISCC Case A**	**ISCC Case A**
Compressor (kW)	62,450	63,695	64,939	66,183	67,428	68,672
Gas turbine (kW)	126,727					
Gas cycle (kW)	64,277	63,032	61,788	60,544	59,299	58,055
Steam cycle (kW)	26,292					
Total net power (kW)	90,569	89,324	88,079	86,835	85,590	84,346
Specific work per fuel unit mass flow (kJ/kg)	26,439	26,446	26,454	26,461	26,468	26,476
Back work ratio (%)	49.28	50.26	51.24	52.22	53.2	54.19
CO_2 emissions (Mt/year)	0.2971	0.2929	0.2888	0.2846	0.2804	0.2763
CO_2 emissions saved (kg CO_2/kWh)	-	0.0014	0.0028	0.0042	0.0057	0.0072

As the compressor power increases, the gas cycle output power will decrease. Considering that the steam cycle is not affected by solar integration, the total output power of the ISCC will decrease as shown in Figure 4.3.

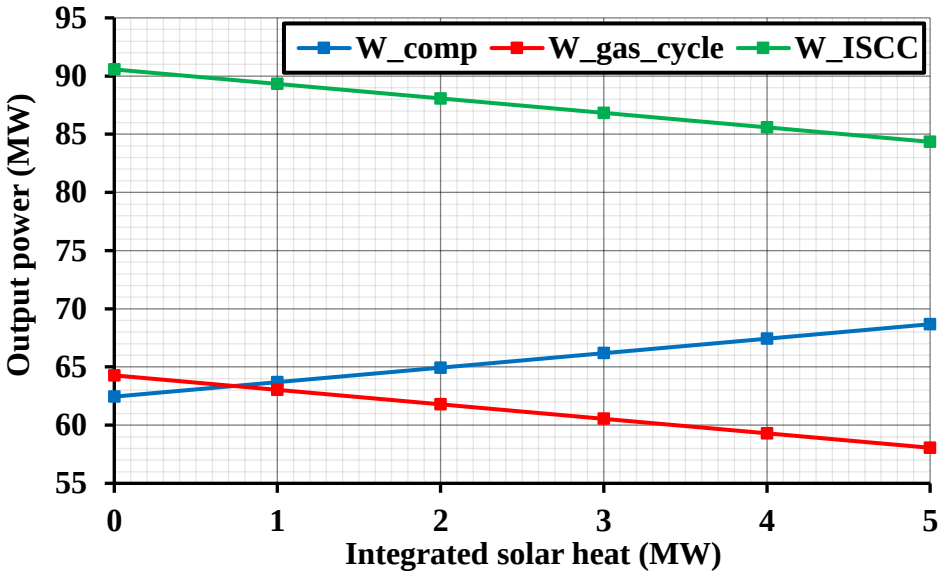

Figure 4.3 Work of compressor & ISCC output power at different integrated solar heat for case A

As the solar thermal power increased from 0 to 5 MW, the compression power increased from 62.45 to 68.67 MW, and the total output power of the ISCC decreased from 90.56 to 84.34 MW. Thermal efficiencies kept falling as the gas cycle efficiency decreased from 39.84% to 37.44%, as shown in Figure 4.4. Therefore, the overall ISCC efficiency was reduced by 1.7%. Despite fuel consumption was reduced in "case A" thanks to the integration of solar thermal power, as shown in Figure 4.5, the result is misleading because the total output power decreased.

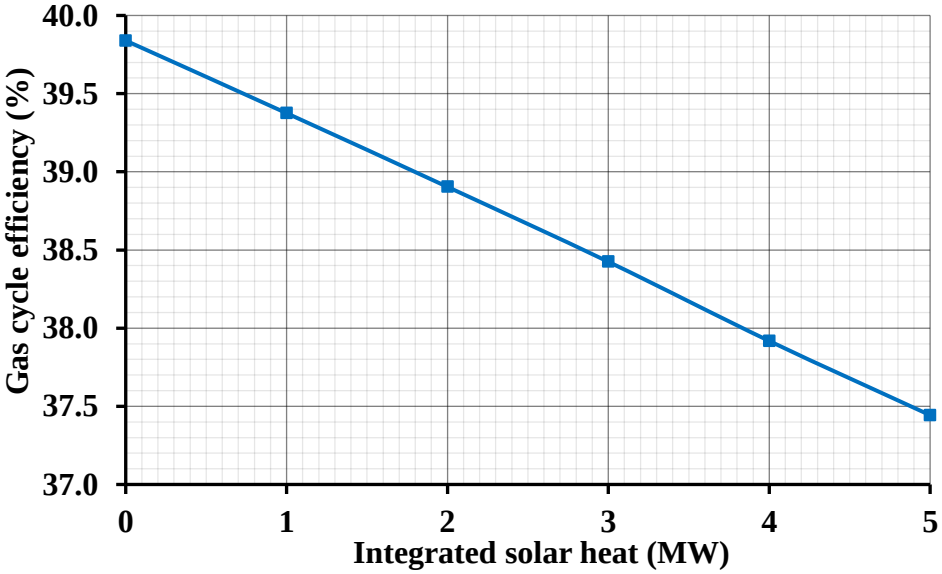

Figure 4.4 Gas cycle efficiency at different integrated solar heat for case A

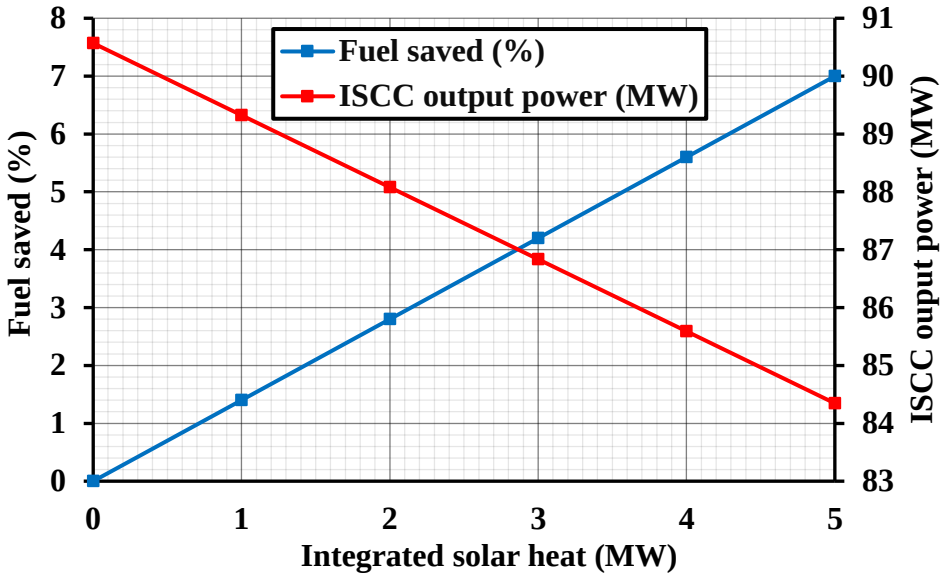

Figure 4.5 Fuel saved & ISCC output power at different integrated solar heat for case A

The results obtained clearly stress that the fuel saving scheme cannot be applied to "case A", as the gas cycle output power cannot be kept constant with solar power integration before the air compressor.

4.1.1.2 Case B "After air compressor"

In "case B", the integrated solar thermal power heats up compressed air before being mixed with the added fuel in the combustion chamber, as shown in Figure 4.6. Results were investigated at different solar thermal power values from 1-10 MW in 2 MW increments, as shown in Table 4.2.

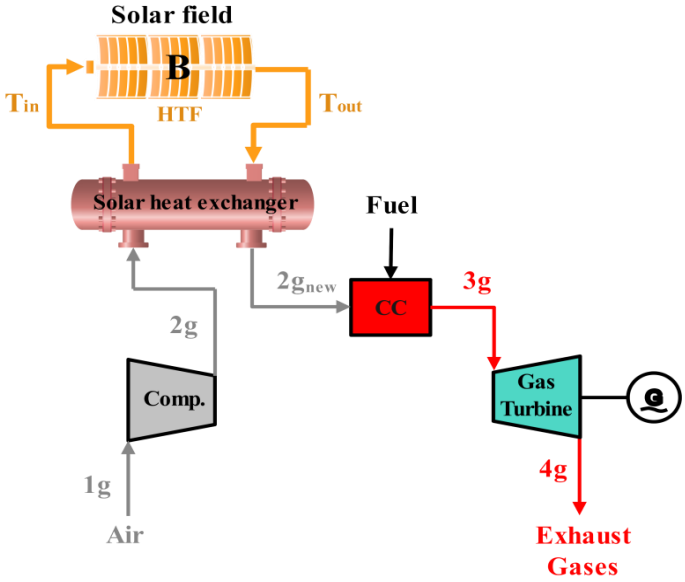

Figure 4.6 Case B: solar field integrated before combustion chamber for fuel saving

Table 4.2 Original CC vs ISCC (case B) "Fuel saving"

Solar heat integration	**Original CC**	**ISCC Case B**	**ISCC Case B**	**ISCC Case B**	**ISCC Case B**	**ISCC Case B**
Integrated solar heat (MW)	--	2	4	6	8	10
Mass flow rates	**Original CC**	**ISCC Case B**	**ISCC Case B**	**ISCC Case B**	**ISCC Case B**	**ISCC Case B**
Air to fuel ratio	50	50.64	51.3	51.98	52.67	53.39
Turbine gas flowrate (kg/s)	174.7					
Air flowrate (kg/s)	171.27	171.31	171.36	171.4	171.44	171.49
Fuel flowrate (kg/s)	3.42	3.38	3.34	3.29	3.25	3.21
Fuel saving (%)	--	1.25	2.49	3.74	4.98	6.23
LP evaporator mass low rate (kg/s)	5					
HP evaporator mass low rate (kg/s)	25					
Operating temperatures	**Original CC**	**ISCC Case B**	**ISCC Case B**	**ISCC Case B**	**ISCC Case B**	**ISCC Case B**
Compressor inlet (°C)	24					
Combustion chamber inlet (°C)	378	388.5	399.5	410	420.5	431
Gas turbine inlet (°C)	1174					
Gas turbine outlet (°C)	549					
Cycle efficiency	**Original CC**	**ISCC Case B**	**ISCC Case B**	**ISCC Case B**	**ISCC Case B**	**ISCC Case B**
Gas turbine cycle (%)	39.84	39.84	39.84	39.84	39.85	39.85
Combined cycle (%)	56.13	56.14	56.14	56.14	56.15	56.15
Cycle power breakdown	**Original CC**	**ISCC Case B**	**ISCC Case B**	**ISCC Case B**	**ISCC Case B**	**ISCC Case B**
Compressor (kW)	62,450					
Gas turbine (kW)	126,727					
Gas cycle (kW)	64,277					
Steam cycle (kW)	26,292					
Total net power (kW)	90,569					
Back work ratio (%)	49.279					
Specific work per fuel unit mass flow (kJ/kg)	26,439	26,677	27,116	27,467	27,828	28,198
CO_2 emissions (Mt/year)	0.2971	0.2934	0.2897	0.286	0.2822	0.2785
CO_2 emissions saved (kg CO_2/kWh)	-	0.0012	0.0025	0.0037	0.0051	0.0064

The relationship between the integrated solar thermal power, the fuel flowrate and the combustion chamber inlet temperature is shown in Figure 4.7. The combustion chamber inlet temperature shows a linear increase from roughly 378 °C to 431 °C as the integrated solar thermal power increases from 0 to 10 MW. On the other hand, the fuel flowrate shows a linear reduction from roughly 3.42 kg/s to 3.21 kg/s. Accordingly, a higher solar contribution increases the temperature at the combustion chamber inlet, while lowering the system fuel dependence. This pattern highlights how solar heat integration can reduce emissions and operating costs, optimizing energy efficiency.

At around 5 MW of integrated solar power, the temperature of the combustion chamber inlet is approximately 405°C, and the fuel flowrate is approximately 3.32 kg/s. From this point on, higher thermal power integration values significantly lower the amount of fuel required to keep the combustion chamber temperature at the optimal level.

Overall ISCC and gas cycle efficiencies both exhibit nearly constant stability from 0 to 10 MW of integrated solar power, as shown in Figure 4.8. ISSC efficiency increases slightly from 56.13% to 56.15%, while gas cycle efficiency increases from about 39.84% to 39.85%. The specific work per fuel unit mass increased to 28.2 MJ/kg.

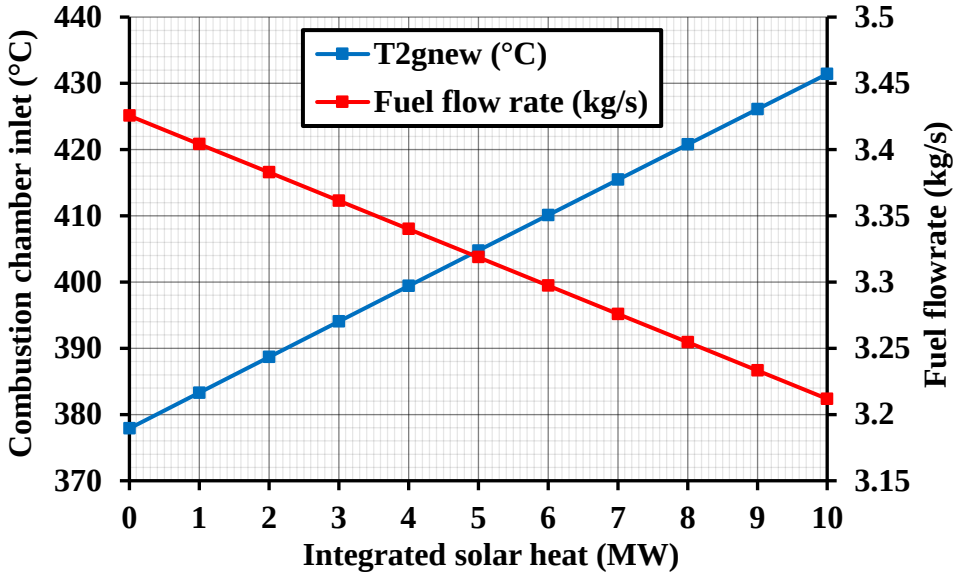

Figure 4.7 Combustion chamber inlet & fuel flowrate at different integrated solar heat for case B

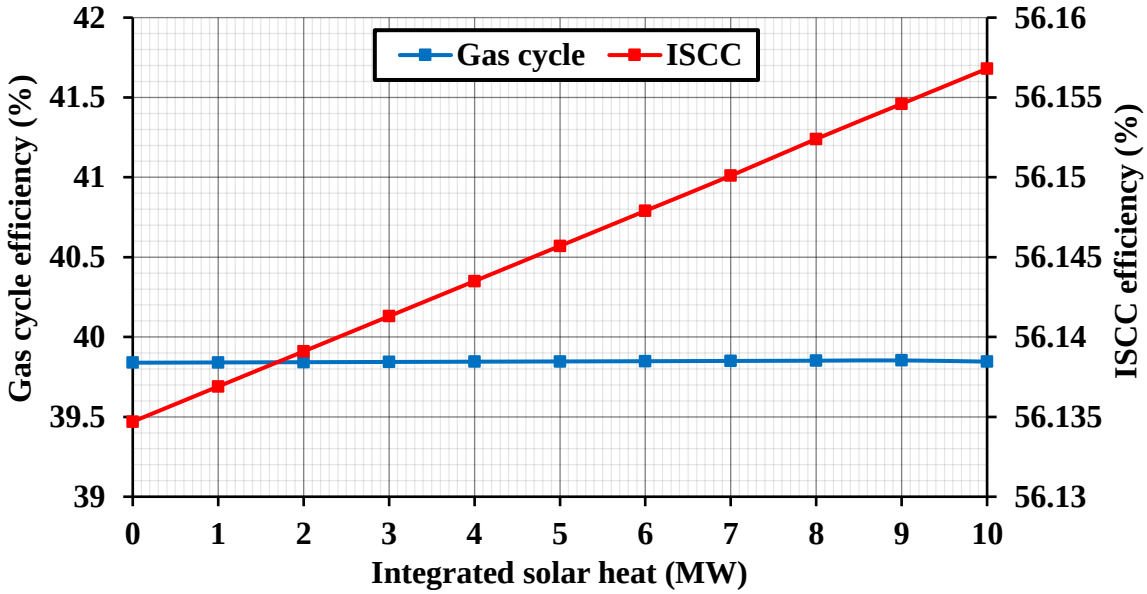

Figure 4.8 Efficiencies at different integrated solar heat for case B

Concerning the choice of a suitable solar field, PTC could be used, but the temperature of stage 2g reaches 378 °C, while the output temperature of the solar heat exchanger ($T2_{gnew}$) could reach 433 °C at 10 MW of integrated thermal power. As the operating temperature range of the commonly used synthetic oil "Therminol VP-1" is 290-390°C [189], molten salts should be used, as they have higher operating temperatures, up to 550°C [190]. Case B, hence, is superior to the original CC; however, the heat transfer fluid should be altered, or a different technology with higher temperature ranges should be employed. Suitable options could be heliostat field collectors or Parabolic dish reflectors (PDRs), as presented in Table 3.3.

Fuel saving increases with solar power integration, as represented in Figure 4.9. 1 MW increase in solar power translates into about 0.62 % of fuel saved. A maximum of 6.23% of fuel could be saved at an integrated thermal power of 10 MW, avoiding 6.4 g/kWh of CO_2 emissions.

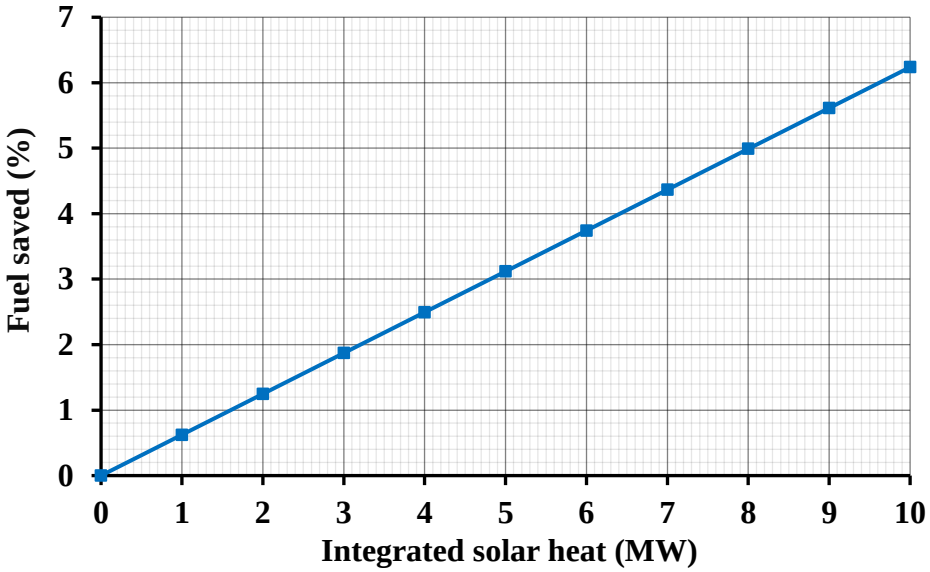

Figure 4.9 Fuel saved at different integrated solar heat for case B

4.1.1.3 Case C "After combustion chamber"

In "case C", the solar field is integrated after the combustion chamber, where the hot gases are heated up by the integrated solar thermal power before entering the gas turbine, as shown in Figure 4.10. Similar results to "case B" were found, due to the fixed gas turbine operating conditions (the turbine inlet temperature is 1174ºC as in the original CC). However, different temperature distributions along the cycle states were observed. Reducing fuel consumption in the combustion chamber requires an increase in the temperature of state ($T3_{gnew}$) before entering the chamber, as shown in Figure 4.11.

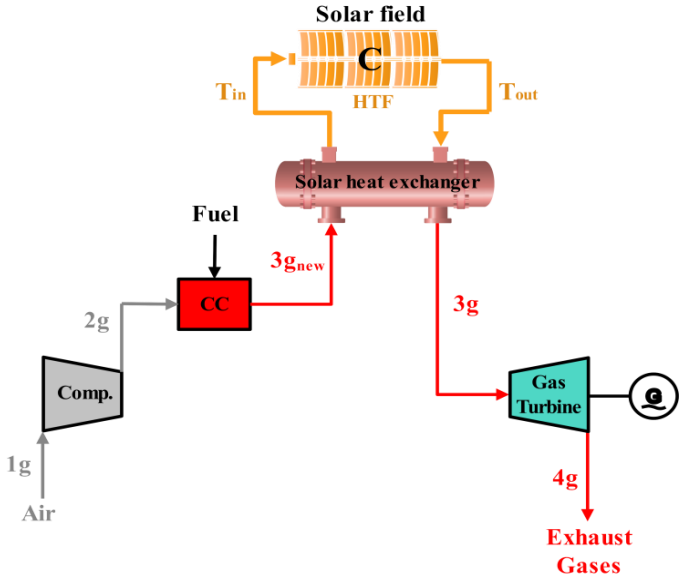

Figure 4.10 Case C: solar field integrated after combustion chamber for fuel saving

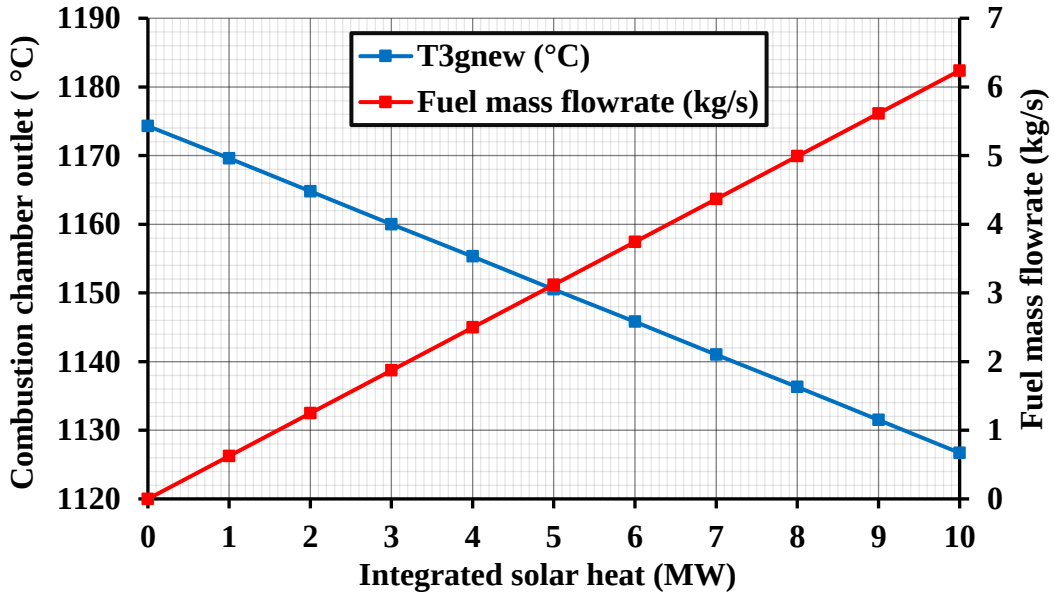

Figure 4.11 Combustion chamber outlet & fuel mass flowrate as a function of integrated solar heat for case C

The same problem as for "case B" is faced in this configuration, with the temperature of stage (3g) reaching 1126 °C. This temperature is too high for PTC or most solar technologies, so, according to the data in Table 3.3, the heliostat field is the only technology that can deal properly with these high operating temperatures. In this sense, “Case B” outperforms “case C”, as more solar field technologies can be installed.

Fuel mass flowrate decreased by increasing integrated solar power. The fuel rate at no solar heat (0 MW) was 3.42 kg/s, while with 10 MW, it was 3.21 kg/s (6.23% saving).

4.1.2 Solar field integration at the bottom steam cycle

When the solar field is integrated into the bottom steam cycle under the fuel saving strategy, the required output power from the top gas cycle is reduced so the total output power of the ISCC remains constant. As steam temperatures rise, there may be a reversal in the direction of heat transfer inside the HRSG. To avoid this problem, steam temperatures were monitored, and a maximum integrated solar thermal power was calculated for each case. The results of two integration configurations will be presented:

a. **Case D “Integration before superheater”:** The integrated solar field heats the outlet steam from the HP drum before the superheater stage.
b. **Case E “Integration before Economizer”:** The feedwater is preheated before entering the economizer stage.

4.1.2.1 Case D “Integration before superheater”

In this configuration, as shown in Figure 4.12, the solar field heats the steam from the HP drum before entering the superheater. As the steam temperature rises, the temperature distribution inside the HRSG changes. The steam turbine generates more power, allowing for reducing the top gas cycle power and fuel consumption. It was found that solar thermal power could not exceed 15 MW to prevent heat transfer reversal inside the HRSG. The results from “case D” configuration are collected in Table 4.3, where the performance was studied at solar powers of 5, 10 and 15 MW.

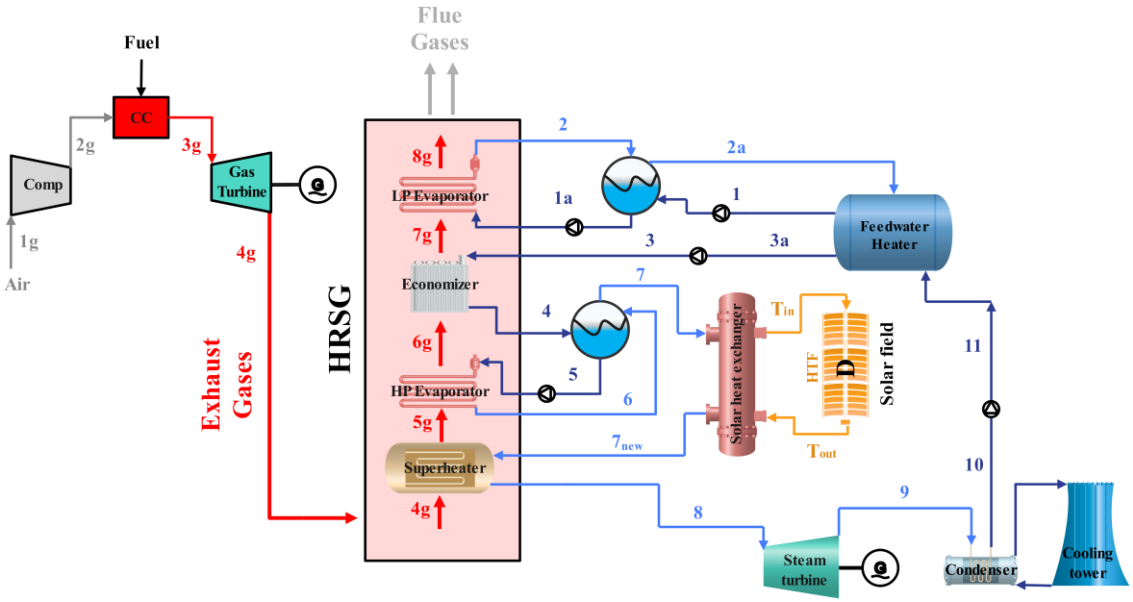

Figure 4.12 Case D: solar field integrated at superheater for fuel saving

Table 4.3 Original CC vs ISCC (case D) "Fuel saving"

Mass flowrates	**Original CC**	**ISCC Case D**	**ISCC Case D**	**ISCC Case D**
Air to fuel ratio	50			
Turbine gas flow rate (kg/s)	174.7	172.73	170.66	168.59
Air flowrate (kg/s)	171.28	169.35	167.32	165.28
Fuel flowrate (kg/s)	3.42	3.38	3.34	3.3
Fuel saving (%)	--	1.12	2.3	3.49
LP evaporator mass flowrate (kg/s)	5			
HP evaporator mass flowrate (kg/s)	25			
Operating temperatures	**Original CC**	**ISCC Case D**	**ISCC Case D**	**ISCC Case D**
Compressor inlet (°C)	24			
Combustion chamber inlet (°C)	378			
Gas turbine inlet (°C)	1174			
Gas turbine outlet (°C)	549			
Solar heat integration	**Original CC**	**ISCC Case D**	**ISCC Case D**	**ISCC Case D**
Integrated solar heat (MW)	--	5	10	15
Cycle efficiency	**Original CC**	**ISCC Case D**	**ISCC Case D**	**ISCC Case D**
Gas turbine cycle (%)	39.84	39.84	39.84	39.84
Combined cycle (%)	56.13	55.05	54.03	53.06
Cycle power breakdown	**Original CC**	**ISCC Case D**	**ISCC Case D**	**ISCC Case D**
Compressor (kW)	62,450	61,749	61,009	60,266
Gas turbine (kW)	126,727	125,303	123,802	122,294
Gas cycle (kW)	64,277	63,555	62,793	62,028
Steam cycle (kW)	26,292	27,016	27,777	28,542
Total net power (kW)	90,569	90,569	90,569	90,569
Back work ratio (%)	49.279			
Specific work per unit fuel mass (kJ/kg)	26,439	26,741	27,065	27,399
CO_2 emissions (Mt/year)	0.2971	0.2937	0.2902	0.2867
CO_2 emissions saved (kg CO_2/kWh)	--	0.0011	0.0023	0.0035

Fuel flowrate was reduced from 3.42 kg/s to 3.3 kg/s, saving 3.49% of the initial fuel consumption. Overall ISCC efficiency is around 3% less than for the original CC. Due to the fuel saving strategy, a large amount of solar heat power is integrated leaving the ISCC overall output power unaffected. On the other hand, the top gas cycle efficiency was not affected as solar integration was performed into the bottom steam cycle. As a result, the specific work per fuel unit mass increased from 26.4 MJ/kg to 27.4 MJ/kg, saving around 3.5 g/kWh of CO_2 emissions. Based on the operating temperature ranges, PTC with molten salts, parabolic dish reflectors or heliostat field collectors could be used, as temperature of stage (7_{new}) would reach 480 °C at 15 MW of integrated solar power.

Figure 4.13 shows that at 0 MW, the fuel flowrate was about 3.42 kg/s, while, at 15 MW, it dropped to about 3.3 kg/s saving 3.49% of fuel. It can be observed that with the integration of solar power, the system uses less fuel, increasing fuel efficiency. According to the data in Table 4.3, "case D" yields potential benefits.

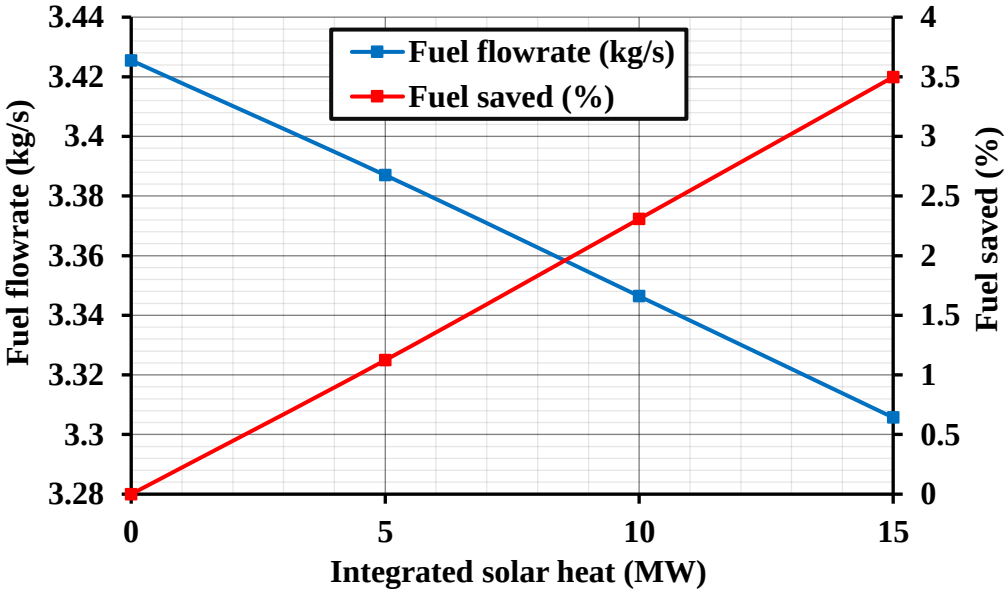

Figure 4.13 Fuel saved at different integrated solar heat for case D

According to the temperature distribution inside the HRSG, the system could integrate up to 15 MW of solar thermal power in "case D". Integration of the solar field before the superheater stage heats saturated steam, as shown in the T-Q diagram in Figure 4.14, which corresponds to 15 MW integrated solar thermal power. The graph shows how the temperature of the steam (blue) and flue gas (orange) varies as they pass through the superheater, evaporator, and economizer sections of the HRSG.

The flue gas cools down to around 210 °C at the economizer outlet after entering the HRSG at around 549 °C. Simultaneously, feedwater is gradually heated from the economizer on. In the evaporator, it reaches saturation and is converted into steam. After that, steam is heated to around 550°C in the superheater before entering the turbine. The critical variable is saturation temperature, which marks the liquid-to-steam phase change.

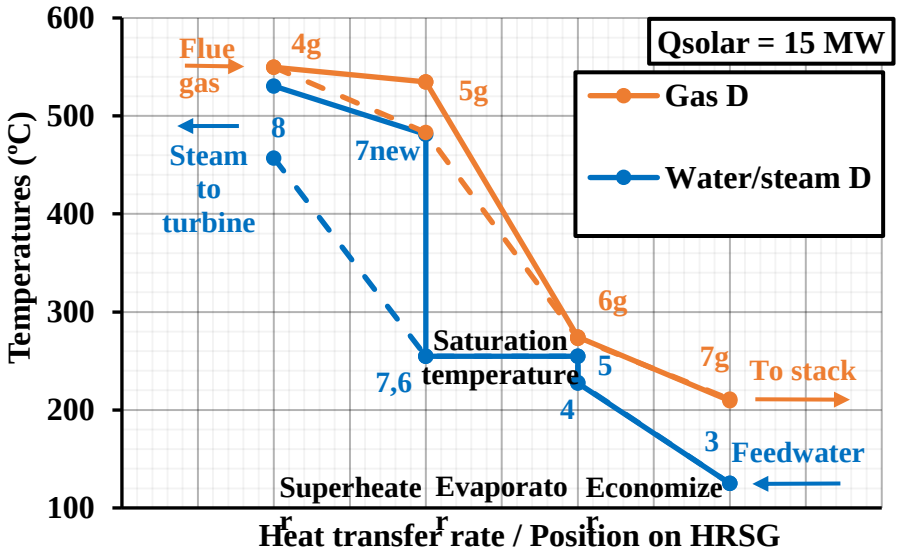

Figure 4.14 T-Q diagram for case D "Fuel saving" at Qsolar = 15 MW

The problem of reverse heat transfer inside the HRSG is crucial, as when the integrated solar thermal power exceeds a maximum limit, steam will begin to heat the flue gases and thermal energy will be lost in the exhaust gases from the HRSG. Figure 4.15 shows the reverse heat transfer problem inside when solar power is higher than 15 MW.

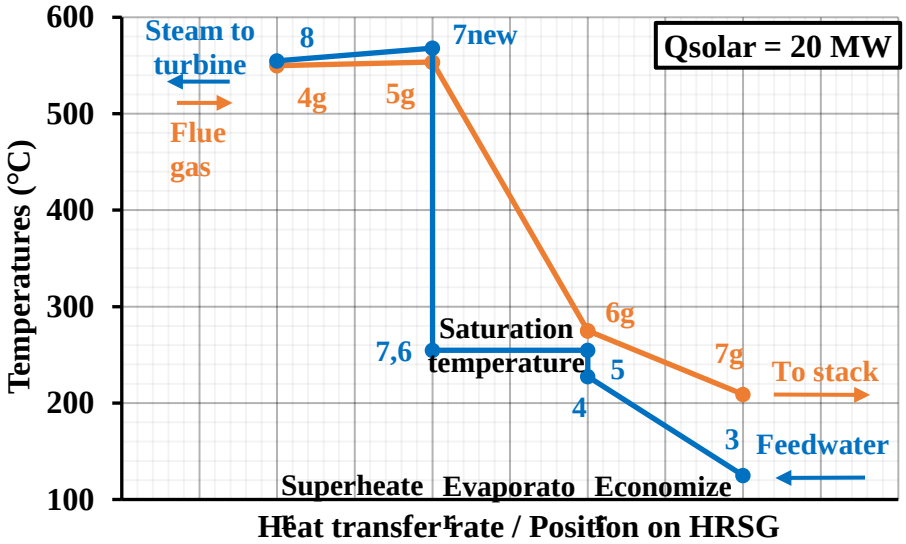

Figure 4.15 T-Q diagram for case D "Fuel saving" at Qsolar = 20 MW

4.1.2.2 Case E "Integration before economizer"

The solar field can be integrated before the steam cycle economizer to preheat the feedwater, as seen in Figure 4.16. Solar integration into the bottom cycle will increase the steam turbine output power and the temperature distribution along the HRSG will change, balancing the loss of power in the gas turbine due to the reduction in fuel consumption. It was found that integrated solar thermal power should not exceed 3 MW to avoid heat transfer reversal in the HRSG. Table 4.4 collects the results for "case E" at integrated solar power values of 1, 2 and 3 MW.

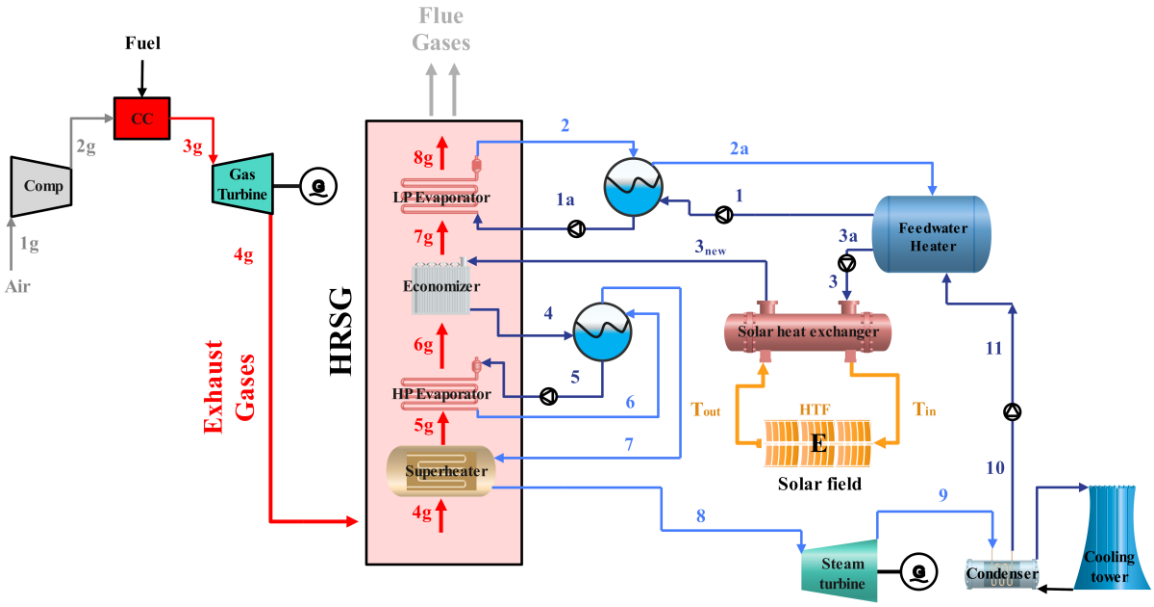

Figure 4.16 Case E: solar field integrated at economizer for fuel saving

Table 4.4 Original CC vs ISCC (case E) "Fuel saving"

Mass flowrates	**Original CC**	**ISCC Case E**	**ISCC Case E**	**ISCC Case E**
Air to fuel ratio	50			
Turbine gas flowrate (kg/s)	174.7	169.74	165.25	160.77
Air flowrate (kg/s)	171.2	166.41	162.01	157.61
Fuel flowrate (kg/s)	3.42	3.33	3.24	3.15
Fuel saving (%)	--	2.84	5.4	7.97
LP evaporator mass flowrate (kg/s)	5			
HP evaporator mass flowrate (kg/s)	25			
Operating temperatures	**Original CC**	**ISCC Case E**	**ISCC Case E**	**ISCC Case E**
Compressor inlet (°C)	24			
Combustion chamber inlet (°C)	379			
Gas turbine inlet (°C)	1174			
Gas turbine outlet (°C)	549			
Solar heat integration	**Original CC**	**ISCC Case E**	**ISCC Case E**	**ISCC Case E**
Integrated solar heat (MW)	--	1	2	3
Cycle efficiency	**Original CC**	**ISCC Case E**	**ISCC Case E**	**ISCC Case E**
Gas turbine cycle (%)	39.84			
Combined cycle (%)	56.13	57.41	58.57	59.79
Cycle power breakdown	**Original CC**	**ISCC Case E**	**ISCC Case E**	**ISCC Case E**
Compressor (kW)	62,450	60,677	59,074	57,471
Gas turbine (kW)	126,727	123,128	119,875	116,622
Gas cycle (kW)	64,277	62,452	60,802	59,152
Steam cycle (kW)	26,292	28,117	29,767	31,417
Total net power (kW)	90,569			
Back work ratio (%)	49.279			
Specific work per unit fuel mass (kJ/kg)	26,439	27,212	27,951	28,730
CO_2 emissions (Mt/year)	0.2971	0.2886	0.281	0.2734
CO_2 emissions saved (kg CO_2/kWh)	--	0.0028	0.0055	0.0083

Fuel saving at 3 MW of integrated solar power was 7.97%. Flowrates of gases, fuel, and air have changed, while thermodynamic states at the top gas cycle have remained constant. In "case E", ISCC efficiency rose from 56.13% to 59.79%. This configuration could avoid 8.3 g CO_2/kWh and generate 28.7 MJ per kg of fuel. However, compared to cases A, B, C and D, it could only integrate 3 MW of solar power. PTC could be a good choice for the solar technology, due to the low temperatures of stage (3_{new}).

Fuel saving operation reduced fuel consumption while keeping the total output power of the ISCC constant at 90.5 MW. The decrease in the power output of the gas cycle, from 64.2 to 59.1 MW, was balanced by the increase in the power output of the steam cycle from 26.2 to 31.4 MW as solar power increased from 0 to 3 MW.

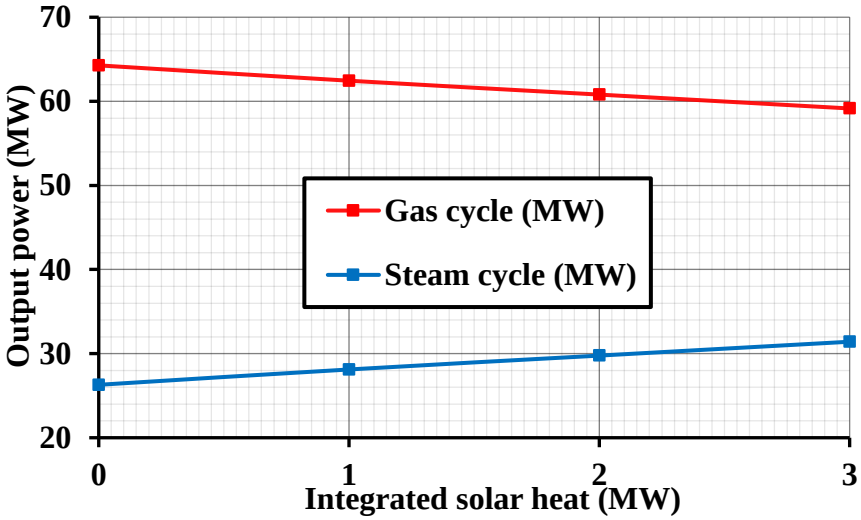

Figure 4.17 Gas & steam cycles output power at different integrated solar heat for case E

The integrated solar thermal power shifted the temperatures inside the HRSG upwards, modifying gas and steam flowrates. Figure 4.18 stresses the importance of controlling integrated solar power. For "case E", at 3.5 MW solar power, an overlap between gas and steam temperatures hints at the reversal of heat transfer inside the HRSG.

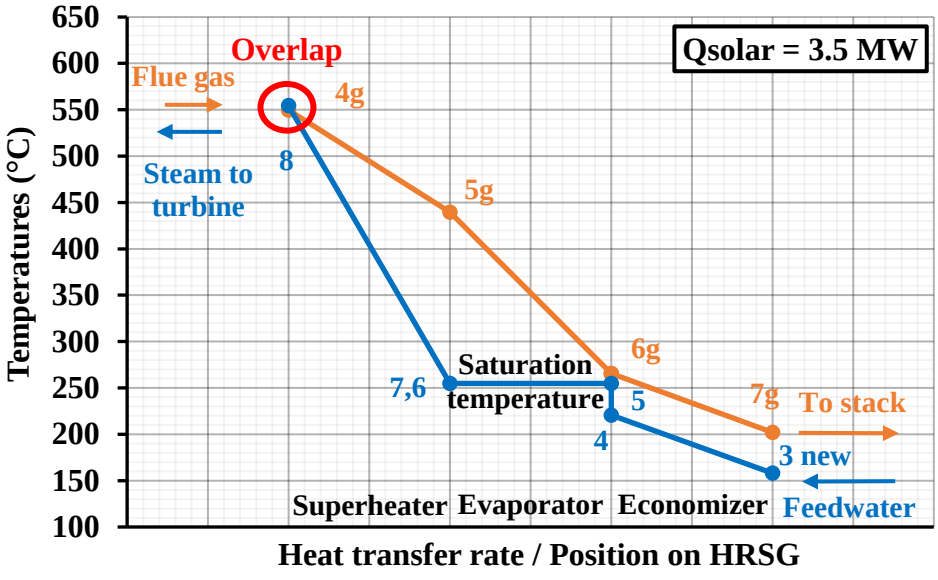

Figure 4.18 T-Q diagram for case E "Fuel saving" at Qsolar = 3.5 MW

Figure 4.19 presents the T-Q diagram inside the HRSG for cases D and E, where the effect of the integration position of the solar field may be observed.

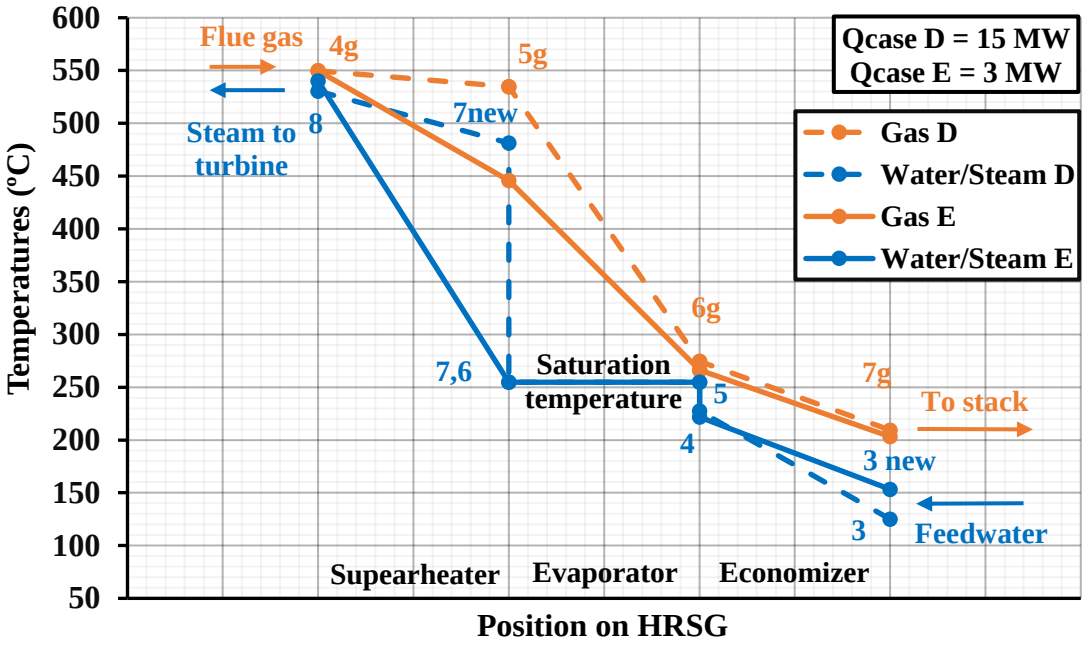

Figure 4.19 T-Q diagram for cases D & E "Fuel saving"

Finally, Figure 4.20 shows the better performance of of "case E" over "case D". For 3 MW of integrated solar heat, fuel saving is 7.97% and 0.65% respectively. For "case D". at 15 MW, fuel saving is only 3.49%. Energy efficiency of "case" E" is 59.79% while for "case D" it is only 53.06% at 15 MW of integrated solar thermal power.

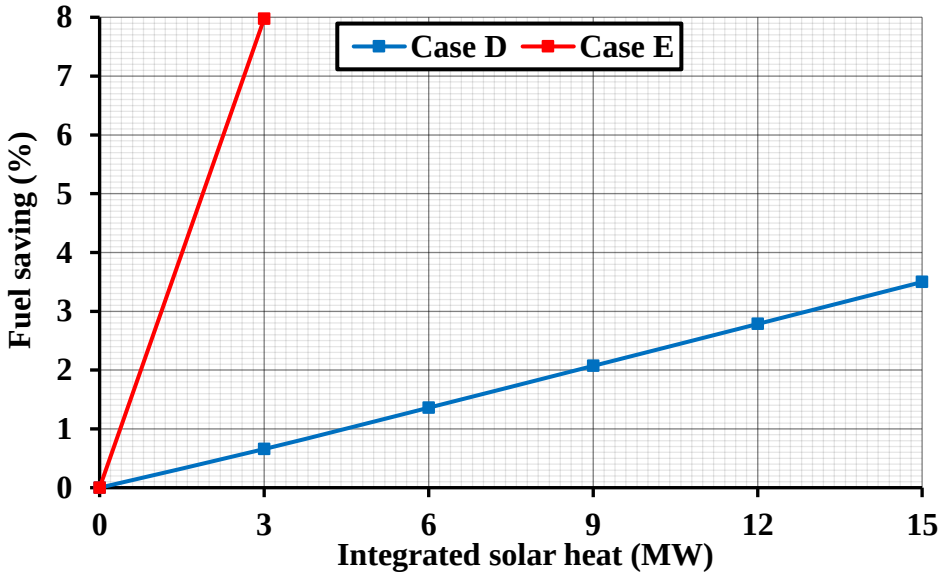

Figure 4.20 Fuel saved at different integrated solar heat for cases D & E

4.1.3 Fuel saving options summary

Fuel saving for cases B, C, D & E ("case A" is excluded from the comparison because it is not applicable to fuel saving strategy) are shown in Figure 4.21. The highest fuel savings could be achieved in "case E", 7.97%. Regarding the overall ISCC efficiency, as shown in Figure 4.2.., "case E" represents also the highest energy efficiency with

59.79% at 3 MW of integrated solar thermal power, while "case D" showed the lowest energy efficiency with 53.06% at 15 MW. "Cases B & C" shows no change in the original overall efficiency.

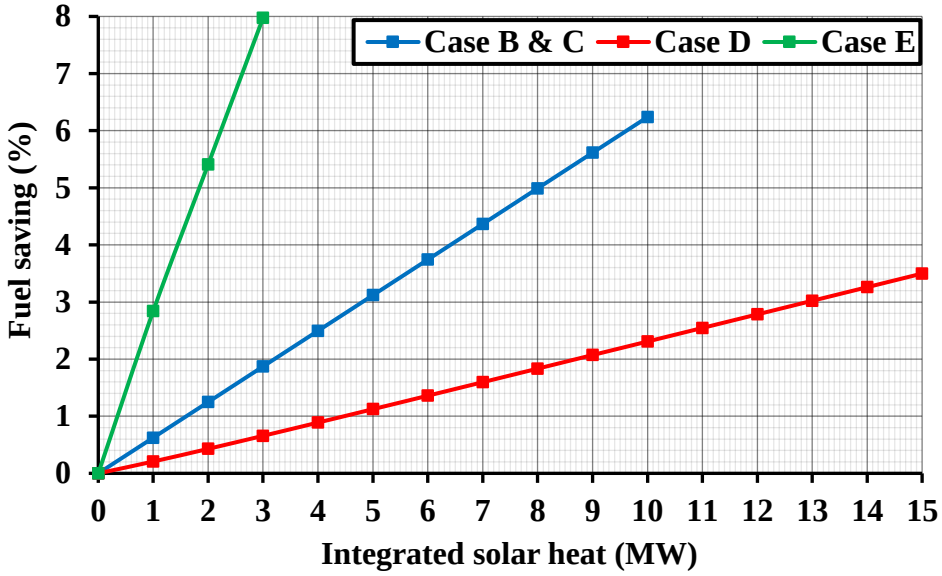

Figure 4.21 Fuel saved at different integrated solar heat integrated for cases B, C, D & E

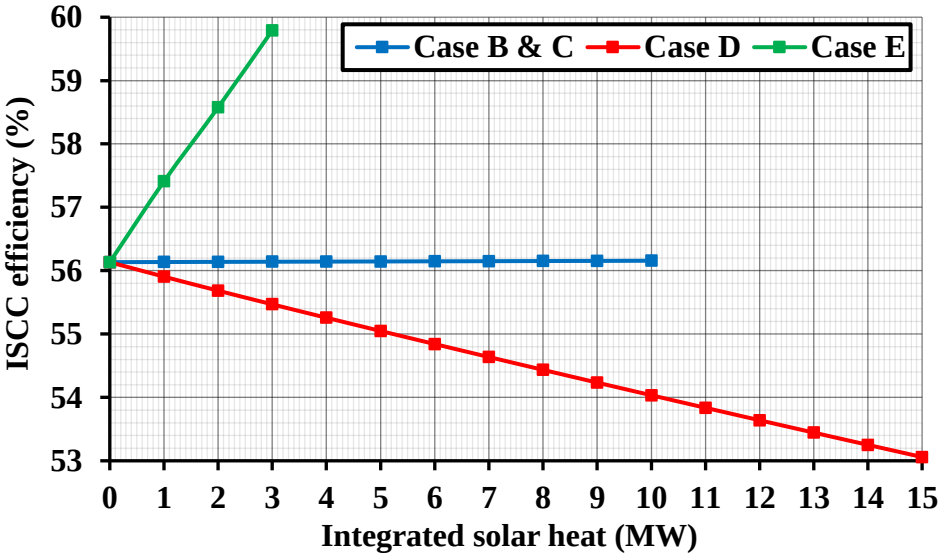

Figure 4.22 Overall efficiency at different integrated solar heat for cases B,C,D&E

Based on the results discussed, a summary for fuel saving configurations is provided:

- **"Case A: before compressor":** solar integration before the compressor increases compression work, reducing overall output power. It cannot be used for fuel saving.
- **"Case B: after compressor":** it is a viable option of solar integration, fuel saving could reach 6.23% at integrated solar heat of 10 MW. For the selection of the solar field, the optimum choice is either to use HTFs with high operating temperatures for the PTC, such molten salts, or to use heliostat fields or parabolic dish reflectors.
- **"Case C: after combustion chamber":** it is also a viable option. Due to the fixed gas turbine operating conditions, "case C" yielded results similar to "case

B", but the temperature values obtained at different cycle states changed. Compared to "case B", "case C" underperformed "case B" since solar field technology that should be utilized would be very challenging at the high operating temperature.

- **"Case D: at superheater":** considered a good option of solar field integration with a limit of 15 MW of solar heat. Fuel saving reaches a maximum of 3.49% with overall ISCC efficiency of 53.06%.
- **"Case E: at economizer":** it is the best option for fuel saving, where the fuel saved could be 7.97% at integrated solar heat of only 3 MW with an overall ISCC efficiency of 59.79%. It has the best environmental impact, with 8.3 g CO_2/kWh that may be avoided.

4.2 Power boosting

The power boosting strategy increases the plant output power thanks to the solar field while consuming fuel at the same rate. The same five integration positions studied for the fuel saving mode were studied for the power boosting mode, as shown in Figure 4.23. Cases F, G and H represent the gas cycle integration options, while cases I and J are the steam cycle integration schemes.

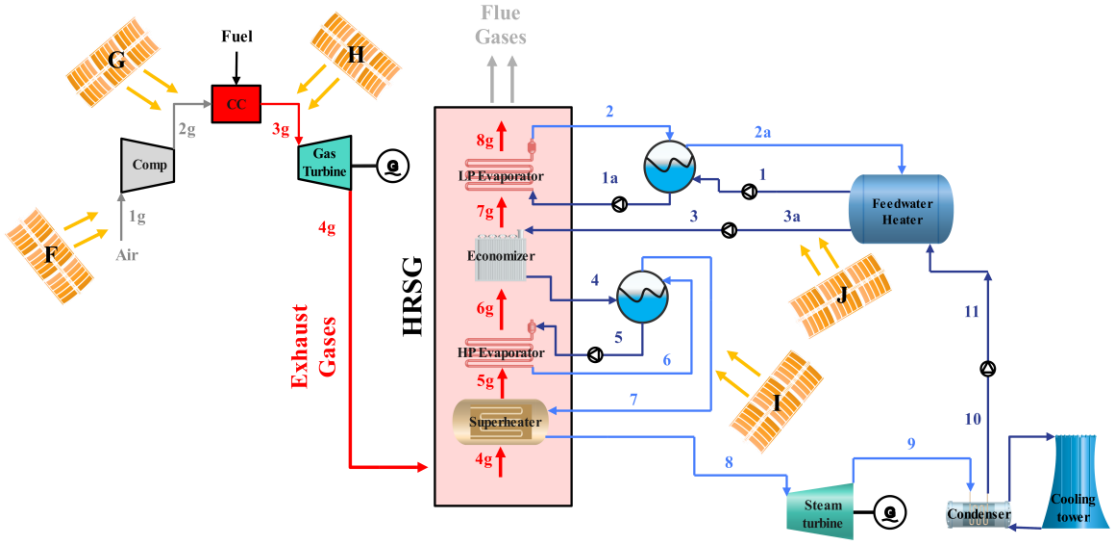

Figure 4.23 Solar field integration options for power boosting

The power boosting strategy for solar thermal power integration into the bottom steam cycle may be performed by flowrate boosting or parameter boosting. Both power boosting operating schemes will be studied for the two steam cycle integration positions, allowing to identify the optimum scenario for operating the ISCC.

4.2.1 Solar field integration at the top gas cycle

a. **Case F "Before air compressor":** ambient air is heated by solar field before entering the compressor.
b. **Case G "After compressor / Before combustion chamber":** compressed air is heated before entering the combustion chamber.
c. **Case H "After combustion chamber / Before gas turbine":** combustion chamber hot gases are heated up before entering the gas turbine.

4.2.1.1 Case F "Before air compressor"

In "case F", the solar field heats up the ambient air before entering the air compressor, as shown in Figure 4.24. Different integrated solar power values, 1, 2, 3, 4 and 5 MW were analyzed, as shown in Table 4.5.

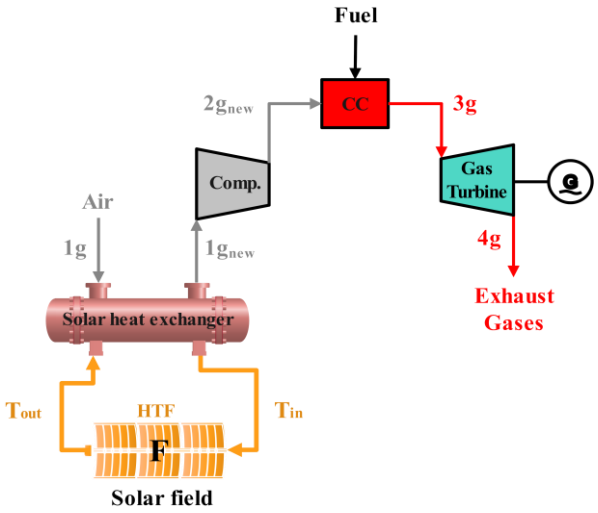

Figure 4.24 Case F: solar field integrated before air compressor for power boosting

Table 4.5 Original CC vs ISCC (case F) "Power boosting"

Mass flowrates	**Original CC**	**ISCC Case F**	**ISCC Case F**	**ISCC Case F**	**ISCC Case F**	**ISCC Case F**
Air to fuel ratio	50	50.71	51.43	52.14	52.85	53.57
Turbine gas flowrate (kg/s)	174.7	177.14	179.59	182.03	184.48	186.93
Air flowrate (kg/s)	171.27	173.72	176.16	178.61	181.05	183.5
Fuel flowrate (kg/s)	3.42					
LP evaporator mass flowrate (kg/s)	5					
HP evaporator mass flowrate (kg/s)	25					
Operating temperatures	**Original CC**	**ISCC Case F**	**ISCC Case F**	**ISCC Case F**	**ISCC Case F**	**ISCC Case F**
Compressor inlet (°C)	24	30	35	41	46	51
Combustion chamber inlet (°C)	378	391	402	414	425	435.5
Gas turbine inlet (°C)	1174					
Gas turbine outlet (°C)	549					
Solar heat integration	**Original CC**	**ISCC Case F**	**ISCC Case F**	**ISCC Case F**	**ISCC Case F**	**ISCC Case F**
Integrated solar heat (MW)	--	1	2	3	4	5
Cycle efficiency	**Original CC**	**ISCC Case F**	**ISCC Case F**	**ISCC Case F**	**ISCC Case F**	**ISCC Case F**
Gas turbine cycle (%)	39.84	39.38	38.93	38.48	38.04	37.6
Combined cycle (%)	56.13	55.58	55.03	54.49	53.96	53.43
Cycle power breakdown	**Original CC**	**ISCC Case F**	**ISCC Case F**	**ISCC Case F**	**ISCC Case F**	**ISCC Case F**
Compressor (kW)	62,450	64,569	66,688	68,806	70,925	73,044
Gas turbine (kW)	126,727	128,501	130,275	132,049	133,823	135,597
Gas cycle (kW)	64,277	63,932	63,588	63,243	62,899	62,553
Steam cycle (kW)	26,292	26,301	26,308	26,314	26,320	26,328
Total net power (kW)	90,569	90,023	89,895	89,557	89,219	88,883
Power boosted (%)	--	-0.37	-0.74	-1.11	-1.49	-1.86
Back work ratio (%)	49.28	50.24	51.19	52.1	53	53.86
Specific work per unit fuel mass (kJ/kg)	26,439	26,342	26,243	26,144	26,045	25,947

The results from Table 4.5 show that integrating a solar field to heat the ambient air before compression increases the compressor power. Air and gas flowrates increase as solar thermal power is being integrated to boost power generation. The gas turbine output power increases as well with solar power integrated, as shown in Figure 4.25, but the overall output power of the gas cycle will decrease because the increase in the compressor power is higher. On the other hand, the steam cycle output power increased as the exhaust flowrate increased. However, the ISCC output power because the loss of power in the gas cycle could not be balanced by the increase in the steam cycle power. Compressor power increased from 62.4 to 73 MW and gas turbine power increased from 126.7 to 135.59 MW when the integrated solar thermal power increased from 0 to 5 MW. Consequently, the gas cycle output power decreased from 64.2 to 62.5 MW as solar power increased from 0 to 5 MW.

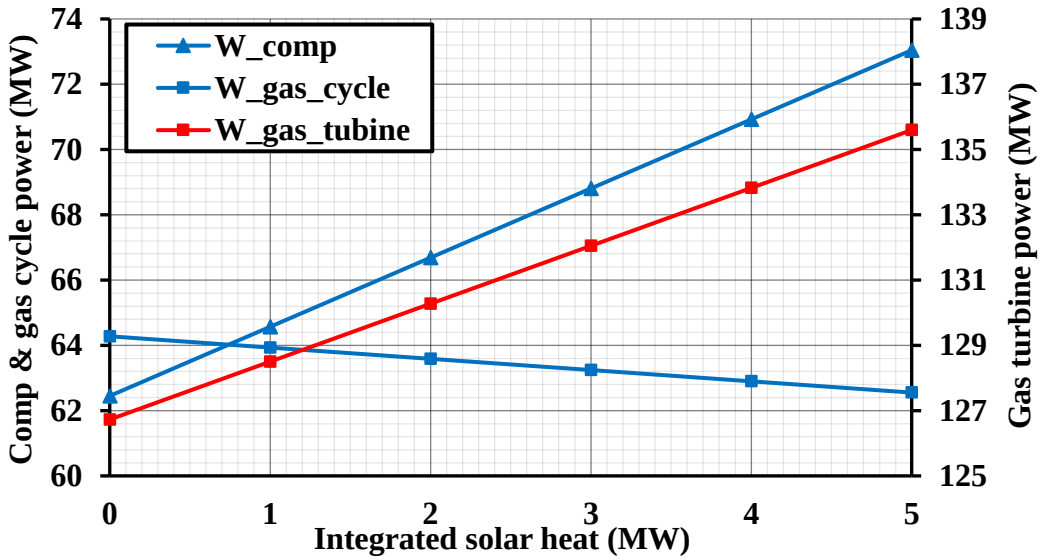

Figure 4.25 Compressor, gas turbine and gas cycle power output at different integrated solar heat for case F

The gas cycle and ISCC efficiency values decreased by 2.24% and 27% respectively as the integrated solar thermal power increased from 0 to 5 MW, as shown in Figure 4.26.

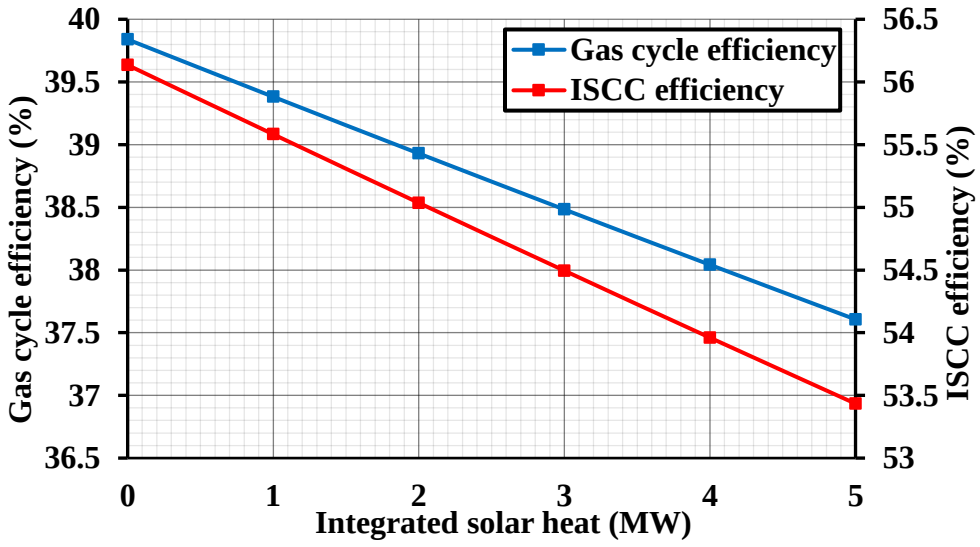

Figure 4.26 Gas cycle & ISCC overall efficiencies at different integrated solar heat for case F

Overall output power decreased linearly with integrated solar power, proving that it is not possible to boost power with this configuration. Figure 4.27 shows this relationship, where output power decreased by 1.86% at 5 MW of integrated solar power.

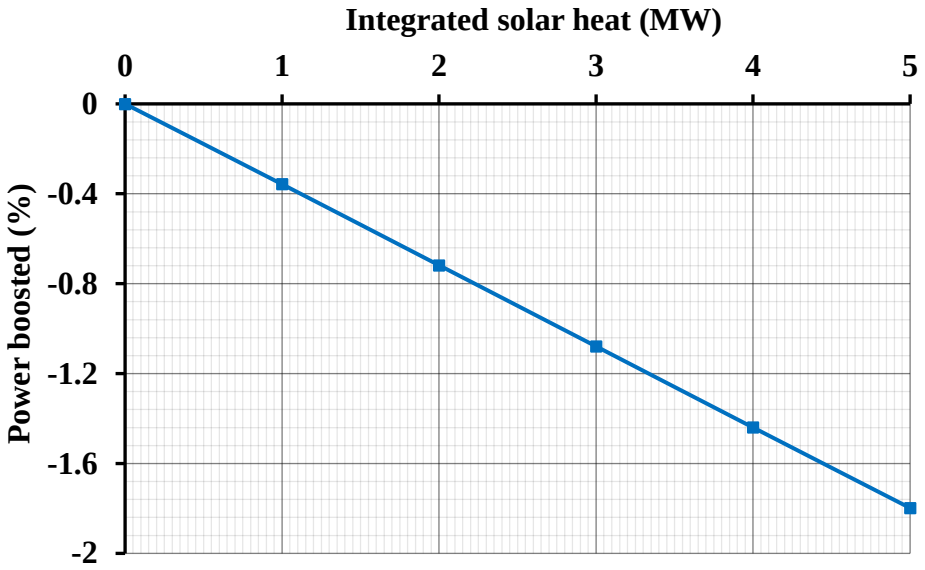

Figure 4.27 Power boosted at different integrated solar heat integrated for case F

4.2.1.2 Case G "After air compressor"

When the solar field is integrated after the air compressor (before the combustion chamber), as shown in Figure 4.28, compressed air is heated up by the integrated solar power added to the cycle. The preheated compressed air is then mixed with fuel and burns in the combustion chamber to generate hot gases to power the gas turbine.

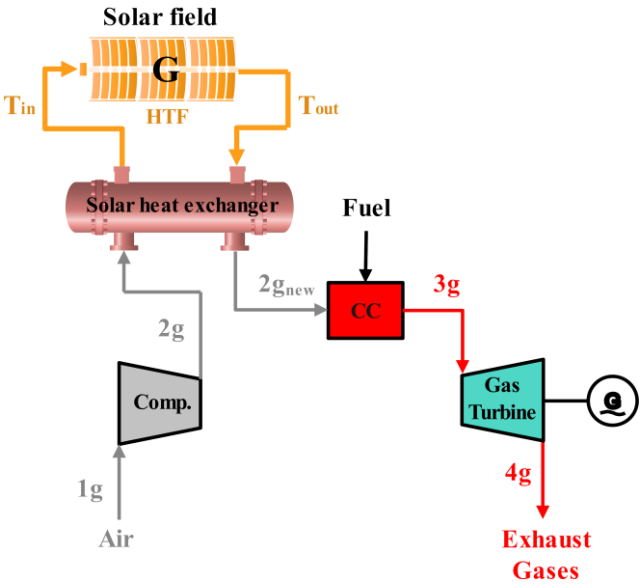

Figure 4.28 Case G: solar field integrated after air compressor for power boosting

For this solar integration option, results were analyzed at integrated solar power values from 2 to 10 MW in 2 M increments, as shown in Table 4.6. A linear increase in the

combustion chamber inlet temperature from 378 to 430ºC was found as integrated solar heat rose from 0 to 10 MW.

Table 4.6 Original CC vs ISCC (case G) "Power boosting"

Mass flowrates	**Original CC**	**ISCC Case G**	**ISCC Case G**	**ISCC Case G**	**ISCC Case G**	**ISCC Case G**
Air to fuel ratio	50	50.64	51.28	51.92	52.56	53.2
Turbine gas flowrate (kg/s)	174.7	176.89	179.09	181.29	183.48	185.68
Air flowrate (kg/s)	171.27	173.47	175.66	177.86	180.06	182.25
Fuel flowrate (kg/s)	3.42					
LP evaporator mass flowrate (kg/s)	5					
HP evaporator mass flowrate (kg/s)	25					
Operating temperatures	**Original CC**	**ISCC Case G**	**ISCC Case G**	**ISCC Case G**	**ISCC Case G**	**ISCC Case G**
Compressor inlet (°C)	24					
Combustion chamber inlet (°C)	378	389.5	400	410.5	420.5	430
Gas turbine inlet (°C)	1174					
Gas turbine outlet (°C)	549					
Solar heat integration	**Original CC**	**ISCC Case G**	**ISCC Case G**	**ISCC Case G**	**ISCC Case G**	**ISCC Case G**
Integrated solar heat (MW)	--	2	4	6	8	10
Cycle efficiency	**Original CC**	**ISCC Case G**	**ISCC Case G**	**ISCC Case G**	**ISCC Case G**	**ISCC Case G**
Gas turbine cycle (%)	39.84	39.83	39.83	39.83	39.83	39.83
Combined cycle (%)	56.13	55.94	55.74	55.55	55.37	55.19
Cycle power breakdown	**Original CC**	**ISCC Case G**	**ISCC Case G**	**ISCC Case G**	**ISCC Case G**	**ISCC Case G**
Compressor (kW)	62,450	63,251	64,052	64,853	65,654	66,455
Gas turbine (kW)	126,727	128,320	129,913	131,507	133,100	134,693
Gas cycle (kW)	64,277	65,069	65,862	66,654	67,447	68,239
Steam cycle (kW)	26,292	26,300	26,306	26,312	26,318	26,323
Total net power (kW)	90,569	91,370	92,168	92,966	93,764	94,562
Power boosted (%)	--	0.88	1.76	2.64	3.53	4.41
Back work ratio (%)	49.279	49.291	49.303	49.315	49.326	49.33
Specific work per unit fuel mass (kJ/kg)	26,439	26,673	26,907	27,139	27,372	27,605

Consequently, overall ISSC power increased from 90.5 MW to 94.5 MW at 10 MW of integrated solar heat, as shown in Figure 4.29.

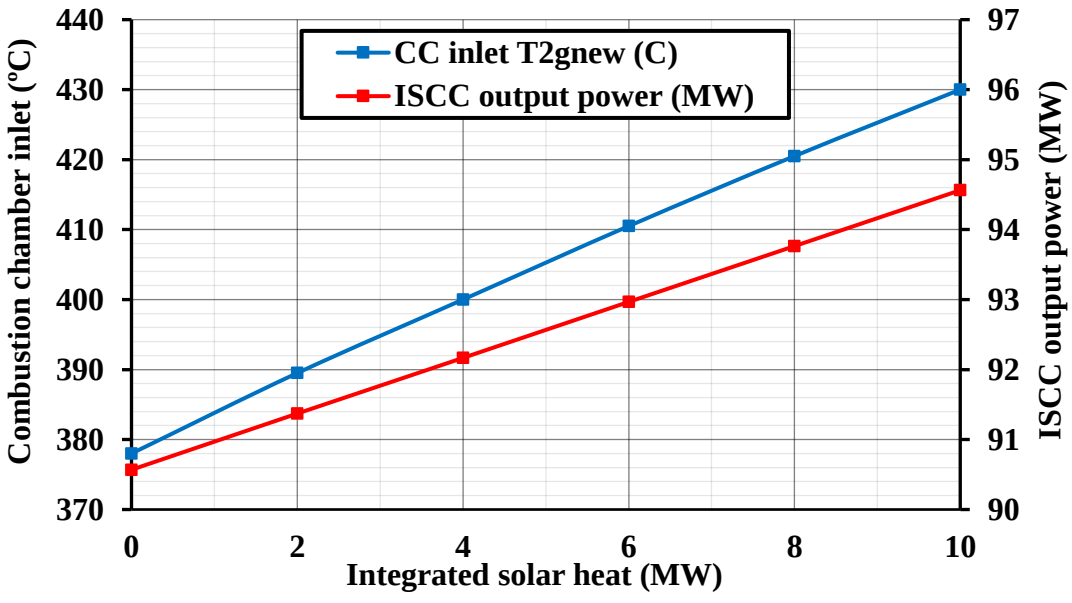

Figure 4.29 Combustion chamber inlet & ISCC output power at different integrated solar heat for case G

In "case G", output power could be boosted by 4 MW (a 4.41% increase) by integrating 10 MW of solar thermal power, as shown in Figure 4.30.

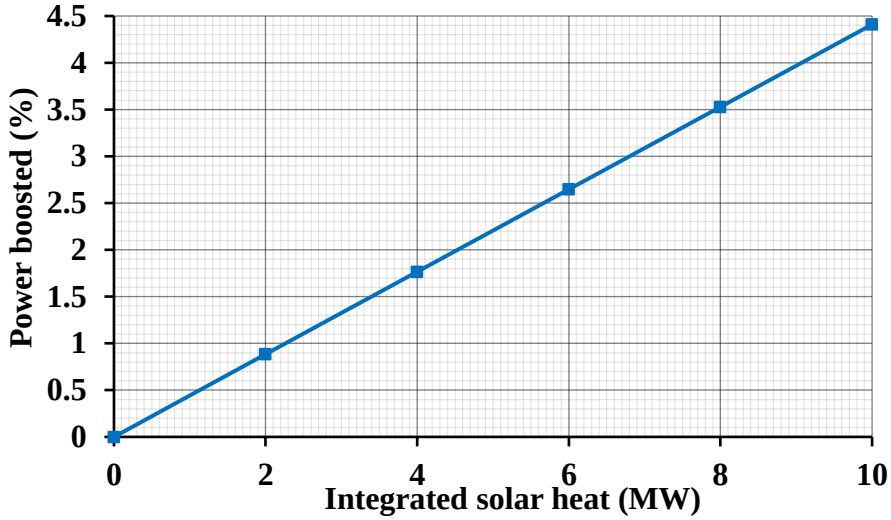

Figure 4.30 Power boosted at different integrated solar heat for case G

Regarding energy efficiency, gas cycle and overall ISCC efficiencies experienced very little change, with the gas cycle efficiency almost constant. Overall ISCC efficiency dropped 0.94%, as depicted in Figure 4.31. With the same fuel consumption, specific work per fuel unit mass increased to 27.6 MJ/kg, as shown in Table 4.6. However, the back work ratio increased slightly to 49.33%, due to the higher air-fuel ratio.

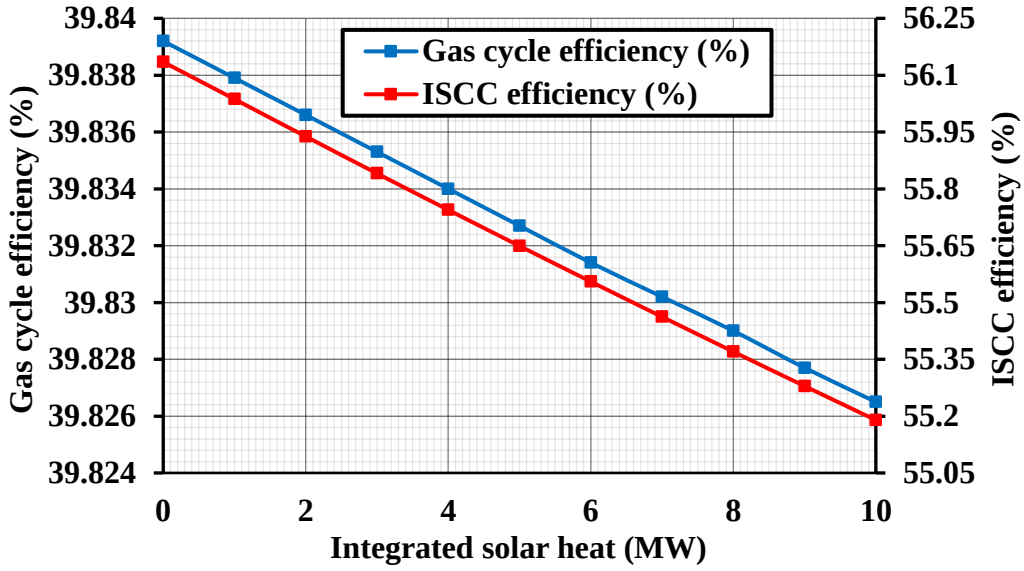

Figure 4.31 Gas cycle & ISCC efficiencies (%) at different integrated solar heat for case G

The selection of the solar field technology for "case G" could be PTC with molten salts (high operating temperatures that could be up to 550 °C [190]), as the temperature would reach 430 ºC at state ($2g_{new}$). Other technologies with a wider temperature range,

such as Parabolic dish reflectors (PDR) or Heliostat field collectors could be used as well.

4.2.1.3 Case H "After combustion chamber"

In this integration option, the solar field is integrated in the gas cycle after the combustion chamber stage (before the gas turbine), as shown in Figure 4.32. Hot gases mixed with fuel and burnt in the combustion chamber pass through the solar collector to be heated before entering the gas turbine.

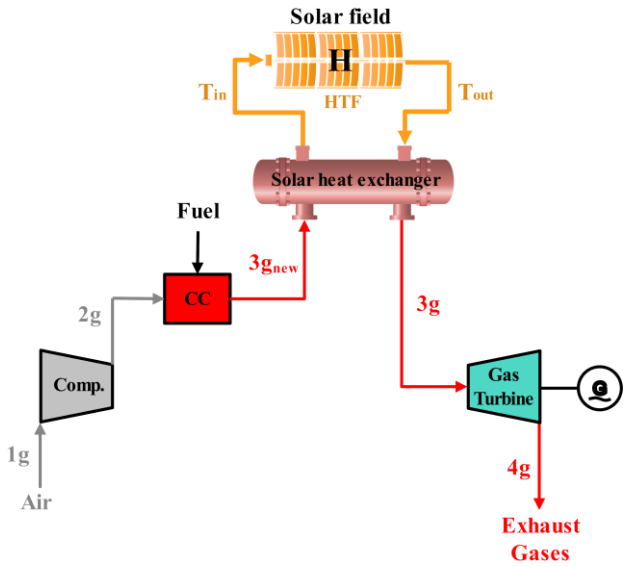

Figure 4.32 Case H: Solar field integrated after combustion chamber for power boosting

Since operating conditions at the gas turbine inlet and outlet are kept constant, similar results as "case G" were obtained. However, different temperatures for the intermediate states were observed. The integrated solar thermal power before the gas turbine reduced the temperature of state ($3g_{new}$) by increasing the hot gases flowrate, in order to keep the inlet conditions of the turbine constant. The combustion chamber outlet temperature ($T3g_{new}$) and hot exhaust gases flowrate as a function of the integrated solar power are presented in Figure 4.33.

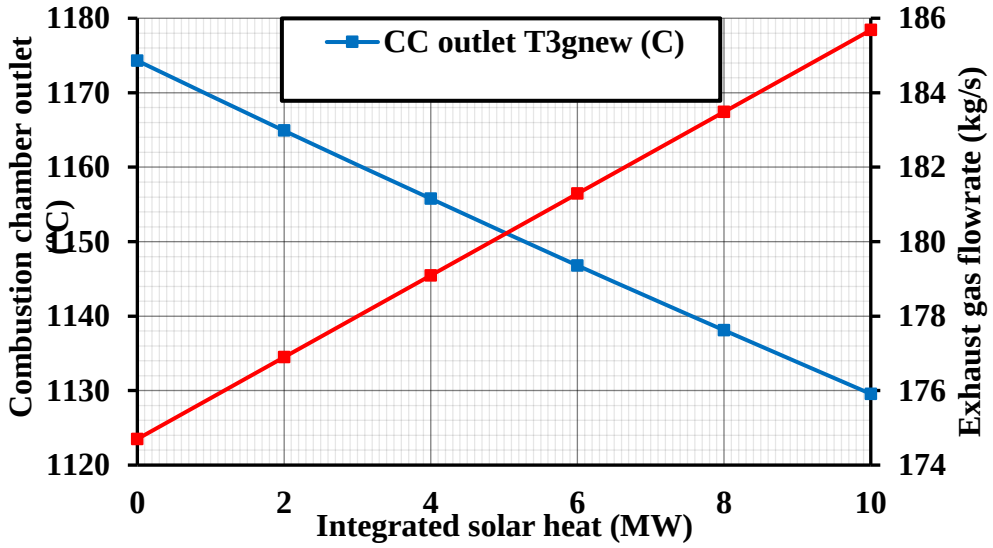

Figure 4.33 Solar HX inlet & exhaust gases flowrate at different integrated solar heat for case H

The combustion chamber outlet temperature ($T3_{gnew}$) falls linearly from 1174°C to 1129°C as the integrated solar thermal power increases from 0 to 10 MW. On the other, the exhaust gases mass flowrate increases linearly from 174.7 kg/s to 185.7 kg/s, indicating a direct link. In this configuration, operating temperatures at state ($3g_{new}$) are 1174-1129°C, only heliostat technology could be used.

4.2.2 Solar field integration at the bottom steam cycle

Solar power might be incorporated into the bottom steam cycle, leaving the top Brayton cycle unaffected. The operating fluid (water/steam) mass flowrate and thermodynamic states increase thanks to the integrated solar power, boosting the steam cycle output power and consequently the ISCC overall output power. Power boosting operating strategies were examined for the integration positions at the steam cycle (before the superheater and before the economizer).

4.2.2.1 Flowrate boosting mode

Operating conditions of the bottom steam cycle were kept constant while the flowrate of steam was increased.

a) Case I "Integration at superheater"

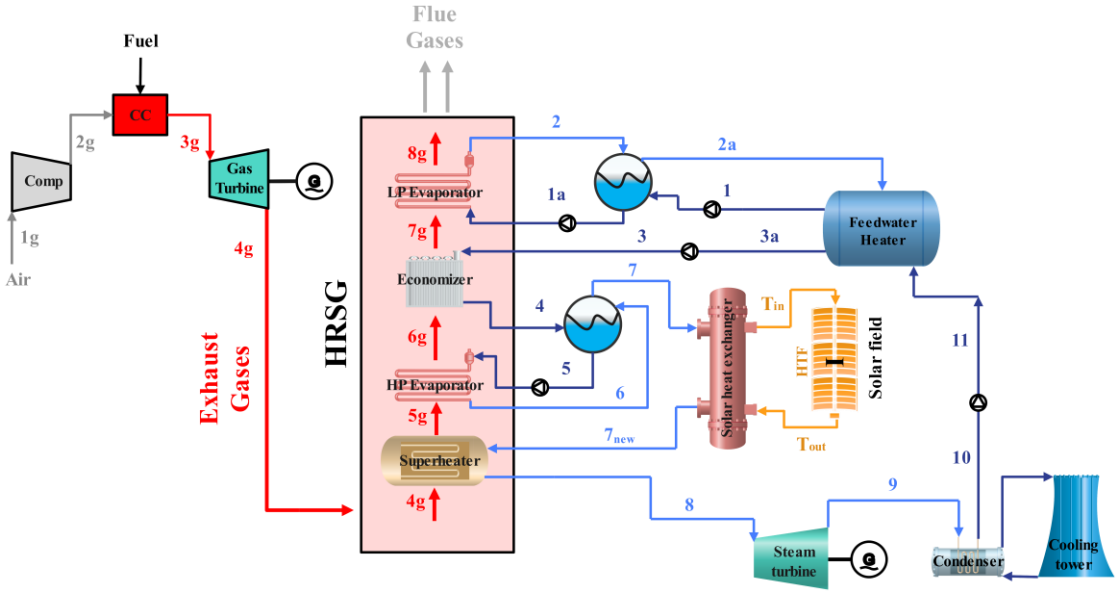

Figure 4.34 Case I: solar field integrated at superheater for power boosting

The results of "case I: flowrate" are discussed based on an integrated solar heat of 4 MW, the maximum amount of thermal solar power that could be integrated before the superheater stage without causing heat transfer reversal inside the HRSG. The temperature evolution within the HRSG is presented in Figure 4.35.

As collected in Table 4.7, the steam flowrate increased by 20.8 kg/s over the original value at an integrated solar thermal power of 4 MW, reaching 45.8 kg/s. The LP flowrate also increases by 4.17 kg/s reaching 9.17 kg/s, as shown in Figure 4.37. This increase is a consequence of integrating solar thermal power without changing the thermodynamic states of the cycle.

Table 4.7 Original CC vs ISCC (case I) "Flowrate boosting"

Mass flowrates	**Original CC**	**ISCC Case I**	**ISCC Case I**	**ISCC Case I**	**ISCC Case I**
Air to fuel ratio	50				
Turbine gas flowrate (kg/s)	174.7				
Air flowrate (kg/s)	171.27				
Fuel flowrate (kg/s)	3.42				
LP evaporator mass flowrate (kg/s)	5	5.79	6.72	7.83	9.17
HP evaporator mass flowrate (kg/s)	25	28.97	33.62	39.15	45.84
Operating temperatures	**Original CC**	**ISCC Case I**	**ISCC Case I**	**ISCC Case I**	**ISCC Case I**
Compressor inlet (°C)	24				
Combustion chamber inlet (°C)	379				
Gas turbine inlet (°C)	1174				
Gas turbine outlet (°C)	549				
Inlet steam temperature (°C)	457	444	432.5	423.5	416.5
Pinch temperature (°C)	17.5	17.3	17.2	17.2	17.3
Economizer outlet temperature (°C)	228	218	209.5	201	192.5
Approach temperature (°C)	28	36.5	45	54	62
Operating pressures	**Original CC**	**ISCC Case I**	**ISCC Case I**	**ISCC Case I**	**ISCC Case I**
Inlet steam pressure (bar)	43				
LP evaporator pressure (bar)	2.4				
Condenser pressure (bar)	0.08				

Solar heat integration	Original CC	ISCC Case I	ISCC Case I	ISCC Case I	ISCC Case I
Integrated solar heat (MW)	--	1	2	3	4
Cycle efficiency	**Original CC**	**ISCC Case I**	**ISCC Case I**	**ISCC Case I**	**ISCC Case I**
Gas turbine cycle (%)	39.84				
Combined cycle (%)	56.13	58.36	61	64.17	68.03
Cycle power breakdown	**Original CC**	**ISCC Case I**	**ISCC Case I**	**ISCC Case I**	**ISCC Case I**
Compressor (kW)	62,450				
Gas turbine (kW)	126,727				
Gas cycle (kW)	64,277				
Steam cycle (kW)	29,292	30,469	35,364	41,183	48,214
Total net power (kW)	90,569	94,746	99,641	105,459	112,491
Power boosted (%)	--	4.61	10.01	16.44	24.2
Back work ratio (%)	49.279				
Specific work per unit fuel mass (kJ/kg)	26,439	27,659	29,088	30,787	32,840

In this configuration, it was found that the ISCC boosted power as directly proportional to the integrated solar thermal power, with overall output power increasing from 90.5 to 112.5 MW (~24.2% power boosting) as the integrated solar power increased from 0 to 4 MW, as shown in Figure 4.36.

Although the gas cycle output power and energy efficiency were constant, the ISCC energy efficiency increased by 11.9% with respect to the original CC. A total work of 32.8 MJ per unit fuel mass was found, 6.4 MJ higher than for the original CC, as depicted in Figure 4.38. State (7_{new}) reached a temperature slightly over 300°C, PTC with synthetic oil as HTF would be a suitable selection for the solar field technology.

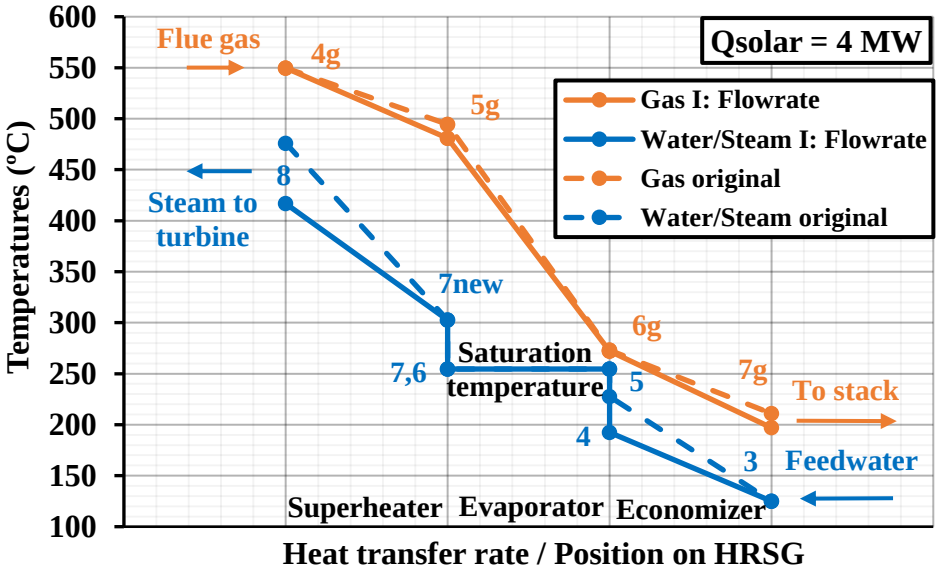

Figure 4.35 T-Q diagram for case I "Flowrate boosting" at Qsolar = 4 MW

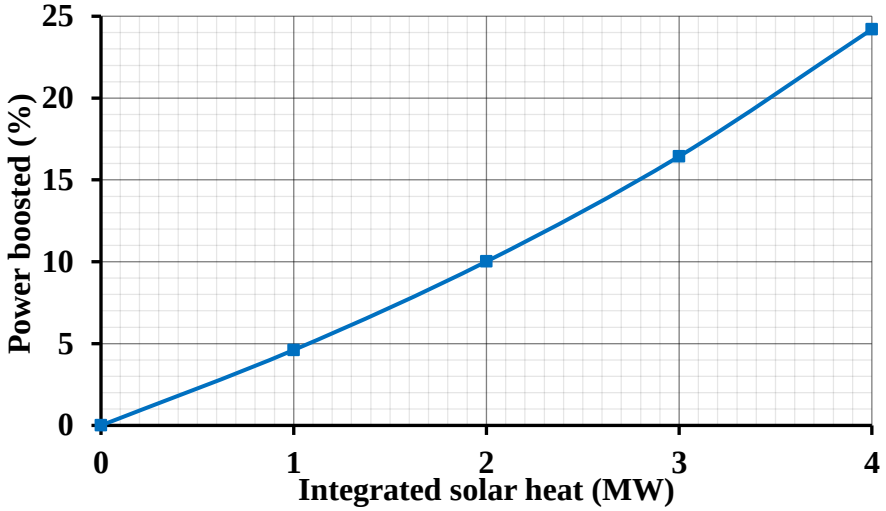

Figure 4.36 Flowrate power boosted at different integrated solar heat for case I

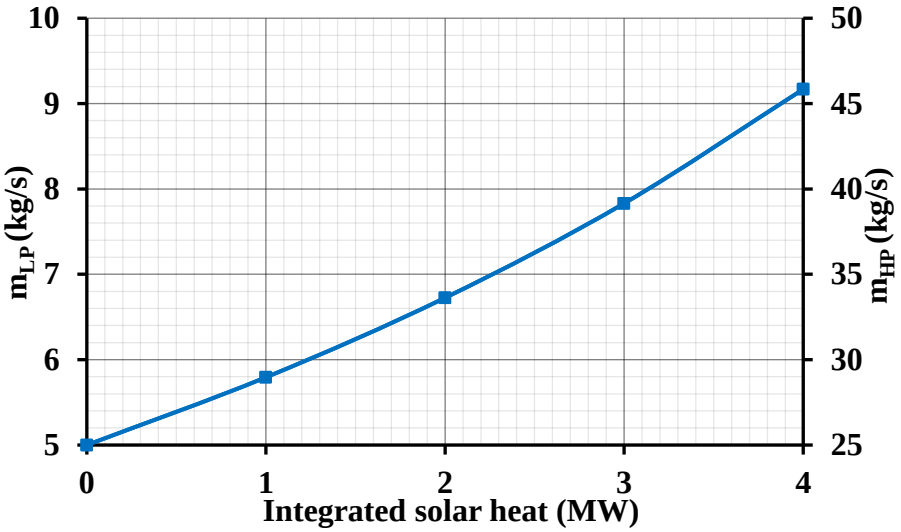

Figure 4.37 Mass flowrates at different integrated solar heat for case I: Flowrate

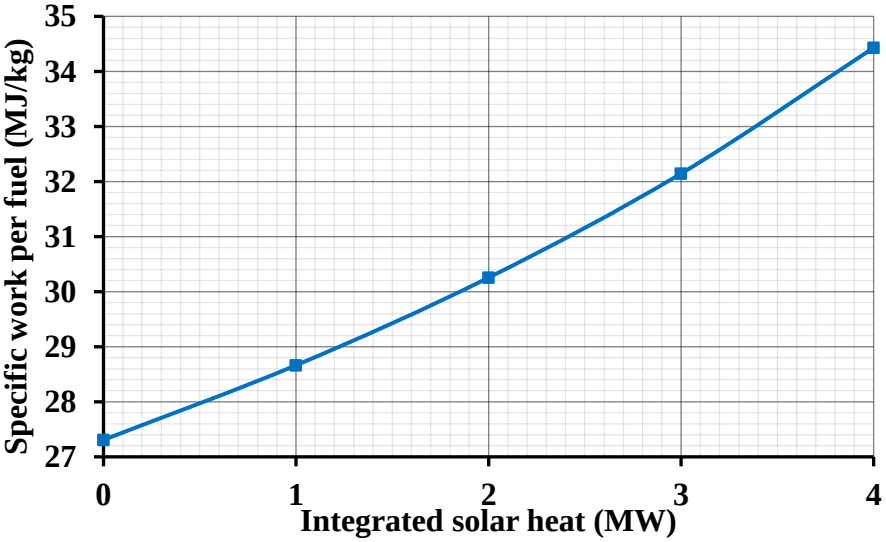

Figure 4.38 Specific work per unit fuel mass at different integrated solar heat for case I: Flowrate

b) Case J "Integration at economizer"

In "case J", the solar field was integrated into the bottom steam cycle before the economizer stage to preheat feedwater temperature, as shown in Figure 4.39.

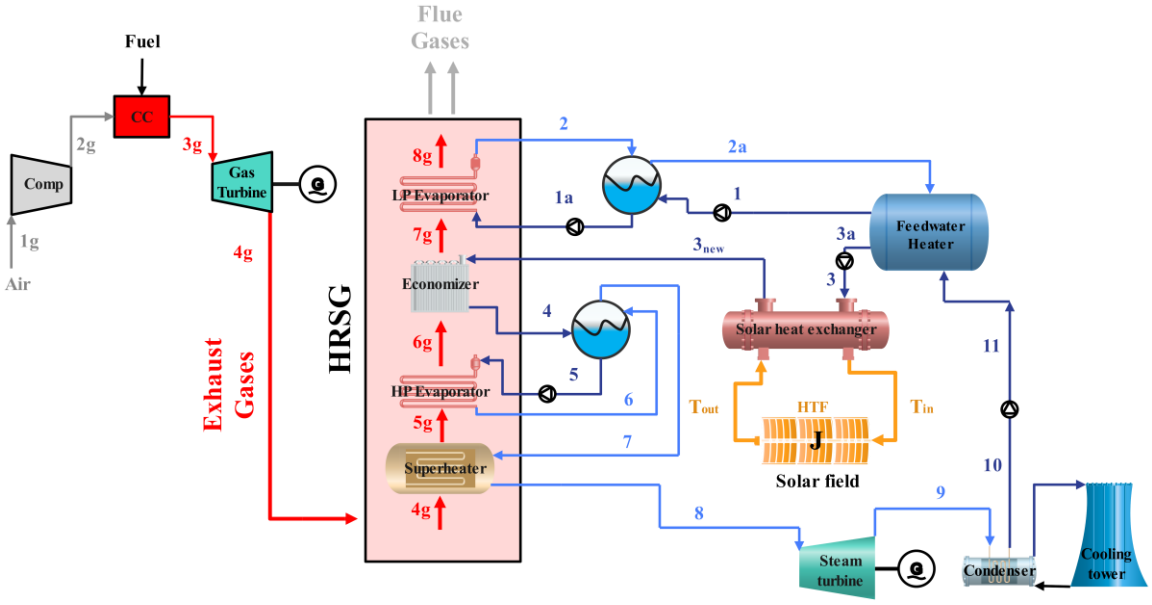

Figure 4.39 Case J: solar field integrated at economizer for power boosting

It was found that the maximum possible integrated solar thermal power should not exceed 12 MW to avoid heat transfer reversal inside the HRSG. The temperature evolution inside the HRSG is shown in Figure 4.40. As the solar power is integrated into the economizer stage, water and gas lines are brought closer. Table 4.8 displays the results for this configuration for integrated solar power values from 0 to 12 MW in 3 MW increments.

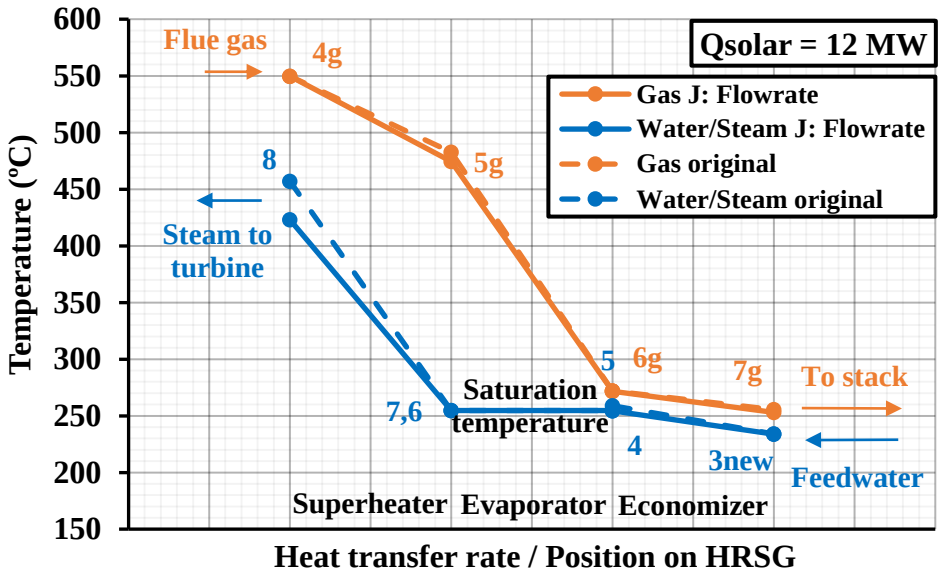

Figure 4.40 T-Q diagram for case J "Flowrate boosting" at Qsolar = 12 MW

Table 4.8 Original CC vs ISCC (case J) "Flowrate boosting"

Mass flowrates	**Original CC**	**ISCC Case J**	**ISCC Case J**	**ISCC Case J**	**ISCC Case J**
Air to fuel ratio (kg/s)	50				
Turbine gas flowrate (kg/s)	174.7				
Air flowrate (kg/s)	171.27				
Fuel flowrate (kg/s)	3.42				
LP evaporator mass flowrate (kg/s)	5	5.38	5.77	6.16	6.54
JHP evaporator mass flowrate (kg/s)	25	26.93	28.86	30.79	32.72
Operating temperatures	**Original CC**	**ISCC Case J**	**ISCC Case J**	**ISCC Case J**	**ISCC Case J**
Compressor inlet (°C)	24				
Combustion chamber inlet (°C)	379				
Gas turbine inlet (°C)	1174				
Gas turbine outlet (°C)	549				
Inlet steam temperature (°C)	457	477.5	439	430.5	423
Pinch temperature (°C)	17.5	17.3	17.5	17	16.8
Economizer outlet temperature (°C)	228	231	237	245	254.5
Approach temperature (°C)	28	23.69	17.5	9.5	0.5
Operating pressures	**Original CC**	**ISCC Case J**	**ISCC Case J**	**ISCC Case J**	**ISCC Case J**
Inlet steam pressure (bar)	43				
LP evaporator pressure (bar)	2.4				
Condenser pressure (bar)	0.08				
Solar heat integration	**Original CC**	**ISCC Case J**	**ISCC Case J**	**ISCC Case J**	**ISCC Case J**
Integrated solar heat (MW)	--	3	6	9	12
Cycle efficiency	**Original CC**	**ISCC Case J**	**ISCC Case J**	**ISCC Case J**	**ISCC Case J**
Gas turbine cycle (%)	39.84				
Combined cycle (%)	56.13	56.34	56.55	56.74	56.93
Cycle power breakdown	**Original CC**	**ISCC Case J**	**ISCC Case J**	**ISCC Case J**	**ISCC Case J**
Compressor (kW)	62,450				
Gas turbine (kW)	126,727				
Gas cycle (kW)	64,277				
Steam cycle (kW)	26,292	28,322	30,352	32,382	34,412
Total net power (kW)	90,569	92,599	94,629	96,659	98,689
Power boosted (%)	--	2.24	4.48	6.72	8.96
Back work ratio (%)	49.279				
Specific work per unit fuel mass (kJ/kg)	26,439	27,032	27,625	28,218	28,810

The overall output increased from 90.5 to 98.6 MW (8.96% boost) when solar heat increased from 0 to 12 MW, as shown in Figure 4.41.

At 12 MW of integrated solar power, the HP steam flowrate increased from 25 to 32.7 kg/s, while the LP flowrate increased from 5 to 6.5 kg/s, as shown in Figure 4.42. Both flowrates showed this increasing trend with the addition of solar power. Compared to the original CC, the ISCC total energy efficiency was improved by 0.8%. The specific work per unit fuel mass of 28.81 MJ per fuel unit mass, or 2.37 MJ greater than the original CC as shown in Figure 4.43. Selecting the solar field technology is much easier by integrating the solar field at low temperature stages (economizers) rather than to high temperature stages. In this instance, PTCs would match the low operating temperature range.

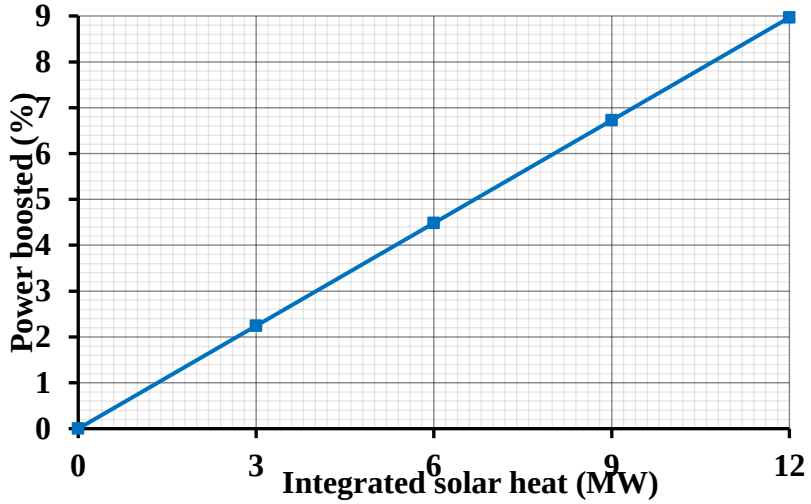

Figure 4.41 Flowrate power boosted at different integrated solar heat for case J

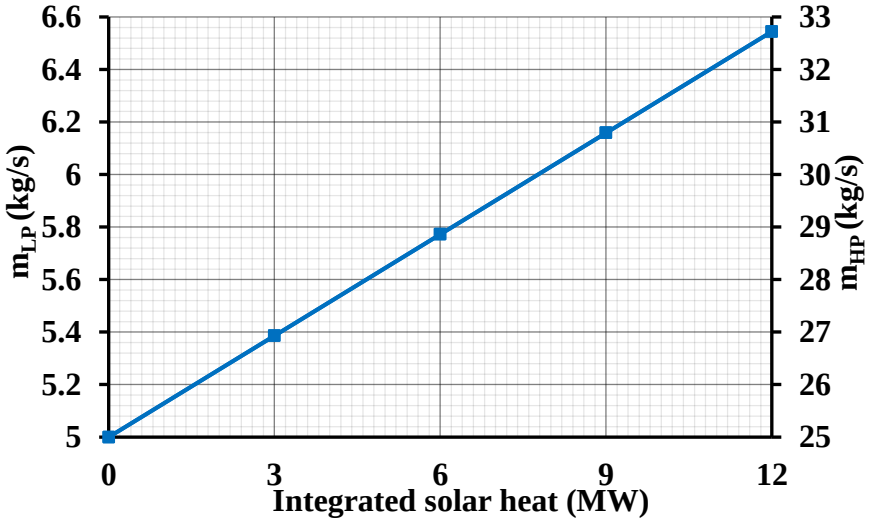

Figure 4.42 Mass flowrates at different integrated solar heat for case J: Flowrate

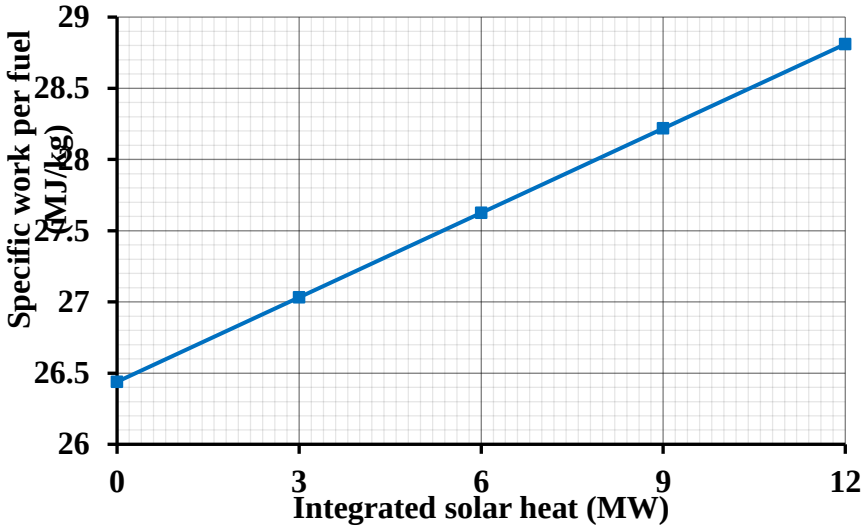

Figure 4.43 Specific work per unit fuel mass at different integrated solar heat for case J: Flowrate

In Figure 4.44, the power boosted by flowrate for the steam cycle integration configurations is presented as a function of the integrated solar thermal power. Despite the limitation for the integrated solar thermal power of 4 MW and 12 MW for case I and J respectively, case I can almost provide a 24.2% boost, almost three times the 8.96% boost of case J.

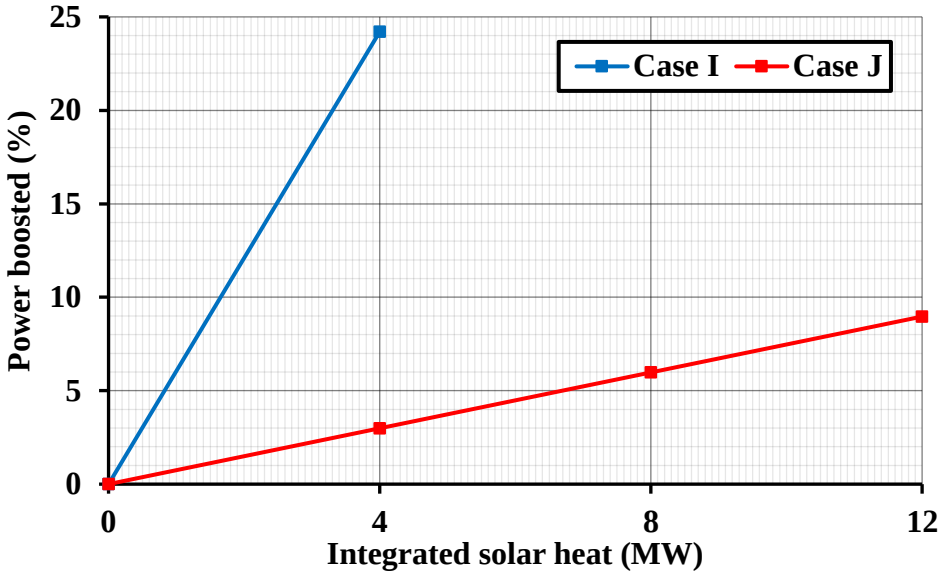

Figure 4.44 Flowrate power boosted for steam cycle integration configurations

4.2.2.2 Parameter boosting mode

The parameter boosting operating mode keeps steam flowrate constant while increasing its thermodynamic properties (temperature, pressure, etc.) when solar thermal power is available. The top Brayton cycle remains unaffected.

a) Case I "Integration at superheater"

Considering the same configuration of Figure 4.34, solar thermal power is integrated before the superheater. A range of operating pressure values from -50% to +50% of the original value in 10% increments were studied. The results are presented in Tables 4.9 and 4.10.

The maximum allowable integrated solar thermal power varies from case to another, increasing with the working pressure. The maximum limit is 9 MW of integrated solar thermal power at +50% of the original pressure, while the minimum is 7 MW at -50% of the pressure. Therefore, a value of 7 MW was selected to compare the results of the performance of all scenarios studied. The integration of solar power can increase power by itself independently of the operating pressure, but, as shown in Figure 4.45, the cases in which the working pressure was reduced are superior to the cases where the the working pressure was increased. Power was boosted by 2.82% for the -50% case, compared to a value of 1.37% for the +50% case. In all cases, PTC solar filed technology with synthetic oil can match the solar heat exchanger required temperatures.

Table 4.9 ISCC vs Parameter boosting "case I" (+10%,+20%,+30%,+40% & +50%)

Mass flowrates	**Original ISCC**	**ISCC "case I" (Superheater)**				
		+10%	**+20%**	**+30%**	**+40%**	**+50%**
Air to fuel ratio	50					
Turbine gas flowrate (kg/s)	174.7					
Air flowrate (kg/s)	171.27					
Fuel flowrate (kg/s)	3.42					
LP evaporator mass flowrate (kg/s)	5					
HP evaporator mass flowrate (kg/s)	25					
Operating temperatures	**Original ISCC**	**+10%**	**+20%**	**+30%**	**+40%**	**+50%**
Compressor inlet (°C)	24					
Combustion chamber inlet (°C)	379					
Gas turbine inlet (°C)	1174					
Gas turbine outlet (°C)	549					
Inlet steam temperature (°C)	491	491	490.5	490.5	490	489.5
Pinch temperature (°C)	19.3	19	18.5	18.2	17.9	17.5
Economizer outlet temperature (°C)	228	232.5	237	241	244.5	48
Approach temperature (°C)	26.5	27.5	29	30	31	32
Operating pressures	**Original ISCC**	**+10%**	**+20%**	**+30%**	**+40%**	**+50%**
Inlet steam pressure (bar)	2.4	2.64	2.88	3.12	3.36	3.6
LP evaporator pressure (bar)	43	47.3	51.6	55.9	60.2	64.5
Condenser pressure (bar)	0.08					
Solar heat integration	**Original ISCC**	**+10%**	**+20%**	**+30%**	**+40%**	**+50%**
Integrated solar heat (MW)	7					
Cycle efficiency	**Original ISCC**	**+10%**	**+20%**	**+30%**	**+40%**	**+50%**
Gas turbine cycle (%)	39.84					
Combined cycle (%)	54.97	54.89	54.81	54.72	54.63	54.54
Cycle power breakdown	**Original ISCC**	**+10%**	**+20%**	**+30%**	**+40%**	**+50%**
Compressor (kW)	62,450					
Gas turbine (kW)	126,727					
Gas cycle (kW)	64,277					
Steam cycle (kW)	28,265	28,128	27,987	27,843	27,694	27,539
Total net power (kW)	92,542	92,405	92,264	92,120	91,971	91,816
Power boosted (%)	2.18	2.02	1.87	1.71	1.55	1.37
Back work ratio (%)	49.279					
Specific work per unit fuel mass (kJ/kg)	27,016	26,976	26,935	26,892	26,849	26,804

The results showed that an increase in the integrated solar thermal power at the superheater stage causes a noticeable increase in the turbine inlet steam temperature (7_{new}), increase thus the steam cycle output power.

It was observed that increasing the operating pressure caused the steam turbine inlet temperature to drop, reducing the output power of the steam cycle. The studied schemes exhibit variations in the ISCC overall efficiency, with the highest being 55.32% (-50% operating pressure case) and the lowest being 54.54% (+50% operating pressure case), as shown in Figure 4.46.

Table 4.10 ISCC vs Parameter boosting "case I" (-10%,-20%,-30%,-40% & -50%)

Mass flowrates	**Original ISCC**	**ISCC "case I" (Superheater)**				
		-10%	**-20%**	**-30%**	**-40%**	**-50%**
Air to fuel ratio	50					
Turbine gas flowrate (kg/s)	174.7					
Air flowrate (kg/s)	171.27					
Fuel flowrate (kg/s)	3.42					
LP evaporator mass flowrate (kg/s)	5					
HP evaporator mass flowrate (kg/s)	25					
Operating temperatures	**Original ISCC**	**-10%**	**-20%**	**-30%**	**-40%**	**-50%**
Compressor inlet (°C)	24					
Combustion chamber inlet (°C)	379					
Gas turbine inlet (°C)	1174					
Gas turbine outlet (°C)	549					
Inlet steam temperature (°C)	491	491	491	491	491	490.5
Pinch temperature (°C)	19.3	19.7	20	20.5	21	21.5
Economizer outlet temperature (°C)	228	223	218	212	205	197.5
Approach temperature (°C)	26.5	25	23.5	22	20.5	18.5
Operating pressures	**Original ISCC**	**-10%**	**-20%**	**-30%**	**-40%**	**-50%**
Inlet steam pressure (bar)	43	38.7	34.4	30.1	25.8	21.5
LP evaporator pressure (bar)	2.4	2.16	1.92	1.68	1.44	1.2
Condenser pressure (bar)	0.08					
Solar heat integration	**Original ISCC**	**-10%**	**-20%**	**-30%**	**-40%**	**-50%**
Integrated solar heat (MW)	7					
Cycle efficiency	**Original ISCC**	**-10%**	**-20%**	**-30%**	**-40%**	**-50%**
Gas turbine cycle (%)	39.84					
Combined cycle (%)	54.97	55.05	55.12	55.19	55.26	55.32
Cycle power breakdown	**Original ISCC**	**-10%**	**-20%**	**-30%**	**-40%**	**-50%**
Compressor (kW)	62,450					
Gas turbine (kW)	126,727					
Gas cycle (kW)	64,277					
Steam cycle (kW)	28,265	28,396	28,521	28,640	28,750	28,849
Total net power (kW)	92,542	92,673	92,798	92,917	93,027	93,126
Power boosted (%)	2.18	2.32	2.46	2.59	2.71	2.82
Back work ratio (%)	49.279					
Specific work per unit fuel mass (kJ/kg)	27,016	27,054	27,091	27,125	27,157	27,186

Since the maximum power boosting is reached for the -50% operating pressure case, values of power boosting were presented for different integrated solar thermal power values at this operating pressure in Figure 4.47. At no solar heat, total output power already increased by 0.78 MW (0.86%), while, at 7 MW, of integrated solar heat, it rose by a maximum of 2.5 MW (2.82%). The temperature distribution in the HRSG at a solar power integration of 7 MW for -50% operating pressure case is shown in Figure 4.48. The output power and the cycle efficiency show remarkable increase thanks to the upward shift in the steam temperatures distribution as a result of the integrated solar thermal power.

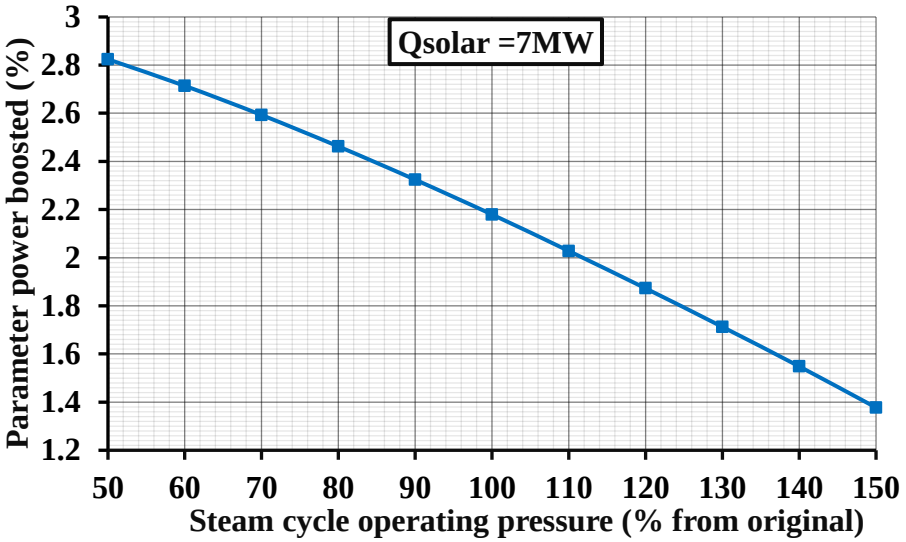

Figure 4.45 Parameter power boosted at different pressure levels for case I

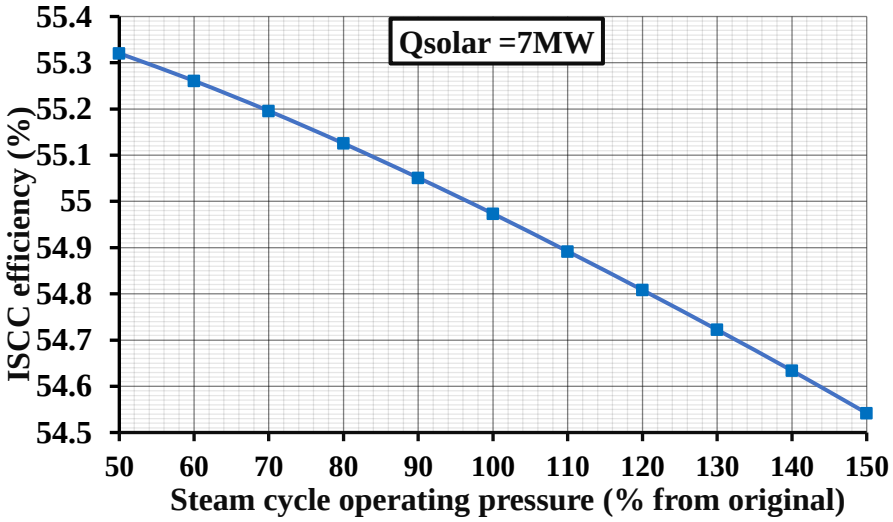

Figure 4.46 ISCC efficiency at different pressure levels for case I

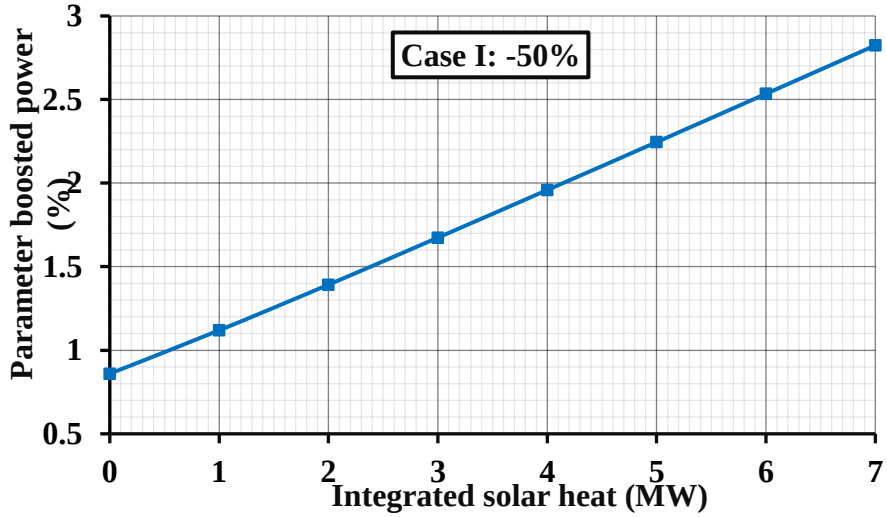

Figure 4.47 Parameter power boosted at different integrated solar heat for case C:-50%

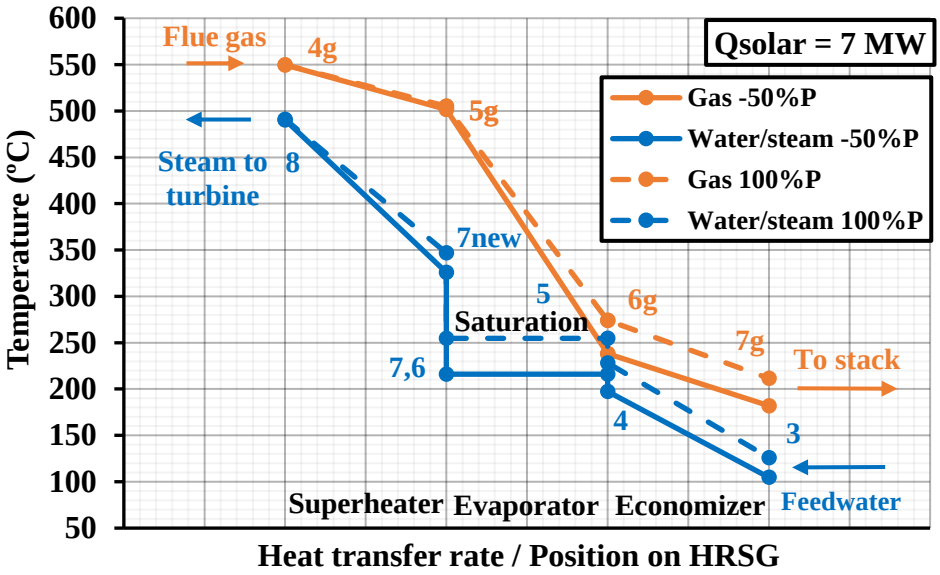

Figure 4.48 T-Q diagram for case I (-50%)"Parameter boosting" at Qsolar = 7MW

b) Case J "Integration at economizer"

The feedwater was heated by the integrated solar thermal power before entering the economizer, as shown in Figure 4.39. Several operating pressure values have been studied, from -50% to +50% of the original operating pressure at 10% intervals. The solar thermal power that could be integrated increases with operating pressure, passing from 1.5 MW at -50% pressure to 2 MW at +50%. Therefore, to compare all pressure conditions, a value of 1.5 MW integrated solar power was selected. Tables 4.11 and 4.12 collect the results obtained. Figure 4.49 shows the boosted power as a function of operating pressure, passing from 4.92% (4.45 MW) at -50% operating pressure to 4.35% (3.94 MW) at +50% operating pressure. In this case, it was possible to find a maximum at -30% operating pressure, boosting power by 5.01% (+4.53 MW).

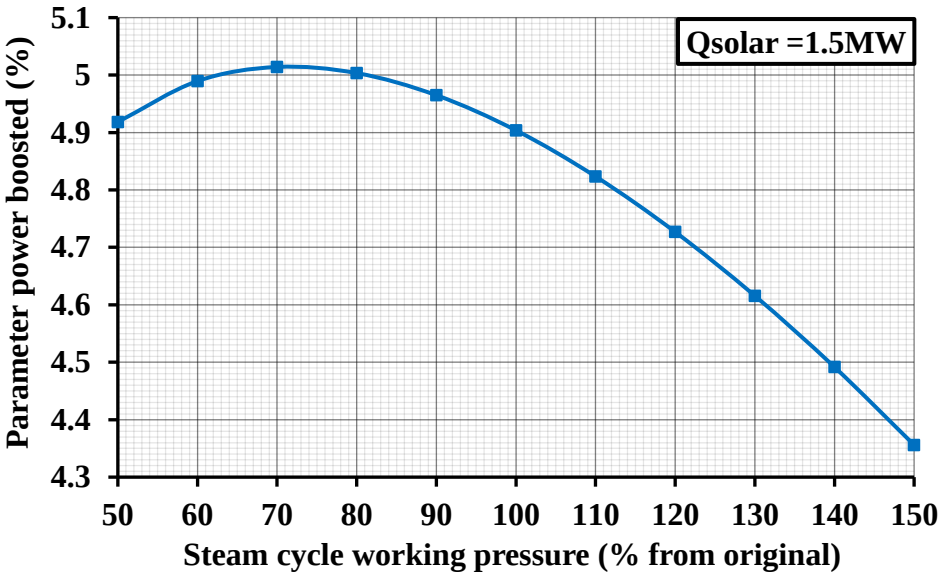

Figure 4.49 Parameter power boosted at different pressure levels for case J

Table 4.11 ISCC vs Parameter boosting "case J" (+10%,+20%,+30%,+40% & +50%)

Mass flowrates	**Original ISCC**	**ISCC "case J" (Economizer)**				
		+10%	**+20%**	**+30%**	**+40%**	**+50%**
Air to fuel ratio	50					
Turbine gas flowrate (kg/s)	174.7					
Air flowrate (kg/s)	171.27					
Fuel flowrate (kg/s)	3.42					
LP evaporator (kg/s)	5					
HP evaporator kg/s)	25					
Operating temperatures	**Original ISCC**	**+10%**	**+20%**	**+30%**	**+40%**	**+50%**
Compressor inlet (°C)	24					
Combustion chamber inlet (°C)	379					
Gas turbine inlet (°C)	1174					
Gas turbine outlet (°C)	549					
Inlet steam temperature (°C)	534	534.5	535	535	535	534.5
Pinch temperature (°C)	15	15	14.5	14	13.5	13.5
Economizer outlet temperature (°C)	229	233	236	239.5	242	245
Approach temperature (°C)	25.5	27.5	29.5	31.5	33.5	35
Operating pressures	**Original ISCC**	**+10%**	**+20%**	**+30%**	**+40%**	**+50%**
Inlet steam (bar)	43	47.3	51.6	55.9	60.2	64.5
LP evaporator (bar)	2.4	2.64	2.88	3.12	3.36	3.6
Condenser (bar)	0.08					
Solar heat integration	**Original ISCC**	**+10%**	**+20%**	**+30%**	**+40%**	**+50%**
Solar heat (MW)	1.5					
Cycle efficiency	**Original ISCC**	**+10%**	**+20%**	**+30%**	**+40%**	**+50%**
Gas turbine cycle (%)	39.84					
Combined cycle (%)	58.34	58.3	58.24	58.18	58.11	58.04
Cycle power breakdown	**Original ISCC**	**+10%**	**+20%**	**+30%**	**+40%**	**+50%**
Compressor (kW)	62,450					
Gas turbine (kW)	126,727					
Gas cycle (kW)	64,277					
Steam cycle (kW)	30,733	30,660	30,573	30,472	30,360	30,237
Total net power (kW)	95,010	94,937	94,850	94,749	94,637	94,514
Power boosted (%)	4.9	4.82	4.72	4.61	4.49	4.35
Back work ratio (%)	49.279					
Specific work per unit fuel mass (kJ/kg)	27,736	27,715	27,689	27,660	27,627	27,591

The ISCC overall efficiency also changed with operating pressure, as shown in Figure 4.50. It may be observed that, from a value of 58.35% for the lowest operating pressure (-50%), it drops to 58.04% for the highest operating pressure (+50). Again, there is a maximum efficiency of 58.04% at the optimum operating pressure (-30%). Thanks to the relatively low steam operating temperatures, PTCs would be a suitable choice for the solar field technology when it is integrated before the economizer stage.

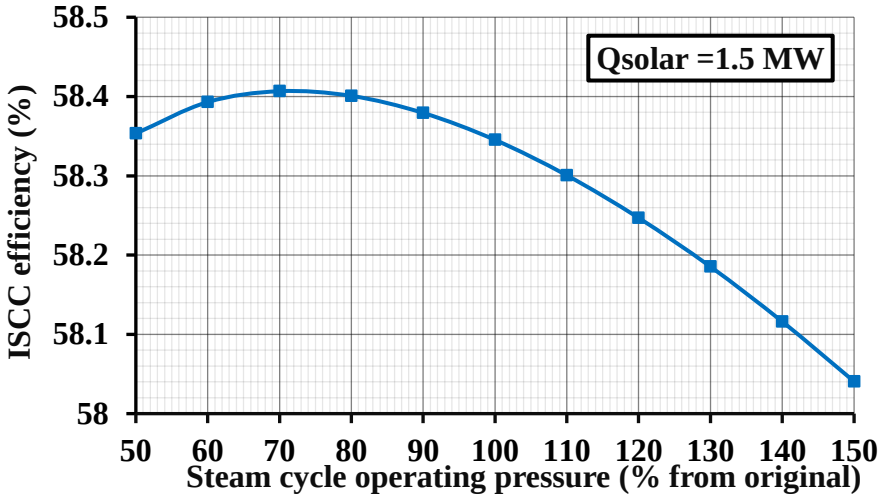

Figure 4.50 ISCC efficiency at different pressure levels for "case J"

Table 4.12 ISCC vs Parameter boosting "case J" (-10%,-20%,-30%,-40% & -50%)

Mass flowrates	**Original ISCC**	**ISCC "case J" (Economizer)**				
		-10%	**-20%**	**-30%**	**-40%**	**-50%**
Air to fuel ratio	50					
Turbine gas flowrate (kg/s)	174.7					
Air flowrate (kg/s)	171.27					
Fuel flowrate (kg/s)	3.42					
LP evaporator (kg/s)	5					
HP evaporator kg/s)	25					
Operating temperatures	**Original ISCC**	**-10%**	**-20%**	**-30%**	**-40%**	**-50%**
Compressor inlet (°C)	24					
Combustion chamber inlet (°C)	379					
Gas turbine inlet (°C)	1174					
Gas turbine outlet (°C)	549					
Inlet steam temperature (°C)	534	533	532	530	527.5	524.5
Pinch temperature (°C)	15	15.5	16	16.5	17.5	18
Economizer outlet temperature (°C)	229	225	221	216	211	205
Approach temperature (°C)	25.5	23	20.5	18	14.5	11
Operating pressures	**Original ISCC**	**-10%**	**-20%**	**-30%**	**-40%**	**-50%**
Inlet steam (bar)	43	38.7	34.4	30.1	25.8	21.5
LP evaporator (bar)	2.4	2.16	1.92	1.68	1.44	1.2
Condenser (bar)	0.08					
Solar heat integration	**Original ISCC**	**-10%**	**-20%**	**-30%**	**-40%**	**-50%**
Solar heat (MW)	1.5					
Cycle efficiency	**Original ISCC**	**-10%**	**-20%**	**-30%**	**-40%**	**-50%**
Gas turbine cycle (%)	39.84					
Combined cycle (%)	58.34	58.38	58.4	58.4	58.39	58.35
Cycle power breakdown	**Original ISCC**	**-10%**	**-20%**	**-30%**	**-40%**	**-50%**
Compressor (kW)	62,450					
Gas turbine (kW)	126,727					
Gas cycle (kW)	64,277					
Steam cycle (kW)	30,733	30,788	30,823	30,833	30,811	30,746
Total net power (kW)	95,010	95,065	95,100	95,110	95,088	95,023
Power boosted (%)	4.9	4.96	5	5.01	4.98	4.92
Specific work per unit fuel mass (kJ/kg)	27,736	27,752	27,762	27,765	27,759	27,740

Focusing on the results for the best-case scenario (-30% operating pressure), Figure 4.51 shows the power boosted as a function of the different integrated solar thermal power. Just reducing the pressure to 70% of the original value already increases output power by 0.04% (41 kW), but when 1.5 MW of solar thermal power is integrated, power can be boosted by 5.01% (4.54 MW). Figure 4.52 displays the temperature distribution inside the HRSG in that case, where it may be observed that the pressure reduction leads to a lower saturation temperature, leading the steam cycle to extract more heat from the exhaust gases before they leave the HRSG.

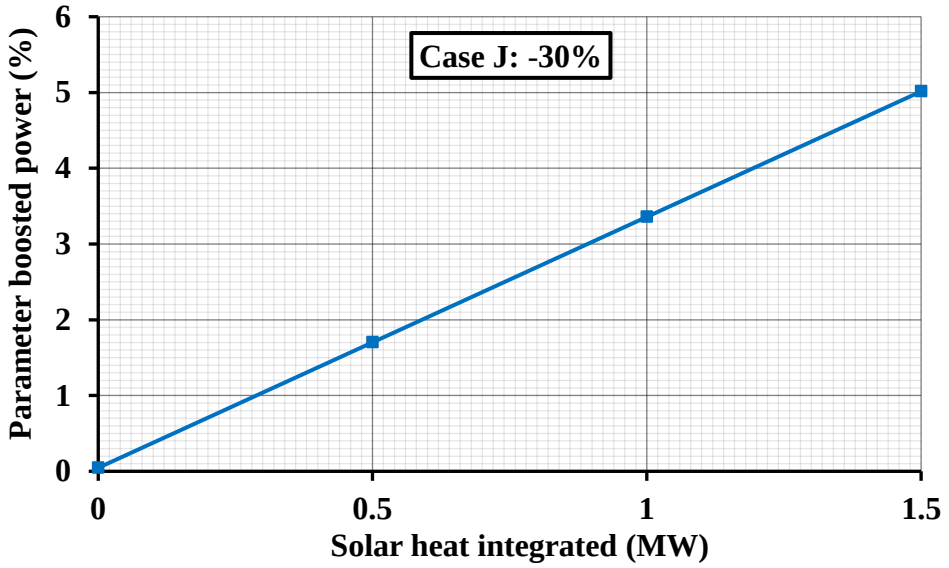

Figure 4.51 Parameter power boosted at different integrated solar heat for "case J:-30%"

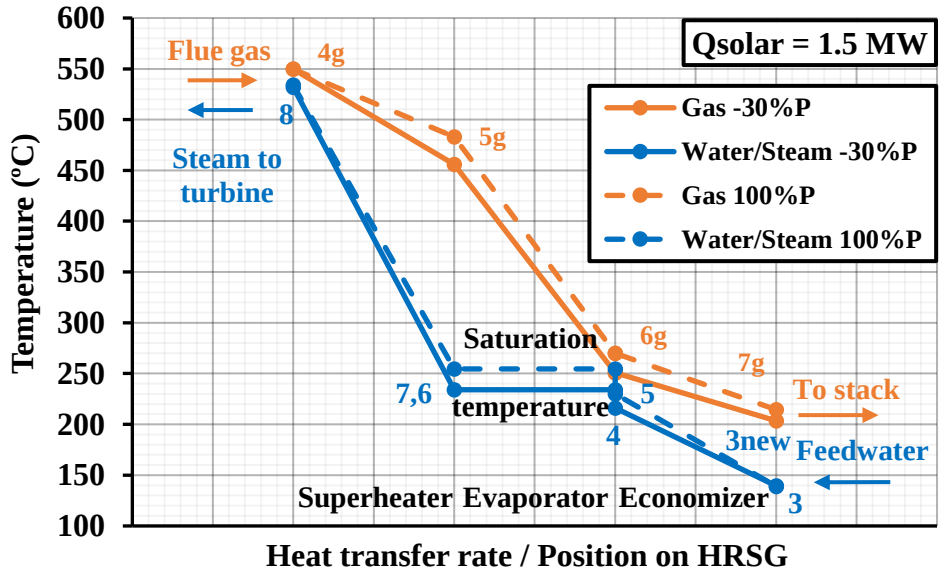

Figure 4.52 T-Q diagram for case J (-30%) "Parameter boosting" at Qsolar = 1.5 MW

In addition, the reduction of saturation pressure may translate into a higher steam quality at the turbine outlet for the same steam inlet temperature.

4.2.3 Power boosting options summary

To summarize the results from the power boosting operating schemes:

- **Case F: before compressor**
  It was impossible to apply power boosting operation, as preheating ambient air before entering the compressor increased compression work. Despite the increase in the gas turbine power, the overall gas cycle output power decreased, obtaining the opposite effect that was sought.
- **Case G: after compressor**
  It is a reliable option for power boosting, allowing a boost of 4.41% (4 MW) at an integrated solar power of 10 MW. Specific work per fuel unit mass increased to 27.6 MJ/kg (a 1.16 MJ/kg increase). Since the solar heat exchanger maximum temperature was 430 °C at 10 MW of integrated solar thermal power, it allows using PTC with molten salts as solar field technology, PDR or heliostat field collectors.
- **Case H: after combustion chamber**
  Similar results as for case G were found, due to the fixed gas turbine operating conditions. However, in this case, the maximum temperature of the solar heat exchanger would be 1129.5 °C, so only heliostat field technology could be used. Hence, this option is not the optimum one for power boosting.
- **Case I (flowrate): at superheater**
  The maximum amount of solar heat that could be integrated at this position is 4 MW. Power could be boosted by 24.2% (21.92 MW), with an overall efficiency of 68.03%. This option showed the best results, with 32.84 MJ/kg specific work per fuel unit mass (a 6.4 MJ/kg increase).
- **Case J (Flowrate): at economizer**
  In this case, up to 12 MW solar power could be integrated into the cycle. Power could be boosted by 8.96% (8.12 MW), with an overall cycle efficiency of 56.94%. It is a suitable option, allowing the specific work per fuel unit mass to increase by 2.37 MJ/kg to reach 28.81 MJ/kg.
- **Case I (parameter): at superheater**
  The best performance was found when the original operating pressure was reduced to 50% (21.5 bar). Power could be boosted by 2.82% (2.55 MW) with 7 MW of integrated solar power, leading to a specific work per fuel unit mass of 27.18 MJ/kg.
- **Case J (parameter): at economizer**
  Finally, for case J, the best performance was observed when the operating pressure of the steam cycle was reduced by 30% (to 30.1 bar). The ISCC overall power was boosted by 5.01% (4.54 MW) at an integrated solar power of 1.5 MW. The ISCC overall efficiency reached 58.4% (a 2.2% increase), and the specific work per fuel unit mass increased by 1.32 MJ/kg to reach 27.76 MJ/kg.

4.3 *Approaches for integrating solar energy into current combined cycles*

In this section, some considerations for integrating solar thermal power into an existing combined cycle power plant are presented, based on the previous results. Figure 4.53 shows the strategy to be followed depending on the desired outcome of solar power integration, and a summary of all cases is provided in Table 4.13, alongside guidelines for solar power integration.

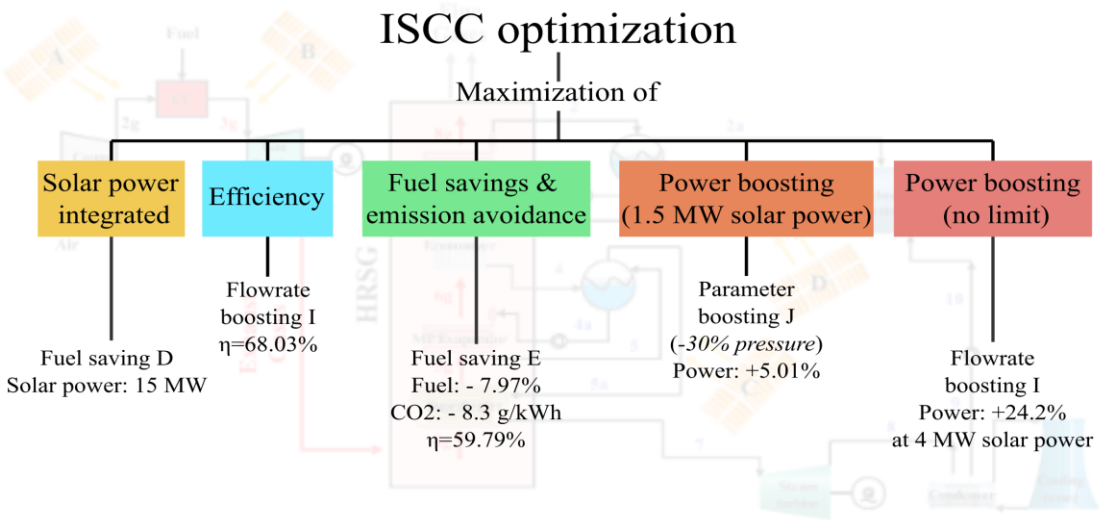

Figure 4.53 Optimum ISCC strategies depending on the desired outcome

Table 4.13 Considerations for coupling solar thermal power with a combined cycle power pant

Case	Guidelines for solar power integration – Fuel saving
A Before compressor	▪ Not applicable due to the increase in compression work.
B Before combustion chamber	▪ Solar field technology: PTC with molten salts, PDR or heliostat field. ▪ Best option for integration into the top gas cycle.
C After combustion chamber	▪ Solar field technology: only heliostat field (high temperatures). ▪ Not recommended due to solar technology restrictions.
D At superheater	▪ Solar field technology: PTC with molten salts, PDR or heliostat field. ▪ Lowest fuel saving effect per MW of solar thermal power. ▪ Can integrate the maximum solar thermal power. ▪ Recommended only for high values of solar power integration.
E At economizer	▪ Solar field technology: all technologies and HTFs (PTC, PDR, heliostat). ▪ Highest fuel saving effect per MW of solar thermal power. ▪ Best option, high energy efficiency, strongly recommended.

Case		Guidelines for solar power integration – Power boosting
F Before compressor		▪ Not applicable due to the increase in compression work.
G Before combustion chamber		▪ Solar field technology: PTC with molten salts, PDR or heliostat field. ▪ Lowest power boosting obtained per MW of solar thermal power. ▪ Best option for integration into the top gas cycle.
H After combustion chamber		▪ Solar field technology: only heliostat field (high temperatures). ▪ Lowest power boosting obtained per MW of solar thermal power. ▪ Not recommended due to solar technology restrictions and low efficiency.
I At superheater	**Flowrate**	▪ Solar field technology: all technologies and HTFs (PTC, PDR, heliostat). ▪ Highest power boosting per MW of solar thermal power. ▪ Highest ISCC efficiency achieved. ▪ Best option for power boosting strategy.
	Paramete	▪ Solar field technology: all technologies and HTFs (PTC, PDR, heliostat). ▪ Low power boosting per MW of solar thermal power. ▪ Low energy efficiency. ▪ Not recommended.
J At economizer	**Flowrate**	▪ Solar field technology: all technologies and HTFs (PTC, PDR, heliostat). ▪ Lower performance than case I, not recommended.
	Paramete	▪ Solar field technology: all technologies and HTFs (PTC, PDR, heliostat). ▪ Maximum power boosting for integrated solar power below 1.5 MW. ▪ High energy efficiency. ▪ Recommended option for low solar thermal power integrated.

4.3.1 Fuel saving considerations

For gas cycle integration, it has been observed that case A cannot operate under a fuel saving scheme, as the increase of compression work decreases output power. Despite saving 6.99% of fuel consumption at an integrated solar power of 5 MW, it fails to fulfill the premise of keeping power generation constant when fuel consumption is reduced. Both cases B and C show a saving of 6.23% in fuel consumption when integrating 10 MW solar thermal power. Nevertheless, case B shows more flexibility regarding the solar field technology, allowing to use parabolic dish reflectors or heliostat field collectors, due to the lower temperatures at the solar heat exchanger.

Regarding steam cycle integration, case D was able to save 3.49% in fuel consumption at an integrated solar thermal power of 15 MW, low value compared to other options. On the other hand, case E showed the highest percentage of fuel saving per MW of integrated solar thermal power, with 7.97% savings at only 3 MW. When compared to the other options for the same amount of integrated solar power, 3 MW, cases B and C can only save 1.87% of the fuel, while case D shows the lowest performance, with savings of only 0.65%.

4.3.2 Power boosting considerations

Considering gas cycle integration under a power boosting scheme, case F has failed to follow the operating strategy for the same reasons mentioned earlier for case A for fuel saving. On the other hand, cases G and H were able to boost power by 4.41% when 10 MW of solar power was integrated into the gas cycle.

For the steam cycle options, flowrate boosting shows better performance than parameter boosting, with case I boosting power by 24.2% at only 4 MW of integrated solar power. With the same integrated solar power, case J could only boost power by 2.98%. For the parameter boosting mode, the behavior of cases I and J changed, with case J boosting more power than case I. When the evaporator pressure was reduced to half of that of the original combined cycle, case I: superheater" was able to boost power by 2.82%, requiring 7 MW of solar thermal power. On the other hand, with only 1.5 MW of solar thermal power, case J boosted output power by 5.01% when evaporator pressure was reduced by 30%.

4.4 Results compared with literature

In this section, some of the results are compared to relevant findings in recent literature. Comparing the results of this work with the work of Barigozzi et al. [164] it was also found that power boosting techniques with solar integration at the bottom steam cycle outperformed those with integration at the top gas cycle. When solar thermal power was integrated before the superheater of the bottom steam cycle, Ameri and Mohammadzadeh [153] found a 6 MW improvement in power generation and carbon emissions reduction of 10 g/kWh for a 300 MW power plant. In this work, for the same integrating position, flowrate and parameter boosting strategies increased output power by 22 MW (24.2%) and 2.6 MW (2.82%), respectively, leading to a total power output of 112.5 and 93.1 MW. In addition, carbon emissions could be reduced by 3.5 g/kWh for an ISCC with output power of 90.5 MW. Behar [147] indicated that using PTCs with synthetic oil as HTF was the most efficient method for integrating solar thermal power at the bottom steam cycle. In this work, it has been observed that PTC can be applied to most steam cycle integration cases, except case D for fuel saving. In the work of Aghdam et al. [143], it was claimed that the power plant capacity increased from 714 to 728 MW and its efficiency increased by 2% when the solar field was integrated before the bottom steam cycle superheater. In this work, power was enhanced by 24.2% and cycle efficiency by 11.9% using flowrate boosting strategy for the same integration point. Elmohlawy [152] found that a 1.2% increase in thermal efficiency was achieved by introducing steam at a high pressure level of the bottom steam cycle. In this work, the integration of solar thermal power before the high pressure superheater to heat saturated steam resulted in the highest efficiency increase of 11%. Finally, Abdel Dayem et al. [124] found that increase in DNI due to climate conditions change might lead to a 10% increase in steam turbine production. According to this study, a flowrate boosting technique could raise the steam turbine power by 24.2% using just 4 MW of integrated solar thermal power.

4.5 Optimization of solar field

In this final section, an appropriate size of the solar field that could be installed to optimize the operating conditions of the ISCC is estimated. Each integration option, for the two operating strategies: fuel saving and power boosting, was analyzed based on the average solar irradiation for Alexandria-Egypt. The monthly average daily direct normal radiation (G_{bn}) for Alexandria is shown in Figure 4.53, which shows a maximum of 321 W/m^2 in July and a minimum of 133 W/m^2 in December [201].

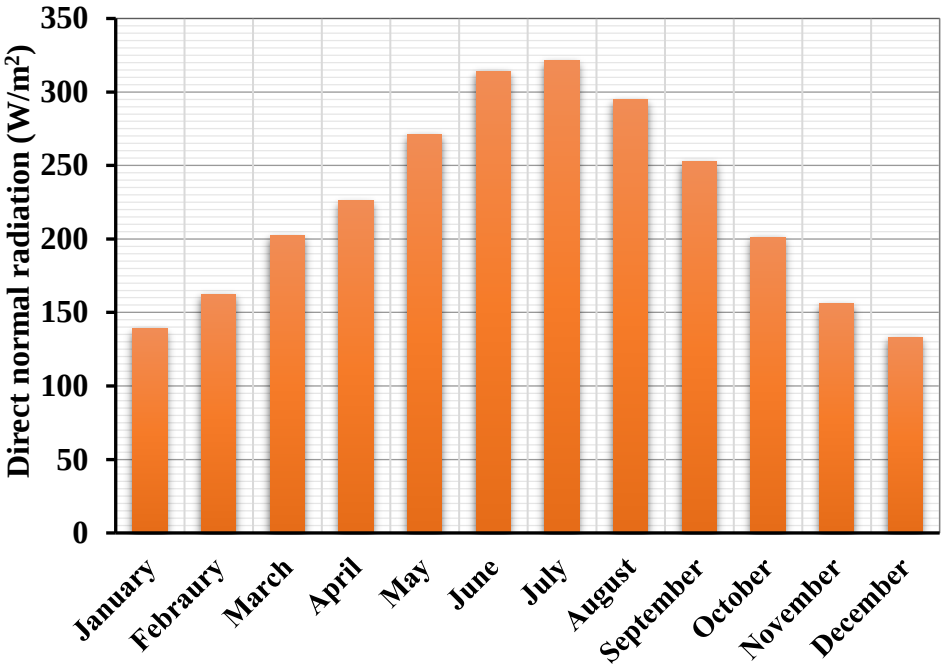

Figure 4.54 Monthly average daily direct normal irradiation (W/m^2) for Alexandria-Egypt [201]

The calculations were based on the solar collector model presented in Chapter 3, with the amount of solar heat absorbed presented in Equation (3.61) [197]. Cases A and F were not considered, as they could not fulfill the requirements of fuel saving and power boosting operation. In addition, for the other cases, the maximum limit for integrated solar thermal power was considered to determine the appropriate solar field size.

To ensure that the ISCC power plant will operate at maximum solar capacity for the whole year, the solar field size was based on the lowest average direct normal radiation of 133 W/m^2 reached in December. The solar thermal power integration process should be monitored not to surpass the maximum limit of integrated solar heat, opening the possibility of storing the extra absorbed solar energy.

4.5.1 Fuel saving configurations

First, the fuel saving cases will be analyzed. Since cases B and C have the same maximum limit for solar thermal power integration, 10 MW, the estimated solar field size will be the same for both, 208,500 m^2. Surplus solar energy will be obtained in the rest of months other than December, as shown in Figure 4.54.

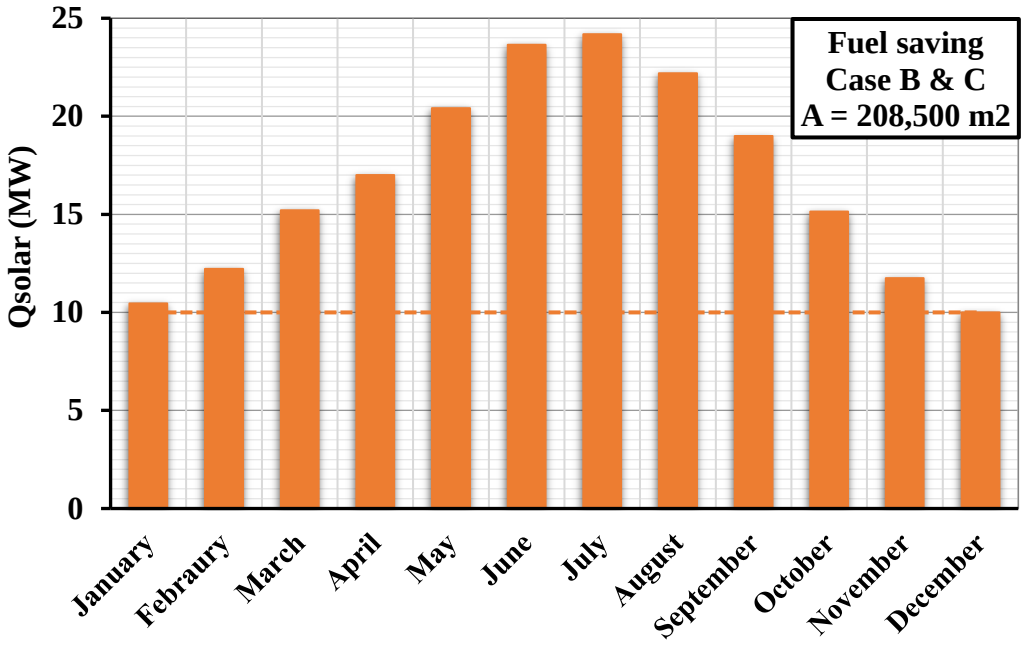

Figure 4.55 Absorbed solar thermal power for cases (B & C) for fuel saving

As case D is able to integrate 15 MW of solar thermal power, it will require the largest estimated solar field area, 312,500 m^2 (50% larger than for cases B and C). In this case, in July, it will be possible to absorb 36.2 MW, as shown in Figure 4.55.

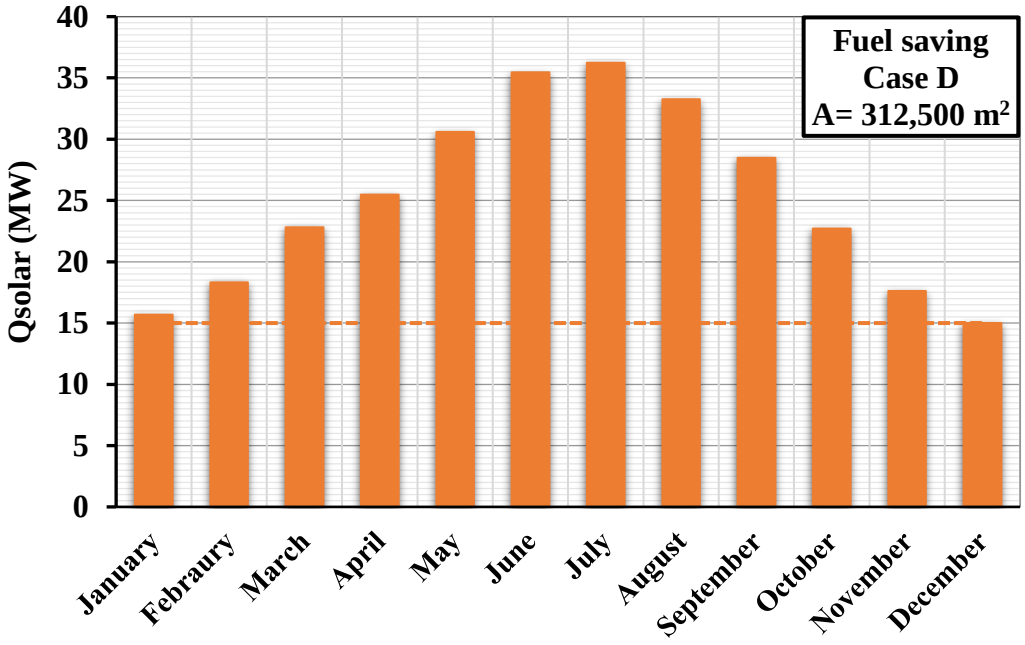

Figure 4.56 Absorbed solar thermal power for case D for fuel saving

Finally, the smallest solar field size, 62,500 m^2, is enough for integrating solar power into the configuration presented for case E, as it can only integrate 3 MW, as shown in Figure 4.56. This configuration will produce the least amount of solar energy surplus.

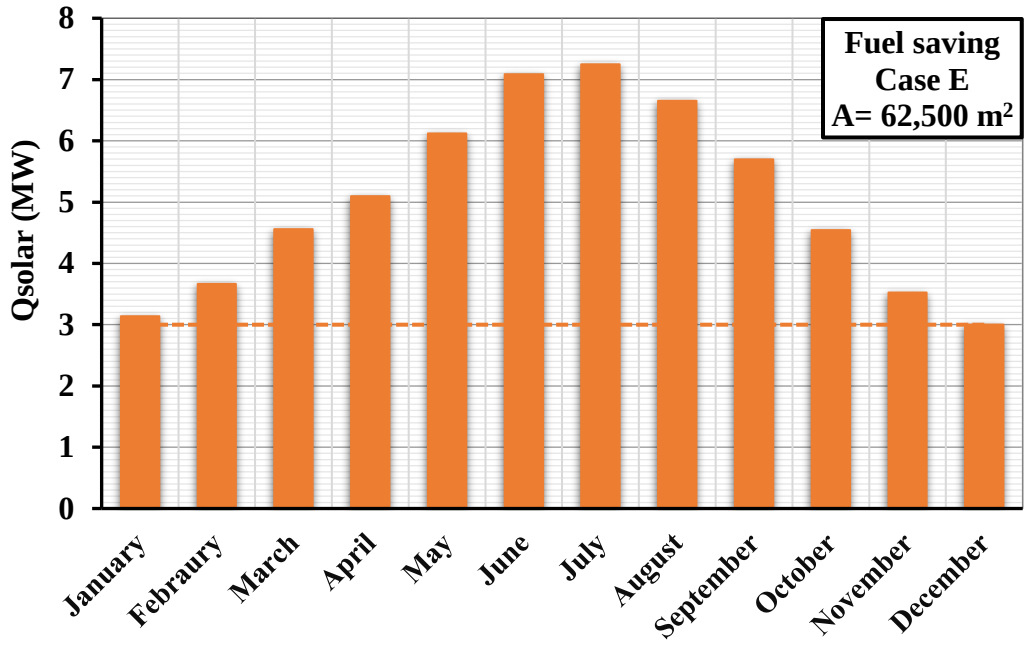

Figure 4.57 Absorbed solar thermal power for case E for fuel saving

4.5.2 Power boosting configurations

As cases G and H have the same value of maximum solar power that can be integrated as cases B and C, the expected solar field area is the same, 208,500 m^2. Figure 4.57 shows the evolution of the thermal power absorbed throughout the year.

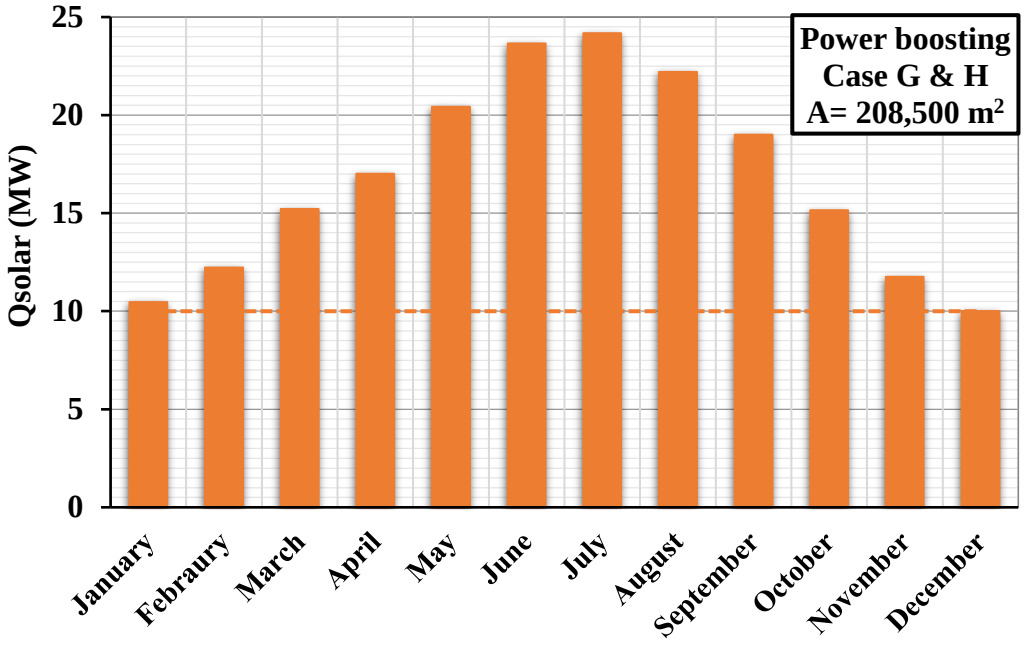

Figure 4.58 Absorbed solar thermal power for cases (G & H) for power boosting

For integration of solar power into the steam cycle, flowrate boosting and parameter boosting were considered. For the flowrate boosting, case I requires one of the smallest solar field areas, 83,400 m^2, according to the 4 MW limit in integrated solar power. Figure 4.58 shows the evolution of the monthly absorbed power, with maximum values around 9.7 MW in July.

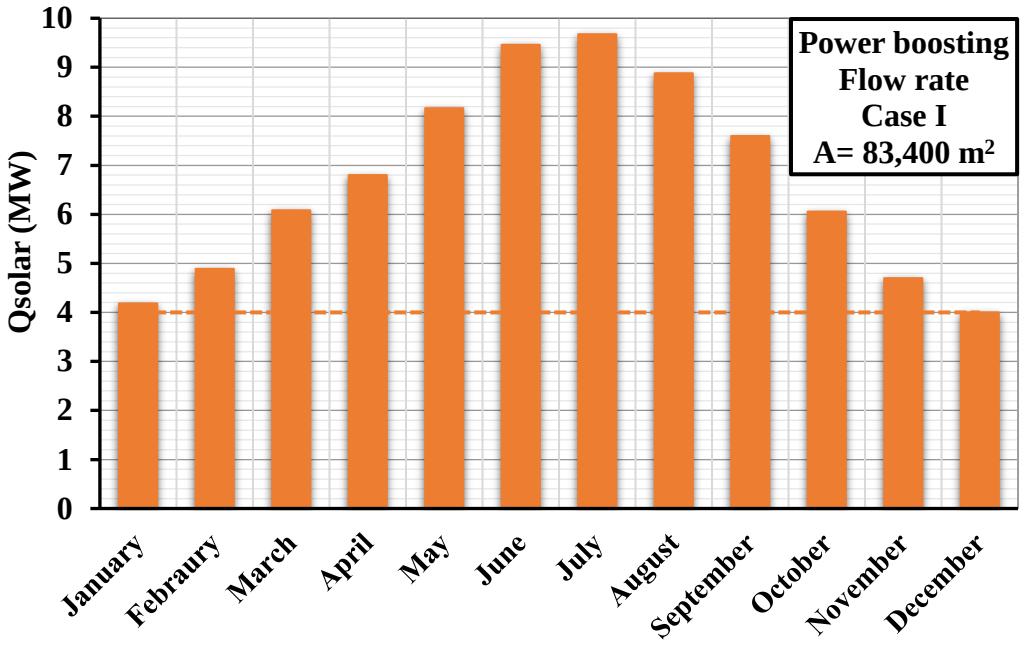

Figure 4.59 Absorbed solar thermal power for case I for flowrate boosting

For case J, on the other hand, up to 12 MW solar thermal power can be integrated, leading to 250,000 m^2 of solar field area, one of the largest values. The evolution of solar absorbed power is shown in Figure 4.59, where it may be observed that, in July, a huge amount of energy will be lost if it is not stored.

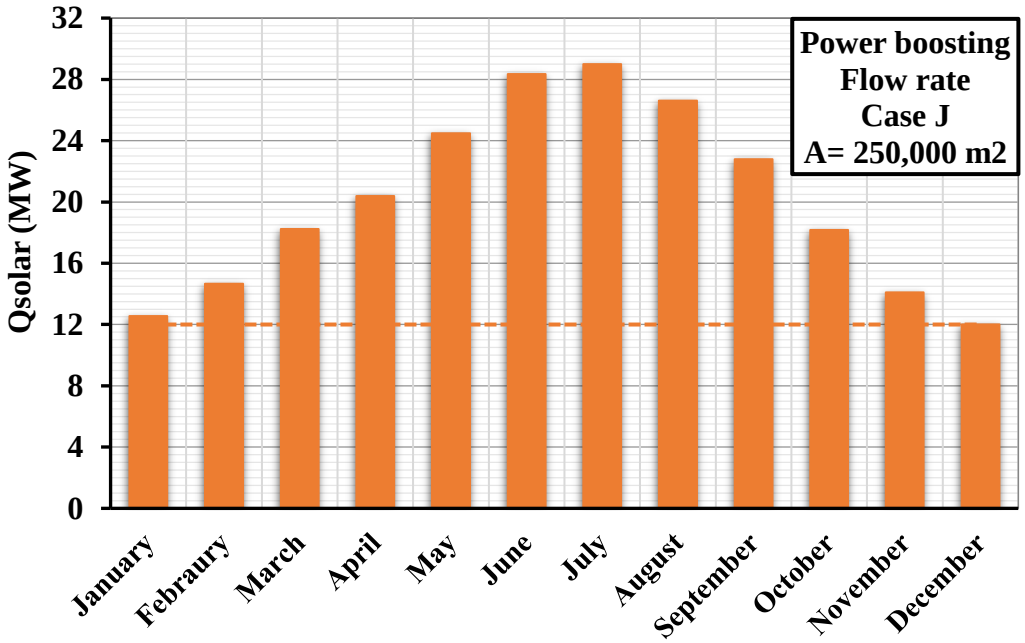

Figure 4.60 Absorbed solar thermal power for case J for flowrate boosting

For the parameter boosting mode, the solar area required for integrating 7 MW in the configuration of case I is 149,900 m^2. Finally, for case J, as only 1.5 MW of solar power needs to be integrated, the smallest solar field area, 13,100 m^2, is enough. Figures 4.60

and 4.61 shown the monthly solar power absorbed by the solar field for both cases, where it may be observed that solar integration in case J for power boosting will lead to the least energy surplus.

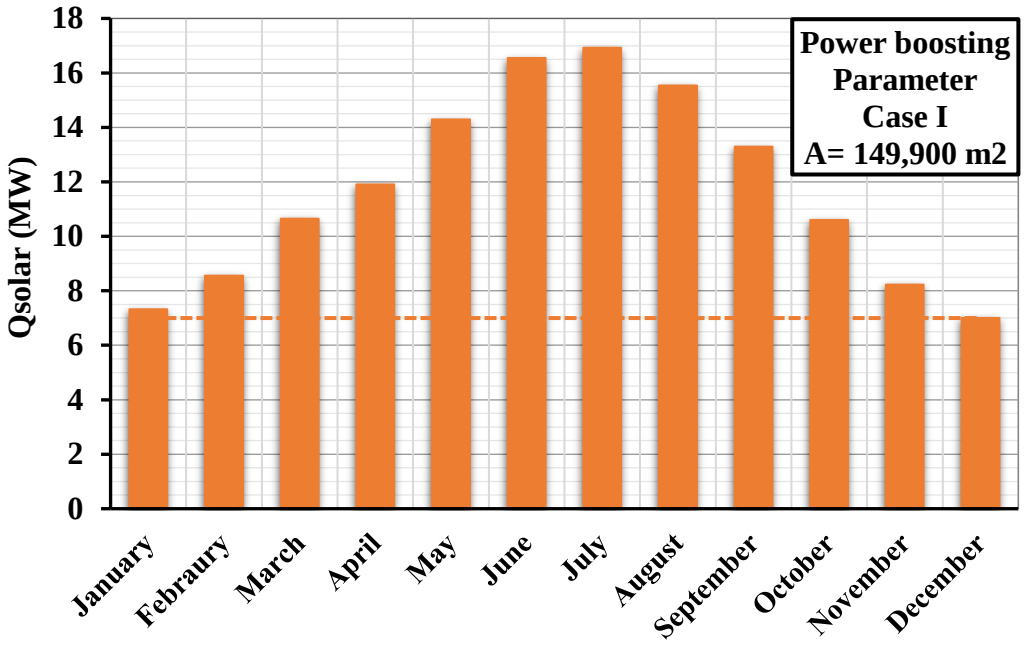

Figure 4.61 Absorbed solar thermal power for case I for parameter boosting

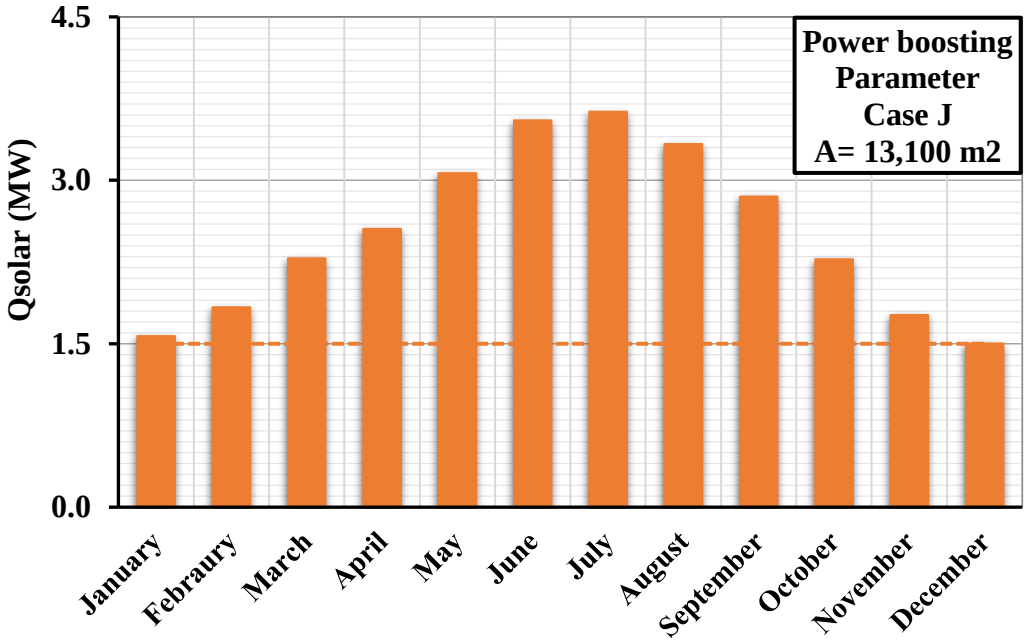

Figure 4.62 Absorbed solar thermal power for case J for parameter boosting

When the solar integrated power values and the solar field areas are plotted together, as in Figure 4.62, the clear direct relationship between the estimated solar field size and the amount of solar thermal power integrated becomes apparent. The largest solar field area, 312,500 m^2, was found in case D (integration with superheater) for the fuel saving scheme as it had the highest limit for the integrated solar thermal power, 15 MW. On

the other hand, the smallest area, 13,100 m^2, was obtained for case J (integration before the economizer) for parameter boosting, as it could only integrate a maximum of 1.5 MW of solar thermal power. Considering the surplus energy that will be generated in months other than December, coupling the ISCC with a thermal storage system could be beneficial for allowing to continue operating under the fuel saving or power boosting schemes during the night.

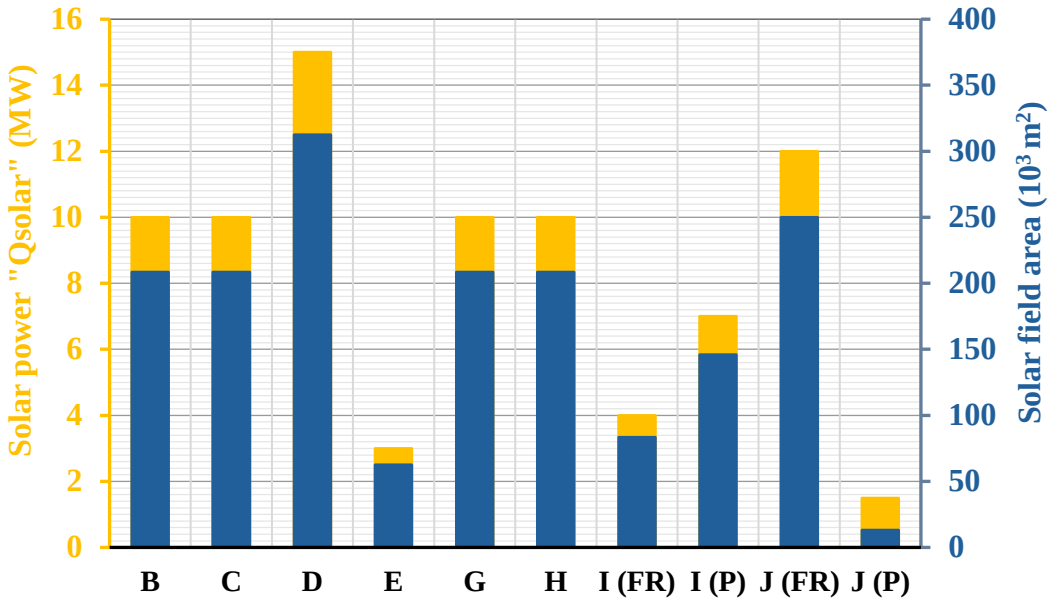

Figure 4.63 Solar field total area for all cases

CHAPTER FIVE

CONCLUSION AND FUTURE WORK

In this final chapter, the conclusions of the thesis are presented. The achievement of the research objectives is assessed, the main findings are presented, and future research lines are suggested.

5.1 Research objectives achievement

The main objective of the thesis was to perform a comprehensive study on the impact of integrating solar field in a combined cycle power plant for fuel saving and power boosting at different integrating positions at the top gas cycle and at the bottom steam cycle. The main objective, as well as the specific ones, has been satisfactorily achieved. A model of a real operating combined cycle power plant has been developed and modified to integrate a solar field, and the optimum operating conditions for fuel saving and power boosting for different configurations have been studied.

5.2 Main findings

- Integrating solar power before the air compressor in the gas cycle is not a good option either for fuel saving or power boosting. The increase in compression work becomes too high and the cycle power output is reduced.
- Integrating solar heat into the top gas cycle may constrain the solar field technology that can be used. Parabolic dish reflectors and heliostat fields are alternative options instead of parabolic field collectors. In addition, higher temperature heat transfer fluids, such as molten salts, must be used
- It is preferrable to integrate solar thermal power into the bottom steam cycle to allow using parabolic trough collectors and synthetic oils as heat transfer fluids.
- For the fuel saving operating mode, the best option is to reduce fuel consumption and carbon emissions is the integration of the solar field before the economizer at the bottom steam cycle.
- Reducing the evaporator operating pressure in the bottom steam cycle increases output power thanks to the better use of heat.
- For maximizing the integrated solar thermal power, the fuel saving scheme with integration before the superheater of the steam cycle is the best option.
- The highest energy efficiency is reached by flowrate power boosting with solar integration before the superheater of the steam cycle.
- Flowrate power boosting performs better than parameter power boosting, especially for integration before the superheater.
- For maximizing power boosting for small solar fields, parameter boosting with solar integration before the economizer of the steam cycle should be applied. If there is no limit on the solar field size, flowrate boosting with solar integration before the economizer stage is the optimum selection.

5.3 Recommendations for future work

Based on the findings of this study, the following research lines could be followed in future works:

- Study off-design operating conditions for the different integration options.
- Perform a dynamic analysis for a specific place, using actual solar thermal data collected over a period of time.

- A heat storage system could be coupled with the ISCC to allow fuel saving and power boosting during non-solar times.
- The configurations studied in this work could be combined to study the impact of integrating solar thermal power into several integration positions at the same time.

CAPÍTULO CINCO

CONCLUSIONES Y TRABAJOS FUTUROS

En este último capítulo, se presentan las conclusiones de la tesis. Se evalúa la consecución de los objetivos de la investigación, se presentan los principales resultados obtenidos y se sugieren futuras líneas de investigación.

5.1. Consecución de los objetivos de la investigación

El principal objetivo de esta tesis era la realización de un estudio completo sobre el impacto de la integración de un campo solar en una planta de producción de energía de ciclo combinado para el ahorro de combustible y el aumento de su potencia en diferentes posiciones de integración en el ciclo de gas y el de vapor. El objetivo principal, así como los objetivos específicos de la tesis, se han logrado de forma satisfactoria. Se ha desarrollado un modelo de una planta de producción de energía de ciclo combinado real y se ha modificado para integrar un campo solar, estudiando las condiciones de operación óptimas para el ahorro de combustible y el aumento de la potencia para diferentes configuraciones del ciclo.

5.2. Principales resultados de la investigación

- La integración de la energía solar previa a la compresión del aire en el compresor del ciclo de gas no es una buena opción ni para el ahorro de combustible ni para el aumento de la potencia. El aumento en el trabajo de compresión aumenta demasiado, reduciendo la potencia del ciclo.
- Integrar la energía solar en el ciclo de gas puede restringir la tecnología de campo solar utilizable. Los reflectores de disco parabólicos y heliostatos son alternativas a los colectores parabólicos en este caso. Además, se deben emplear fluidos de transferencia de calor de mayor temperatura, como sales fundidas.
- Es preferible integrar la energía solar en el ciclo de vapor y así permitir el empleo de colectores solares parabólicos y aceites sintéticos como fluidos de transferencia de calor.
- Para el modo de ahorro de combustible, la mejor opción es la integración del ciclo solar antes del economizador del ciclo de vapor.
- La reducción de la presión de evaporación del ciclo de vapor aumenta la potencia generada gracias a un mejor aprovechamiento de la energía térmica.
- Para maximizar la potencia solar integrada, la mejor opción es el modo de ahorro de combustible con la integración solar antes del sobrecalentador del ciclo de vapor.
- La eficiencia energética máxima se alcanza mediante el aumento de potencia con integración solar antes del sobrecalentador del ciclo de vapor, incrementando el flujo másico de vapor.
- El aumento de la potencia mediante el aumento del flujo másico de vapor proporciona mejores resultados que el aumento de los parámetros termodinámicos del vapor, especialmente si la energía solar se integra antes del sobrecalentador.
- Para maximizar la potencia utilizando pequeños campos solares, la mejor estrategia es la integración de la energía solar antes del economizador del ciclo de vapor para aumentar los parámetros termodinámicos del vapor. Si no hay límite en el tamaño del campo solar, la mejor opción es la integración antes del economizador para aumentar el flujo másico de vapor.

5.3. Recomendaciones para trabajos futuros

Con base en los resultados de este estudio, se proponen las siguientes líneas de trabajo para trabajos futuros:

- Estudio de las condiciones fuera del punto de diseño para las diferentes opciones de integración.
- Análisis dinámico para una localización concreta, utilizando datos sobre la radiación solar a lo largo de un período temporal.
- Acoplamiento de un sistema de almacenamiento de energía térmica al ciclo combinado, para reducir el consumo de combustible y aumentar la potencia del ciclo durante las horas sin sol.
- Combinaciones de las configuraciones estudiadas en esta tesis, para estudiar el impacto de la integración de energía solar en varias posiciones de integración al mismo tiempo.

6.REFERENCES

REFERENCES

[1] National Aeronautics and Space Administration (NASA), "The Effects of Climate Change." Accessed: Sep. 13, 2024. [Online]. Available: https://science.nasa.gov/climate-change/effects/

[2] Intergovernmental Panel on Climate Change (IPCC), "Global Warming of 1.5°C." Accessed: Sep. 13, 2024. [Online]. Available: https://www.ipcc.ch/sr15/

[3] Rebecca Lindsey, "Climate Change: Global Sea Level," Aug. 2023. Accessed: Sep. 13, 2024. [Online]. Available: https://www.climate.gov/news-features/understanding-climate/climate-change-global-sea-level

[4] Susana Ferreira, "Extreme Weather Events and Climate Change: Economic Impacts and Adaptation Policies," Jan. 2024. Accessed: Sep. 13, 2024. [Online]. Available: https://www.econstor.eu/bitstream/10419/282842/1/dp16715.pdf

[5] U.S Energy Information Adminstration (EIA), "Energy Institute Statistical Review of World Energy." [Online]. Available: https://ourworldindata.org/

[6] M. T. Alam *et al.*, "Co-Gasification of Treated Solid Recovered Fuel Residue by Using Minerals Bed and Biomass Waste Blends," *Energies (Basel)*, vol. 13, no. 8, p. 2081, Apr. 2020, doi: 10.3390/en13082081.

[7] Global Status Report, "Support and accelerate the development of renewable energy," 2023. Accessed: Nov. 26, 2023. [Online]. Available: https://www.ren21.net/wp-content/uploads/2019/05/GSR-2023_Energy-Supply-Module.pdf

[8] M. Shahabuddin and S. Bhattacharya, "Effect of reactant types (steam, <scp> CO_2 </scp> and steam + <scp> CO_2 </scp>) on the gasification performance of coal using entrained flow gasifier," *Int J Energy Res*, vol. 45, no. 6, pp. 9492–9501, May 2021, doi: 10.1002/er.6475.

[9] M. T. Alam, B. Dai, X. Wu, A. Hoadley, and L. Zhang, "A critical review of ash slagging mechanisms and viscosity measurement for low-rank coal and bio-slags," *Frontiers in Energy*, vol. 15, no. 1, pp. 46–67, Mar. 2021, doi: 10.1007/s11708-020-0807-8.

[10] M. A. Imteaz, A. Shanableh, A. Rahman, and A. Ahsan, "Optimisation of rainwater tank design from large roofs: A case study in Melbourne, Australia," *Resour Conserv Recycl*, vol. 55, no. 11, pp. 1022–1029, Sep. 2011, doi: 10.1016/j.resconrec.2011.05.013.

[11] D. Gielen, F. Boshell, D. Saygin, M. D. Bazilian, N. Wagner, and R. Gorini, "The role of renewable energy in the global energy transformation," *Energy Strategy Reviews*, vol. 24, pp. 38–50, Apr. 2019, doi: 10.1016/j.esr.2019.01.006.

[12] IRENA (International Renewable Energy Agency), “Renewable energy capacity,” Jul. 2024. Accessed: Sep. 14, 2024. [Online]. Available: https://www.irena.org/Data/View-data-by-topic/Capacity-and-Generation/Statistics-Time-Series

[13] Statista, “Global data and business intelligence platform with an extensive collection of statistics,” Aug. 2023. Accessed: Nov. 26, 2023. [Online]. Available: https://www.statista.com/statistics/1281761/number-of-gas-power-plants-by-country/

[14] Ashok D. Rao, *Combined cycle systems for near-zero emission power generation* . 2012.

[15] B. H. Eddine, B. Riad, Z. Youcef, and M. El-Arkam, “Multiobjective Optimization of the Performance of Safety Systems,” in *ICCEIS 2022*, Basel Switzerland: MDPI, Jan. 2023, p. 10. doi: 10.3390/engproc2023029010.

[16] A. Y. & B. A. 2006 Cengel, *Thermodynamics an Engineering Approach*, 5th ed. 2006.

[17] “TLV CORPORATION,” “Proud member of the Fluid Controls Institute (FCI), a non-profit association of the fluid control equipment manufacturers.” [Online]. Available: https://www2.tlv.com/en-us

[18] I. Dincer, “Proceedings of the world renewable energy congress V, Florence, Italy,” in *Renewable energy, environment and sustainable development.*, 1998, pp. 2559–2562.

[19] Bhatia SC., *Advanced Renewable Energy Systems, (Part 1 and 2)*. WPI Publishing, 2014. doi: 10.1201/b18242.

[20] M. Herrando and C. N. Markides, “Hybrid PV and solar-thermal systems for domestic heat and power provision in the UK: Techno-economic considerations,” *Appl Energy*, vol. 161, pp. 512–532, Jan. 2016, doi: 10.1016/j.apenergy.2015.09.025.

[21] S. A. Kalogirou, “Solar thermal collectors and applications,” *Prog Energy Combust Sci*, vol. 30, no. 3, pp. 231–295, 2004, doi: 10.1016/j.pecs.2004.02.001.

[22] S. Kalogirou, “The potential of solar industrial process heat applications,” *Appl Energy*, vol. 76, no. 4, pp. 337–361, Dec. 2003, doi: 10.1016/S0306-2619(02)00176-9.

[23] S. A. Kalogirou, S. Lloyd, J. Ward, and P. Eleftheriou, “Design and performance characteristics of a parabolic-trough solar-collector system,” *Appl Energy*, vol. 47, no. 4, pp. 341–354, Jan. 1994, doi: 10.1016/0306-2619(94)90041-8.

[24] S. A. Kalogirou, “Solar thermal collectors and applications,” *Prog Energy Combust Sci*, vol. 30, no. 3, pp. 231–295, 2004, doi: 10.1016/j.pecs.2004.02.001.

[25] IEA (International Energy Agency), “Technology Roadmap - Concentrating solar power.” Accessed: May 10, 2024. [Online]. Available: https://www.iea.org/publications/freepublications/publication/csp_roadmap.pdf

[26] H. Müller-Steinhagen and F. Trieb, “Concentrating solar power, - A review of the technology,” 2004.

[27] G. Francia, “Pilot plants of solar steam generating stations,” *Solar Energy*, vol. 12, no. 1, pp. 51–64, Sep. 1968, doi: 10.1016/0038-092X(68)90024-8.

[28] Mills D.R., “Solar thermal electricity,” in *Solar energy: the state of the art*, Gordon J, Ed., Germany: ISES, 2001, pp. 577–651.

[29] B. Zohuri, “Compact Heat Exchangers Application in New Generation of CSP,” 2017, pp. 339–354. doi: 10.1007/978-3-319-29835-1_8.

[30] G. Brakmann, R. Aringhoff, and M. E. Geyer, “Brussels: Greenpeace International, Amsterdam, IEA SolarPACES Implementing Agreement,” *Concentrated solar thermal power â€“now*.

[31] NREL “National Renewable Energy Laboratory” collaborating with SolarPACES “Solar Power and Chemical Energy Systems” the international program of the International Energy Agency", “CSP projects around the world.” [Online]. Available: https://solarpaces.nrel.gov/

[32] I. Purohit and P. Purohit, “Solar Thermal Power Generation☆,” in *Reference Module in Earth Systems and Environmental Sciences*, Elsevier, 2019. doi: https://doi.org/10.1016/B978-0-12-409548-9.11865-2.

[33] P. Schwarzbözl, R. Pitz-Paal, W. Meinecke, and R. Buck, “Cost Optimized Solar Gas Turbine Cycles using Volumetric Air Receiver Technology,” Sydney, Australia, 2000. [Online]. Available: https://api.semanticscholar.org/CorpusID:108272709

[34] J. M. Chavez, G. J. Kolb, W. Meinecke, M. Becker, and P. C. Klimas, “Second Generation Central Receiver Technologies–A Status Report,” *Becker M., Klimas PC, Verlag CF Müller, Karlsruhe, Germany*, 1993.

[35] R. Osunaa *et al.*, *PS10, CONSTRUCTION OF A 11MW SOLAR THERMAL TOWER PLANT IN SEVILLE, SPAIN*. 2006.

[36] Office of Energy Efficiency & Renewable Energy, “Concentrating solar power.” Accessed: May 10, 2024. [Online]. Available: https://www.energy.gov/eere/solar/concentrating-solar-thermal-power

[37] J. D. Nixon, P. K. Dey, and P. A. Davies, “Which is the best solar thermal collection technology for electricity generation in north-west India? Evaluation of options using the analytical hierarchy process,” *Energy*, vol. 35, no. 12, pp. 5230–5240, 2010.

[38] M. T. Islam, N. Huda, A. B. Abdullah, and R. Saidur, “A comprehensive review of state-of-the-art concentrating solar power (CSP) technologies: Current status and research trends,” *Renewable and Sustainable Energy*

Reviews, vol. 91, pp. 987–1018, 2018, doi: https://doi.org/10.1016/j.rser.2018.04.097.

[39] I. and U. Minister of Science, "Plataforma Solar De Almería," 2023. Accessed: Oct. 06, 2024. [Online]. Available: https://www.psa.es/en/techrep/2023/Annual%20Report%202023%20PSA.pdf

[40] Publications office of the European Union, "SOLGATE, solar hybrid gas turbine electric power system." Accessed: Oct. 06, 2024. [Online]. Available: https://op.europa.eu/en/publication-detail/-/publication/e4f88dd1-74ac-4416-aba0-3868cc8ea5ca

[41] M. Z. Malik *et al.*, "A review on design parameters and specifications of parabolic solar dish Stirling systems and their applications," *Energy Reports*, vol. 8, pp. 4128–4154, 2022, doi: https://doi.org/10.1016/j.egyr.2022.03.031.

[42] SolarPACES, "SolarPACES technology characterization solar dish systems.," 2016.

[43] A. Ummadisingu and M. S. Soni, "Concentrating solar power – Technology, potential and policy in India," *Renewable and Sustainable Energy Reviews*, vol. 15, no. 9, pp. 5169–5175, Dec. 2011, doi: 10.1016/j.rser.2011.07.040.

[44] Y. El-Tous, "Assessment of one-axis concentrating solar power technologies in Jordan using fuzzy logic," *Int J Energy Convers (IRECON)*, vol. 1, p. 238â, 2013.

[45] K. Lovegrove *et al.*, "Paraboloidal dish solar concentrators for multi-megawatt power generation," in *ISES Solar World Congress, Göteborg, Sweden*, Citeseer, 2003, pp. 16–19.

[46] R. Affandi, C. K. Gan, and M. R. Ab Ghani, "Performance comparison for parabolic dish concentrating solar power in high level DNI locations with George Town, Malaysia," *Applied Mechanics and Materials*, vol. 699, pp. 570–576, 2015, Accessed: May 23, 2024. [Online]. Available: https://www.nrel.gov/docs/fy13osti/57123.pdf

[47] F. Cavallaro, "Multi-criteria decision aid to assess concentrated solar thermal technologies," *Renew Energy*, vol. 34, no. 7, pp. 1678–1685, Jul. 2009, doi: 10.1016/j.renene.2008.12.034.

[48] A. Poullikkas, G. Kourtis, and I. Hadjipaschalis, "Parametric analysis for the installation of solar dish technologies in Mediterranean regions," *Renewable and Sustainable Energy Reviews*, vol. 14, no. 9, pp. 2772–2783, Dec. 2010, doi: 10.1016/j.rser.2010.07.021.

[49] S. Kalogirou, "Solar energy utilisation using parabolic trough collectors in Cyprus," *The Polytechnic of Wales, Master's thesis*, 1991.

[50] F. J. Cabrera, A. Fernández-García, R. M. P. Silva, and M. Pérez-García, "Use of parabolic trough solar collectors for solar refrigeration and air-conditioning

applications," *Renewable and Sustainable Energy Reviews*, vol. 20, pp. 103–118, 2013, doi: https://doi.org/10.1016/j.rser.2012.11.081.

[51] D. Zhan, H. Zhang, Y. Liu, S. Li, and J. Zhuang, "Investigation on Medium Temperature Heat Pipe Receiver used in Parabolic Trough Solar Collector," in *Proceedings of ISES World Congress 2007 (Vol. I – Vol. V)*, D. Y. Goswami and Y. Zhao, Eds., Berlin, Heidelberg: Springer Berlin Heidelberg, 2009, pp. 1823–1827.

[52] M. Elmnifi, M. Amhamed, N. Abdelwanis, and O. Imrayed, "SOLAR SUPPORTED STEAM PRODUCTION FOR POWER GENERATION IN LIBYA," *Acta Mechanica Malaysia*, vol. 2, no. 2, pp. 05–09, Jan. 2018, doi: 10.26480/amm.02.2018.05.09.

[53] X. Xu, K. Vignarooban, B. Xu, K. Hsu, and A. M. Kannan, "Prospects and problems of concentrating solar power technologies for power generation in the desert regions," *Renewable and Sustainable Energy Reviews*, vol. 53, pp. 1106–1131, 2016.

[54] S. Kalogirou, P. Eleftheriou, S. Lloyd, and J. Ward, "Low cost high accuracy parabolic troughs construction and evaluation," *Renew Energy*, vol. 5, no. 1–4, pp. 384–386, 1994.

[55] E. Lupfert, M. Geyer, W. Schiel, E. Zarza, R. O. Gonzalez-Anguilar, and P. Nava, "Eurotrough: a new parabolic trough collector with advanced light weight structure," in *Proceedings of Solar Thermal 2000 International Conference, on CD-ROM, Sydney, Australia*, 2000.

[56] M. Geyer *et al.*, "EUROTROUGH-Parabolic trough collector developed for cost efficient solar power generation," in *11th SolarPACES international symposium on concentrated solar power and chemical energy technologies*, 2002.

[57] D. Barlev, R. Vidu, and P. Stroeve, "Innovation in concentrated solar power," *Solar Energy Materials and Solar Cells*, vol. 95, no. 10, pp. 2703–2725, Oct. 2011, doi: 10.1016/j.solmat.2011.05.020.

[58] K. Europejska, *European research on concentrated solar Thermal energy*. Office for Official Publications of the European Communities, 2004.

[59] D. Barlev, R. Vidu, and P. Stroeve, "Innovation in concentrated solar power," May 11, 2010, *Davis, CA*.

[60] W. A. K. Al-Maliki, A. G. T. Al-Hasnawi, H. A. Abdul Wahhab, F. Alobaid, and B. Epple, "A Comparison Study on the Improved Operation Strategy for a Parabolic trough Solar Power Plant in Spain," *Applied Sciences*, vol. 11, no. 20, 2021, doi: 10.3390/app11209576.

[61] D. W. Kearney and H. W. Price, "Solar thermal plants-LUZ concept (current status of the SEGS plants)," in *Proceedings of the Second Renewable Energy Congress, Reading UK*, 1992, pp. 582–588.

[62] I.-S. Program and W. Grasse, *Solar PACES: Annual Report*. Deutsche Forschungsanstalt für Luft-und Raumfahrt eV, 1995.

[63] H. L. Zhang, J. Baeyens, J. Degrève, and G. Cacères, "Concentrated solar power plants: Review and design methodology," *Renewable and Sustainable Energy Reviews*, vol. 22, pp. 466–481, Jun. 2013, doi: 10.1016/j.rser.2013.01.032.

[64] U. Desideri and P. E. Campana, "Analysis and comparison between a concentrating solar and a photovoltaic power plant," *Appl Energy*, vol. 113, pp. 422–433, Jan. 2014, doi: 10.1016/j.apenergy.2013.07.046.

[65] D. Tiwari, A. F. Sherwani, D. Atheaya, A. Kumar, and N. Kumar, "Thermodynamic analysis of Organic Rankine cycle driven by reversed absorber hybrid photovoltaic thermal compound parabolic concentrator system," *Renew Energy*, vol. 147, pp. 2118–2127, Mar. 2020, doi: 10.1016/j.renene.2019.10.018.

[66] U. Pelay, L. Luo, Y. Fan, D. Stitou, and M. Rood, "Thermal energy storage systems for concentrated solar power plants," *Renewable and Sustainable Energy Reviews*, vol. 79, pp. 82–100, Nov. 2017, doi: 10.1016/j.rser.2017.03.139.

[67] O. Behar, A. Khellaf, and K. Mohammedi, "A review of studies on central receiver solar thermal power plants," *Renewable and Sustainable Energy Reviews*, vol. 23, pp. 12–39, Jul. 2013, doi: 10.1016/j.rser.2013.02.017.

[68] Office of energy efficiency & renewable energy, "Concentrating Solar Thermal Power."

[69] IRENA (International Renewable Energy Agency), "Solar Energy Data." Accessed: Apr. 27, 2024. [Online]. Available: https://www.irena.org/solar

[70] M. Shahabuddin, M. A. Alim, T. Alam, M. Mofijur, S. F. Ahmed, and G. Perkins, "A critical review on the development and challenges of concentrated solar power technologies," Oct. 01, 2021, *Elsevier Ltd*. doi: 10.1016/j.seta.2021.101434.

[71] X. Ju, C. Xu, Y. Hu, X. Han, G. Wei, and X. Du, "A review on the development of photovoltaic/concentrated solar power (PV-CSP) hybrid systems," *Solar Energy Materials and Solar Cells*, vol. 161, pp. 305–327, Mar. 2017, doi: 10.1016/j.solmat.2016.12.004.

[72] International Energy Agency (IEA), "World Energy Outlook," 2022. [Online]. Available: https://iea.blob.core.windows.net/assets/830fe099-5530-48f2-a7c1-11f35d510983/WorldEnergyOutlook2022.pdf

[73] N. Goyal, A. Aggarwal, and A. Kumar, "Concentrated solar power plants: A critical review of regional dynamics and operational parameters," *Energy Res Soc Sci*, vol. 83, p. 102331, Jan. 2022, doi: 10.1016/j.erss.2021.102331.

[74] A. Rahman, J. Keane, and M. A. Imteaz, "Rainwater harvesting in Greater Sydney: Water savings, reliability and economic benefits," *Resour Conserv Recycl*, vol. 61, pp. 16–21, Apr. 2012, doi: 10.1016/j.resconrec.2011.12.002.

[75] R. Farreny, T. Morales-Pinzón, A. Guisasola, C. Tayà, J. Rieradevall, and X. Gabarrell, "Roof selection for rainwater harvesting: Quantity and quality assessments in Spain," *Water Res*, vol. 45, no. 10, pp. 3245–3254, May 2011, doi: 10.1016/j.watres.2011.03.036.

[76] K. P. Bhandari, J. M. Collier, R. J. Ellingson, and D. S. Apul, "Energy payback time (EPBT) and energy return on energy invested (EROI) of solar photovoltaic systems: A systematic review and meta-analysis," *Renewable and Sustainable Energy Reviews*, vol. 47, pp. 133–141, Jul. 2015, doi: 10.1016/j.rser.2015.02.057.

[77] M. J. (Mariska) de Wild-Scholten, "Energy payback time and carbon footprint of commercial photovoltaic systems," *Solar Energy Materials and Solar Cells*, vol. 119, pp. 296–305, Dec. 2013, doi: 10.1016/j.solmat.2013.08.037.

[78] P. J. Verlinden, "High-Efficiency Back-Contact Silicon Solar Cells for One-Sun and Concentrator Applications," in *Practical Handbook of Photovoltaics*, Elsevier, 2012, pp. 449–475. doi: 10.1016/B978-0-12-385934-1.00014-3.

[79] R. C. Pietzcker, D. Stetter, S. Manger, and G. Luderer, "Using the sun to decarbonize the power sector: The economic potential of photovoltaics and concentrating solar power," *Appl Energy*, vol. 135, pp. 704–720, Dec. 2014, doi: 10.1016/j.apenergy.2014.08.011.

[80] S. P. Energy, "Technology roadmap: Solar photovoltaic energy," Technical Report, IEA, September 2014. Available online: https://www. iea …, 2014.

[81] J. D. Nixon, P. K. Dey, and P. A. Davies, "The feasibility of hybrid solar-biomass power plants in India," *Energy*, vol. 46, no. 1, pp. 541–554, 2012.

[82] R. Soria, J. Portugal-Pereira, A. Szklo, R. Milani, and R. Schaeffer, "Hybrid concentrated solar power (CSP)–biomass plants in a semiarid region: A strategy for CSP deployment in Brazil," *Energy Policy*, vol. 86, pp. 57–72, 2015.

[83] M. B. da Fonseca, W.-R. Poganietz, and H.-J. Gehrmann, "Environmental and economic analysis of SolComBio concept for sustainable energy supply in remote regions," *Appl Energy*, vol. 135, pp. 666–674, 2014.

[84] J. H. Peterseim, S. White, A. Tadros, and U. Hellwig, "Concentrating solar power hybrid plants–Enabling cost effective synergies," *Renew Energy*, vol. 67, pp. 178–185, 2014.

[85] J. H. Peterseim, A. Herr, S. Miller, S. White, and D. A. O'Connell, "Concentrating solar power/alternative fuel hybrid plants: Annual electricity potential and ideal areas in Australia," *Energy*, vol. 68, pp. 698–711, 2014.

[86] J. H. Peterseim, A. Tadros, S. White, U. Hellwig, J. Landler, and K. Galang, "Solar tower-biomass hybrid plants–maximizing plant performance," *Energy Procedia*, vol. 49, pp. 1197–1206, 2014.

[87] C. M. I. Hussain, B. Norton, and A. Duffy, "Technological assessment of different solar-biomass systems for hybrid power generation in Europe," *Renewable and Sustainable Energy Reviews*, vol. 68, pp. 1115–1129, 2017.

[88] J. H. Peterseim, U. Hellwig, A. Tadros, and S. White, "Hybridisation optimization of concentrating solar thermal and biomass power generation facilities," *Solar Energy*, vol. 99, pp. 203–214, 2014.

[89] "Global currency conversions." Accessed: Oct. 26, 2024. [Online]. Available: www.xe.com

[90] National Renewable Energy Laboratory (NREL), "Termosolar Borges power plant in Spain." Accessed: Apr. 29, 2024. [Online]. Available: https://solarpaces.nrel.gov/project/borges-termosolar

[91] A. Cot, A. Amettler, J. Vall-Llovera, J. Aguiló, and J. M. Arque, "Termosolar Borges: a thermosolar hybrid plant with biomass," in *Third international symposium on energy from biomass and waste*, CISA, Environmental Sanitary Engineering Centre, Italy Venice, Italy, 2010.

[92] S. J. Zarrouk and H. Moon, "Efficiency of geothermal power plants: A worldwide review," *Geothermics*, vol. 51, pp. 142–153, 2014.

[93] A. Franco and M. Villani, "Optimal design of binary cycle power plants for water-dominated, medium-temperature geothermal fields," *Geothermics*, vol. 38, no. 4, pp. 379–391, 2009.

[94] D. Wendt, G. Mines, C. Turchi, and G. Zhu, "Geothermal Risk Reduction via Geothermal/Solar Hybrid Power Plants. Final Report," Idaho National Lab.(INL), Idaho Falls, ID (United States), 2015.

[95] G. Dimarzio, L. Angelini, W. Price, C. Chin, and S. Harris, "The Stillwater Triple Hybrid Power Plant: Integrating Geothermal, Solar Photovoltaic and Solar Thermal Power Generation," 2015.

[96] C. Zhou, E. Doroodchi, I. Munro, and B. Moghtaderi, "A feasibility study on hybrid solar–geothermal power generation," in *New Zealand geothermal workshop*, 2011, pp. 1–7.

[97] C. Zhou, E. Doroodchi, and B. Moghtaderi, "An in-depth assessment of hybrid solar–geothermal power generation," *Energy Convers Manag*, vol. 74, pp. 88–101, 2013.

[98] C. Zhou, E. Doroodchi, and B. Moghtaderi, "Figure of merit analysis of a hybrid solar-geothermal power plant," *Engineering*, vol. 5, no. 01, p. 26, 2013.

[99] Á. Lentz and R. Almanza, "Solar–geothermal hybrid system," *Appl Therm Eng*, vol. 26, no. 14, pp. 1537–1544, 2006, doi: https://doi.org/10.1016/j.applthermaleng.2005.12.008.

[100] Á. Lentz and R. Almanza, "Parabolic troughs to increase the geothermal wells flow enthalpy," *Solar Energy*, vol. 80, no. 10, pp. 1290–1295, 2006, doi: https://doi.org/10.1016/j.solener.2006.04.010.

[101] M. Astolfi, L. Xodo, M. C. Romano, and E. Macchi, "Technical and economical analysis of a solar–geothermal hybrid plant based on an Organic Rankine Cycle," *Geothermics*, vol. 40, no. 1, pp. 58–68, 2011, doi: https://doi.org/10.1016/j.geothermics.2010.09.009.

[102] C. Zhou, "Hybridisation of solar and geothermal energy in both subcritical and supercritical Organic Rankine Cycles," *Energy Convers Manag*, vol. 81, pp. 72–82, 2014.

[103] J.G. Boghossian, "Dual-temperature Kalina Cycle for Geothermal-Solar Hybrid Power Systems," Massachusetts Institute of Technology , 2011.

[104] H. M. I. Pousinho, J. Esteves, V. M. F. Mendes, M. Collares-Pereira, and C. Pereira Cabrita, "Bilevel approach to wind-CSP day-ahead scheduling with spinning reserve under controllable degree of trust," *Renew Energy*, vol. 85, pp. 917–927, Jan. 2016, doi: 10.1016/j.renene.2015.07.022.

[105] C. Kost, B. Pfluger, W. Eichhammer, and M. Ragwitz, "Fruitful symbiosis: Why an export bundled with wind energy is the most feasible option for North African concentrated solar power," *Energy Policy*, vol. 39, no. 11, pp. 7136–7145, Nov. 2011, doi: 10.1016/j.enpol.2011.08.032.

[106] R. Sioshansi and P. Denholm, "Benefits of Colocating Concentrating Solar Power and Wind," *IEEE Trans Sustain Energy*, vol. 4, no. 4, pp. 877–885, Oct. 2013, doi: 10.1109/TSTE.2013.2253619.

[107] F. J. Santos-Alamillos, D. Pozo-Vázquez, J. A. Ruiz-Arias, L. Von Bremen, and J. Tovar-Pescador, "Combining wind farms with concentrating solar plants to provide stable renewable power," *Renew Energy*, vol. 76, pp. 539–550, Apr. 2015, doi: 10.1016/j.renene.2014.11.055.

[108] B. D. Vick and T. A. Moss, "Adding concentrated solar power plants to wind farms to achieve a good utility electrical load match," *Solar Energy*, vol. 92, pp. 298–312, Jun. 2013, doi: 10.1016/j.solener.2013.03.007.

[109] J. REICHLING and F. KULACKI, "Utility scale hybrid wind–solar thermal electrical generation: A case study for Minnesota," *Energy*, vol. 33, no. 4, pp. 626–638, Apr. 2008, doi: 10.1016/j.energy.2007.11.001.

[110] F. Petrakopoulou, A. Robinson, and M. Loizidou, "Simulation and evaluation of a hybrid concentrating-solar and wind power plant for energy autonomy on islands," *Renew Energy*, vol. 96, pp. 863–871, Oct. 2016, doi: 10.1016/j.renene.2016.05.030.

[111] G. Zhu, T. Neises, C. Turchi, and R. Bedilion, "Thermodynamic evaluation of solar integration into a natural gas combined cycle power plant," *Renew Energy*, vol. 74, pp. 815–824, Feb. 2015, doi: 10.1016/j.renene.2014.08.073.

[112] A. Rovira, R. Barbero, M. J. Montes, R. Abbas, and F. Varela, “Analysis and comparison of Integrated Solar Combined Cycles using parabolic troughs and linear Fresnel reflectors as concentrating systems,” *Appl Energy*, vol. 162, pp. 990–1000, Jan. 2016, doi: 10.1016/j.apenergy.2015.11.001.

[113] A. AlKassem, “A performance evaluation of an integrated solar combined cycle power plant with solar tower in Saudi Arabia,” *Renewable Energy Focus*, vol. 39, pp. 123–138, Dec. 2021, doi: 10.1016/j.ref.2021.08.001.

[114] A. Al-Rawy and E. Sulaiman, “Integrated combined cycle system with parabolic trough technology: A comprehensive review,” *SVU-International Journal of Engineering Sciences and Applications*, vol. 4, no. 2, pp. 194–208, Dec. 2023, doi: 10.21608/svusrc.2023.174185.1086.

[115] “NREL ‘National Renewable Energy Laboratory’ collaborating with SolarPACES ‘Solar Power and Chemical Energy Systems’ the international program of the International Energy Agency".” [Online]. Available: https://solarpaces.nrel.gov/

[116] R. K. Pal and R. K. K., “Two-fluid modeling of direct steam generation in the receiver of parabolic trough solar collector with non-uniform heat flux,” *Energy*, vol. 226, p. 120308, Jul. 2021, doi: 10.1016/j.energy.2021.120308.

[117] M. J. Montes, A. Rovira, M. Muñoz, and J. M. Martínez-Val, “Performance analysis of an Integrated Solar Combined Cycle using Direct Steam Generation in parabolic trough collectors,” *Appl Energy*, vol. 88, no. 9, pp. 3228–3238, 2011, doi: 10.1016/j.apenergy.2011.03.038.

[118] C. S. Turchi, Z. Ma, and M. Erbes, “Gas Turbine/Solar Parabolic Trough Hybrid Designs,” in *Volume 3: Controls, Diagnostics and Instrumentation; Education; Electric Power; Microturbines and Small Turbomachinery; Solar Brayton and Rankine Cycle*, ASMEDC, Jan. 2011, pp. 989–996. doi: 10.1115/GT2011-45184.

[119] M. Livshits and A. Kribus, “Solar hybrid steam injection gas turbine (STIG) cycle,” *Solar Energy*, vol. 86, no. 1, pp. 190–199, Jan. 2012, doi: 10.1016/j.solener.2011.09.020.

[120] G. Elsaket, “Simulating the integrated solar combined cycle for power plants application in Libya,” *Cranfield: Cranfield University*, 2007.

[121] Y. Li and Y. Yang, “Thermodynamic analysis of a novel integrated solar combined cycle,” *Appl Energy*, vol. 122, pp. 133–142, Jun. 2014, doi: 10.1016/j.apenergy.2014.02.017.

[122] H. Price *et al.*, “Advances in Parabolic Trough Solar Power Technology,” *J Sol Energy Eng*, vol. 124, no. 2, pp. 109–125, May 2002, doi: 10.1115/1.1467922.

[123] A. Rashad, A. Elweteedy, A. Temraz, and A. Gomaa, “Investigating an integrated solar combined cycle power plant,” *Glob. J. Eng. Sci. GJES*, vol. 7, pp. 1–14, 2021.

[124] A. M. A. Dayem, M. N. Metwally, A. S. Alghamdi, and E. M. Marzouk, "Numerical Simulation and Experimental Validation of Integrated Solar Combined Power Plant," *Energy Procedia*, vol. 50, pp. 290–305, 2014, doi: 10.1016/j.egypro.2014.06.036.

[125] R. Hosseini, M. Soltani, and G. Valizadeh, "Technical and economic assessment of the integrated solar combined cycle power plants in Iran," *Renew Energy*, vol. 30, no. 10, pp. 1541–1555, Aug. 2005, doi: 10.1016/j.renene.2004.11.005.

[126] H. Derbal-Mokrane, S. Bouaichaoui, N. El Gharbi, M. Belhamel, and A. Benzaoui, "Modeling and numerical simulation of an integrated solar combined cycle system in Algeria," in *Procedia Engineering*, 2012, pp. 199–208. doi: 10.1016/j.proeng.2012.01.1194.

[127] A. Elhaj Mohammed, K. Matrawy Kassim, and S. Yassin Jamal, "Theoretical analysis of a solar combined cycle power plant," in *Proceedings of the 3rd BSME–ASME international conference on thermal engineering. Dhaka (Bangladesh)*, 2006, pp. 20–22.

[128] O. Behar, A. Kellaf, K. Mohamedi, and M. Belhamel, "Instantaneous performance of the first Integrated Solar Combined Cycle System in Algeria," *Energy Procedia*, vol. 6, pp. 185–193, 2011, doi: 10.1016/j.egypro.2011.05.022.

[129] O. Behar, A. Khellaf, and K. Mohammedi, "Hassi R'Mel hybrid solar thermal power plant: Annual performance and advantages in Sahara desert.," Apr. 2012.

[130] M. Kane and D. Favrat, "Approche de conception et d'optimisation de centrale solaire intégrée à cycle combiné inspirée de la méthode du pincement (partie II: réseau d'échangeurs de chaleur)," *International Journal of Thermal Sciences*, vol. 38, no. 6, pp. 512–524, Jun. 1999, doi: 10.1016/S1290-0729(99)80024-6.

[131] Y. Allani, D. Favrat, and M. R. von Spakovsky, "CO2 mitigation through the use of hybrid solar-combined cycles," *Energy Convers Manag*, vol. 38, pp. S661–S667, Jan. 1997, doi: 10.1016/S0196-8904(97)00012-5.

[132] R. L. Loud and A. A. Slaterpryce, "Gas turbine inlet air treatment," *GE power generation, GER-3419A*, 1991.

[133] S. Wang, G. Zhang, and Z. Fu, "Performance analysis of a novel integrated solar combined cycle with inlet air heating system," *Appl Therm Eng*, vol. 161, p. 114010, Oct. 2019, doi: 10.1016/j.applthermaleng.2019.114010.

[134] S. Barakat, A. Ramzy, A. M. Hamed, and S. H. El Emam, "Enhancement of gas turbine power output using earth to air heat exchanger (EAHE) cooling system," *Energy Convers Manag*, vol. 111, pp. 137–146, Mar. 2016, doi: 10.1016/j.enconman.2015.12.060.

[135] Z. Zhang, L. Duan, Z. Wang, and Y. Ren, "General performance evaluation method of integrated solar combined cycle (ISCC) system," *Energy*, vol. 240, p. 122472, Feb. 2022, doi: 10.1016/j.energy.2021.122472.

[136] S. Semprini, D. Sánchez, and A. De Pascale, "Performance analysis of a micro gas turbine and solar dish integrated system under different solar-only and hybrid operating conditions," *Solar Energy*, vol. 132, pp. 279–293, Jul. 2016, doi: 10.1016/j.solener.2016.03.012.

[137] M. R. Meas and T. Bello-Ochende, "Thermodynamic design optimisation of an open air recuperative twin-shaft solar thermal Brayton cycle with combined or exclusive reheating and intercooling," *Energy Convers Manag*, vol. 148, pp. 770–784, Sep. 2017, doi: 10.1016/j.enconman.2017.06.043.

[138] A. Rovira *et al.*, "Comparison of different technologies for integrated solar combined cycles: Analysis of concentrating technology and solar integration," *Energies (Basel)*, vol. 11, no. 5, 2018, doi: 10.3390/en11051064.

[139] M. Amelio, V. Ferraro, V. Marinelli, and A. Summaria, "An evaluation of the performance of an integrated solar combined cycle plant provided with air-linear parabolic collectors," *Energy*, vol. 69, pp. 742–748, May 2014, doi: 10.1016/J.ENERGY.2014.03.068.

[140] L. Duan, W. Qu, S. Jia, and T. Feng, "Study on the integration characteristics of a novel integrated solar combined cycle system," *Energy*, vol. 130, pp. 351–364, 2017, doi: 10.1016/j.energy.2017.04.118.

[141] E. Okoroigwe and A. Madhlopa, "An integrated combined cycle system driven by a solar tower: A review," *Renewable and Sustainable Energy Reviews*, vol. 57, pp. 337–350, May 2016, doi: 10.1016/j.rser.2015.12.092.

[142] A. Rovira, M. J. Montes, F. Varela, and M. Gil, "Comparison of Heat Transfer Fluid and Direct Steam Generation technologies for Integrated Solar Combined Cycles," *Appl Therm Eng*, vol. 52, no. 2, pp. 264–274, Apr. 2013, doi: 10.1016/j.applthermaleng.2012.12.008.

[143] M. HAJİZADEH AGHDAM, M. H. KHOSHGOFTAR MANESH, N. KHANİ, and M. YAZDİ, "Energy, Exergy-Based and Emergy-Based Analysis of Integrated Solar PTC with a Combined Cycle Power Plant," *International Journal of Thermodynamics*, vol. 24, no. 4, pp. 17–30, Dec. 2021, doi: 10.5541/ijot.902374.

[144] M. Kane, D. Favrat, K. Ziegler, and Y. Allani, "Thermoeconomic Analysis of Advanced Solar-Fossil Combined Power Plants," *International Journal of Thermodynamics*, vol. 3, no. 4, pp. 191–198, 2000, [Online]. Available: https://dergipark.org.tr/en/pub/ijot/issue/5738/76597

[145] M. Falchetta, D. Mazzei, T. Crescenzi, and L. Merlo, "Design of the Archimede 5 MW molten salt parabolic trough solar plant," *Proceedings of the SolarPACES*, 2009.

[146] G. Manente, S. Rech, and A. Lazzaretto, "Optimum choice and placement of concentrating solar power technologies in integrated solar combined cycle

systems," *Renew Energy*, vol. 96, pp. 172–189, Oct. 2016, doi: 10.1016/j.renene.2016.04.066.

[147] O. Behar, "Solar thermal power plants – A review of configurations and performance comparison," *Renewable and Sustainable Energy Reviews*, vol. 92, pp. 608–627, Sep. 2018, doi: 10.1016/j.rser.2018.04.102.

[148] F. Calise, M. D. d'Accadia, L. Libertini, and M. Vicidomini, "Thermoeconomic analysis of an integrated solar combined cycle power plant," *Energy Convers Manag*, vol. 171, pp. 1038–1051, Sep. 2018, doi: 10.1016/J.ENCONMAN.2018.06.005.

[149] P. G. Brodrick, A. R. Brandt, and L. J. Durlofsky, "Operational optimization of an integrated solar combined cycle under practical time-dependent constraints," *Energy*, vol. 141, pp. 1569–1584, Dec. 2017, doi: 10.1016/j.energy.2017.11.059.

[150] G. Bonforte, J. Buchgeister, G. Manfrida, and K. Petela, "Exergoeconomic and exergoenvironmental analysis of an integrated solar gas turbine/combined cycle power plant," *Energy*, vol. 156, pp. 352–359, Aug. 2018, doi: 10.1016/j.energy.2018.05.080.

[151] M. T. Mabrouk, A. Kheiri, and M. Feidt, "A systematic procedure to optimize Integrated Solar Combined Cycle power plants (ISCCs)," *Appl Therm Eng*, vol. 136, pp. 97–107, May 2018, doi: 10.1016/j.applthermaleng.2018.02.098.

[152] A. E. Elmohlawy, V. F. Ochkov, and B. I. Kazandzhan, "Thermal performance analysis of a concentrated solar power system (CSP) integrated with natural gas combined cycle (NGCC) power plant," *Case Studies in Thermal Engineering*, vol. 14, p. 100458, Sep. 2019, doi: 10.1016/j.csite.2019.100458.

[153] M. Ameri and M. Mohammadzadeh, "Thermodynamic, thermoeconomic and life cycle assessment of a novel integrated solar combined cycle (ISCC) power plant," *Sustainable Energy Technologies and Assessments*, vol. 27, pp. 192–205, Jun. 2018, doi: 10.1016/j.seta.2018.04.011.

[154] G. Franchini, A. Perdichizzi, S. Ravelli, and G. Barigozzi, "A comparative study between parabolic trough and solar tower technologies in Solar Rankine Cycle and Integrated Solar Combined Cycle plants," *Solar Energy*, vol. 98, no. PC, pp. 302–314, Dec. 2013, doi: 10.1016/j.solener.2013.09.033.

[155] M. Horn, H. Führing, and J. Rheinländer, "Economic analysis of integrated solar combined cycle power plants," *Energy*, vol. 29, no. 5–6, pp. 935–945, Apr. 2004, doi: 10.1016/S0360-5442(03)00198-1.

[156] J. Dersch *et al.*, "Trough integration into power plants—a study on the performance and economy of integrated solar combined cycle systems," *Energy*, vol. 29, no. 5–6, pp. 947–959, Apr. 2004, doi: 10.1016/S0360-5442(03)00199-3.

[157] S. Gunasekaran, N. D. Mancini, R. El-Khaja, E. J. Sheu, and A. Mitsos, "Solar–thermal hybridization of advanced zero emissions power cycle," *Energy*, vol. 65, pp. 152–165, Feb. 2014, doi: 10.1016/j.energy.2013.12.021.

[158] G. Manente, “High performance integrated solar combined cycles with minimum modifications to the combined cycle power plant design,” *Energy Convers Manag*, vol. 111, pp. 186–197, Mar. 2016, doi: 10.1016/j.enconman.2015.12.079.

[159] H. Price *et al.*, “Advances in Parabolic Trough Solar Power Technology,” *J Sol Energy Eng*, vol. 124, no. 2, pp. 109–125, May 2002, doi: 10.1115/1.1467922.

[160] B. Kelly, U. Herrmann, and M. J. Hale, “Optimization Studies for Integrated Solar Combined Cycle Systems,” in *Solar Engineering 2001: (FORUM 2001: Solar Energy — The Power to Choose)*, American Society of Mechanical Engineers, Apr. 2001, pp. 393–398. doi: 10.1115/SED2001-150.

[161] C. V. Ponce, D. Sáez, C. Bordons, and A. Núñez, “Dynamic simulator and model predictive control of an integrated solar combined cycle plant,” *Energy*, vol. 109, pp. 974–986, Aug. 2016, doi: 10.1016/j.energy.2016.04.129.

[162] S. D. Oda and H. H. Hashem, “A case study for three combined cycles of a solar-conventional power generation unit,” *Solar & Wind Technology*, vol. 5, no. 3, pp. 263–270, Jan. 1988, doi: 10.1016/0741-983X(88)90023-9.

[163] E. J. Sheu, A. Mitsos, A. A. Eter, E. M. A. Mokheimer, M. A. Habib, and A. Al-Qutub, “A Review of Hybrid Solar–Fossil Fuel Power Generation Systems and Performance Metrics,” *J Sol Energy Eng*, vol. 134, no. 4, Nov. 2012, doi: 10.1115/1.4006973.

[164] G. Barigozzi, G. Franchini, A. Perdichizzi, and S. Ravelli, “Simulation of Solarized Combined Cycles: Comparison Between Hybrid GT and ISCC Plants,” in *Volume 4: Ceramics; Concentrating Solar Power Plants; Controls, Diagnostics and Instrumentation; Education; Electric Power; Fans and Blowers*, American Society of Mechanical Engineers, Jun. 2013. doi: 10.1115/GT2013-95483.

[165] S. Sundaray and T. C. Kandpal, “Preliminary feasibility evaluation of solar thermal power generation in India,” *International Journal of Sustainable Energy*, vol. 33, no. 2, pp. 461–469, Mar. 2014, doi: 10.1080/14786451.2013.770395.

[166] H. M. Kwon, T. S. Kim, J. L. Sohn, and D. W. Kang, “Performance improvement of gas turbine combined cycle power plant by dual cooling of the inlet air and turbine coolant using an absorption chiller,” *Energy*, vol. 163, pp. 1050–1061, Nov. 2018, doi: 10.1016/j.energy.2018.08.191.

[167] B. Dawoud, Y. H. Zurigat, and J. Bortmany, “Thermodynamic assessment of power requirements and impact of different gas-turbine inlet air cooling techniques at two different locations in Oman,” *Appl Therm Eng*, vol. 25, no. 11–12, pp. 1579–1598, Aug. 2005, doi: 10.1016/j.applthermaleng.2004.11.007.

[168] International Organizations for Standardization (ISO), "ISO conditions for gas turbine." Accessed: Oct. 14, 2024. [Online]. Available: https://www.iso.org/standard/80055.html

[169] Y. S. H. Najjar, A. M. Abubaker, and A. F. S. El-Khalil, "Novel inlet air cooling with gas turbine engines using cascaded waste-heat recovery for green sustainable energy," *Energy*, vol. 93, pp. 770–785, Dec. 2015, doi: 10.1016/j.energy.2015.09.033.

[170] A. A. El Hadik, "The Impact of Atmospheric Conditions on Gas Turbine Performance," *J Eng Gas Turbine Power*, vol. 112, no. 4, pp. 590–596, Oct. 1990, doi: 10.1115/1.2906210.

[171] M. A. H. El-Sayed, "Solar supported steam production for power generation in Egypt," *Energy Policy*, vol. 33, no. 10, pp. 1251–1259, Jul. 2005, doi: 10.1016/j.enpol.2003.11.021.

[172] a coalition of energy organizations Nebraska Municipal Power Pool "NMPP," "'Understanding the term (dispatchable) regarding electricity generation.'" [Online]. Available: https://www.nmppenergy.org/

[173] National Renewable Energy Laboratory (NREL), *Assessment of parabolic trough and power tower solar technology cost and performance forecasts. Report prepared by Sargent & Lundy LLC Consulting Group.* 2010.

[174] C. Bohtz, S. Gokarn, and E. Conte, "Integrated Solar Combined Cycles (ISCC) to meet renewable targets and reduce CO2 emissions," in *Power Gen Europe Conference, Austria*, 2013.

[175] B. J. Alqahtani and D. Patiño-Echeverri, "Integrated Solar Combined Cycle Power Plants: Paving the way for thermal solar," *Appl Energy*, vol. 169, pp. 927–936, May 2016, doi: 10.1016/j.apenergy.2016.02.083.

[176] Y. Li and Y. Yang, "Impacts of solar multiples on the performance of integrated solar combined cycle systems with two direct steam generation fields," *Appl Energy*, vol. 160, pp. 673–680, Dec. 2015, doi: 10.1016/j.apenergy.2015.08.094.

[177] M. A. Ajaj, "Parametric Analysis and Evaluation of Integrated Solar Combined Cycle Power Plants," 2019.

[178] J. R. Martín, E. B. Rodríguez, I. L. Paniagua, and C. G. Fernández, "Thermoeconomic Evaluation of Integrated Solar Combined Cycle Systems (ISCCS)," *Entropy*, vol. 16, no. 8, pp. 4246–4259, 2014, doi: 10.3390/e16084246.

[179] Math works, "MATLAB software," *https://www.mathworks.com/products.html?s_tid=nav_products*.

[180] Math works, "Ideal Air toolbox," Apr. 19, 2019, *https://www.mathworks.com/matlabcentral/fileexchange/71269-ideal-air-properties-at-constant-pressure-1-atm*.

[181] Math works, "XSteam toolbox," *https://www.mathworks.com/matlabcentral/fileexchange/9817-x-steam-thermodynamic-properties-of-water-and-steam*.

[182] "Egyptian Petrochemicals Company ." Accessed: Nov. 26, 2023. [Online]. Available: egy-petrochem.com

[183] M. Mohammed, "EXERGOECONOMIC ANALYSIS AND OPTIMIZATION OF COMBINED CYCLE POWER PLANTS WITH COMPLEX CONFIGURATION," 2015.

[184] World Nuclear Association, "Heat values of various fuels." Accessed: Nov. 26, 2023. [Online]. Available: https://world-nuclear.org/information-library/facts-and-Figures/heat-values-of-various-fuels.aspx

[185] Bergman T.L, "Heat exchangers," in *Fundamentals of heat and mass transfer*, Seventh., John Wiley & Sons, Ed., 2011, ch. 11.

[186] Z. Kadhim, M. S. Kassim, and A. Y., "Effect of Integral Finned Tube on Heat Transfer Characteristics for Cross Flow Heat Exchanger," *Int J Comput Appl*, vol. 139, pp. 20–25, Apr. 2016, doi: 10.5120/ijca2016909121.

[187] E. and T. and the M. of P. W. "Recognized Document of the Regulation of Thermal Installations in Buildings (RITE)" Joint resolution of the Ministries of Industry, "CO2 emission factors and passage coefficients to primary energy." Accessed: Nov. 26, 2023. [Online]. Available: https://energia.gob.es/desarrollo/EficienciaEnergetica/RITE/Reconocidos/Reconocidos/Otros documentos/Factores_emision_CO2.pdf

[188] "World weather & climate information." Accessed: Nov. 26, 2023. [Online]. Available: https://weather-and-climate.com/average-monthly-hours-Sunshine,Alexandria,Egypt

[189] Solutia, "Therminol VP-1: vapor phase/liquid phase heat transfer fluid." Accessed: Nov. 26, 2023. [Online]. Available: http://twt.mpei.ac.ru/tthb/hedh/htf-vp1.pdf

[190] T. Ruegamer *et al.*, "Molten Salt for Parabolic Trough Applications: System Simulation and Scale Effects," *Energy Procedia*, vol. 49, pp. 1523–1532, 2014, doi: 10.1016/j.egypro.2014.03.161.

[191] D. Barlev, R. Vidu, and P. Stroeve, "Innovation in concentrated solar power," *Solar Energy Materials and Solar Cells*, vol. 95, no. 10, pp. 2703–2725, Oct. 2011, doi: 10.1016/j.solmat.2011.05.020.

[192] J. A. Duffie and W. A. Beckman, "Solar engineering of thermal processes John Wiley & Sons," *Inc. New York*, 1991.

[193] M. Iqbal, "An introduction to solar radiation.," *An introduction to solar radiation.. M. Iqbal. Academic Press Inc*, 1983.

[194] C. L. Tutiempo Network, "Solar radiation in Alexandria." Accessed: May 23, 2024. [Online]. Available: https://en.tutiempo.net/solar-radiation/alexandria.html

[195] S. T. Mohammad, H. H. Al-Kayiem, M. K. Assadi, Osama. Sabir, and A. K. Khlief, "An integrated program of a stand-alone parabolic trough solar thermal power plant: Code description and test," *Case Studies in Thermal Engineering*, vol. 12, pp. 26–37, 2018, doi: https://doi.org/10.1016/j.csite.2018.02.006.

[196] Autodesk instructables, "Single axis tracker (horizontal north-south axis)." Accessed: Oct. 18, 2024. [Online]. Available: https://www.instructables.com/BH1750FVI-Based-Dual-Axis-Solar-Tracker/

[197] Thorsten A.Stuetzle, "Automatic control of a 30 MWe SEGS VI parabolic trough plant," Master of Science, University of Wisconsin Madison, 2002.

[198] I. Khoshrou, M. R. Jafari Nasr, and K. Bakhtari, "New opportunities in mass and energy consumption of the Multi-Stage Flash Distillation type of brackish water desalination process," *Solar Energy*, vol. 153, pp. 115–125, 2017, doi: https://doi.org/10.1016/j.solener.2017.05.021.

[199] National renewable energy laboratory "NREL," "Case Studies of Potential Facility-Scale and Utility-Scale Non-Hydro Renewable Energy Projects across Reclamation," May 2013. Accessed: May 23, 2024. [Online]. Available: https://www.nrel.gov/docs/fy13osti/57123.pdf

[200] A. Goel and G. Manik, "Solar thermal system—an insight into parabolic trough solar collector and its modeling," in *Renewable Energy Systems*, Elsevier, 2021, pp. 309–337.

[201] Global Solar Atlas, "Direct normal irradiation for Alexandria-Egypt." Accessed: Sep. 10, 2024. [Online]. Available: https://globalsolaratlas.info/detail?c=31.199181,29.895172,11&m=

LIST OF PUBLICATIONS

Peer-reviewed articles in indexed journals

Adham M. Abdelhalim, Andrés Meana-Fernández, and Ines Suarez-Ramon, *Integration of thermal solar power in an existing combined cycle for the reduction of carbon emissions and maximization of cycle efficiency, Processes (2025) – accepted for publication.*

Conferences

Adham M. Abdelhalim, Inés M. Suárez-Ramón, *Potential fuel savings in a combined cycle in Egypt by integrating a parabolic trough solar power plant, in 18th International conference on Renewable Energies and Power Quality "ICREPQ'20", (Granada, Spain, September 2020).*

Adham M Abdelhalim, Andrés Meana-Fernández, Ines Suarez-Ramon, *Integration of solar field into a combined cycle power plant for fuel saving in insular subtropical climates, in 36th International conference on efficiency, cost, optimization, simulation and environmental impact of energy systems "ECOS2023", (Las Palmas De Gran Canaria, Spain, June 2023).*

processes

MDPI

Article

Integration of Thermal Solar Power in an Existing Combined Cycle for a Reduction in Carbon Emissions and the Maximization of Cycle Efficiency

Adham Mohamed Abdelhalim [1], Andrés Meana-Fernández [2,*] and Ines Suarez-Ramon [2]

[1] Mechanical Engineering Department, College of Engineering and Technology, Arab Academy for Science, Technology and Maritime Transport, Alexandria 21611, Egypt; adhammuhamed90@aast.edu
[2] Thermal Machines and Engines Area, Department of Energy, University of Oviedo, 33204 Gijon, Spain; ines@uniovi.es
* Correspondence: andresmf@uniovi.es

Abstract: The energy transition towards renewable energy sources is vital for handling climate change, air pollution, and health-related problems. However, fossil fuels are still used worldwide as the main source for electricity generation. This work aims to contribute to the energy transition by exploring the best options for integrating a solar field within a combined cycle power plant. Different integration positions at the gas and steam cycles for the solar field were studied and compared under several operating conditions using a thermodynamic model implemented in MATLAB R2024a. Fuel-saving and power-boosting (flowrate and parameter boosting) strategies were studied. The results revealed that, for a maximum fuel savings of 7.97%, the best option was to integrate the field into the steam cycle before the economizer stage. With an integrated solar thermal power of 3 MW, carbon dioxide emissions from fuel combustion were reduced to 8.3 g/kWh. On the other hand, to maximize power plant generation, the best option was to integrate the field before the superheater, increasing power generation by 24.2% for a solar thermal power of 4 MW. To conclude, guidelines to select the best integration option depending on the desired outcome are provided.

Keywords: integrated solar combined cycle; energy efficiency; carbon emissions reduction; power boosting; fuel saving; flowrate boosting; parameter boosting; solar thermal power

Citation: Abdelhalim, A.M.; Meana-Fernández, A.; Suarez-Ramon, I. Integration of Thermal Solar Power in an Existing Combined Cycle for a Reduction in Carbon Emissions and the Maximization of Cycle Efficiency. *Processes* **2024**, *12*, x. https://doi.org/10.3390/xxxxx

Academic Editors: Roberta Campardelli and Paolo Trucillo

Received: 11 October 2024
Revised: 8 November 2024
Accepted: 13 November 2024
Published: date

1. Introduction

For more than 50 years, global energy consumption has been increasing at rates between 1% and 2% [1], with the only exceptions being the early 1980s (the energy crisis), 2009 (the financial crisis), and 2020 (the COVID crisis). In addition, the average energy consumption annual growth rate of 1.5% from 2010 to 2019 reached a maximum of 2.2% in the year 2023 [2]. Currently, fossil fuels provide more than 80% of the primary energy, with coal representing 27% of this total [3,4]. Between 1965 and 2022, the use of fossil fuels increased globally by 96,796 TWh, becoming around 2.4 times higher. Asia reached a total generation of 775,566 TWh from fossil fuels, and in Europe, fossil fuel generation grew by 21,391 TWh [1]. Iran experienced a growth of 3518%, passing from 92 to 3335 TWh. On the other hand, the United Kingdom reduced fossil fuel generation by 33%, from 2259 to 1519 TWh [1].

As long as fossil fuels lead the energy system, the world will continue to face energy scarcity for millions of people and the worsening of climate change and pollution effects. As the world population increases, so will the energy demand. Therefore, fuel consumption is expected to increase unless the efficiency of power generation systems is improved. In addition, low-carbon energy sources should replace fossil fuels in the energy mix to handle climate change, pollution, and health-related problems.

With the social demand for cleaner energy sources and technologies, most countries are making significant efforts to adopt renewable generation, which increased from 2795 TWh in 1965 to 23,848 TWh in 2022 [1]. Asia had the highest renewable energy consumption in 2022, with 10,879 TWh. South America increased renewable generation by 2270% from 1965 to 2022, passing from 117 TWh to 2773 TWh. As a consequence of those efforts, the global share of renewable energy in electricity generation is now around 30% [5]. The share of solar and wind power increased from 2.8% in 2012 to 12.1% in 2022 [6], with the investment in solar power increasing up to 310 billion dollars, a 36% increase from 2018 to 2022 [5]. The International Renewable Energy Agency (IRENA) expects the share of renewable energy consumption to reach 28% by 2030 and 66% by 2050 [7]. The share of renewables in the electricity sector is expected to increase more, reaching 57% by 2030 and 86% by 2050 [8].

Solar energy is one of the most important renewable energy sources. It is available and affordable, and it requires low maintenance costs [9]. Between 1991 and 2020, solar energy has expanded at an exponential rate and become a common energy source. In fact, it has been claimed that smart solar energy systems could supply the whole world energy demand without additional energy sources [10]. In addition, the carbon footprint of solar panels is 95% lower than coal-based technologies [11]. According to a study by Lawrence Berkeley National Laboratory in USA, the implementation of solar and wind energy between 2019 and 2022 generated USD 249 billion in climate, pollution, and health benefits, avoiding from 1200 to 1600 premature deaths [12]. In addition, the cost of renewable technologies has dropped by around 60%, especially in the case of solar panels [9]. Solar energy is predicted to become extremely cost-competitive by 2030, with prices from 0.02 to 0.08 USD/kWh [12].

Despite the advances in renewable technologies, gas power plants currently generate 22% of global electricity, with natural gas consumption increasing up to 6100 TWh in 2021 [6]. Combined cycles (CC) are the most common power plants, using exhaust gases from a top gas cycle to generate steam in a Heat Recovery Steam Generator (HRSG) and power a bottom steam cycle. A feasible strategy for reducing the environmental impact of combined cycles is the integration of solar energy in the so-called Integrated Solar Combined Cycles (ISCC), especially in tropical regions. These cycles, which combine gas-fired power cycles and Concentrated Solar Power (CSP) technologies, have the advantage of preventing power outer risks that could result from relying only on solar power. The thermal energy obtained from the combustion of natural gas is complemented by the thermal energy produced by solar concentrators, increasing the total efficiency of the system [13]. Although parabolic trough solar power plants were proposed in the 1990s by Luz Solar International [14], economic factors prevented the building of power plants before the 2000s, when the Global Environment Facility financed USD 50 million for the construction of four ISCC power plants in developing countries with intense solar irradiation, most of them in the Middle East. This incentive renewed the interest in Concentrated Solar Power (CSP) technologies, specifically in Parabolic Trough Collectors (PTC) [15]. It has been predicted that CSP power plants will represent 25% of global power generation by 2050 [16]. Due to the lower cost of thermal energy storage with respect to batteries, CSP technologies seem more suitable for baseload power generation than photovoltaic systems. Nevertheless, solar fields are still relatively costly [17].

Research has been conducted on solar thermal power integration at the top (Brayton) and the bottom (Rankine) cycles, with several hybrid setups [18,19]. When integrated into the top gas cycle, solar power is used to preheat compressed air before entering the combustion chamber [14]. When integrated into the bottom steam cycle, it is typically used to generate more steam to power the turbine [20,21]. Barigozzi et al. [22] investigated the performance of an ISCC with solar integration at the top and bottom cycles. A higher solar-to-electricity efficiency was obtained when solar power was integrated at the top cycle, but power generation was higher through integration in the bottom cycle.

According to Behar [23], PTCs with synthetic oils as the heat transfer fluid (HTF) are the most efficient method for solar power integration at the bottom cycle. The results from the work of Manente et al. [24] showed the highest solar-to-electricity efficiency values when synthetic oil was used to evaporate water at the high pressure level of the HRSG. This conclusion matches the results from Elmohlawy et al. [25], who found an increase in the thermal efficiency by 1.2% when injecting the steam at the high pressure level instead of at the intermediate one. El Mohalawy et al. [26] developed a model for two ISCC configurations with PTCs for a plant with an original capacity of 503 MW. In the first configuration, a solar steam generator (SSG) was used to complement the intermediate pressure evaporator and superheater. In the second configuration, the feedwater from the deaerator was superheated using the SSG. They found that the second configuration generated more power than the first one, allowing to reduce CO_2 emissions by around 51,671 ton.

Rovira et al. presented an innovative hybrid configuration [27] with a partially recuperative Brayton cycle for fuel saving with the introduction of solar power, achieving higher solar power shares than standard layouts. The 135 MW Kurymat plant in Egypt, in operation since 2011 [28], works by heating synthetic oil with PTCs and heating a portion of the high-pressure water of the steam cycle before it returns to the HRSG. Abdel Dayem et al. [28] developed a model of this plant, finding that the increase in direct normal irradiance (DNI) could increase the turbine power and the solar share by 10% and 25%, respectively. All these sources, along with the work of Muñoz, Rovira, and Montes [29], show that solar integration into the bottom cycle with PTCs and synthetic oils is the most common configuration in current or developing projects, with solar share values from 3% to 14%. The best thermodynamic performance is obtained when integrating solar energy at the high pressure level of the HRSG for steam evaporation and/or superheating. Javadi et al. [30] examined different possibilities for integrating solar power into a combined cycle with two pressure levels: preheating the fuel or air before the combustion chamber or integrating it at the high pressure level of the HRSG. In line with previous studies, the highest power generation at the lowest cost was found when solar power was integrated into the high-pressure line of the HRSG.

Hosseini et al. [31] compared six thermal power plants, claiming an ISCC with a 67 MW solar field to be the optimal configuration. This plant could avoid the emission of 2.4 Mt of CO_2 and save USD 59 million in fuel consumption over its 30-year operational life. Compared to a combined cycle and a simple gas turbine, its levelized cost of electricity (LCOE) is 10% and 33% less expensive. Aghdam et al. [32] explored the integration of solar power into an operating power plant in Iran, finding an increase in plant capacity and electrical efficiency from 714 to 728 MW and from 45 to 47%, respectively. A similar study was performed by Anwar [33] to assess the performance of solar integration of PTCs into the Al-Abdaliya CC in Kuwait with an Engineering Equation Solver (EES) model. The plant and solar capacities were 280 MW and 60 MW, respectively. The results showed that the ISCC efficiency was 20% higher than the original CC and that carbon emissions fall by around 64 kton/year. Ameri and Mohammadzadeh [34] conducted a thermodynamic, thermo-economic, and Life Cycle Analysis of three hybrid designs for a conventional plant in Iran. They reported an increase in power production of 6 MW and a reduction in carbon emissions of 10 g/kWh when the solar field was integrated into the superheater of the bottom steam cycle. Achour et al. [35] developed a thermodynamic model to calculate the thermal performance of an ISCC in Algeria. The overall plant efficiency reached 60%, while the solar-to-electricity efficiency reached 14.4%. Another model was generated by Manente [36] to evaluate the integration of solar energy into a combined cycle, finding that the solar-to-electricity efficiency was between 24 and 29%, but the drop in the gas turbine efficiency at lower load values decreased the ISCC thermal efficiency. Durán-García et al. [37] examined solar thermal power integration in parallel to the HRSG of a combined cycle with two pressure levels. When they introduced the solar field in parallel to the high-pressure economizer, the cycle efficiency increased by 1.32%, but when the solar

field was coupled to the low-pressure superheater, the efficiency increase was higher at 3.22%.

Regarding earlier studies that examined the integration of solar thermal power in a combined cycle power plant, some of them focused on solar integration at the top gas cycle, others focused on the bottom steam cycle, and most of them sought to increase plant output power generation. In this work, a study of solar thermal power integration in an existing combined cycle power plant is presented. A real combined cycle power plant in Egypt was examined with the aim of optimizing cycle efficiency and reducing fuel consumption and carbon emissions. Solar thermal power integration was studied at several positions in the top gas and bottom steam cycles and considering different operating strategies, namely fuel saving (FS) and power boosting (PB), providing a comprehensive study of the different possibilities for solar power integration. Firstly, the development of the thermodynamic model of the original combined cycle is presented. Then, the modifications of the model to be adapted to the different ISCC configurations and operating strategies are explained. Finally, the results from the model are assessed, providing guidelines for solar thermal power integration depending on the benefits sought: increasing cycle efficiency, maximizing power delivery, or reducing fuel consumption and carbon emissions.

2. Thermodynamic Model of the Original Combined Cycle

2.1. Description of the Combined Cycle

The combined cycle studied in this work is a 90.5 MW power plant in Alexandria, Egypt (latitude 31°12′ N, longitude 29°55′ E, altitude 18 m), property of Egyptian Petrochemicals Co. (EPC) [38]. Figure 1 shows the main components of the power plant: the top gas cycle, the bottom steam cycle, and the HRSG. The steam turbine is a DK-M 045 model fabricated by Brown, Boveri, and Cie (Baden, Switzerland), and the gas turbine is a GT8C model fabricated by ASEA Brown Boveri (Zurich, Switzerland).

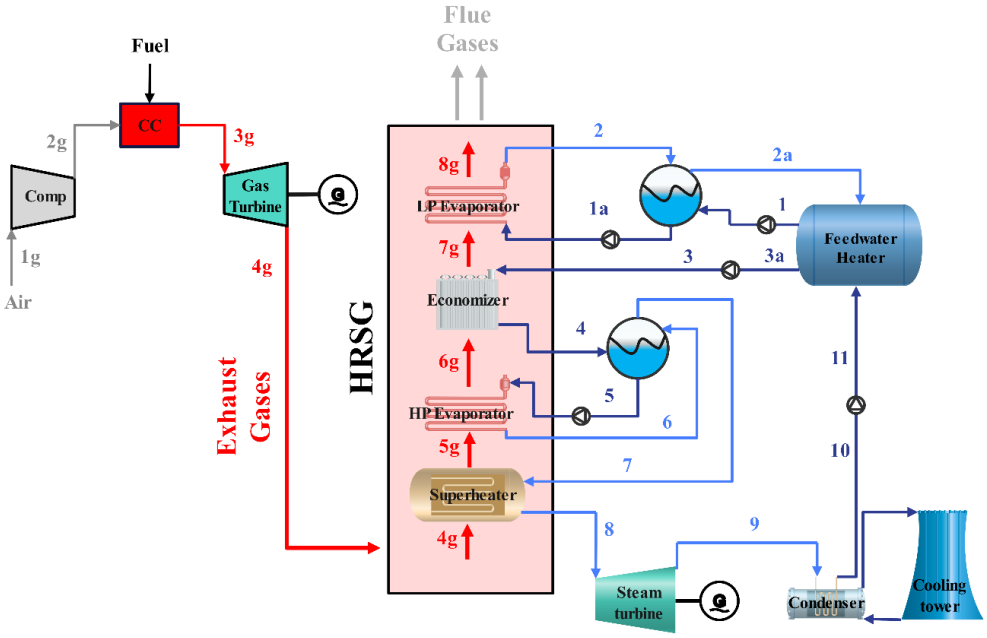

Figure 1. Diagram of the original combined cycle power plant.

Table 1 collects the main characteristics of the cycle, with a cycle efficiency of 56.1%, whereas Figure 2 displays its T-s diagram.

Table 1. Technical data of the combined cycle power plant.

Gas Cycle		Steam Cycle	
Ambient temperature	24 °C	Steam inlet pressure	43 bar
Ambient pressure	1 bar	Steam inlet temperature	457 °C
Combustion chamber inlet temperature	379 °C	LP evaporator pressure	2.4 bar
Turbine pressure	15.7 bar	Condenser pressure	0.08 bar
Turbine inlet temperature	1174 °C	Economizer outlet temperature	228 °C
Turbine exhaust temperature	549 °C	LP evaporator mass flowrate	5 kg/s
Exhaust mass flowrate	174.7 kg/s	HP evaporator mass flowrate	25 kg/s

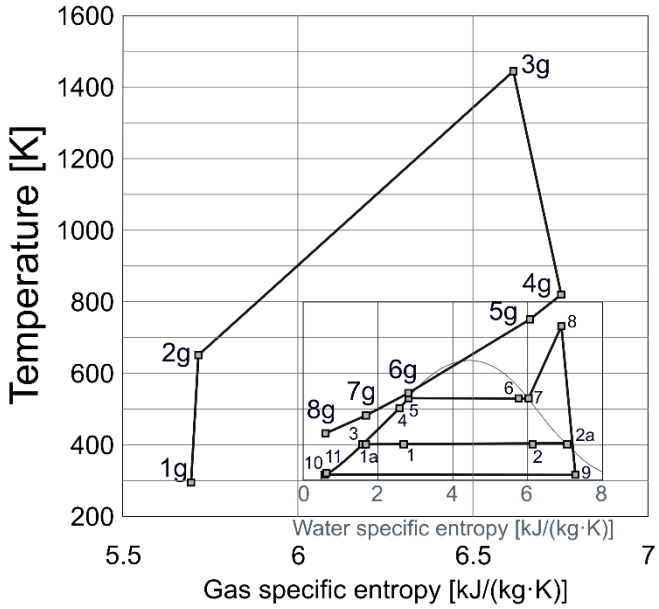

Figure 2. T-s diagram of the original combined cycle.

2.2. Thermodynamic Model

The thermodynamic model of the power plant was developed with MATLAB software [39], using the toolboxes Ideal Air [40] and X-Steam [41] to obtain water and air thermodynamic properties. As depicted on the left side of Figure 1, ambient air enters the compressor (1g), where it increases its temperature and pressure (2g). Then, it is mixed with fuel and burns in the combustion chamber, producing high-temperature gases (3g), which are expanded in the turbine up to ambient pressure (4g), generating power and entering the HRSG afterwards. From the pressure ratio r_P, pressures P_{ig} in bar and temperatures T_{ig} in K may be calculated as follows:

$$r_p = \frac{P_{2g}}{P_{1g}} = \frac{P_{3g}}{P_{4g}} \quad (1)$$

$$r_p^{\frac{k-1}{k}} = \frac{T_{2g}}{T_{1g}} \quad (2)$$

where the heat capacity ratio k is the ratio between the specific heat at constant pressure c_p and at constant volume c_v in kJ/(kg·K). The following equations were used to obtain the power of the gas turbine $\dot{W}_{GT}$ and compressor $\dot{W}_{comp}$, the thermal power supplied in the combustion chamber Q_{cc}, and the net power of the gas cycle $\dot{W}_{G_{net}}$ in kW:

$$\dot{W}_{GT} = \dot{m}_g \cdot (h_{3g} - h_{4g}) \quad (3)$$

$$\dot{W}_{comp} = \dot{m}_a(h_{2g} - h_{1g}) \quad (4)$$

$$\dot{Q}_{cc} = \dot{m}_f \cdot LHV = \dot{m}_g h_{3_g} - \dot{m}_a h_{2g} \quad (5)$$

$$\dot{W}_{G_{net}} = \dot{W}_{GT} - \dot{W}_{comp} \quad (6)$$

The mass flowrates of gases $\dot{m}_g$, air $\dot{m}_a$, and fuel $\dot{m}_f$ are expressed in kg/s, and the enthalpy h is expressed in kJ/kg. The natural gas lower heating value LHV is 47,000 kJ/kg [42]. The thermal efficiency of the top gas cycle is obtained as follows:

$$\eta_T = \frac{\dot{W}_{G_{net}}}{\dot{Q}_{cc}} \quad (7)$$

The main components of the bottom steam cycle, on the right side of Figure 1, are the turbine, condenser, and preheater. The steam turbine power in kW may be obtained:

$$\dot{W}_{ST} = \dot{m}_s \cdot (h_8 - h_9) \quad (8)$$

The power values of the high-pressure pump $\dot{W}_{hp_{pump}}$ and the feedwater pump $\dot{W}_{fw_{pump}}$ are as follows:

$$\dot{W}_{hp_{pump}} = \dot{m}_s \cdot (h_3 - h_{3a}) \quad (9)$$

$$\dot{W}_{fw_{pump}} = \dot{m}_s \cdot (h_{11} - h_{10}) \quad (10)$$

Then, the net power of the steam cycle can be calculated:

$$\dot{W}_{S_{net}} = \dot{W}_{ST} - \dot{W}_{hp_{pump}} - \dot{W}_{fw_{pump}} \quad (11)$$

where $\dot{m}_s$ is the steam flowrate in kg/s, and h_i is the steam enthalpy in kJ/kg. Consequently, the power plant net power and efficiency can be calculated:

$$\dot{W}_{Total} = \dot{W}_{G_{net}} + \dot{W}_{S_{net}} \quad (12)$$

$$\eta_{CC} = \frac{\dot{W}_{G_{net}} + \dot{W}_{S_{net}}}{\dot{Q}_{cc}} \quad (13)$$

The HRSG allows the exchange of thermal energy between the gas turbine exhaust gases and the water from the steam cycle. It consists of four heat exchangers: a superheater, a high-pressure (HP) evaporator, an economizer, and a low-pressure (LP) evaporator. As the UA values and specific configurations of the heat exchangers of the real power plant were not available, it was decided to calculate equivalent UA values using the effectiveness-Number of Transfer Units (ε-NTU) method [43] with a simplified analysis of an equivalent counterflow heat exchanger that operates with the same terminal temperatures and heat transfer rates as the original power plant. The pinch and approach temperatures were obtained from the available power plant data, allowing to adjust the model to match real operating conditions.

Initially, fluid outlet temperatures were guessed to calculate a first value of the Logarithmic Mean Temperature Difference (LMTD). Then, calculations were performed to obtain new values of the outlet temperatures. The LMTD is calculated as follows:

$$LMTD = \frac{\Delta T_1 - \Delta T_2}{\ln\left(\Delta T_1 / \Delta T_2\right)} \quad (14)$$

where ΔT_1 and ΔT_2 are the temperature differences between the hot and cold fluids at the inlet and outlet in K. The product of the heat transfer area A in m^2 and the heat transfer coefficient U in $W/(m^2 \cdot K)$ can be determined:

$$UA = \frac{\dot{Q}}{LMTD} \tag{15}$$

where $\dot{Q}$ is the heat transfer rate in kW. Once (UA) is calculated, the Number of Transfer Units (NTU) is obtained:

$$NTU = \frac{UA}{C_{min}} \tag{16}$$

where C_{min} is the smaller of the two heat capacity rates, i.e., C_{cold} and C_{hot}, of the cold and hot fluids in kW/K, determined from the mass flowrates $\dot{m}_i$ in kg/s and the fluid specific heats C_{P_i} in kJ/(kg·K):

$$C_{hot} = \dot{m}_{hot} . C_{P_{hot}} \qquad C_{cold} = \dot{m}_{cold} . C_{w_{cold}} \tag{17}$$

To obtain the relationship between the heat exchanger effectiveness ε and the NTU, the ratio between the smaller and greater heat capacity rates is calculated as follows:

$$C_r = \frac{C_{min}}{C_{max}} \tag{18}$$

The relationship between ε and NTU is obtained from the equation for heat exchangers in counterflow arrangement with a single pass:

$$\varepsilon = \frac{1 - \exp[-NTU \cdot (1 - C_r)]}{1 - C_r \cdot \exp[-NTU \cdot (1 - C_r)]} \tag{19}$$

Which, for a phase change heat exchanger ($C_r \cong 0$), becomes the following:

$$\varepsilon = 1 - \exp[-NTU] \tag{20}$$

The value of ε obtained allows to relate the actual and maximum possible thermal energy transfer rates $\dot{Q}_{actual}$ and $\dot{Q}_{maximum}$ in kW:

$$\varepsilon = \frac{\dot{Q}_{actual}}{\dot{Q}_{maximum}} \tag{21}$$

The maximum possible heat exchanged $\dot{Q}_{maximum}$ can be expressed as given below:

$$\dot{Q}_{maximum} = C_{min}(T_{hot,in} - T_{cold,in}) \tag{22}$$

This equation can be specified for two different cases:

$$C_c < C_h: \; C_{min} = C_c \rightarrow \; \varepsilon = \frac{(T_{cold,out} - T_{cold,in})}{(T_{hot,in} - T_{cold,in})} \tag{23a}$$

$$C_h < C_c: \; C_{min} = C_h \rightarrow \; \varepsilon = \frac{(T_{hot,in} - T_{hot,out})}{(T_{hot,in} - T_{cold,in})} \tag{23b}$$

where $T_{i,in}$ and $T_{i,out}$ are the fluid inlet and outlet temperatures and are in K. A new value for the first fluid (with C_{min}) outlet temperature $T_{1,out}$ is then obtained. Assuming no heat losses in the exchanger, the actual heat transfer rate and the outlet temperature of the second fluid (with C_{max}) are calculated from the following equations:

$$\dot{Q}_{actual} = \dot{m}_{hot} . C_{p_{hot}} . (T_{hot,in} - T_{hot,out}) \tag{24a}$$

$$\dot{Q}_{actual} = \dot{m}_{cold} . C_{p_{cold}} . (T_{cold,out} - T_{cold,in}) \tag{24b}$$

Figure 3 shows the temperature–heat transfer rate diagram of the original combined cycle, where the evolution of temperatures across the HRSG may be observed. The pinch and approach temperatures are 17.5 K and 28 K, whereas the UA values that fit the power plant data are 449 kW/K for the feedwater heater, 164.5 kW/K for the low-pressure

evaporator, 175.5 kW/K for the economizer, 475 kW/K for the high-pressure evaporator, and 84.5 kW/K for the superheater.

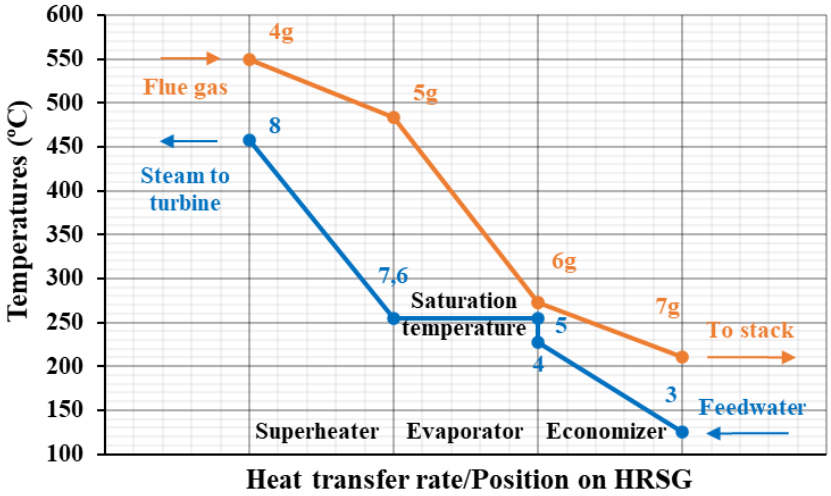

Figure 3. T-Q diagram of the original combined cycle.

2.3. Validation of the Model

As explained in the previous subsection, one part of the data obtained from the EPC power plant was used as input data for the model, whereas the rest (intermediate temperatures, pinch, and approach points) were used to validate the model. A comparison between the EPC power plant real values and the values obtained from the model is presented in Table 2. The results show good agreement, enabling the developed model to be used for the study of solar power integration into the original combined cycle.

Table 2. Results of the thermodynamic model vs. actual values from the EPC power plant.

Operating & Design Conditions	Model	EPC Power Plant
Gas turbine cycle		
Air mass flowrate, kg/s	171.2	171.2
Air to fuel ratio	50	50
Pressure ratio, r_p	15.7	15.7
Turbine inlet temperature, °C	1174	1100
Exhaust temperature, °C	549	540
Power output, MW	90,569	90,569
Top gas cycle efficiency, %	39.84%	39.84%
Steam Turbine cycle		
LP steam mass flowrate, kg/s	5	5
HP steam mass flowrate, kg/s	25	25
Turbine inlet pressure, bar	43	43
Power output, MW	26,292	26,292
Bottom steam cycle efficiency, %	27.1	NA
Heat recovery steam generator (HRSG)		
Pinch point temperature, K	17.5	17.5
Approach temperature, K	28	28
Stack temperature, °C	160	172
(UA) Feedwater heater, kW/K	449	NA
(UA) Low-pressure evaporator, kW/K	164.5	NA
(UA) Economizer, kW/K	175.5	NA
(UA) High-pressure evaporator, kW/K	475	NA

(UA) Superheater, kW/K	84.5	NA
Combined cycle		
Total output power, MW	90,569	90,569
Efficiency, %	56.13	56.13

3. Study of Solar Power Integration (ISCC)

The validated model presented in the previous section was modified to integrate solar thermal power into the combined cycle. Two operating strategies, fuel saving (FS) and power boosting (PB), were analyzed. Figure 4 shows the four possible solar integration positions A, B, C, and D in the gas and steam cycles.

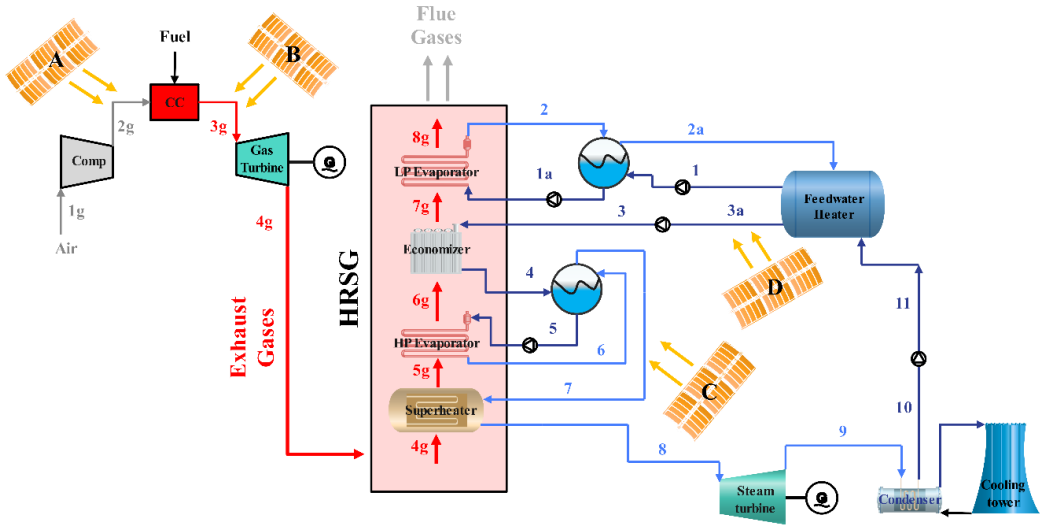

Figure 4. Solar field integration options.

3.1. Fuel-Saving Mode

For fuel-saving operation, the solar field was integrated into the gas or steam cycle to allow a reduction in fuel consumption while keeping the output power of the cycle constant. Once the amount of saved fuel was obtained, the direct reduction in CO_2 emissions was calculated from the natural gas LHV and the natural gas/CO_2 emission ratio $EF_{NG \to CO_2}$ = 0.252 kg/kWh [44]:

$$CO_{2,avoided} = \dot{m}_{f_{saved}} \cdot LHV \cdot EF_{NG \to CO_2} \cdot \Delta t \quad (25)$$

where Δt is the mean solar operation time for Alexandria, i.e., 275 h/month [45], and $\dot{m}_{f_{saved}}$ is the fuel consumption reduction thanks to solar thermal power integration in kg/h. Solar integration at the gas cycle differs from integration at the steam, as explained in the following two subsections.

3.1.1. Gas Cycle Integration

As shown in Figure 4, solar thermal power can be integrated at two positions: after the air compressor in order to heat compressed air before it enters the combustion chamber (case A) and after the combustion chamber in order to heat combustion gases before they enter the turbine (case B). According to the literature, case A is the most typical alternative, but case B is worth investigating. The assumptions considered for gas cycle integration in the FS scheme are as follows:

- Mass flowrates of fuel and air are altered depending on the solar thermal power;
- Compression specific work is constant;
- Gas turbine inlet and outlet conditions are constant;
- The turbine specific work is constant;

- The top gas cycle output power is constant;
- The mass flowrate of fuel is reduced;
- The bottom steam cycle is unaffected;
- The ISCC overall output power remains constant.

(a) Case A: After air compressor

As shown in Figure 5, the solar field is integrated after the compressor, heating the compressed air before it enters the combustion chamber.

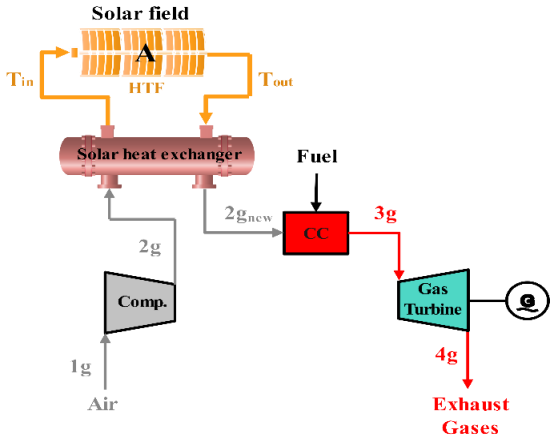

Figure 5. Case A: solar field integration after air compressor.

The original thermodynamic model was adapted by modifying the air and fuel mass flowrates $\dot{m}_{a_{new}}$ and $\dot{m}_{f_{new}}$, so compression power $\dot{W}_{comp}$ becomes the following:

$$\dot{W}_{comp} = \dot{m}_{a_{new}}(h_{2g} - h_{1g}) \quad (26)$$

The energy balance in the combustion chamber is reformulated as given below:

$$\dot{m}_{a_{new}} \cdot h_{2g_{new}} + \dot{Q}_{cc} = \dot{m}_{a_{new}} \cdot h_{2g_{new}} + \dot{m}_{f_{new}} \cdot LHV = \dot{m}_g h_{3_g} \quad (27)$$

The solar heat power integrated $\dot{Q}_{Solar}$ in kW, assuming no heat losses, becomes the following:

$$\dot{Q}_{Solar} = \dot{m}_{a_{new}} \cdot (h_{2g_{new}} - h_{2g}) \quad (28)$$

(b) Case B: After combustion chamber

As depicted in Figure 6, the solar field is integrated after the combustion chamber to heat combustion gases before they enter the gas turbine, resulting in the new thermodynamic state $3g_{new}$. The challenge of heating hot gases from the combustion chamber is significant since they must reach a very high temperature before entering the turbine. The thermodynamic model uses the same assumptions as for case A. As the turbine inlet and outlet conditions are the same as for the original cycle, solar thermal power will allow to reduce fuel consumption in the combustion chamber, reducing the temperature of $3g_{new}$.

An energy balance in the combustion chamber yields the following:

$$\dot{m}_{a_{new}} \cdot h_{2g} + \dot{Q}_{cc} = \dot{m}_{a_{new}} \cdot h_{2g} + \dot{m}_{f_{new}} \cdot LHV = \dot{m}_g h_{3g_{new}} \quad (29)$$

And the solar thermal power integrated, assuming no heat losses, becomes the following:

$$\dot{Q}_{Solar} = \dot{m}_{a_{new}} \cdot (h_{3g} - h_{3g_{new}}) \quad (30)$$

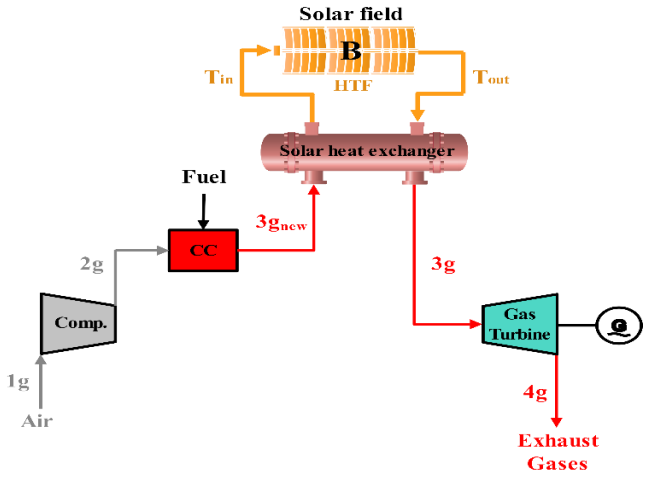

Figure 6. Case B: solar field integration after combustion chamber.

3.1.2. Steam Cycle Integration

When working in the fuel-saving operation mode, solar thermal power can be integrated into the bottom steam cycle as well. In this case, the solar integration will compensate for the loss of the gas turbine output power due to the reduction in fuel consumption. Two integration positions were examined: before the superheater, so that saturated steam from the HP drum is heated before entering the actual superheater stage (case C), and before the economizer, with feedwater being preheated before the economizer (case D).

(a) Case C: Integration before superheater

In this configuration, as shown in Figure 7, outlet steam from the HP drum is heated by the solar field before it enters the superheater. The HRSG temperature distribution will change as water and steam temperatures increase. Hence, the steam turbine will generate more power to compensate for the reduction in the top gas cycle power, allowing to reduce fuel consumption.

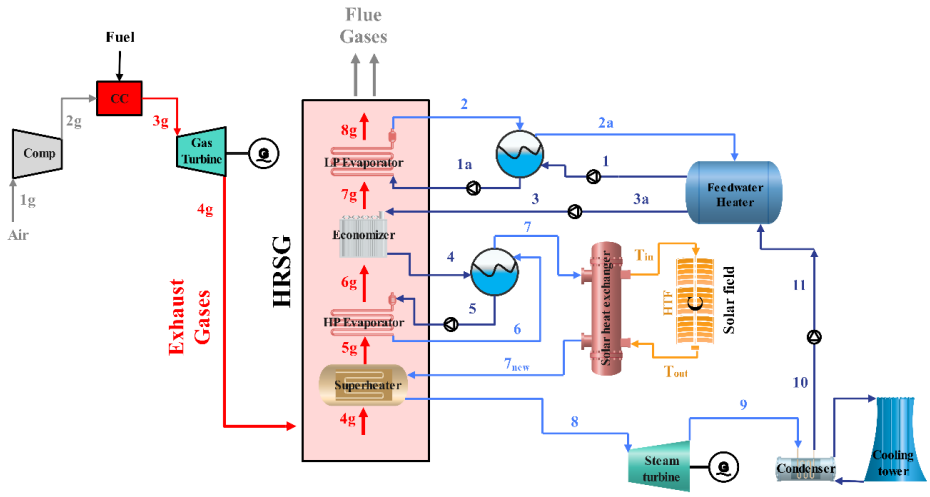

Figure 7. Case C: solar field integration before superheater.

The solar heat power integrated, assuming no heat losses, results in the following:

$$\dot{Q}_{Solar} = \dot{m}_s \cdot \left(h_{7_{new}} - h_7\right) \quad (31)$$

(b) Case D: Integration at economizer

The solar field can be integrated into the bottom steam cycle after the feedwater outlet to preheat water before it enters the economizer, as depicted in Figure 8. As in case C, the

temperature distribution along the HRSG will be shifted upwards, increasing the steam turbine output power and allowing the use of less fuel in the gas cycle.

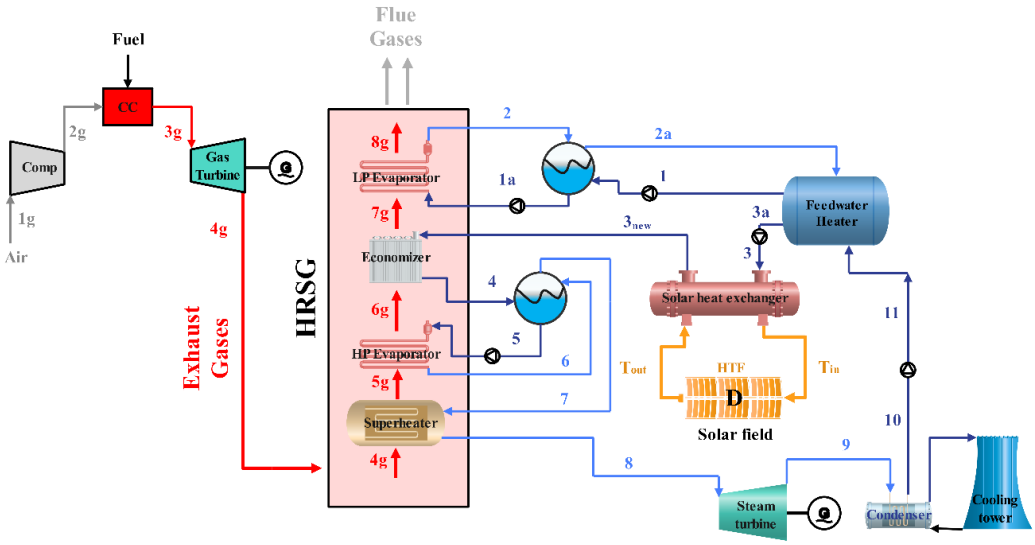

Figure 8. Case D: solar field integration at economizer.

The solar heat power integrated, assuming no heat losses, is as follows:

$$\dot{Q}_{Solar} = \dot{m}_s \cdot (h_{3_{new}} - h_3) \quad (32)$$

3.2. Power-Boosting Mode

In the power-boosting mode, the same fuel consumption as for the original combined cycle is kept constant, so the integration of the solar field increases the output power of the plant. The same four integration positions examined for the fuel-saving mode, indicated in Figure 4, were studied, but the assumptions for the model change.

3.2.1. Gas Cycle Integration

In this case, the added solar heat will result in an increase in the power output of the gas turbine. Solar thermal power integration was studied after the air compressor (case A, Figure 5) and after the combustion chamber (case B, Figure 6). The developed thermodynamic models were modified with the following assumptions:

- Air and gas mass flowrates change depending on the integrated solar thermal power;
- Fuel mass flowrate is steady;
- Compression work increases;
- Gas turbine inlet and outlet conditions are constant;
- The total output power of the upper gas cycle increases;
- The bottom steam cycle is unaffected. The ISCC overall output power increases.

3.2.2. Steam Cycle Integration

In this case, the gas cycle works at the same conditions as in the original cycle, and the integration of solar power increases the power output of the bottom steam cycle. The same two integration positions as for fuel saving, i.e., before the superheater (case C, Figure 7) and before the economizer (case D, Figure 8) of the HRSG, were studied. Two different operating modes, flowrate and parameter boosting, were considered for each integration position. In the flowrate-boosting mode, the integrated power is used to increase the steam flowrate, whereas in the parameter boosting, it modifies the thermodynamic states of the steam cycle, which continues working with the same steam flowrate.

3.3. Solar Field Technology Selection

Before moving on to the results, considerations about the solar field technology to be used are presented, depending on their operating temperatures. Table 3 collects the characteristics of different solar concentration technologies so that, depending on the solar power integration position, the most suitable technology can be selected. According to the literature, the most common technology in ISCCs is the use of PTCs with Therminol VP-1 as HTF. Therminol VP-1 is characterized by a low dynamic viscosity and a high heat capacity over a large operational temperature range [46]. However, its maximum operating temperature is 390 °C. As the temperature of the cycle working fluids could be higher, solar molten salts could be an alternative HTF [47], as they are able to reach much higher temperatures up to 550 °C. Nevertheless, for temperatures too high, PDR or heliostats will be the only option.

Table 3. Concentrating solar collectors [48,49].

Collector Type	Parabolic Trough Collectors (PTC)	Parabolic Dish Reflectors (PDR)	Heliostat Field Collectors (Solar Power Tower)
Description	Parabolic sheet of reflective material.Linear receiver (metal pipe with heat transfer fluid)	Large reflective parabolic dish with stirring high engine receiver at focal point	Large heliostat field with tall tower in its center.Receiver: water/HTF boiler at top
Operating range (°C)	50–400	150–1500	300–2000
Relative cost	Low	Very high	High
Concentration ratio [1]	15–45	100–1000	150–1500
Tracking	One-Axis	Two-Axis	Two-Axis
Efficiency (%)	~18	~30	~25–28

[1] Ratio of the effective area of the aperture to the receiver/absorber area of the collector.

4. Results

Every studied configuration was considered in both fuel-saving and power-boosting operating modes. For fuel saving, maximum reductions in fuel consumption and CO_2 emissions were the target; for power boosting, maximization of the output power was the goal. In addition, the maximum solar thermal power that can be integrated into the cycle was evaluated. To make reading easier, the detailed results of all the studied configurations are collected in Appendix A (Tables A1–A8), leaving only the most relevant data in this section.

4.1. Fuel-Saving Mode

4.1.1. Gas Cycle Integration

The results of the fuel-saving cases alongside the original values of the combined cycle are collected in Table 4. Total net power remains constant and equal to the original cycle value, 90,569 MW, but the cycle efficiency increases slightly to 56.15%. When compared to the original CC, cases A and B show significant benefits, such as the reduction in fuel consumption of 6.23% when 10 MW solar thermal power is integrated into the cycle. Fuel saving as a function of the integrated solar thermal power is represented in Figure 9a, showing linear behavior. With 28.2 MJ/kg specific work per fuel unit mass, both cases A and B result in cutting carbon emissions by 6.4 g CO_2/kWh. In case A, PTC technology could be employed for the solar field placed after the compressor. However, molten salts should be used as HTF, as the maximum output temperature of the solar heat exchanger ($T2g_{new}$) reaches 433 °C at 10 MW of integrated solar power, as shown in Figure 9b.

Table 4. Original CC vs. ISCC (case A and case B) "Fuel saving".

Mass Flowrates	Original CC	ISCC Case A	ISCC Case B
Fuel flowrate (kg/s)	3.42	3.21	
Fuel saving (%)	--	6.23	
Solar heat integration	**Original CC**	**ISCC Case A**	**ISCC Case B**
Integrated solar heat (MW)	--	10	
Cycle efficiency	**Original CC**	**ISCC Case A**	**ISCC Case B**
Gas turbine cycle (%)	39.84	39.85	
Combined cycle (%)	56.13	56.15	
Cycle power breakdown	**Original CC**	**ISCC Case A**	**ISCC Case B**
Gas cycle (kW)	64,277	64,277	64,277
Steam cycle (kW)	26,292	26,292	26,292
Total net power (kW)	90,569	90,569	90,569
Specific work per fuel unit mass flow (kJ/kg)	26,439	28,198	28,198
CO_2 emissions (Mt/year)	0.2971	0.2785	0.2785
CO_2 emissions saved (kg CO_2/kWh)	-	0.0064	0.0064

In case B, although global values are the same as in case A, the temperatures of the different states of the gas cycle change, as collected in Table A1. The outlet temperature of the combustion chamber state $3g_{new}$ becomes lower, requiring less fuel because the solar heat exchanger will provide the additional heat necessary for reaching the temperature of the state 3g just before the turbine inlet. In case B, when solar power is integrated into the cycle, heat must be transferred to gases at temperatures from 1126.5 °C ($3g_{new}$) to 1174 °C (3g), as depicted in Figure 9b. Only heliostat field collectors will be able to provide the required solar thermal power at those temperatures. Comparing options A and B, case A shows a clear advantage, as it allows integrating more solar field technologies.

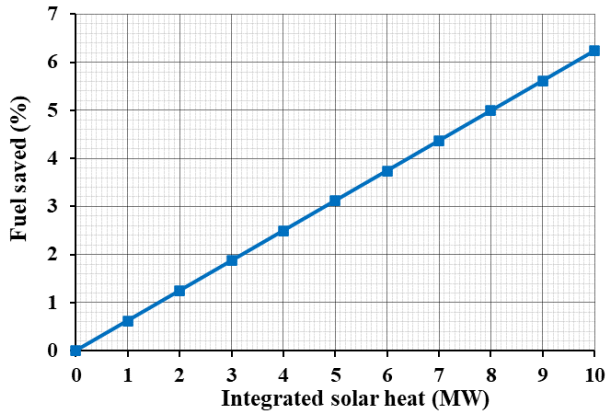

(**a**) Fuel saving (%) as a function of integrated solar heat

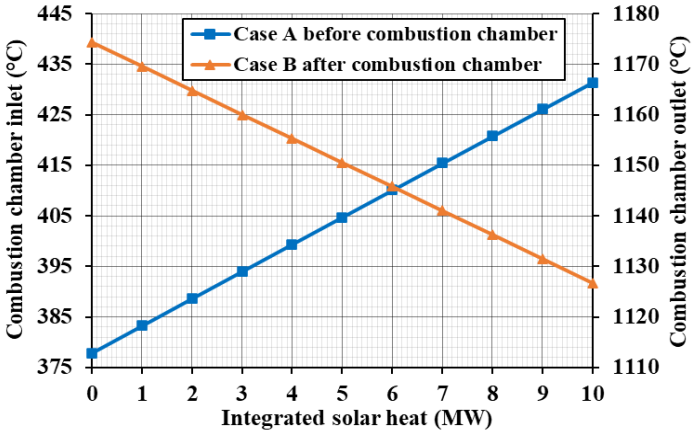

(**b**) Temperature changes as a function of integrated solar heat

Figure 9. Fuel saving (**a**) and temperature changes (**b**) for integration options A and B.

4.1.2. Steam Cycle Integration

When solar thermal power is integrated into the bottom steam cycle, attention must be paid to steam temperatures. If they rise too much, the direction of heat transfer might be reversed inside the HRSG. To prevent this issue, temperature evolutions inside the HRSG were controlled, obtaining the maximum solar thermal power that may be integrated into the cycle. The detailed results from cases C and D are collected in Table A2.

The results from the study of cases C and D are collected in Table 5. In both cases, the top gas cycle was unaffected by solar power integration. The configuration of case C allowed to integrate a maximum of 15 MW solar thermal power before the superheater stage, avoiding the heat transfer reversal inside the HRSG, as depicted in the T-Q diagram shown in Figure 10. This configuration could reduce fuel consumption to 3.3 kg/s, a decrease of 3.49% of the original value. However, the total ISCC efficiency was 53.06%, lower than for the original cycle. On the other hand, the specific work per fuel unit mass increased to 27.4 MJ/kg, leading to a potential reduction in emissions of 3.5 g CO_2/kWh. For the configuration presented in case C, as the maximum temperature reached is 480 °C for 15 MW of integrated solar power, the solar field used could be either PDR, heliostats, or even PTCs with molten salts as HTF.

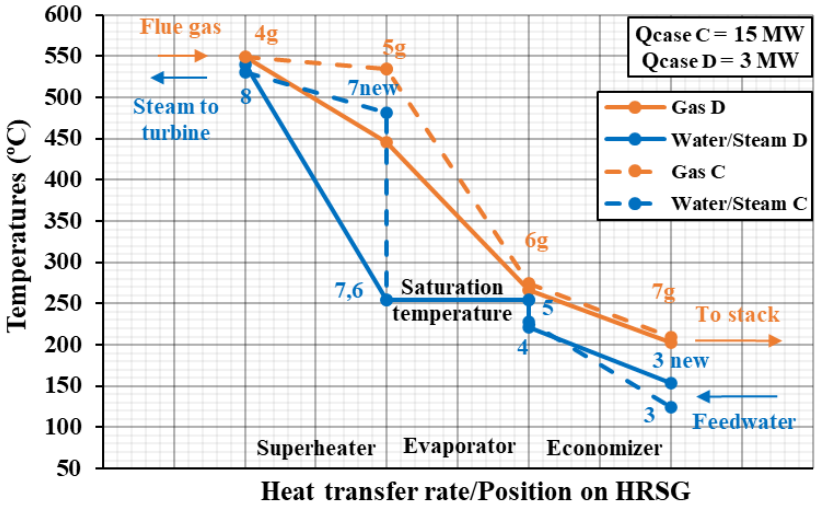

Figure 10. T-Q diagram for cases C and D (fuel saving).

Table 5. Original CC vs. ISCC (case C and case D) "Fuel saving".

Mass Flowrates	Original CC	ISCC Case C	ISCC Case D
Fuel flowrate (kg/s)	3.42	3.3	3.15
Fuel saving (%)	--	3.49	7.97
Solar heat integration	**Original CC**	**ISCC Case C**	**ISCC Case D**
Integrated solar heat (MW)	--	15	3
Cycle efficiency	**Original CC**	**ISCC Case C**	**ISCC Case D**
Gas turbine cycle (%)	39.84	39.84	39.84
Combined cycle (%)	56.13	53.06	59.79
Cycle power breakdown	**Original CC**	**ISCC Case C**	**ISCC Case D**
Compressor (kW)	62,450	60,266	57,471
Gas turbine (kW)	126,727	122,294	116,622
Gas cycle (kW)	64,277	62,028	59,152
Steam cycle (kW)	26,292	28,542	31,417

Total net power (kW)	90,569	90,569	90,569
Specific work per unit fuel mass flow (kJ/kg)	26,439	27,399	28,730
CO_2 emissions (Mt/year)	0.2971	0.2867	0.2734
CO_2 emissions saved (kg CO_2/kWh)	--	0.0035	0.0083

Regarding the configuration of case D, the maximum solar thermal power that could be integrated before the economizer was limited to 3 MW. However, looking at the T-Q diagram in Figure 10, the temperature evolutions of gas and steam are nearer, hinting at a more effective heat transfer inside the HRSG. Indeed, fuel saving reaches a maximum of 7.97%, more than twice the value obtained with 15 MW solar power in case C with just one-fifth of the solar power integrated, as may be observed in Figure 11. Consequently, overall cycle efficiency increases up to 59.79%, the highest value of the four configurations studied for the fuel-saving operation mode. As collected in Table 5, case D reaches a specific work of 28.7 kJ/kg fuel, leading to potential savings of 8.3 g CO_2/kWh with only 3 MW of integrated solar power. In addition, due to the lower operating temperatures for the solar heat exchanger, PTCs and PDRs could be used, with PTC and synthetic oils becoming a feasible option.

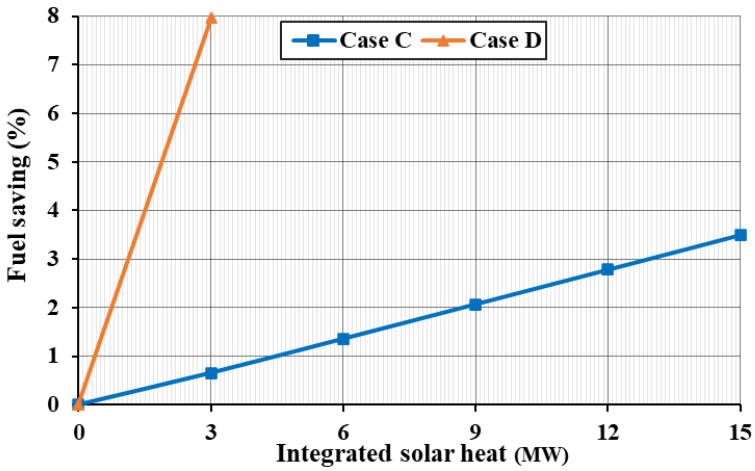

Figure 11. Fuel saving (%) for steam cycle integration options.

4.2. Power-Boosting Mode

4.2.1. Gas Cycle Integration

Table 6 collects the results from power-boosting operation when solar power is integrated into the top gas cycle. For case A, an extra power of 4 MW (4.41%) could be obtained by integrating 10 MW of solar thermal power. Generation capacity increased to 27.6 MJ/kg. However, the back work ratio increases slightly to 49.3% due to the higher air-fuel ratio, and the cycle efficiency drops to 55.19%. Temperatures for this case reaches 379 °C at state 2g and 430 °C at state $2g_{new}$, allowing the use of PTCs with solar molten salts, PDRs, or a heliostat field. Considering case B, global cycle parameters are the same as for case A. The main difference is the temperature of state 3g, which reaches 1129.5 °C for 10 MW of integrated solar thermal power, thus requiring a heliostat as the solar field technology. The evolution of power boosting and cycle efficiency as a function of the solar thermal power is depicted in Figure 12, where the increase in the power output alongside a slight decrease in the cycle efficiency becomes apparent.

Table 6. Original CC vs. ISCC (case A and case B) "Power boosting".

Solar Heat Integration	Original CC	ISCC Case C	ISCC Case D
Integrated solar heat (MW)	--	10	
Cycle efficiency	**Original CC**	**ISCC Case C**	**ISCC Case D**
Gas turbine cycle (%)	39.84	39.83	
Combined cycle (%)	56.13	55.19	
Cycle power breakdown	**Original CC**	**ISCC Case C**	**ISCC Case D**
Compressor (kW)	62,450	66,455	
Gas turbine (kW)	126,727	134,693	
Gas cycle (kW)	64,277	68,239	
Steam cycle (kW)	26,292	26,323	
Total net power (kW)	90,569	94,562	
Power boosted (%)	--	4.41	
Back work ratio (%)	49.279	49.33	
Specific work per unit fuel mass flow (kJ/kg)	26,439	27,605	

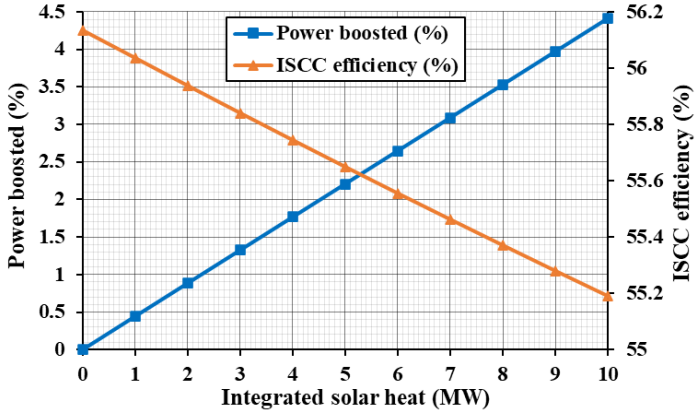

Figure 12. Power boosting (%) and cycle efficiency (%) for integration options A and B.

4.2.2. Steam Cycle Integration: Flowrate Boosting

Firstly, the results from flowrate boosting are discussed. In the configuration proposed in case C, a maximum of 4 MW solar thermal power could be integrated before the superheater, resulting in the T-Q diagram represented in Figure 13. As shown in Table 7, the cycle output power increased to 112.5 MW (24.2% boost) thanks to the increase in the steam flowrate from 25 to 45.84 kg/s. Consequently, overall cycle efficiency increased by 11.9%. Leaving the top gas cycle unaffected, it was possible to generate 32.8 MJ/kg fuel, increasing power production in 6.4 MJ/kg fuel. In case C, the maximum steam temperature at the solar heat exchanger was slightly above 300 °C, so selecting PTC technology with synthetic oil as HTF for the solar field becomes a feasible option.

Regarding the configuration of case D, the maximum solar thermal power that could be integrated before the economizer reached 12 MW. In the T-Q diagram of the HRSG shown in Figure 14, it may be appreciated how water and gas temperatures became slightly closer at the economizer stage. As collected in Table 7, the maximum output power was around 98.7 MW (8.96% boost), with overall cycle efficiency increasing up to 56.93%. The work per fuel unit mass increased to 28.8 MJ/kg. In this configuration, solar integration at the economizer allows to use both PDRs and PTCs, with PTC easily matching the low operating temperature ranges for case D.

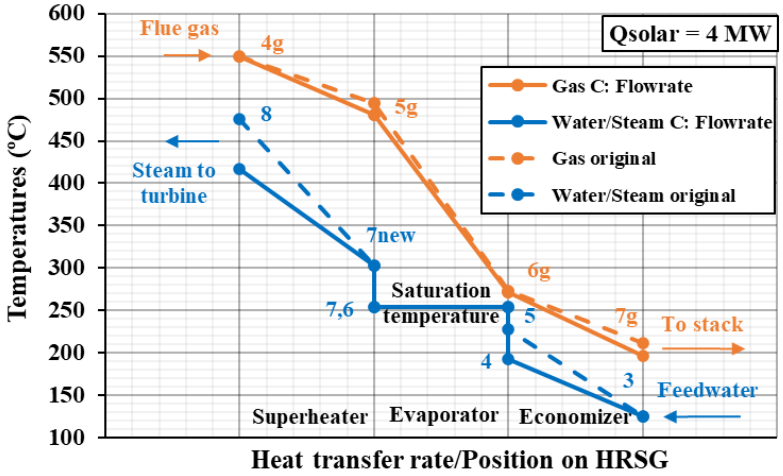

Figure 13. T-Q diagram for case C (flowrate power boosting).

Table 7. Original CC vs. Flowrate boosting (case C and case D).

Mass Flowrates	Original CC	ISCC Case C	ISCC Case D
LP evaporator mass flowrate (kg/s)	5	9.17	6.54
HP evaporator mass flowrate (kg/s)	25	45.84	32.72
Solar heat integration	**Original CC**	**ISCC Case C**	**ISCC Case D**
Integrated solar heat (MW)	--	4	12
Cycle efficiency	**Original CC**	**ISCC Case C**	**ISCC Case D**
Gas turbine cycle (%)	39.84	39.84	39.84
Combined cycle (%)	56.13	68.03	56.93
Cycle power breakdown	**Original CC**	**ISCC Case C**	**ISCC Case D**
Gas cycle (kW)	64,277	64,277	64,277
Steam cycle (kW)	26,292	48,214	34,412
Total net power (kW)	90,569	112,491	98,689
Power boosted (%)	--	24.2	8.96
Specific work per unit fuel mass flow (kJ/kg)	26,439	32,840	28,810

The evolution of the power boosted with respect to solar thermal power is depicted in Figure 15. Despite the limitation in the integrated solar power of 4 MW, the power boosting in case C, i.e., 24.2%, is almost three times the boost in case D for 12 MW of solar power: 8.96%.

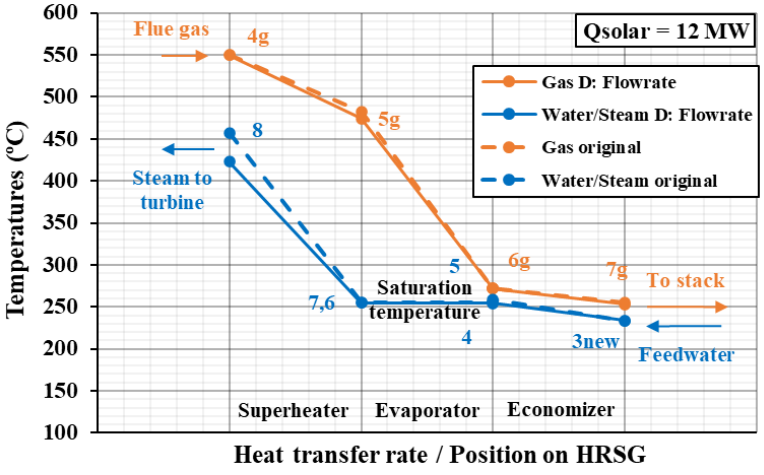

Figure 14. T-Q diagram for case D (flowrate power boosting).

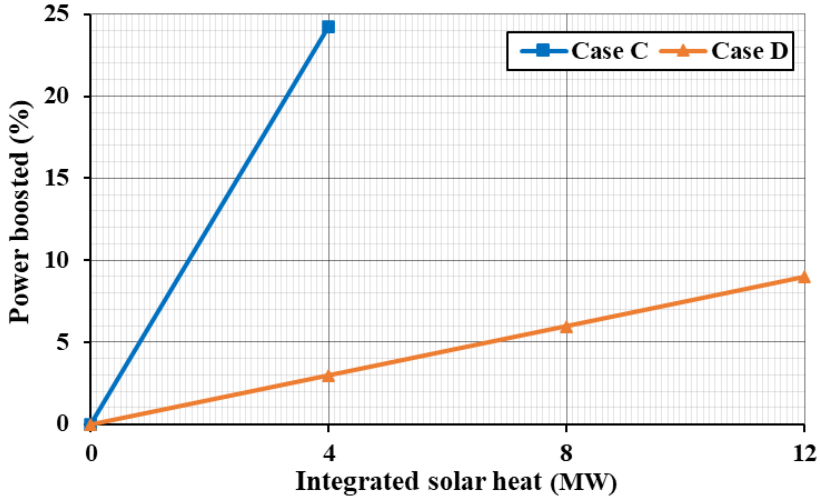

Figure 15. Flowrate power boosting (%) for steam cycle integration configurations.

4.2.3. Steam Cycle Integration: Parameter Boosting

Parameter boosting was the other option studied for power boosting through solar power integration at the bottom steam cycle. For the configuration of case C, several HP evaporator pressure values were studied, from −50% to +50% of the original value in 10% interval steps. (Please refer to Tables A5 and A6 for detailed results.) Operating pressure affected the maximum solar power that could be integrated into the cycle, increasing from 7 MW at −50% pressure to 9 MW at +50% pressure. Therefore, the comparison was performed at 7 MW to select the optimum operating pressure. It was observed that integrating 7 MW of solar power at the original HP evaporator pressure increased power generation by 2.18%, as shown in Figure 16. This figure shows the evolution of power boosting as a function of working pressure for 7 MW of integrated solar power, where it may be appreciated that reducing the pressure increases the power boosted. The minimum and maximum power-boosting values of 1.37 and 2.82% were obtained for the extremes of the studied pressure range: −50% pressure and + 50% pressure. Overall cycle efficiency also varied between 54.54% for the +50% pressure case and 55.32% for the −50% pressure case, as depicted in Figure 17. For case C, PTC can be used as the solar field technology for all the pressure values studied.

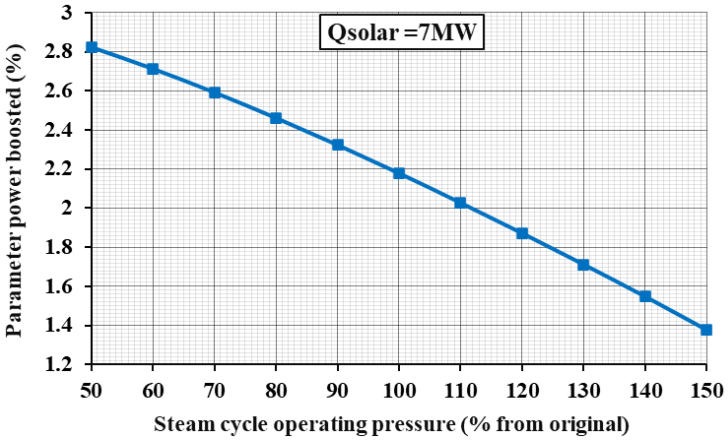

Figure 16. Parameter power boosting (%) at different pressure levels for case C.

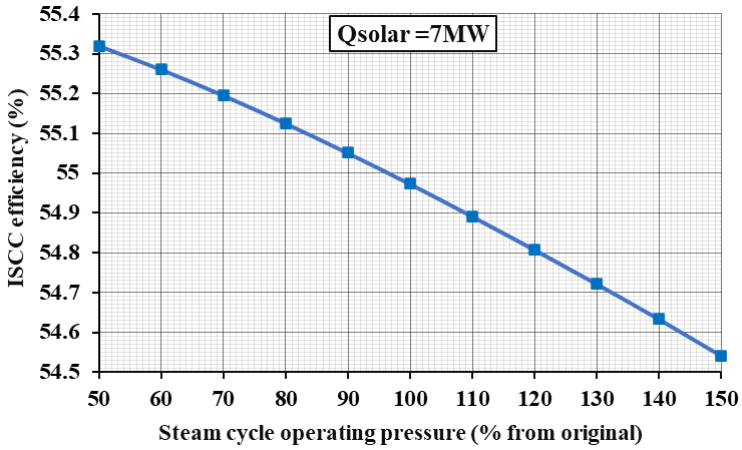

Figure 17. Overall efficiency at different pressure levels for case C.

As with −50% HP evaporator pressure the maximum power boost was obtained, the evolution of power boosting with respect to the integrated solar power is shown in Figure 18. It may be observed that just reducing evaporating pressure increases overall output power by 0.86% (0.77 MW) even without solar power; however, for 7 MW, power is boosted by 2.82% (2.5 MW). Figure 19 shows the temperature distribution inside the HRSG for this last case, where it may be appreciated that exhaust gas temperatures come nearer to steam temperatures.

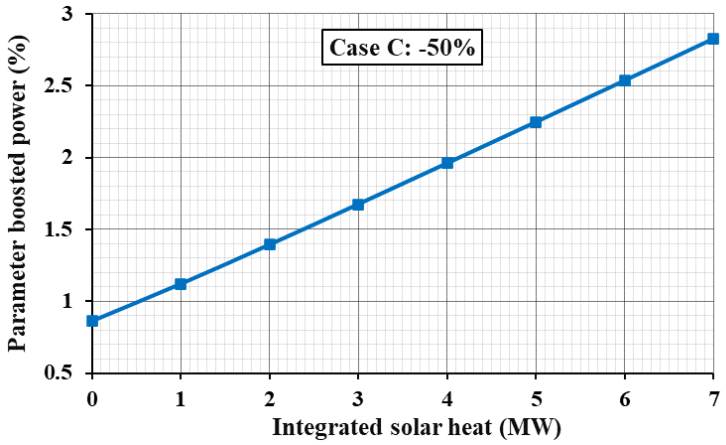

Figure 18. Parameter power boosting as a function of integrated solar power for case C: −50% HP.

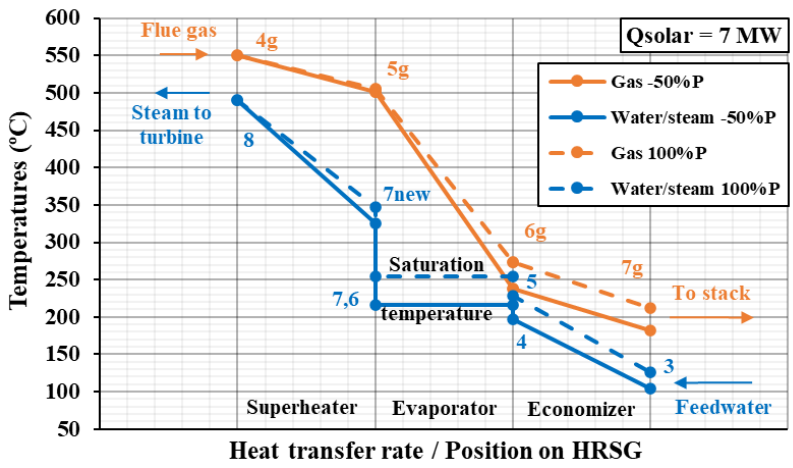

Figure 19. T-Q diagram for case C parameter power boosting (−50% HP evaporator pressure).

Considering solar power integration before the economizer (case D), the evaporator operating pressure was also changed between −50% and +50% of the original pressure at 10% intervals, with the detailed results collected in Tables A7 and A8. Again, the maximum solar thermal power that could be integrated was affected by the operating pressure, varying in the range between 1.5 and 2 MW. Hence, to compare results, a value of 1.5 MW was chosen. Figure 20 shows the power boosting as a function of the HP evaporator pressure. When 1.5 MW solar power was integrated at original operating conditions, the delivered power increased by 4.9%. As in case C, the increase in operating pressure decreased output power, reaching the lowest increase of 4.35% at the +50% pressure case (58.04% cycle efficiency). Nevertheless, for case D, it was possible to find a maximum in power boosting for the −30% pressure case, reaching 5.01% power boosting with respect to the original CC. As with flowrate boosting in case D, integrating the solar field before the economizer makes PTC technology with synthetic oils a suitable option.

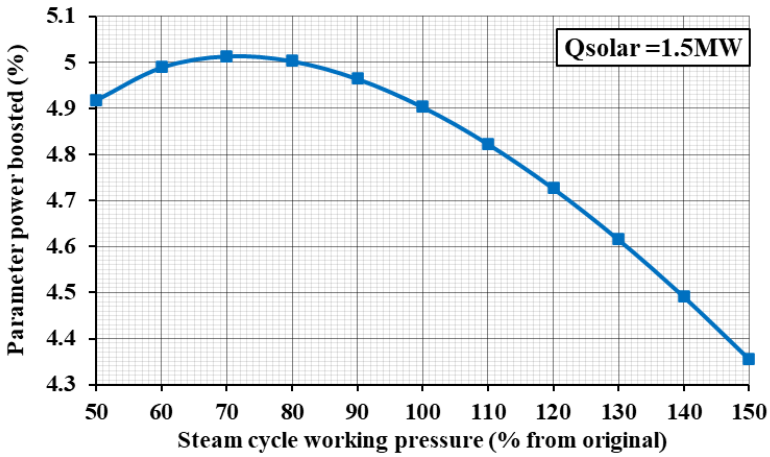

Figure 20. Parameter power boosting (%) at different pressure levels for case D.

Focusing on the −30% HP evaporator pressure, Figure 21 shows power boosting as a function of the integrated solar power, up to the maximum limit of 1.5 MW. It may be observed that the decrease in the evaporator pressure only increases overall output power by 41 kW (0.04%), so the effect of solar power integration becomes more determinant. Even with just 1.5 MW of solar power, power boosting is 5.01% (4.54 MW), with an overall cycle efficiency of 58.4%. Looking at the T-Q diagram of the HRSG under these conditions, shown in Figure 22, it may be appreciated that gas temperatures come much closer to water temperatures in both the economizer and superheater.

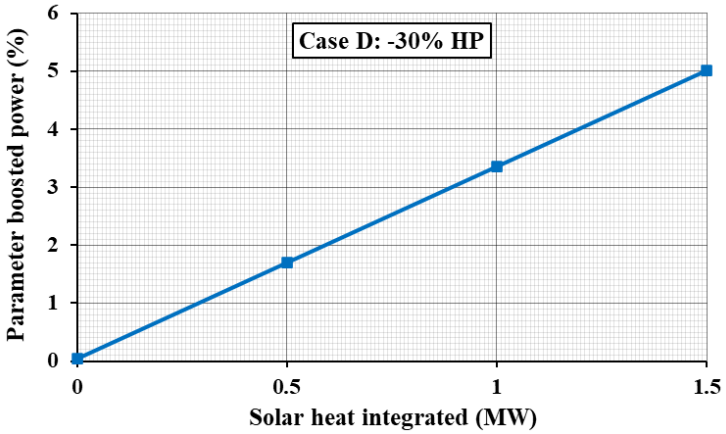

Figure 21. Parameter power boosting (%) as a function of integrated solar power for case D: −30%.

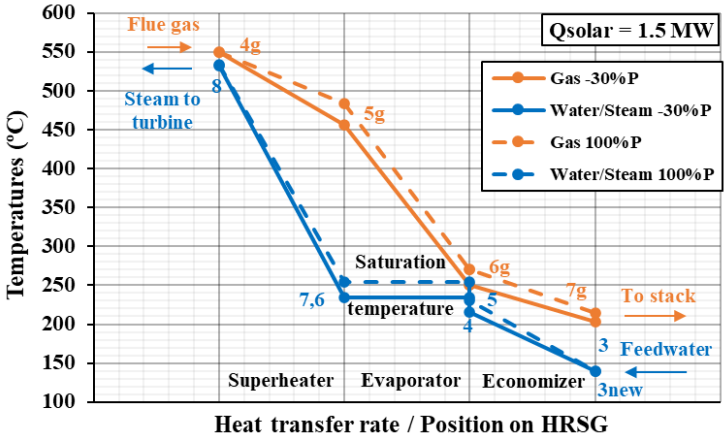

Figure 22. T-Q diagram for case D parameter power boosting (−30% LP evaporator pressure).

5. Discussion

From the analysis of the results, some considerations for solar thermal power integration in existing combined cycles were derived. Table 8 collects the main considerations obtained, while Figure 23 shows graphically the main guidelines to be followed for solar power integration, with the aim of providing the best course of action depending on the desired outcome.

Regarding fuel-saving operation, cases A and B must adapt to the same gas turbine inlet conditions, so both were able to save the same amount of fuel when 10 MW solar thermal power was integrated: 6.23%. However, case A exhibited better flexibility in terms of the solar field technology to be used (parabolic dish reflectors or heliostat field collectors), as it benefits from lower operating temperatures. For the steam cycle integration options, case C was only able to save 3.49% by requiring 15 MW of integrated solar thermal power, resulting in the lowest fuel savings per MW of solar power. However, it was the configuration that could integrate the highest solar power: 15 MW. The configuration presented in case D, on the contrary, allowed to reduce fuel consumption by 7.97% with just 3 MW of solar power. Due to its lower operating temperatures, parabolic trough collectors are a suitable option for solar power integration in the steam cycle. In addition, for the same integrated solar power of 3 MW, cases A and B were only able to save 1.87% of fuel, whereas case C had the lowest savings of all configurations: 0.65%.

Considering power-boosting operation, cases A and B can boost power by 4.41% with 10 MW of integrated solar power. However, the flowrate-boosting strategy with integration of solar power before the steam cycle superheater was found to have the best impact on the cycle. In this sense, an increase in cycle output power of 24.2% was found for case C when 4 MW of solar power was integrated. With the same solar power, case D was only able to increase cycle output power by 2.98%. Nevertheless, for the parameter-boosting strategy, the opposite behavior was observed. With 7 MW of integrated solar power, case C showed the lowest boosting performance, with only 2.82% when the HP evaporator pressure was reduced to half of that of the original cycle. On the other hand, with only 1.5 MW of integrated solar power, case D was able to boost power by 5.01% when the HP evaporator pressure was reduced to 70% of the original value.

Table 8. Considerations for integration of solar thermal power in existing combined cycles.

Strategy		Considerations/Recommendations for Solar Thermal Power Integration	
Fuel saving	A	• Parabolic dish reflector or heliostat field collector technology must be used. • Parabolic trough collector could be an alternative, but HTF must withstand high temperatures (molten salts). • Recommended if implementation at the top gas cycle is requested.	
	B	• Heliostat field collector technology must be used. • Not recommended due to technology restrictions.	
	C	• Parabolic dish reflector or heliostat field collector technology must be used. • Parabolic trough collector could be an alternative, but HTF must withstand high temperatures (molten salts). • Lowest fuel saving per MW of solar thermal power. • Can absorb the highest solar thermal power. • Recommended for maximizing solar power integration.	
	D	• Can work with all solar field technologies and HTFs. • Highest fuel saving per MW of solar thermal power. • Highest ISCC efficiency achieved among fuel-saving cases. • Recommended for fuel-saving operation.	
Power boosting	A	• Parabolic dish reflector or heliostat field collector technology must be used. • Parabolic trough collector could be an alternative, but HTF must withstand high temperatures (molten salts). • Lowest power boosting per MW of solar thermal power. • Recommended if implementation at the top gas cycle is requested.	
	B	• Heliostat field collector technology must be used. • Lowest power boosting per MW of solar thermal power. • Not recommended due to technology restrictions and low efficiency.	
	C	Flowrate	• Can work with all solar field technologies and HTFs. • Highest power boosting per MW of solar thermal power. • Highest ISCC efficiency achieved. • Recommended for power-boosting operation.
		Parameter	• Can work with all solar field technologies and HTFs. • Low power boosting per MW of solar thermal power. • Not recommended.
	D	Flowrate	• Can work with all solar field technologies and HTFs. • Is clearly outperformed by flowrate option C. • Not recommended.
		Parameter	• Can work with all solar field technologies and HTFs. • Maximizes power boosting for solar power < 1.5 MW. • Recommended for low solar thermal power values.

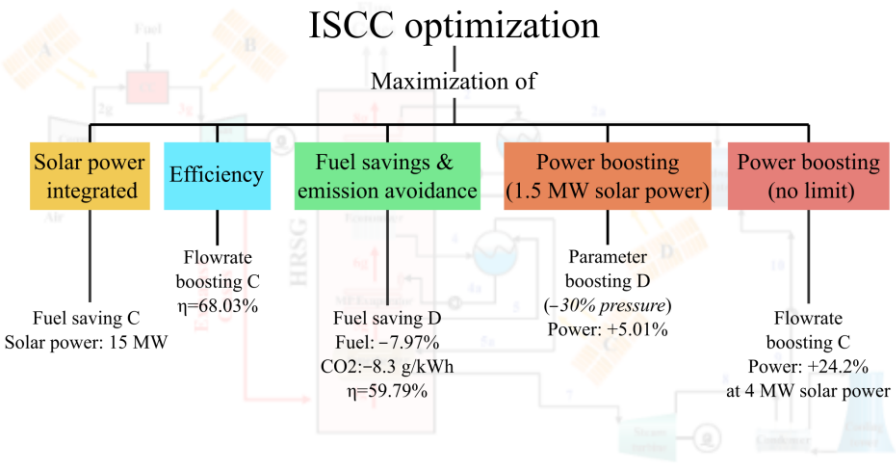

Figure 23. Optimum ISCC strategies depending on the desired outcome.

Finally, the results of this work may be compared with relevant findings from the recent literature. Abdel Dayem et al. [28] found that the increase in DNI, due to changes in climate conditions, could increase steam turbine power by 10%. In the present work, it was found that with only 4 MW of solar power, the steam turbine power could be increased by 24.2% with a flowrate-boosting strategy. The results from Aghdam et al. [32] revealed an increase of 2% in the plant efficiency and from 714 to 728 MW in the plant capacity when the solar field was integrated before the superheater of the bottom steam cycle. In the present work, for the same integration point and with a flowrate-boosting strategy, power was boosted by 24.2%, and the cycle efficiency increased by 11.9%. Comparing the results of the present work with the work of Barigozzi et al. [22], it was also found that power-boosting strategies with solar integration at the bottom steam cycle performed better than those with integration at the top gas cycle. Behar [23] proposed PTCs with synthetic oil as HTF as the most efficient method for solar power integration at the bottom steam cycle. However, it was found that this technology is not suited for all types of solar integration at the bottom steam cycle (see case C for fuel saving). Nevertheless, PTC is the most suitable technology for most of the bottom steam cycle-integration cases. Elmohalawy [25] found an increase in thermal efficiency of 1.2% when steam was injected at the high pressure level. In the present work, the highest efficiency increase, 11%, was found when integrating solar power before the high-pressure superheater to heat saturated steam. Finally, Ameri and Mohammadzadeh [34] found an increase of 6 MW in power generation and a reduction of 10 g/kWh in carbon emissions when the solar field was integrated before the superheater of the bottom steam cycle for a total power output of 300 MW. In the present work, output power was boosted by 22 MW (24.2%) and 2.6 MW (2.82%) for flowrate and parameter boosting, respectively, and carbon emissions could be reduced by 3.5 g/kWh for total power outputs of 112.5 and 93.1 MW.

6. Conclusions

With the focus set on the optimization of the efficiency of combined cycles and a reduction in fuel consumption and carbon emissions, the integration of solar power in a real and existing combined cycle power plant was analyzed in this work. Using a thermodynamic model, it is possible to provide recommendations for solar power integration in combined cycles depending on the desired outcome. In this sense, the results from this work could be valuable for the specific retrofitting of existing combined cycle power plants with different technical or environmental constraints.

The integration of solar power increases the energy content of the cycle streams. Integration at the top gas cycle level may be constrained due to the higher temperatures and technical requirements of the solar field and heat transfer fluid. In this sense, integration

should be performed after the compressor and before the combustion chamber to allow for the use of either parabolic dish reflectors or heliostat field collectors. However, high-temperature heat transfer fluids such as molten salts should be used. It is thus advisable to integrate solar power at the bottom steam cycle to also allow for the use of parabolic trough collectors and other heat transfer fluids.

Considering the effects of power integration on the cycle, if the objective is to integrate as much solar power as possible, then the best option is to perform the integration before the superheater of the steam cycle for fuel saving. If the aim is to increase overall cycle efficiency, the best option is integrating solar power before the steam cycle superheater with a flowrate-boosting strategy. If focus is set on reducing fuel consumption and avoiding carbon emissions, then a fuel-saving strategy by solar power integration before the economizer is the best option. Finally, if the objective is to boost power as much as possible, depending on the available solar resource, two different strategies are recommended. For small solar field sizes, a parameter-boosting strategy with solar integration before the economizer is the best choice. If there is no limit on the solar field size, flowrate boosting by integrating solar power before the superheater is the best option.

Future works could focus on the dynamic study of the ISCC configurations proposed in this work, coupling the model to a comprehensive solar database for different locations. Another research interest could be coupling the ISCC with a heat storage system to continue using renewable energy during the night. In addition, combinations of the proposed integrating positions could be studied at the same time and compared with the single-integration cases. Finally, a solar field design based on the maximum solar power to be integrated and an economic study could help to decide the best option for solar power integration for each particular situation.

Author Contributions: Conceptualization, I.S.-R. and A.M.-F.; methodology, A.M.A., A.M.-F., and I.S.-R.; software, A.M.A., A.M.-F., and I.S.-R.; validation, I.S.-R. and A.M.-F.; formal analysis, A.M.A., A.M.-F., and I.S.-R.; investigation, A.M.A., A.M.-F., and I.S.-R.; resources, A.M.-F. and I.S.-R.; data curation, A.M.A., A.M.-F., and I.S.-R.; writing—original draft preparation, A.M.A. and A.M.-F.; writing—review and editing, A.M.-F. and I.S.-R.; visualization, A.M.A., A.M.-F., and I.S.-R.; supervision, A.M.-F. and I.S.-R.; project administration, I.S.-R. All authors have read and agreed to the published version of the manuscript.

Funding: This research received no external funding.

Data Availability Statement: The original contributions presented in the study are included in the article material; further inquiries can be directed to the corresponding author.

Conflicts of Interest: The authors declare no conflicts of interest.

Appendix A. Detailed Results of Each Studied Configuration

Table A1. Original CC vs. ISCC (Case A and Case B) "Fuel saving".

Mass Flowrates	Original CC	ISCC Case A	ISCC Case B
Air to fuel ratio	50	53.39	53.39
Turbine gas flowrate (kg/s)	174.7	174.7	174.7
Air flowrate (kg/s)	171.28	171.49	171.49
Fuel flowrate (kg/s)	3.42	3.21	3.21
Fuel saving (%)	--	6.23	6.23
LP evaporator mass flowrate (kg/s)	5	5	5
HP evaporator mass flowrate (kg/s)	25	25	25
Operating temperatures	**Original CC**	**ISCC Case A**	**ISCC Case B**
Compressor inlet (°C)	24	24	24
Combustion chamber inlet (°C)	378	431	378
Gas turbine inlet (°C)	1174	1174	1174

Gas turbine outlet (°C)	549	549	549
Solar heat integration	**Original CC**	**ISCC Case A**	**ISCC Case B**
Integrated solar heat (MW)	--	10	
Cycle efficiency	**Original CC**	**ISCC Case A**	**ISCC Case B**
Gas turbine cycle (%)	39.84	39.85	
Combined cycle (%)	56.13	56.15	
Cycle power breakdown	**Original CC**	**ISCC Case A**	**ISCC Case B**
Compressor (kW)	62,450	62,450	62,450
Gas turbine (kW)	126,727	126,727	126,727
Gas cycle (kW)	64,277	64,277	64,277
Steam cycle (kW)	26,292	26,292	26,292
Total net power (kW)	90,569	90,569	90,569
Back work ratio (%)	49.279	49.279	49.279
Specific work per unit fuel mass flow (kJ/kg)	26,439	28,198	28,198
CO_2 emissions (Mt/year)	0.2971	0.2785	0.2785
CO_2 emissions saved (kg CO_2/kWh)	--	0.0064	0.0064

Table A2. Original CC vs. ISCC (Case C and Case D) "Fuel saving".

Mass Flowrates	**Original CC**	**ISCC Case C**	**ISCC Case D**
Air to fuel ratio	50	50	50
Turbine gas flowrate (kg/s)	174.7	168.59	160.7
Air flowrate (kg/s)	171.28	165.28	157.61
Fuel flowrate (kg/s)	3.42	3.3	3.15
Fuel saving (%)	--	3.49	7.97
LP evaporator mass flowrate (kg/s)	5	5	5
HP evaporator mass flowrate (kg/s)	25	25	25
Operating temperatures	**Original CC**	**ISCC Case C**	**ISCC Case D**
Compressor inlet (°C)	24	24	24
Combustion chamber inlet (°C)	378	378	378
Gas turbine inlet (°C)	1174	1174	1174
Gas turbine outlet (°C)	549	549	549
Solar heat integration	**Original CC**	**ISCC Case C**	**ISCC Case D**
Integrated solar heat (MW)	--	15	3
Cycle efficiency	**Original CC**	**ISCC Case C**	**ISCC Case D**
Gas turbine cycle (%)	39.84	39.84	39.84
Combined cycle (%)	56.13	53.06	59.79
Cycle power breakdown	**Original CC**	**ISCC Case C**	**ISCC Case D**
Compressor (kW)	62,450	60,266	57,471
Gas turbine (kW)	126,727	122,294	116,622
Gas cycle (kW)	64,277	62,028	59,152
Steam cycle (kW)	26,292	28,542	31,417
Total net power (kW)	90,569	90,569	90,569
Back work ratio (%)	49.279	49.279	49.279
Specific work per unit fuel mass flow (kJ/kg)	26,439	27,399	28,730
CO_2 emissions (Mt/year)	0.2971	0.2867	0.2734
CO_2 emissions saved (kg CO_2/kWh)	--	0.0035	0.0083

Table A3. Original CC vs. ISCC (Case A and Case B) "Power boosting".

Mass Flowrates	**Original CC**	**ISCC Case A**	**ISCC Case B**
Air to fuel ratio	50	53.2	
Turbine gas flowrate (kg/s)	174.7	185.68	
Air flowrate (kg/s)	171.28	182.25	
Fuel flowrate (kg/s)	3.42	3.42	3.42
LP evaporator mass flowrate (kg/s)	5	5	5
HP evaporator mass flowrate (kg/s)	25	25	25
Operating temperatures	**Original CC**	**ISCC Case A**	**ISCC Case B**
Compressor inlet (°C)	24	24	24
Combustion chamber inlet (°C)	378	430	378
Gas turbine inlet (°C)	1174	1174	1174
Gas turbine outlet (°C)	549	549	549
Solar heat integration	**Original CC**	**ISCC Case A**	**ISCC Case B**
Integrated solar heat (MW)	--	10	
Cycle efficiency	**Original CC**	**ISCC Case A**	**ISCC Case B**
Gas turbine cycle (%)	39.84	39.83	
Combined cycle (%)	56.13	55.19	
Cycle power breakdown	**Original CC**	**ISCC Case A**	**ISCC Case B**
Compressor (kW)	62,450	66,455	
Gas turbine (kW)	126,727	134,693	
Gas cycle (kW)	64,277	68,239	
Steam cycle (kW)	26,292	26,323	
Total net power (kW)	90,569	94,562	
Power boosted (%)	--	4.41	
Back work ratio (%)	49.279	49.33	
Specific work per unit fuel mass flow (kJ/kg)	26,439	27,605	

Table A4. Original CC vs. ISCC (Case C and Case D) "Flowrate boosting".

Mass Flowrates	**Original CC**	**ISCC Case C**	**ISCC Case D**
Air to fuel ratio	50	50	50
Turbine gas flowrate (kg/s)	174.7	174.7	174.7
Air flowrate (kg/s)	171.28	171.28	171.28
Fuel flowrate (kg/s)	3.42	3.42	3.42
LP evaporator mass flowrate (kg/s)	5	9.17	6.54
HP evaporator mass flowrate (kg/s)	25	45.84	32.72
Operating temperatures	**Original CC**	**ISCC Case C**	**ISCC Case D**
Compressor inlet (°C)	24	24	24
Combustion chamber inlet (°C)	378	378	378
Gas turbine inlet (°C)	1174	1174	1174
Gas turbine outlet (°C)	549	549	549
Inlet steam temperature (°C)	457	416.5	423
Pinch temperature (°C)	17.5	17.3	17
Economizer outlet temperature (°C)	228	192.5	254.5
Approach temperature (°C)	28	62	0.5
Operating pressures	**Original CC**	**ISCC Case C**	**ISCC Case D**
Inlet steam pressure (bar)	43	43	43
LP evaporator pressure (bar)	2.4	2.4	2.4
Condenser pressure (bar)	0.08	0.08	0.08
Solar heat integration	**Original CC**	**ISCC Case C**	**ISCC Case D**

Integrated solar heat (MW)	--	4	12
Cycle efficiency	**Original CC**	**ISCC Case C**	**ISCC Case D**
Gas turbine cycle (%)	39.84	39.84	39.84
Combined cycle (%)	56.13	68.03	56.93
Cycle power breakdown	**Original CC**	**ISCC Case C**	**ISCC Case D**
Compressor (kW)	62,450	62,450	62,450
Gas turbine (kW)	126,727	126,727	126,727
Gas cycle (kW)	64,277	64,277	64,277
Steam cycle (kW)	26,292	48,214	34,412
Total net power (kW)	90,569	112,491	98,689
Power boosted (%)	--	24.2	8.96
Back work ratio (%)	49.279	49.279	49.279
Specific work per unit fuel mass flow (kJ/kg)	26,439	32,840	28,810

Table A5. Original CC vs. Parameter boosting "Case C" (+10%, +20%, +30%, +40%, and +50%).

Mass Flowrates	**Original ISCC**	**ISCC "Case C" (Superheater)**				
		+10%	**+20%**	**+30%**	**+40%**	**+50%**
Turbine gas flowrate (kg/s)	174.7					
Air flowrate (kg/s)	171.27					
Fuel flowrate (kg/s)	3.42					
LP evaporator mass flowrate (kg/s)	5					
HP evaporator mass flowrate (kg/s)	25					
Operating temperatures	**Original ISCC**	**+10%**	**+20%**	**+30%**	**+40%**	**+50%**
Compressor inlet (°C)	24					
Combustion chamber inlet (°C)	379					
Gas turbine inlet (°C)	1174					
Gas turbine outlet (°C)	549					
Inlet steam temperature (°C)	491	491	490.5	490.5	490	489.5
Pinch temperature (°C)	19.3	19	18.5	18.2	17.9	17.5
Economizer outlet temperature (°C)	228	232.5	237	241	244.5	48
Approach temperature (°C)	26.5	27.5	29	30	31	32
Operating pressures	**Original ISCC**	**+10%**	**+20%**	**+30%**	**+40%**	**+50%**
Inlet steam pressure (bar)	2.4	2.64	2.88	3.12	3.36	3.6
LP evaporator pressure (bar)	43	47.3	51.6	55.9	60.2	64.5
Condenser pressure (bar)	0.08					
Solar heat integration	**Original ISCC**	**+10%**	**+20%**	**+30%**	**+40%**	**+50%**
Integrated solar heat (MW)	7					
Cycle efficiency	**Original ISCC**	**+10%**	**+20%**	**+30%**	**+40%**	**+50%**
Gas turbine cycle (%)	39.84					
Combined cycle (%)	54.97	54.89	54.81	54.72	54.63	54.54
Cycle power breakdown	**Original ISCC**	**+10%**	**+20%**	**+30%**	**+40%**	**+50%**
Compressor (kW)	62,450					
Gas turbine (kW)	126,727					
Gas cycle (kW)	64,277					

Steam cycle (kW)	28,265	28,128	27,987	27,843	27,694	27,539
Total net power (kW)	92,542	92,405	92,264	92,120	91,971	91,816
Power boosted (%)	2.18	2.02	1.87	1.71	1.55	1.37
Back work ratio (%)	49.279					
Specific work per unit fuel mass flow (kJ/kg)	27,016	26,976	26,935	26,892	26,849	26,804

Table A6. Original CC vs. Parameter boosting "Case C" (−10%, −20%, −30%, −40%, and −50%).

Mass Flowrates	**Original ISCC**	**ISCC "Case C" (Superheater)**				
		−10%	**−20%**	**−30%**	**−40%**	**−50%**
Turbine gas flowrate (kg/s)	174.7					
Air flowrate (kg/s)	171.27					
Fuel flowrate (kg/s)	3.42					
LP evaporator mass flowrate (kg/s)	5					
HP evaporator mass flowrate (kg/s)	25					
Operating temperatures	**Original ISCC**	**−10%**	**−20%**	**−30%**	**−40%**	**−50%**
Compressor inlet (°C)	24					
Combustion chamber inlet (°C)	379					
Gas turbine inlet (°C)	1174					
Gas turbine outlet (°C)	549					
Inlet steam temperature (°C)	491	491	491	491	491	490.5
Pinch temperature (°C)	19.3	19.7	20	20.5	21.	21.5
Economizer outlet temperature (°C)	228	223	218	212	205	197.5
Approach temperature (°C)	26.5	25	23.5	22	20.5	18.5
Operating pressures	**Original ISCC**	**−10%**	**−20%**	**−30%**	**−40%**	**−50%**
Inlet steam pressure (bar)	43	38.7	34.4	30.1	25.8	21.5
LP evaporator pressure (bar)	2.4	2.16	1.92	1.68	1.44	1.2
Condenser pressure (bar)	0.08					
Solar heat integration	**Original ISCC**	**−10%**	**−20%**	**−30%**	**−40%**	**−50%**
Integrated solar heat (MW)	7					
Cycle efficiency	**Original ISCC**	**−10%**	**−20%**	**−30%**	**−40%**	**−50%**
Gas turbine cycle (%)	39.84					
Combined cycle (%)	54.97	55.05	55.12	55.19	55.26	55.32
Cycle power breakdown	**Original ISCC**	**−10%**	**−20%**	**−30%**	**−40%**	**−50%**
Compressor (kW)	62,450					
Gas turbine (kW)	126,727					
Gas cycle (kW)	64,277					
Steam cycle (kW)	28,265	28,396	28,521	28,640	28,750	28,849
Total net power (kW)	92,542	92,673	92,798	92,917	93,027	93,126
Power boosted (%)	2.18	2.32	2.46	2.59	2.71	2.82
Back work ratio (%)	49.279					
Specific work per unit fuel mass flow (kJ/kg)	27,016	27,054	27,091	27,125	27,157	27,186

Table A7. Original CC vs. Parameter boosting "Case D" (+10%, +20%, +30%, +40%, and +50%).

Mass Flowrates	Original ISCC	ISCC "Case D" (Economizer)				
		+10%	+20%	+30%	+40%	+50%
Turbine gas flowrate (kg/s)			174.7			
Air flowrate (kg/s)			171.27			
Fuel flowrate (kg/s)			3.42			
LP evaporator (kg/s)			5			
HP evaporator kg/s)			25			
Operating temperatures	**Original ISCC**	**+10%**	**+20%**	**+30%**	**+40%**	**+50%**
Compressor inlet (°C)			24			
Combustion chamber inlet (°C)			379			
Gas turbine inlet (°C)			1174			
Gas turbine outlet (°C)			549			
Inlet steam temperature (°C)	534	534.5	535	535	535	534.5
Pinch temperature (°C)	15	15	14.5	14	13.5	13.5
Economizer outlet temperature (°C)	229	233	236	239.5	242	245
Approach temperature (°C)	25.5	27.5	29.5	31.5	33.5	35
Operating pressures	**Original ISCC**	**+10%**	**+20%**	**+30%**	**+40%**	**+50%**
Inlet steam (bar)	43	47.3	51.6	55.9	60.2	64.5
LP evaporator (bar)	2.4	2.64	2.88	3.12	3.36	3.6
Condenser (bar)			0.08			
Solar heat integration	**Original ISCC**	**+10%**	**+20%**	**+30%**	**+40%**	**+50%**
Integrated solar heat (MW)			1.5			
Cycle efficiency	**Original ISCC**	**+10%**	**+20%**	**+30%**	**+40%**	**+50%**
Gas turbine cycle (%)			39.84			
Combined cycle (%)	58.34	58.3	58.24	58.18	58.65	58.04
Cycle power breakdown	**Original ISCC**	**+10%**	**+20%**	**+30%**	**+40%**	**+50%**
Compressor (kW)			62,450			
Gas turbine (kW)			126,727			
Gas cycle (kW)			64,277			
Steam cycle (kW)	30,733	30,660	30,573	30,472	30,360	30,237
Total net power (kW)	95,010	94,937	94,850	94,749	94,637	94,514
Power boosted (%)	4.9	4.82	4.72	4.61	4.49	4.35
Back work ratio (%)			49.279			
Specific work per unit fuel mass flow (kJ/kg)	27,736	27,715	27,689	27,660	27,627	27,591

Table A8. Original CC vs. Parameter boosting "Case D" (−10%, −20%, −30%, −40%, −50%).

Mass Flowrates	Original ISCC	ISCC "Case D" (Economizer)				
		−10%	−20%	−30%	−40%	−50%
Turbine gas flowrate (kg/s)			174.7			
Air flowrate (kg/s)			171.27			
Fuel flowrate (kg/s)			3.42			
LP evaporator (kg/s)			5			
HP evaporator kg/s)			25			
Operating temperatures	**Original ISCC**	**−10%**	**−20%**	**−30%**	**−40%**	**−50%**
Compressor inlet (°C)			24			
Combustion chamber inlet (°C)			379			
Gas turbine inlet (°C)			1174			

Gas turbine outlet (°C)			549			
Inlet steam temperature (°C)	534	533	532	530	527.5	524.5
Pinch temperature (°C)	15	15.5	16	16.5	17.5	18
Economizer outlet temperature (°C)	229	225	221	216	211	205
Approach temperature (°C)	25.5	23	20.5	18	14.5	11
Operating pressures	**Original ISCC**	**−10%**	**−20%**	**−30%**	**−40%**	**−50%**
Inlet steam (bar)	43	38.7	34.4	30.1	25.8	21.5
LP evaporator (bar)	2.4	2.16	1.92	1.68	1.44	1.2
Condenser (bar)			0.08			
Solar heat integration	**Original ISCC**	**−10%**	**−20%**	**−30%**	**−40%**	**−50%**
Solar heat (MW)			1.5			
Cycle efficiency	**Original ISCC**	**−10%**	**−20%**	**−30%**	**−40%**	**−50%**
Gas turbine cycle (%)			39.84			
Combined cycle (%)	58.34	58.38	58.4	58.4	58.39	58.35
Cycle power breakdown	**Original ISCC**	**−10%**	**−20%**	**−30%**	**−40%**	**−50%**
Compressor (kW)			62,450			
Gas turbine (kW)			126,727			
Gas cycle (kW)			64,277			
Steam cycle (kW)	30,733	30,788	30,823	30,833	30,811	30,746
Total net power (kW)	95,010	95,065	95,100	95,110	95,088	95,023
Power boosted (%)	4.9	4.96	5	5.01	4.98	4.92
Back work ratio (%)			49.279			
Specific work per unit fuel mass flow (kJ/kg)	27,736	27,752	27,762	27,765	27,759	27,740

References

1. U.S Energy Information Administration "EIA". Energy Institute Statistical Review of World Energy. 2012. Available online: https://ourworldindata.org/ (accessed on15 November 2024).
2. Enerdata. World Energy & Climate Statistics—Yearbook 2024. Available online: https://yearbook.enerdata.net/total-energy/world-consumption-statistics.html (accessed on 1 November 2024).
3. Shahabuddin, M.; Bhattacharya, S. Effect of reactant types (steam, CO_2 and steam + CO_2) on the gasification performance of coal using entrained flow gasifier. *Int. J. Energy Res.* **2021**, *45*, 9492–9501. https://doi.org/10.1002/er.6475.
4. Alam, M.T.; Dai, B.; Wu, X.; Hoadley, A.; Zhang, L. A critical review of ash slagging mechanisms and viscosity measurement for low-rank coal and bio-slags. *Front. Energy* **2021**, *15*, 46–67. https://doi.org/10.1007/s11708-020-0807-8.
5. REN21. Renewables 2023 Global Status Report: Energy Supply Module. 2023. Available online: https://www.ren21.net/wp-content/uploads/2019/05/GSR-2023_Energy-Supply-Module.pdf (accessed on 15 November 2024).
6. Statista. Global Data and Business Intelligence Platform with an Extensive Collection of Statistics. 2023. Available online: https://www.statista.com/ (accessed on 5 August 2024).
7. Imteaz, M.A.; Shanableh, A.; Rahman, A.; Ahsan, A. Optimisation of rainwater tank design from large roofs: A case study in Melbourne, Australia. *Resour. Conserv. Recycl*. **2011**, *55*, 1022–1029. https://doi.org/10.1016/j.resconrec.2011.05.013.
8. Gielen, D.; Boshell, F.; Saygin, D.; Bazilian, M.D.; Wagner, N.; Gorini, R. The role of renewable energy in the global energy transformation. *Energy Strateg. Rev.* **2019**, *24*, 38–50. https://doi.org/10.1016/j.esr.2019.01.006.
9. Zhu, L.; Fang, W.; Rahman, S.U.; Khan, A.I. How solar-based renewable energy contributes to CO_2 emissions abatement? Sustainable environment policy implications for solar industry". *Energy Environ.* **2023**, *34*, 359–378. https://doi.org/10.1177/0958305X211061886.
10. Weldekidan, H.; Strezov, V.; Town, G. Review of solar energy for biofuel extraction. Renew. Sustain. *Energy Rev.* **2018**, *88*, 184–192. https://doi.org/10.1016/j.rser.2018.02.027.
11. Tsoutsos, T.; Frantzeskaki, N.; Gekas, V. Environmental impacts from the solar energy technologies. *Energy Policy* **2005**, *33*, 289–296. https://doi.org/10.1016/S0301-4215(03)00241-6.
12. International Renewable Energy Agency "IRENA". Future of Solar Photovoltaic. 2019. Available online: https://www.irena.org/-/media/Files/IRENA/Agency/Publication/2019/Nov/IRENA_Future_of_Solar_PV_2019.pdf (accessed on 25 October 2024).

13. U.S. Department of Energy. Solar Parabolic Trough. 2009. Available online: https://www1.eere.energy.gov/ba/pba/pdfs/solar_trough.pdf (accessed on 31 October 2024).
14. Rovira, A.; Montes, M.J.; Varela, F.; Gil, M. Comparison of Heat Transfer Fluid and Direct Steam Generation technologies for Integrated Solar Combined Cycles. *Appl. Therm. Eng*. **2013**, *52*, 264–274. https://doi.org/10.1016/j.applthermaleng.2012.12.008.
15. The World Bank. Implementation Completion and Results Report (TF-91289) on A Grand in The Amount of US $49.80 Million to the Arab Republic of Egypt for the Kuraymat Solar Thermal Hybrid Project. 2012. Available online: http://documents.worldbank.org/curated/en/168831468332487486/Main-report (accessed on 15 November 2024).
16. Islam, M.T.; Huda, N.; Abdullah, A.B.; Saidur, R. A comprehensive review of state-ofthe-art concentrating solar power (CSP) technologies: Current status and research trends. *Renew. Sustain. Energy Rev.* **2018**, *91*, 987–1018. https://doi.org/10.1016/j.rser.2018.04.097.
17. Sumayli, H.; El-Leathy, A.; Danish, S.N.; Al-Ansary, H.; Almutairi, Z.; Al-Suhaibani, Z.; Saleh, N.S.; Saeed, R.S.; Alswaiyd, A.; Djajadiwinata, E.; et al. Integrated CSP-PV hybrid solar power plant for two cities in Saudi Arabia. *Case Stud. Therm. Eng.* **2023**, *44*, 102835. https://doi.org/10.1016/j.csite.2023.102835.
18. Powell, K.M.; Rashid, K.; Ellingwood, K.; Tuttle, J.; Iverson, B.D. Hybrid concentrated solar thermal power systems: A review. *Renew. Sustain. Energy Rev*. **2017**, *80*, 215–237. https://doi.org/10.1016/j.rser.2017.05.067.
19. Pramanik, S.; Ravikrishna, R.V. A review of concentrated solar power hybrid technologies. *Appl. Therm. Eng*. **2017**, *127*, 602–637. https://doi.org/10.1016/j.applthermaleng.2017.08.038.
20. Wang, S.; Zhang, G.; Fu, Z. Performance analysis of a novel integrated solar combined cycle with inlet air heating system. *Appl. Therm. Eng*. **2019**, *161*, 114010. https://doi.org/10.1016/j.applthermaleng.2019.114010.
21. Barakat, S.; Ramzy, A.; Hamed, A.M.; El Emam, S.H. Enhancement of gas turbine power output using earth to air heat exchanger (EAHE) cooling system. *Energy Convers. Manag*. **2016**, *111*, 137–146. https://doi.org/10.1016/j.enconman.2015.12.060.
22. Barigozzi, R.; Franchini, G.; Perdichizzi, A.; Ravelli, S. Simulation of Solarized Combined Cycles: Comparison Between Hybrid GT and ISCC Plants. In Proceedings of the ASME Turbo Expo 2013: Turbine Technical Conference and Exposition, San Antonio, TX, USA, 3–7 June 2013; Volume 4. https://doi.org/10.1115/GT2013-95483.
23. Behar, O. Solar thermal power plants—A review of configurations and performance comparison. *Renew. Sustain. Energy Rev*. **2018**, *92*, 608–627. https://doi.org/10.1016/j.rser.2018.04.102.
24. Manente, G.; Rech, S.; Lazzaretto, A. Optimum choice and placement of concentrating solar power technologies in integrated solar combined cycle systems. *Renew. Energy* **2016**, *96*, 172–189. https://doi.org/10.1016/j.renene.2016.04.066.
25. Elmohlawy, A.E.; Ochkov, V.F.; Kazandzhan, B.I. Thermal performance analysis of a concentrated solar power system (CSP) integrated with natural gas combined cycle (NGCC) power plant. *Case Stud. Therm. Eng.* **2019**, *14*, 100458. https://doi.org/10.1016/j.csite.2019.100458.
26. Elmohlawy, A.E.; Ochkov, V.F.; Kazandzhan, B.I. Study and prediction the performance of an integrated solar combined cycle power plant. *Energy Procedia* **2019**, *156*, 72–78. https://doi.org/10.1016/j.egypro.2018.11.094.
27. Rovira, A.; Abbas, R.; Sánchez, C.; Muñoz, M. Proposal and analysis of an integrated solar combined cycle with partial recuperation. *Energy* **2020**, *198*, 117379. https://doi.org/10.1016/j.energy.2020.117379.
28. Dayem, A.M.A.; Metwally, M.N.; Alghamdi, A.S.; Marzouk, E.M. Numerical Simulation and Experimental Validation of Integrated Solar Combined Power Plant. *Energy Procedia* **2014**, *50*, 290–305. https://doi.org/10.1016/j.egypro.2014.06.036.
29. Muñoz, M.; Rovira, A.; Montes, M.J. Thermodynamic cycles for solar thermal power plants: A review. *WIREs Energy Environ*. **2022**, *11*, e420. https://doi.org/10.1002/wene.420.
30. Javadi, M.; Jafari Najafi, N.; Khalili Abhari, M.; Jabery, R.; Pourtaba, H. 4E analysis of three different configurations of a combined cycle power plant integrated with a solar power tower system. *Sustain. Energy Technol. Assess*. **2021**, *48*, 101599. https://doi.org/10.1016/j.seta.2021.101599.
31. Hosseini, R.; Soltani, M.; Valizadeh, G. Technical and economic assessment of the integrated solar combined cycle power plants in Iran. *Renew Energy* **2005**, *30*, 1541–1555. https://doi.org/10.1016/j.renene.2004.11.005.
32. Hajizadeh Aghdam, M.; khoshgoftar Manesh, M.H.; khani, N.; Yazdi, M. Energy, Exergy-Based and Emergy-Based Analysis of Integrated Solar PTC with a Combined Cycle Power Plant. *Int. J. Thermodyn*. **2021**, *24*, 17–30. https://doi.org/10.5541/ijot.902374.
33. Binamer, A.O. Al-Abdaliya integrated solar combined cycle power plant: Case study of Kuwait, part I. *Renew. Energy* **2019**, *131*, 923–937. https://doi.org/10.1016/j.renene.2018.07.076.
34. Ameri, M.; Mohammadzadeh, M. Thermodynamic, thermoeconomic and life cycle assessment of a novel integrated solar combined cycle (ISCC) power plant. *Sustain. Energy Technol. Assess*. **2018**, *27*, 192–205. https://doi.org/10.1016/j.seta.2018.04.011.
35. Achour, L.; Bouharkat, M.; Behar, O. Performance assessment of an integrated solar combined cycle in the southern of Algeria. *Energy Rep.* **2018**, *4*, 207–217. https://doi.org/10.1016/j.egyr.2017.09.003.
36. Manente, G. High performance integrated solar combined cycles with minimum modifications to the combined cycle power plant design. *Energy Covers. Manag.* **2016**, *111*, 186–197. https://doi.org/10.1016/j.enconman.2015.12.079.
37. Dolores, D.G.; Rafael, A.S.; Galileo, M.C. Estudio del acoplamiento de diferentes configuraciones de ciclo combinado con planta solar de canal parabólico. *Ing. Investig. Tecnol.* **2015**, *16*, 253–264. https://doi.org/10.1016/j.riit.2015.03.009.
38. Egyptian Petrochemicals Company. Available online: www.egy-petrochem.com (accessed on 26 November 2023).
39. Math Works. MATLAB Software. Available online: https://www.mathworks.com/products.html?s_tid=nav_products (accessed on 15 November 2024).

40. Math Works. Ideal Air Toolbox. Available online: https://www.mathworks.com/matlabcentral/fileexchange/71269-ideal-air-properties-at-constant-pressure-1-atm. (accessed on 19 April 2019).
41. Math Works. XSteam Toolbox. Available online: https://www.mathworks.com/matlabcentral/fileexchange/9817-x-steam-thermodynamic-properties-of-water-and-steam (accessed on 19 April 2019).
42. World Nuclear Association. Heat Values of Various Fuels. Available online: https://world-nuclear.org/information-library/facts-and-Figures/heat-values-of-various-fuels.aspx (accessed on 22 December 2023).
43. Bergman, T.L.; Lavine, A.S.; Incropera, F.P.; Dewitt, D.P. Heat Exchangers. In *Fundamentals of Heat and Mass Transfer*, 7th ed.; John Wiley & Sons, Inc.: Hoboken, NJ, USA, 2011; pp. 706–747.
44. "Recognized Document of the Regulation of Thermal Installations in Buildings (RITE)" Joint Resolution of the Ministries of Industry, Energy and Tourism, and the Ministry of Public Works. CO_2 Emission Factors and Passage Coefficients to Primary Energy. Available online: https://energia.gob.es/desarrollo/EficienciaEnergetica/RITE/Reconocidos/Reconocidos/Otrosdocumentos/Factores_emision_CO2.pdf (accessed on 15 October 2023).
45. World Weather & Climate Information. 2023. Available online: https://weather-and-climate.com/average-monthly-hours-Sunshine,Alexandria,Egypt (accessed on 20 July 2023).
46. Solutia. Therminol VP-1: Vapor Phase/Liquid Phase Heat Transfer Fluid. Available online: http://twt.mpei.ac.ru/tthb/hedh/htf-vp1.pdf (accessed on 18 July 2021).
47. Ruegamer, T.; Kamp, H.; Kuckelkorn, T.; Schiel, W.; Weinrebe, G.; Nava, P.; Riffelmann, K.; Richert, T. Molten Salt for Parabolic Trough Applications: System Simulation and Scale Effects. *Energy Procedia* **2014**, *49*, 1523–1532. https://doi.org/10.1016/j.egypro.2014.03.161.
48. Barlev, D.; Vidu, R.; Stroeve, P. Innovation in concentrated solar power. *Sol. Energy Mater. Sol. Cells*. **2011**, *95*, 2703–2725. https://doi.org/10.1016/j.solmat.2011.05.020.
49. Kalogirou, S.A. Solar thermal collectors and applications. *Prog. Energy Combust. Sci.* **2004**, *30*, 231–295. https://doi.org/10.1016/j.pecs.2004.02.001.